

Emergent Dynamics in Neocortical Microcircuits

THÈSE N° 4705 (2010)

PRÉSENTÉE LE 31 MAI 2010

À LA FACULTÉ SCIENCES DE LA VIE
LABORATOIRE DE NEUROSCIENCE DES MICROCIRCUITS
PROGRAMME DOCTORAL EN NEUROSCIENCES

ÉCOLE POLYTECHNIQUE FÉDÉRALE DE LAUSANNE

POUR L'OBTENTION DU GRADE DE DOCTEUR ÈS SCIENCES

PAR

Rodrigo DE CAMPOS PERIN

acceptée sur proposition du jury:

Prof. R. Schneggenburger, président du jury
Prof. H. Markram, directeur de thèse
Prof. M. Larkum, rapporteur
Prof. C. Petersen, rapporteur
Prof. M. Richardson, rapporteur



ÉCOLE POLYTECHNIQUE
FÉDÉRALE DE LAUSANNE

Suisse
2010

True wisdom comes to each of us when we realize how little we understand about life, ourselves,
and the world around us.

Socrates

Abstract

Interactions among neurons can take place in a wide variety of forms. It is the goal of this thesis to investigate the properties and implications of a number of these interactions that we believe are relevant for information processing in the brain.

Neuroscience has progressed considerably in identifying the diverse neuronal cell-types and providing detailed information about their individual morphological, genetic and electrophysiological properties. It remains a great challenge to identify how this diversity of cells interacts at the microcircuit level. This task is made more complex by the fact that the forms of interaction are not always obvious or simple to observe, even with advanced scientific equipment. In order to achieve a better understanding and envision possible implications of the concerted activity of multiple neurons, experiments and models must often be used jointly and iteratively.

In this thesis I first present the development of a computer-assisted system for multi-electrode patch-clamp that enabled new kinds of experiments, allowing qualitatively different information to be obtained concerning the interaction of multiple neurons.

In the following chapters I describe the different questions addressed and approaches utilized in the investigation of neuronal interactions using multi-electrode patch-clamp experiments. The principles behind the clustered organization of synaptic connectivity in Layer V of the somatosensory cortex are the first experimental finding presented. I then quantify the ephaptic coupling between neurons and how apparently minute signals might help correlate the activity of many neurons. Next, the ubiquity of a neocortical microcircuit responsible for frequency-dependent disynaptic inhibition is demonstrated and the summation properties of this microcircuit are then analyzed. Finally a model to explain the interactions between gap junctions and synaptic transmission in the olfactory bulb is proposed.

Keywords: neocortical microcircuitry, somatosensory cortex, juvenile rat, *in vitro* electrophysiology, multi-electrode, patch-clamp recording, synapse, gap junction, connectivity, clustering, plasticity, ephaptic, extracellular field, excitation, frequency-dependent disynaptic inhibition, acute brain slices, pyramidal cell, Martinotti cell.

Résumé

Les interactions entre les neurones peuvent se produire dans une large variété de formes. Le but de cette thèse est d'étudier les propriétés et les implications d'un certain nombre de ces interactions qui nous semblent importantes pour le traitement des informations dans le cerveau.

Les neurosciences ont considérablement progressé dans l'identification des divers types neuronaux ainsi qu'en fournissant des informations détaillées au niveau cellulaire concernant la morphologie, la génétique et les propriétés électrophysiologiques. C'est toutefois un défi de taille que d'identifier comment cette immense diversité de cellules interagissent au niveau du microcircuit neuronal. Cette tâche rencontre une difficulté supplémentaire dans le fait que les formes d'interactions ne sont pas toujours évidentes ou faciles à observer, même avec une technologie avancée. Pour parvenir à mieux comprendre et visualiser les implications possibles de l'activité commune de neurones multiples, des modèles doivent très souvent être utilisés et de façon répétée, conjointement aux expériences.

Dans cette thèse, nous décrivons tout d'abord le développement d'un système assisté par ordinateur pour le patch-clamp à électrodes multiples, qui a rendu possible des nouveaux types d'expériences, permettant d'obtenir informations qualitativement différentes concernant l'interaction de neurones multiples.

Dans les chapitres suivants nous décrivons les différentes questions abordées et les approches utilisées, pour l'investigation des interactions neuronales lors d'expériences de patch-clamp à électrodes multiples. Les premières découvertes expérimentales présentées dans cette thèse sont les principes derrière l'organisation synaptique regroupée dans la couche V du cortex somatosensoriel. Nous décrivons alors le couplage ephaptique entre neurones et comment des minuscules signaux semblent aider à corrélérer l'activité de nombreux neurones. Puis, nous présentons l'ubiquité d'un microcircuit néocortical responsable d'inhibition disynaptique fréquence-dépendante et quantifions les propriétés de intégration de ce microcircuit. Finalement un modèle est proposé pour expliquer les interactions entre les connexions électriques et synaptiques dans le bulbe olfactif.

Mots-Clés: microcircuit néocortical, cortex somatosensoriel, rat juvénile, électrophysiologie *in-vitro*, multi-électrodes, enregistrement patch-clamp, synapse, gap junction, regroupement, plasticité, ephaptique, champ extracellulaire, excitation, inhibition disynaptique fréquence-dépendante, section de cerveau, cellule pyramidale, cellule de Martinotti.

Table of Contents

ABSTRACT	I
RÉSUMÉ.....	II
TABLE OF CONTENTS	III
CHAPTER 1 INTRODUCTION - THE CORTICAL ORGANIZATION.....	1
<i>Somatic Sensation.....</i>	<i>1</i>
<i>Somatotopy.....</i>	<i>3</i>
<i>The Cortical Laminar and Columnar Organization.....</i>	<i>3</i>
Cortical Columns.....	4
Cortical Layers	5
<i>The canonical Microcircuit.....</i>	<i>7</i>
<i>Plasticity</i>	<i>8</i>
<i>Activity-dependence and critical periods.....</i>	<i>12</i>
<i>Disynaptic Frequency-Dependent Inhibition.....</i>	<i>13</i>
<i>Thesis Outline</i>	<i>15</i>
CHAPTER 2 COMPUTER ASSISTED MULTI-ELECTRODE PATCH-CLAMP	17
<i>INTRODUCTION</i>	<i>17</i>
<i>RESULTS</i>	<i>19</i>
Graphic Interface.....	19
Input Device	21
Position Control.....	22
Amplifier Control	24
Oscilloscope Control.....	25
Pressure Control	25
Video Acquisition and Display	26

Experimental Data Acquisition	27
<i>DISCUSSION</i>	28
Tissue Distortion	28
Micro and Nano-electrode Technology	29
Near Future Perspective for Multi-electrode Patch-clamp	30
CHAPTER 3 CLUSTERED CONNECTIVITY IN THE NEOCORTEX	33
<i>INTRODUCTION</i>	33
Distance-dependent connection probabilities	34
Assembly of pseudo-random networks	35
Single cell connectivity	37
Mathematical description of connectivity patterns	38
Clustering Algorithms	40
<i>RESULTS</i>	44
Non-Random, Non-Lattice Connectivity	48
Distributed and Interlaced Assemblies	50
Common Neighbors Predict Connection Probability	53
Connectivity Predicts Synaptic Weights	54
Construction of Hebbian Assemblies	56
Concluding remarks	58
<i>SUPPLEMENTARY METHODS</i>	64
<i>SUPPLEMENTARY MATERIAL</i>	74
CHAPTER 4 EPHAPTIC COUPLING OF NEURONS	77
<i>INTRODUCTION</i>	77
<i>METHODS</i>	79
<i>RESULTS</i>	81

<i>DISCUSSION</i>	90
<i>SUPPLEMENTARY FIGURES</i>	93
CHAPTER 5 FREQUENCY-DEPENDENT DISYNAPTIC INHIBITION IN THE PYRAMIDAL NETWORK – A UBIQUITOUS PATHWAY IN THE RODENT NEOCORTEX	101
<i>SUMMARY</i>	103
<i>INTRODUCTION</i>	104
<i>METHODS</i>	105
<i>RESULTS</i>	108
FDDI is a generic sub-circuit of the neocortex	110
Similar kinetics but different short-term dynamics of EPSPs between PCs	115
Distance-dependent drop of connectivity.....	117
Fatigue of the PC–interneuron synapse.....	119
<i>DISCUSSION</i>	122
FDDI as a functionally relevant generic neocortical sub-circuit motif	122
Area-specific specializations	123
Lateral extent of connectivity.....	125
Activity dependence of FDDI signaling.....	125
CHAPTER 6 BRIEF BURSTS SELF-INHIBIT AND CORRELATE THE PYRAMIDAL NETWORK	129
<i>SUMMARY</i>	131
<i>INTRODUCTION</i>	132
<i>RESULTS</i>	133
Components of FDDI	133
I _h in PCs spatiotemporally separates synaptic inputs	135
Selective non-linear summation of excitatory inputs with FDDI	137
FDDI mediated by few MCs	140

FDDI correlates subthreshold activity between neighboring PCs	144
Diversity of FDDI summation and cooperativity	145
Few PCs saturate FDDI.....	148
Predicting FDDI amplitude from number and frequency of stimulated PCs	150
<i>DISCUSSION</i>	150
Summation, saturation, and limits of FDDI recruitment.....	151
Subthreshold correlations between PCs	151
FDDI targeting the apical dendrite.....	152
I _h in PCs as a frequency-dependent gain modulator.....	153
FDDI in other cell types	154
Modulation affecting FDDI.....	155
CHAPTER 7 INTERACTIONS BETWEEN SYNAPTIC CONNECTIONS AND GAP JUNCTIONS IN THE OLFACTORY BULB	163
<i>INTRODUCTION</i>	163
<i>RESULTS</i>	164
Experimentally Measured Connectivity.....	164
Morphological interaction between Mitral cells	166
Functional interaction between synaptic and electric connections	167
Experimental confirmation of the predictions.....	171
Experimental verification of the assumptions.....	173
Physiological impact of propagation mediated by gap junctions.....	174
<i>DISCUSSION</i>	175
Synaptic transmission between Mitral cells: potential alternatives	176
Synaptic connections between Mitral cells in the OB of Cx36 ^{-/-} mice	177
Physiological considerations	177

Future directions.....	179
<i>METHODS</i>	180
CHAPTER 8 CONCLUSION	189
<i>The impact of new technologies on neuroscience</i>	189
<i>Clustered connectivity in the neocortex</i>	189
<i>The influence of local extracellular electrical fields</i>	190
<i>The ubiquity of FDDI and its recruitment</i>	190
<i>Interacting networks</i>	191
<i>Future directions</i>	192
BIBLIOGRAPHY	193
APPENDIX A ABBREVIATIONS	203
APPENDIX B SOFTWARE	205
APPENDIX C CLUSTERED CONNECTIVITY ANALYSIS	207
APPENDIX D ANALYSIS OF INTERACTIONS BETWEEN SYNAPSES AND GAP JUNCTIONS IN THE OLFACTORY BULB	209
ACKNOWLEDGEMENTS	211
CURRICULUM VITAE	212

Chapter 1 Introduction - The Cortical Organization

The majority of the work contained in this thesis examined the primary somatosensory cortex of the rat. A brief review of the architecture of the neocortex and the somatosensory system is therefore of considerable interest in this introduction. An overview of different forms of plasticity relevant to the different projects is also presented. The basic features of the disynaptic inhibition mediated by Martinotti cells, which is thoroughly investigated in two chapters of this thesis, are then introduced. An overview of the thesis concludes this introduction.

Somatic Sensation

The somatosensory system is responsible for processing a large variety of sensory modalities such as touch, temperature, proprioception and nociception. Touch constitutes an ensemble of different modalities in itself. Somatosensory receptors spread over the body are responsible for mediating somatic sensations and occur in three different kinds: thermoreceptors, mechanoreceptors and chemoreceptors. Pain and temperature information go mainly to the insular cortex and cingulate gyrus, while touch is processed by the somatosensory cortex.

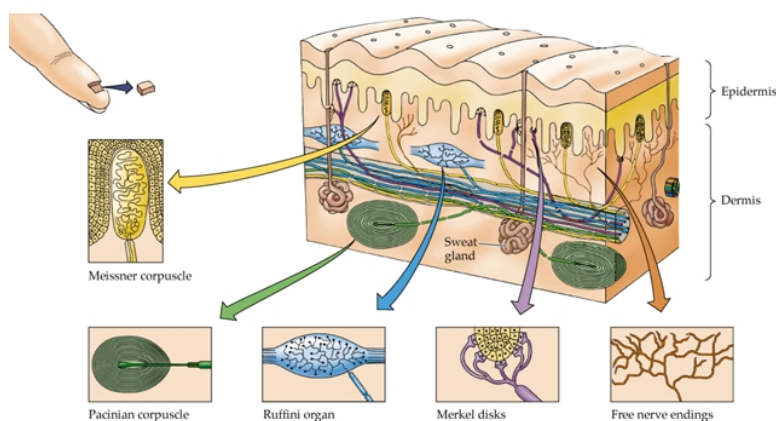


Figure 1-1 The various types of mechanoreceptors

The various mechanoreceptors deliver different modalities of touch. Meissner's corpuscles are responsible for sensitivity to light touch. In particular, they have highest sensitivity to vibrations at frequencies lower than 50 Hertz and rapidly adapt to continued stimulation. Pacinian corpuscles are nerve endings in the skin responsible for sensitivity to deep pressure touch and high frequency vibration. Ruffini organs are located in the deep layers of the skin, and register mechanical deformation within joints, more specifically, angle change as well as continuous pressure states. Merkel disks are found in the skin and mucosa of vertebrates and provide information regarding pressure and texture while free nerve endings are unspecialized afferent nerves endings that bring information from the body's periphery to the brain, essentially to detect pain. The information coded by the different low-threshold mechanoreceptors are carried separately until the somatosensory cortex and activate different cortical domains in primates (Figure 1-2)(Friedman, Chen et al. 2004). It is important to note that in general primates have much larger cortices with more visible organization than rodents. The fine organization observed in primates is however suggestive of a possibly important level of segregation of the neocortical networks processing different somatosensory modalities which might occur in rodents in a different manner.

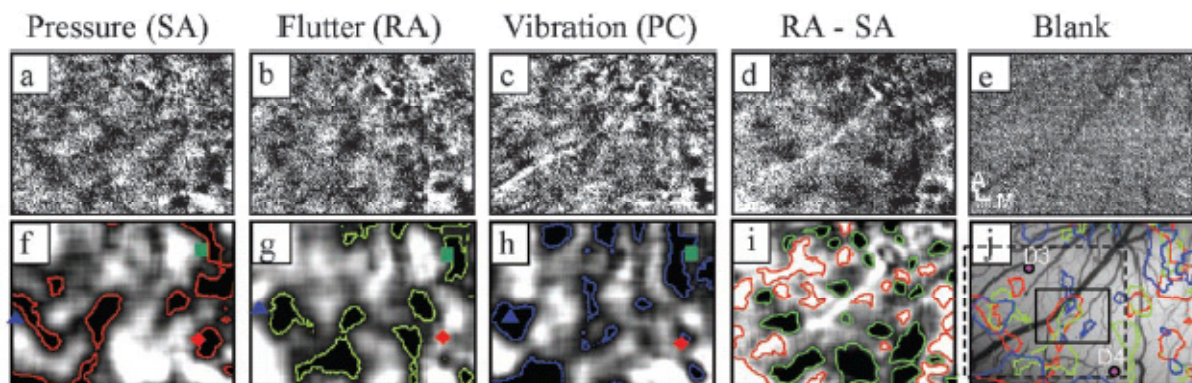


Figure 1-2 Different sensory modalities produce different activation patterns that can be intrinsically imaged on the surface of the cortex (Friedman, Chen et al. 2004). (a–c) Single-condition blank-subtracted maps show modality-specific activation patterns. (d and i) Subtraction maps of flutter–pressure (RA–SA) illustrate irregular alternating dark (preference for flutter) and light (preference for pressure) domains (gray pixels indicate equal preference for both). (e) Blank condition map. (f–i) Activation outlines of a–d obtained by low-pass filtering and thresholding. (j) Blood vessel map with pressure, flutter, and vibration activation outlines superimposed.

Somatotopy

The somatosensory cortex displays somatotopic organization, i.e. sensation from different parts of the body is mapped to specific parts of the brain.

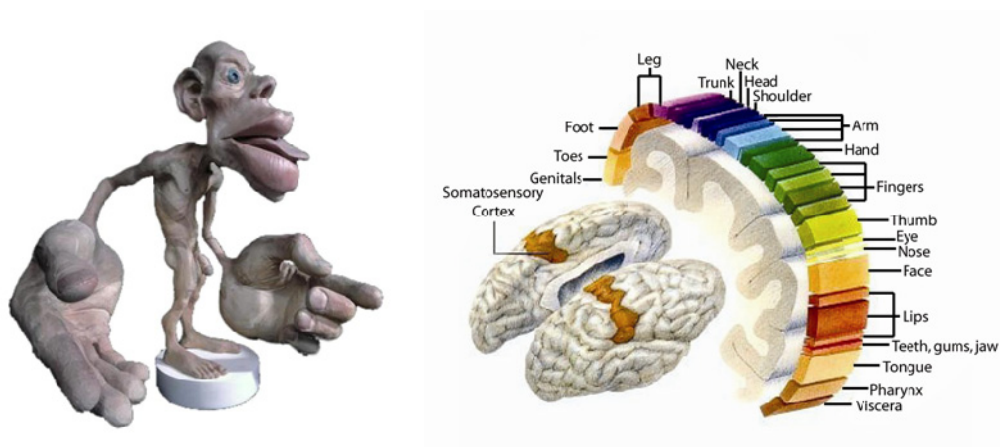


Figure 1-3 Sensory homunculus and cortical mapping

It is interesting to note that not all body regions are equally represented in the brain. In humans the hands and face are greatly overrepresented as evidenced by their size in the sensory homunculus and cortical surface in Figure 1-3. In the rat the large regions of the somatosensory cortex are dedicated to the incisors and vibrissae. The somatosensory cortex is not the only brain region to display somatotopy; motor cortex, cerebellum and thalamus also have been shown to be organized somatotopically (Land and Kandler 2002; Lu, Miyachi et al. 2007). In the majority of the work presented here the recordings were performed in the somatosensory region corresponding to the hind limbs.

The Cortical Laminar and Columnar Organization

The Neocortex is organized in columns normal to the surface of the brain. In convoluted cortices, as is the case of humans, columns remain normal to the surface following the gyri and sulci. A

layered organization also exists, parallel to the surface of the brain, similarly following sulci and gyri.

Cortical Columns

Neurons in many cortical areas are arranged into functional columnar structures spanning from the pia to the white matter. A cortical column in sensory regions can be defined as a group of neurons arranged vertically that share a similar receptive field. One of the common examples of the columnar organization is the orientation preference of neurons in the visual cortex where *in vivo* experiments imaging superficial layers of the cortex provide exquisitely organized responses with sharp transitions (Godde, Leonhardt et al. 2002; Ohki, Chung et al. 2005). The stimuli most commonly used to observe such maps are bars at different orientations which produce the column patterns of orientation selectivity as shown in Figure 1-4.

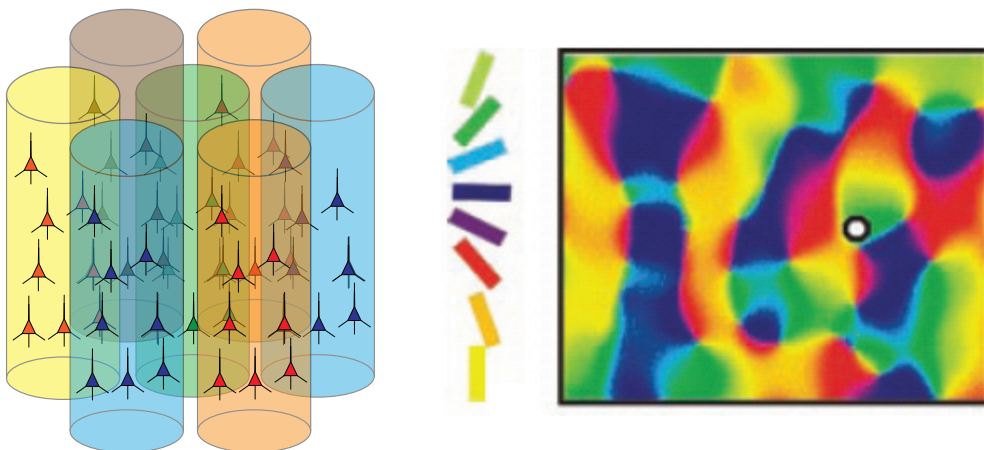


Figure 1-4 Cortical columns where colors indicate receptive fields (Godde, Leonhardt et al. 2002).

Different animals have different levels of columnar organization. Cats, for example, have well-developed visual cortices and different inputs are segregated spatially in different columns. Other animals such as rats show no such spatial segregation (Ohki, Chung et al. 2005). As previously discussed, segregation of different input modalities is not an exclusive feature of the visual system.

Cortical Layers

The neocortex is divided in six layers and according to the cortical region observed these layers can be more or less distinctively identifiable.

Layer I. Layer I is scarcely populated and contains only a small number of interneurons that release GABA_A and often GABA_B, the latter having been implicated in long-lasting inhibition of dendritic calcium spikes in Layer V Pyramidal neurons (Perez-Garci, Gassmann et al. 2006). However, a very large number of synaptic connections take place in this layer since the apical tuft of most pyramidal neurons branches towards the pia. Some interneurons such as Martinotti Cells innervate Layer I extensively. Projections from different brain areas such as the thalamus (Rieck and Carey 1985) are also reported to innervate Layer I

Layers II/III. The distinction between layers II and III is unclear in most of the neocortex with the exception of the visual cortex. Layers II/III are believed to constitute an intermediate layer in the flow of information between the cortical input in Layer IV and output in Layer V. Neurons in layers II/III are suggested to form fine-scale subnetworks according to common innervation from Layer IV (Yoshimura, Dantzker et al. 2005).

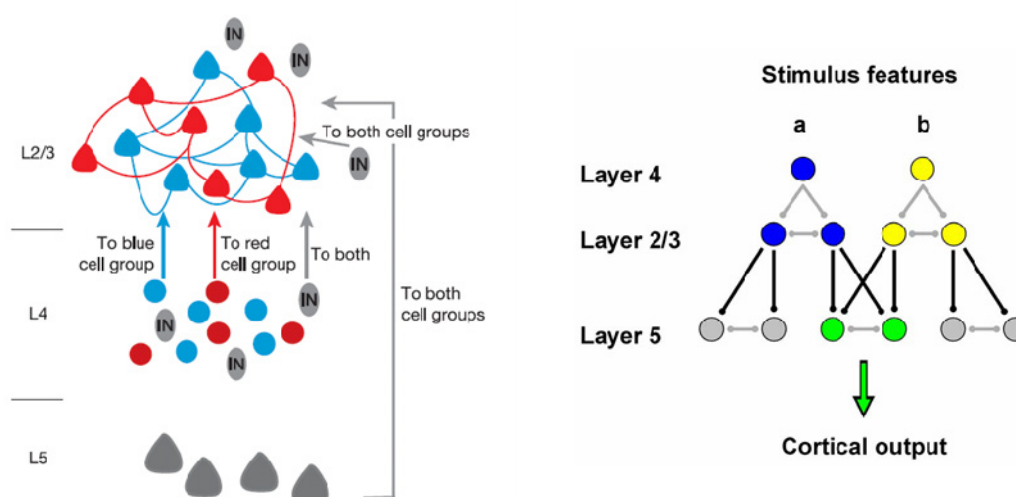


Figure 1-5 Organization of cortical connections proposed in (Yoshimura, Dantzker et al. 2005) and (Kampa, Letzkus et al. 2006).

Layer IV. Thalamic input to the cortex arrives primarily in Layer IV (Bruno and Sakmann 2006). Slice preparations that conserve some intact thalamic projections to the cortex have revealed several properties of the integrative dynamics of the thalamic innervations (Gabernet, Jadhav et al. 2005; MacLean, Watson et al. 2005; Hull, Isaacson et al. 2009). Very precise timing is enforced on the PSPS of Layer IV excitatory neurons by readily recruited FS interneurons that display many properties favoring fast integration such as high input-resistance and GluR2-lacking AMPA receptors (Hull, Isaacson et al. 2009).

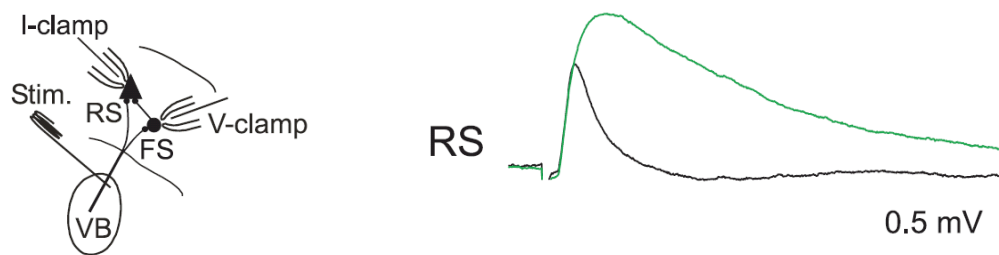


Figure 1-6 Thalamic EPSP on excitatory Layer IV neuron in the presence (black) and absence (green) of FS inhibition as described in (Hull, Isaacson et al. 2009)

Layer V. Many authors subdivide Layer V into an upper sub-layer 5A and a lower one 5B. The distinction is clearer in some cortical regions such as visual or barrel cortices unlike most of the somatosensory cortex, where this distinction is not clear. Layer V is considered to provide the output of cortical processing to various other regions (Groh, de Kock et al. 2008), to other columns and also to the corresponding region of the opposite hemisphere (Le Be, Silberberg et al. 2007). This layer is where most of the experiments in this work are concentrated. Layer V is also abundantly connected to Martinotti cells, considerably more so than Layers II/III (Perin unpublished data).

Layer VI. Layer VI contains neurons of great morphological diversity. Many neurons in this layer project to subcortical regions such as thalamic nuclei (Landisman and Connors 2007), while others project vertically to upper layers or horizontally to adjacent columns (Chen, Abrams et al. 2009).

The canonical Microcircuit

It has been a long-standing goal in the field of neuroscience to identify a canonical microcircuit in the neocortex, a processing unit capable of greatly diverse forms of computation, for such diversity is expressed in the functions performed by the neocortex. The similarities in the neocortical microcircuits across species further support the idea of a general-purpose circuitry that can be scaled efficiently. Since the first morphological stainings done by Santiago Ramón Y Cajal the structure of such circuits has been studied and outlined with increasing detail. It is currently possible to propose overall circuit architectures with some confidence, even if several elements, especially involving connectivity across areas, might still be missing or not completely understood. One of the most detailed descriptions of neocortical microcircuit is that of the barrel cortex. Careful identification of connection probabilities and synaptic strengths within and across layers has been performed in precisely determined barrels corresponding to specific whiskers (Lefort, Tómm et al. 2009). Moreover, long-range inputs and outputs of the barrel cortex are better understood than those of most other cortical regions (Woolsey and Van der Loos 1970; Yu, Derdikman et al. 2006; Lubke and Feldmeyer 2007).

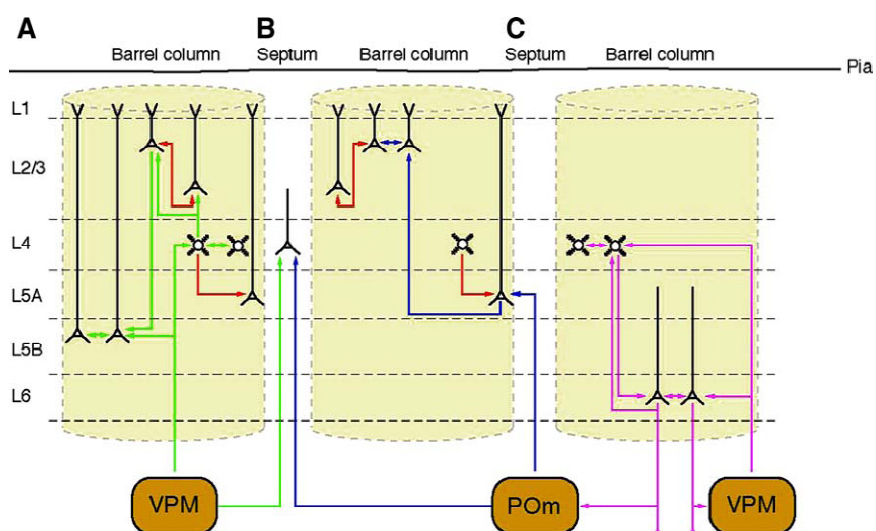


Figure 1-7 Barrel cortex microcircuitry proposed in (Lubke and Feldmeyer 2007)

While differences are known to exist across cortical regions, especially in terms of long-range connectivity, as should be expected, such differences remain limited compared to the overall uniformity of the neocortex. Brodmann's determination of brain areas on a neuroanatomical basis generally does not suffice to describe functionally determined regions, further illustrating this point. In fact, important contributions to the function and organization of neocortical circuits have been shown to derive from the nature of inputs (von Melchner, Pallas et al. 2000). Therefore, essential aspects of cortical organization involve both, developmental cues and plasticity, in addition to neuroanatomical features.

Plasticity

Innumerable forms of plasticity are currently described in the literature and the term has been applied to describe very different kinds of modification in neuronal networks. In this work we refer to four main plasticity mechanisms in our discussions with greater focus on plasticity of excitatory synapses although inhibitory synapses display interesting and varied forms of plasticity as well (Kurotani, Yamada et al. 2008).

LTP and LTD. Long-term potentiation is probably the first and most studied form of synaptic plasticity (Bliss and Lomo 1973; Kirkwood, Dudek et al. 1993; Singer 1995; Malenka and Nicoll 1999; McNaughton 2003; Holtmaat and Svoboda 2009) and is largely associated with learning and memory (Kandel 2001; Martin and Morris 2002). LTP encompasses a broad set of mechanisms, some cell-type specific, leading to potentiated synaptic transmission over long periods. Traditionally LTP is attributed to NMDA receptor (NMDAR) activation during postsynaptic depolarization leading to Ca^{2+} influx through the NMDAR channel. Following Ca^{2+} influx it has been suggested that different LTP induction protocols activate different signaling cascades (Hoffman, Sprengel et al. 2002; Lisman 2003).

Similarly, long-term depression has also been described in a plurality of forms. The traditional view is that a weak flux of Ca^{2+} through NMDAR channels is responsible for LTD. The frequency of stimuli leading to LTD is much lower (0.5-5 Hz) when compared to usual LTP

induction protocols (100 Hz). While LTP seems to require abundant calcium levels to occur, LTD only requires moderate calcium levels in combination with the accumulation of an effector other than Ca^{2+} (Sabatini, Oertner et al. 2002). Both mechanisms require calcium influx from calcium permeable channels since postsynaptic APs alone fail to induce LTP or LTD.

STDP. Spike-timing dependent plasticity is a bidirectional form of plasticity that depends on the relative spike-timing between pre- and postsynaptic neurons. While variations of STDP rules have been described in the literature (Letzkus, Kampa et al. 2006; Sjostrom and Hausser 2006) the first observations state that a postsynaptic spike following a presynaptic spike increases the synaptic strength, while a postsynaptic spike preceding a presynaptic one leads to a decrease in synaptic strength (Markram, Lubke et al. 1997; Bi and Poo 1998). While STDP is the synaptic mechanism most closely related to Hebb's postulate that '*neurons that fire together wire together*', it doesn't necessarily lead to that outcome.

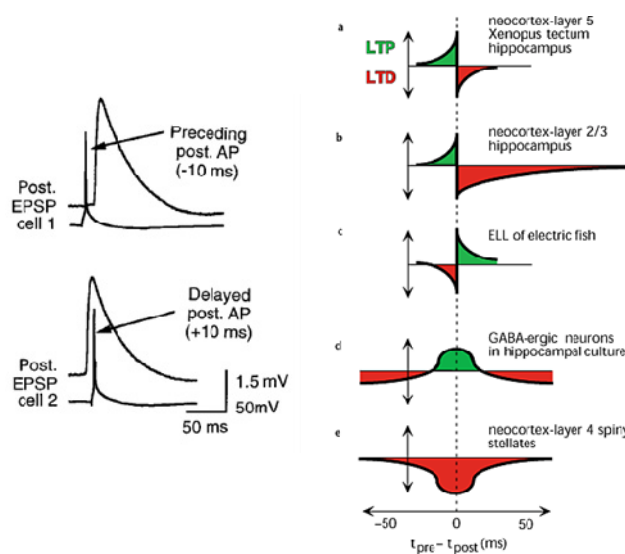


Figure 1-8 STDP protocol applied in (Markram, Lubke et al. 1997) and different forms of STDP described in (Abbott and Nelson 2000).

STDP is a bidirectional form of plasticity and it is important to bear in mind that neuronal networks are in continual activity and that each synapse may experience many spike-timing

relationships over time, causing many parameters to contribute to the changes in synaptic strength (Sjostrom, Turrigiano et al. 2001).

Structural plasticity. Neuronal morphology is not static; processes such as dendrites and axons grow and shrink, especially during the initial phases of development. Chemical guidance of axonal growth in the CNS and its effect on the organization of neuronal networks is a field where new mechanisms are constantly being discovered (Maskery and Shinbrot 2005; Mumm, Williams et al. 2006). However, as animals grow older, microcircuits consolidate and the extracellular matrix becomes less favorable to the growth of neuronal processes (Hofer, Mrsic-Flogel et al. 2009). Meanwhile, the consolidation of the extracellular matrix provides additional support to other forms of plasticity (Wright, Kramar et al. 2002).

Another mechanism that may be classified as structural plasticity, the appearance and disappearance of dendritic spines, continues throughout life (Trachtenberg, Chen et al. 2002) and functional maturation of new spines can take place relatively fast, within hours (Zito, Scheuss et al. 2009). Synapses are then believed to be stabilized or eliminated by activity-dependent processes similar to the forms of plasticity previously described (Ehrlich, Klein et al. 2007). Evidence is accumulating supporting a greater instability of nascent synapses and strong dependence on dendritic protein synthesis (Sebeo, Hsiao et al. 2009).

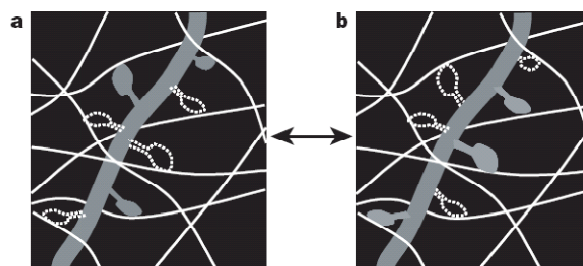


Figure 1-9 Structural plasticity with fixed potential connectivity as described in (Chklovskii, Mel et al. 2004)

Short-term plasticity. These alterations to synaptic transmission properties provide a short history-dependent context to synaptic transmission. In this work we will refer to short-term

plasticity as synaptic dynamics. Facilitation and depression, observable features of short-term plasticity, can be explained through a model (Tsodyks and Markram 1997) that assumes that neurotransmitter vesicles are in one of three states: effective, inactive or recovered.

$$\frac{dR}{dt} = \frac{I}{\tau_{rec}}$$

$$\frac{dE}{dt} = -\frac{E}{\tau_{inact}} + U_{SE} * R * \delta(t - t_{AP})$$

$$I = 1 - R - E$$

$$EPSC_{n+1} = EPSC_n(1 - U_{SE})e^{-\Delta t / \tau_{rec}} + A_{SE} * U_{SE}(1 - e^{-\Delta t / \tau_{rec}})$$

Equation 1-1 Model of synaptic dynamics proposed in (Tsodyks and Markram 1997)

The time constants τ_{rec} and τ_{inact} define the speed of transition to the recovered and inactive states, respectively. The spike-timings are defined in t_{AP} and Δ_t represents the inter-spike interval between successive action potentials (APs). The actual EPSC amplitudes elicited are then defined by these states and the following parameters:

- Absolute synaptic efficacy (A_{SE}), which reflects the total amount of neurotransmitter available at the synapses.
- Utilization factor (U_{SE}) which accounts for the fraction of available vesicles that get released at a given moment.
- Depression time-constant (D), which determines how long used vesicles take to be restored in the pool.
- Facilitation time-constant (F), which determines how previous spikes lead to an increase in the probability of release.

This model captures very well the average synaptic transmission in depressive connections. Facilitation, however, seems to require a more detailed description than only a time constant and strongly facilitating synaptic transmission can't always be accurately predicted with this model. The most important concept that becomes clear with this model is that when plasticity of synapses is measured by change in the amplitude of PSPs a distinction is necessary between changes in the absolute synaptic efficacy and changes in the release probability. Pairing protocols commonly meant to study the mechanisms of STDP or LTP often produce measurable changes on release probability (Markram and Tsodyks 1996), thus the importance of indications, such as paired-pulse ratios of the nature (Ase or U) of the plasticity studied. Short-term plasticity has important implications for the dynamic range of inputs that a neuronal circuit can process (Abbott, Varela et al. 1997; Rothman, Cathala et al. 2009).

Activity-dependence and critical periods

The activity of neurons is known to be an important factor in shaping the organization of cortical microcircuits. In the visual, auditory and somatosensory systems there is considerable evidence of circuit reorganization following sensory deprivation (Wiesel 1971; Blakemore, Garey et al. 1978; Trachtenberg, Chen et al. 2002; Lu, Cui et al. 2008).

The organization of neural microcircuits is not complete at the time of birth in mammals. Development continues with important modifications and structure formation. However not all brain regions are consolidated at the same pace or time. Periods when input is essential to structuring neural circuits are called critical periods and can have varied onset and duration according to the species and brain region. What is evident is that the lack of input or impoverishment of its diversity can lead to performance deficits associated with circuitry consolidation (Wiesel and Hubel 1965; Hubel and Wiesel 1970).

Probably the most direct evidence of critical periods can be observed through experiments that employ monocular deprivation, which consists in blindfolding or surgically closing one eye for a long period. Animals exposed to such treatment during a certain period in

development show altered organization of their visual cortices (Fagiolini and Hensch 2000; Hofer, Mrsic-Flogel et al. 2009). However, if the monocular deprivation takes place before this period, the animal can recover and develop normally. Finally, if monocular deprivation takes place after the critical period the effects are also reversible within days (Lehmann and Lowel 2008).

The onset of critical periods has been associated with the release of GABA and the cascade of events it triggers (Fagiolini and Hensch 2000), namely the consolidation of the extracellular matrix which provides physical support for neurons but also makes the growth of neural processes more difficult. From this moment on the plasticity of neural circuits becomes more likely to take place between neuronal processes that are close to each other rather than through the growth of such processes. Events that destroy or remove the extracellular matrix also restore some potential for growth to neuronal processes. Unfortunately such events also tend to be destructive in nature, such as strokes, and usually cause extensive damage to the existing circuitry.

The relevance of critical periods to the current study resides in the fact that structural plasticity is restricted after the critical period window and the available forms of plasticity play an important role on the degree of reorganization a neuronal network can experience. Our recordings are performed at the end of the critical period for somatosensation in rats (Broser, Grinevich et al. 2008) and connectivity observed at this period is likely to be stable to some extent through adult life, especially in the absence of major sensory deprivation (Hofer, Mrsic-Flogel et al. 2009).

Disynaptic Frequency-Dependent Inhibition

Previous work in the LNMC identified a frequent interaction between pyramidal cells (PCs) (Silberberg and Markram 2007). High frequency stimulation (70 Hz) of a PC often leads to hyperpolarization of simultaneously recorded neighboring PCs with delayed onset. Fast-spiking interneurons (FS) simply cannot generate such delayed inhibitory responses due to the depressive character of the PC-FS synapse (Figure 1-10a upper trace). Martinotti cells (MC) were identified

as the neurons responsible for this kind of response and display slower integration of successive EPSPs (Figure 1-10a lower trace). The facilitatory nature of the PC-MC synapse enables a regime of inhibition complementary to that of FS interneurons, thus increasing the network dynamic range of operation (Murayama, Perez-Garci et al. 2009).

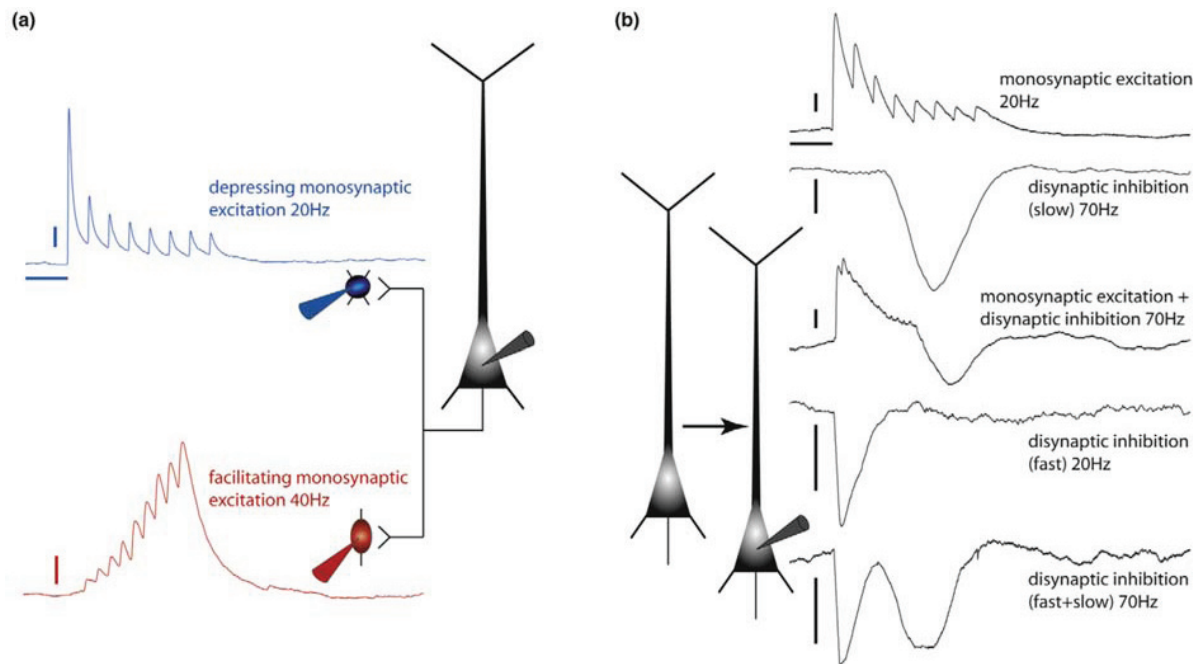


Figure 1-10 Different forms of disynaptic inhibition discussed in (Silberberg and Markram 2007). (a) PC-IN connections that underlie disynaptic inhibition between PCs. PCs synapse to blue interneurons (multipolar, basket cells, fast-spiking) with depressing dynamics, and to red interneurons (bitufted, Martinotti cells, adapting) with facilitating dynamics. (b) in case of suprathreshold PC-IN connections, the following disynaptic responses can be observed. Slow, frequency-dependent disynaptic inhibition (FDDI, only visible at high enough stimulation frequencies), or fast frequency-independent disynaptic inhibition, or, together with direct excitation, a combination thereof. Horizontal scale bar 0.1 s, vertical scale bars 0.5 mV.

Many patterns of activity can be observed involving PC-PC excitation and the different forms of disynaptic inhibition, the most common of which are illustrated in Figure 1-10b.

Thesis Outline

In this thesis various forms of interactions between neurons were studied, with focus on Layer V of the somatosensory cortex of the rat. Aimed at increasing the level of detail in the investigation of neuronal interactions the initial part of this work was devoted to the development of a computer assisted patch-clamp system capable of stimulating and recording from up to twelve neurons simultaneously. Chapter 2 of this thesis describes the development, the features and advantages of such a system as well as its limitations and evaluates its potential in the future.

Chapter 3 contains an introduction to the analytical methods applied in the study of the observed connectivity among Layer V PCs in the somatosensory cortex. The main findings are presented, describing spatially distributed groups of neurons where the number of connections and average synaptic strengths are significantly greater than expected by chance. We demonstrate that a fundamental organizing principle for the Layer V network is a connection probability within pairs of neurons that is proportional to the number of common inputs and outputs shared by the pairs.

In chapter 4 the effect of extracellular fields onto the sub- and suprathreshold activity of neurons is quantified. With precise arrangements of multiple electrodes the membrane potential and the extracellular fields at many sites were recorded in the presence and absence of controlled extracellular oscillations within physiological ranges. This data allowed us to show that fields of relatively small amplitudes can have a significant impact on spike-timing of individual neurons, but also assist in synchronizing neurons subject to similar fields. Based on the requirements for a significant influence of the extracellular field on spike-timing we discuss its relevance to different activity regimes.

Chapter 5 is dedicated to the description of the ubiquitous character of disynaptic frequency-dependent inhibition (FDDI). The occurrence of this microcircuit in the various cortical regions investigated (primary somatosensory, auditory, and motor cortex, secondary visual cortex and medial prefrontal cortex) demonstrate it constitutes a generic circuit motif. The

differences in the properties of FDDI across regions is discussed and the unexpected sensitivity of FDDI to repetitive high-frequency stimulation is shown not to be caused by endocannabinoids, reported to mediate sustained self-inhibition in low-threshold spiking neurons (Bacci, Huguenard et al. 2004).

We continue with the experimental quantification of the summation properties of FDDI in chapter 6. Simultaneous stimulation of increasing numbers of neurons allowed us to identify the saturation curve of FDDI in terms of numbers of PC and their respective spiking frequencies. We demonstrate that FDDI is a widespread form of inhibition even when few PCs spike at frequencies that can be observed *in vivo*, potentially correlating the membrane potentials of many PCs. Possible implications and modulation mechanisms are discussed.

In chapter 7, we present a model of interaction between gap junctions and synaptic connections in the tuft of Mitral cells in the olfactory bulb. Motivated by the intriguing observation of apparent synaptic couplings between morphologically segregated MCs we hypothesized that synaptic transmission might be propagated by an additional neuron through a gap junction. This model not only could explain certain connectivity patterns that should not occur according to current models, but could also provide testable predictions that were experimentally confirmed. We conclude with the reasoning that such an interaction between networks greatly enhances the responsiveness of individual glomeruli, while reducing drastically the energetic cost of this modality of sensory processing.

Finally, a conclusion is presented with an overview of the most important results and a discussion of future perspectives.

Chapter 2 Computer Assisted Multi-electrode Patch-Clamp

In this chapter the development of the twelve-electrode patch-clamp setup, which represented the initial part of the work contained in this thesis, is addressed. The motivation and applications, implementation and perspectives are discussed.

INTRODUCTION

There are several reasons for multiple independently moving electrodes to be of great interest in experimental neuroscience. Recording potentials and currents at precisely chosen sites is especially interesting for studying connectivity of diverse cell types in various brain regions but can find many other applications such as the characterization of extracellular potential fluctuations or their precise effect on neuronal activity.

The minimal requirement to study synaptic connectivity is the ability to record sub-threshold neuronal activity along with reliable means of stimulation. Since the first study that established chemical synaptic transmission in the central nervous system (Brock, Coombs et al. 1952) much progress has been made. With the advent of single-cell recordings different kinds of electrodes came into use. First, sharp-electrodes which impale the neurons, followed by larger patch-clamp electrodes that enabled better and more stable recordings (Hamill, Marty et al. 1981). However a qualitative leap took place with the introduction of paired patch-clamp recordings, in which the control over the recorded neurons and the quality of the recordings were unprecedented, opening way to new kinds of experiments and discoveries (Markram and Tsodyks 1996; Markram, Lubke et al. 1997). The possibility to test multiple pairs of specifically chosen neurons led to the prevailing description of connectivity in terms of connection probabilities within and across cell-types (Feldmeyer, Egger et al. 1999; Thomson, West et al. 2002). However since the early days of paired patch-clamp experiments it became clear that a single parameter p , the connection probability, could not properly explain connectivity in many cases where neurons showed a strong tendency towards forming reciprocal connections (Markram 1997). More recently, with quadruple patch-clamp recordings, it became clear that

accounting for reciprocity tendencies is still not enough to explain connectivity patterns in the neocortex (Song, Sjöström et al. 2005). Here lies the great advantage of multiple-electrode recordings for describing connectivity. First the number of connections that are observed and the number of pathways tested grows proportionally to the square of the number of neurons recorded (Figure 2-1). Second, some of the properties that can be observed with multiple simultaneous recordings simply cannot be observed in smaller scales as will be discussed in detail the following chapter.

Recorded Neurons	3	6	12
Possible Connections	6	30	132
Avg. Observed Connections	0.6	3	13.2
Connections/Neuron	0.2	0.5	1.1

Hypothetically $p = 0.1$

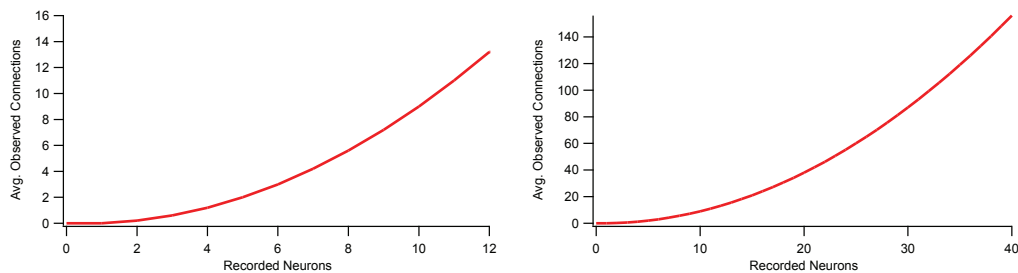
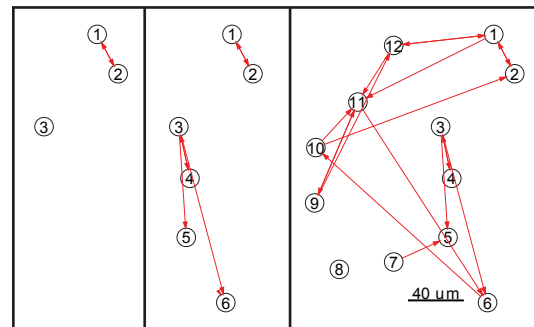


Figure 2-1 Estimates of observed connections as a function of the number of recorded neurons

The level of complexity of an experiment becomes the most important variable in influencing its rate of success when considering experiments with large numbers of electrodes. Procedures which are simple to execute when using two or three electrodes become prohibitively demanding when using twelve. Even the time consumed positioning and establishing the seal with the membrane of the cells becomes of major importance and needs to be minimized. The requirement to make experimental steps faster, simpler and more reliable led to the development of a powerful computer-assisted system that controls the hardware involved in patch-clamp experiments such as micro-manipulators, amplifiers, oscilloscopes, pressure control and video acquisition and display.

RESULTS

The computer-assisted patch-clamp interface is based on a continuous polling of the status of the multiple devices it connects to, while listening to user generated events that result in the appropriate commands to one or more devices. The polled information is then displayed in either graphic or text form, or both. Several different communication protocols and code libraries are integrated so that the experimenter can concentrate on the experimental task rather than the intricate controls of the equipment.

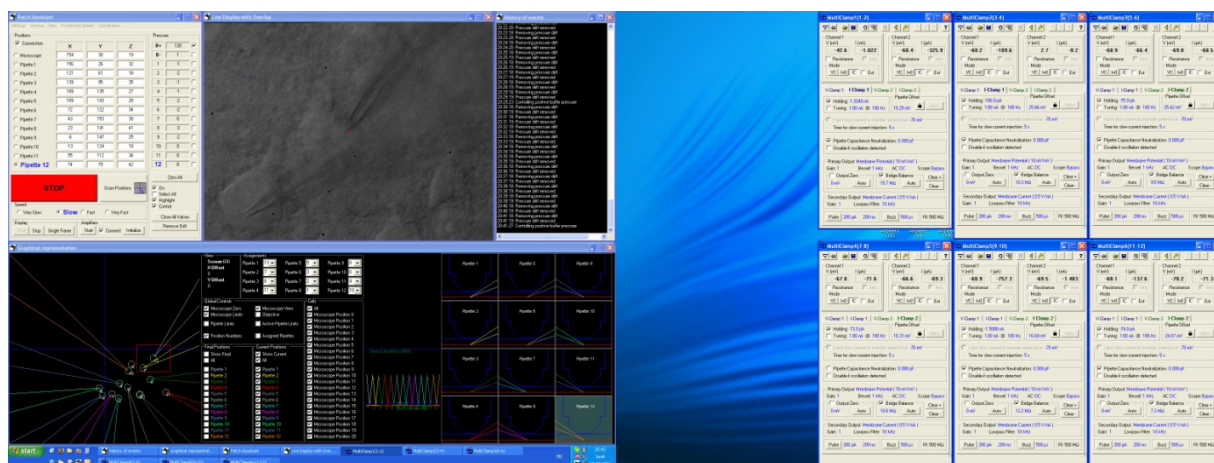


Figure 2-2 Overall aspect of the patch-clamp computer interface

Graphic Interface

One of the most important requirements for successfully recording from many neurons is the ability to monitor a large amount of information. The goal in programming a graphic interface for patch-clamp experiments was to make all such information available in one single location in a user-friendly form. The possibility to visualize the position of the pipettes even when these are far from the field of view of the objective is essential to avoid damage to the pipettes and follow the progression of the experiment. This representation alone is responsible for a three-fold increase in experimental success rate. Other information such as the position of cells of interest,

electrode coordinates and pipette pressure allow experiments to be better controlled and documented.



Figure 2-3 Graphic representation of the positions of 12 electrodes in multiple views and top-view representation of positions of cells of interest (left panel).

Another essential feature of the graphic interface is the possibility to preview the final experimental configuration. Ensuring the feasibility of a given configuration for the final positions of the electrodes prevents the eventual under-utilization of the equipment due to the impossibility of reaching a cell of interest by inadvertently positioning one or more of the electrodes across the path of another electrode.

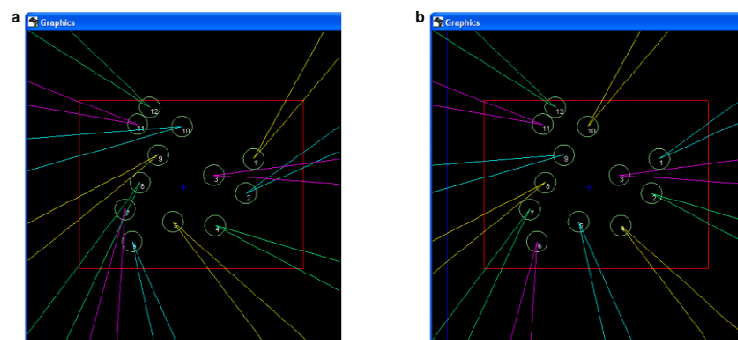


Figure 2-4 Example of preview of final experimental configuration with twelve electrodes. **(a)** Typical problematic electrode configuration that can occur when no preview is available. Notice how the magenta electrodes or their respective neurons potentially collide with other electrodes. **(b)** Successful configuration reorganization obtained after previewing.

Furthermore, the preview of the final electrode positions can be accompanied by the superposition of morphological guidelines. This step requires the identification of reference points and calibration but can be useful, for example, to identify the position of nuclei of interest where stimulation may be applied.

Finally, tracing layer boundaries or morphological features, such as an apical dendrite, can be done easily on the screen with the mouse for future reference. This allows for example, using low-magnification to identify and trace layer boundaries and visualizing these traces at the appropriate scale at high magnification when boundaries become less distinguishable. This information can be exported for detailed documentation of experiments along with screen captures or acquired image stacks.

Input Device

Efficiently centralizing controls is just as important as concentrating the necessary information on the display. Using any commercially available wireless USB gamepad (we used Logitech's Wingman II) the most common experimental steps could be quickly performed from a single device. The controller can address the microscope manipulators at all times as well as the manipulators for one pipette and the corresponding amplifier, oscilloscope and pressure commands. The implementation performed relied on standard technology to ensure speed and reliability at the expense of larger numbers of controls that could possibly have made interaction more intuitive. The strategy employed was to assign categories of functions to individual buttons. For example, voltage-clamp related functions were assigned to button X, pressure-related functions to button Z and so on. Pressing one of such buttons in combination with other controls results in a specific instruction in the same way a text editor writes a capital letter when the shift key is pressed. For example the combination X+R2 results in a command that turns on or off the seal-test signal in voltage-clamp. The instruction set is illustrated below and detailed in Appendix B.



Figure 2-5 Input device commands

Position Control

Position control constitutes the central goal in the development of the computer-assisted patch-clamp system. Not only does it represent the most time-consuming task in experimental procedures but also the one most likely to result in serious errors. The controllers of the Luigs & Neumann manipulators can communicate with a computer via serial port. Due to communication speed concerns, each controller, responsible for motion control of up to six manipulators, connects to a different port. The communication follows a master-slave configuration where the computer is the master and initiates communication to which the motion controllers, slaves, will reply or simply acknowledge. Three kinds of messages are exchanged: queries, parameter setting and motion commands. Queries are commands that are replied to by the controller to obtain the value of a setting. The most common query which usually takes place every few milliseconds is a position query for one of the 39 axes. Parameter setting commands usually influence motion commands by defining the desired motion speed or some other setting. Finally, motion commands inform the controllers to produce motion of some sort or absolute or simply to stop.

The most crucial step to achieve efficient positioning of the electrodes is to create a single reference system common to all elements. In this case we chose this reference system to coincide with that of the microscope. To that end, the projections of each manipulator axis onto each microscope axis was measured. The measurements consisted of placing a pipette in the

centre of the field of view of the microscope and then to issue a movement of one millimeter. The microscope was then displaced to the tip of the pipette and the difference between the final and initial microscope positions was calculated. Therefore, to position the microscope at any position given in the local coordinates of a manipulator it suffices to solve the equation with three variables:

$$\begin{bmatrix} X_{mic} \\ Y_{mic} \\ Z_{mic} \end{bmatrix} = \begin{bmatrix} a_{n11} & a_{n12} & a_{n13} \\ a_{n21} & a_{n22} & a_{n23} \\ a_{n31} & a_{n32} & a_{n33} \end{bmatrix} \begin{bmatrix} X_n \\ Y_n \\ Z_n \end{bmatrix} + \begin{bmatrix} d_{nx} \\ d_{ny} \\ d_{nz} \end{bmatrix}$$

Equation 2-1 Conversion to microscope coordinate system

where a is the matrix of cosines, i.e. where the projections of each axis have been stored. The last vector accounts for the offset between the coordinate systems and is determined once all the other terms are known. In fact the offset is adjusted at the beginning of each experiment due to the slight variations in shape of each pipette that is pulled. Offsets may even be adjusted during the experiment to reset errors that might accumulate over large displacements of several millimeters. The inverse problem, to move the manipulator towards a position given in the microscope coordinate system, the inverse matrix a^{-1} is used. Given that we want to be free to modify the offset without necessarily modifying the matrix of cosines we can calculate the local coordinates as follows:

$$\begin{bmatrix} X_n \\ Y_n \\ Z_n \end{bmatrix} = a_n^{-1} \begin{bmatrix} X_{mic} - d_{nx} \\ Y_{mic} - d_{ny} \\ Z_{mic} - d_{nz} \end{bmatrix}$$

Equation 2-2 Conversion to manipulator coordinate system

A visual interpretation of the transformations described can be seen in Figure 2-6. A similar, but simpler, transformation converts coordinates from the screen, in pixels, to microscope coordinates and vice-versa. In order to achieve precise conversions it is necessary to

calibrate once each objective employed and store the parameters. It then suffices to define which objective is used and the image-based positioning can work effectively.

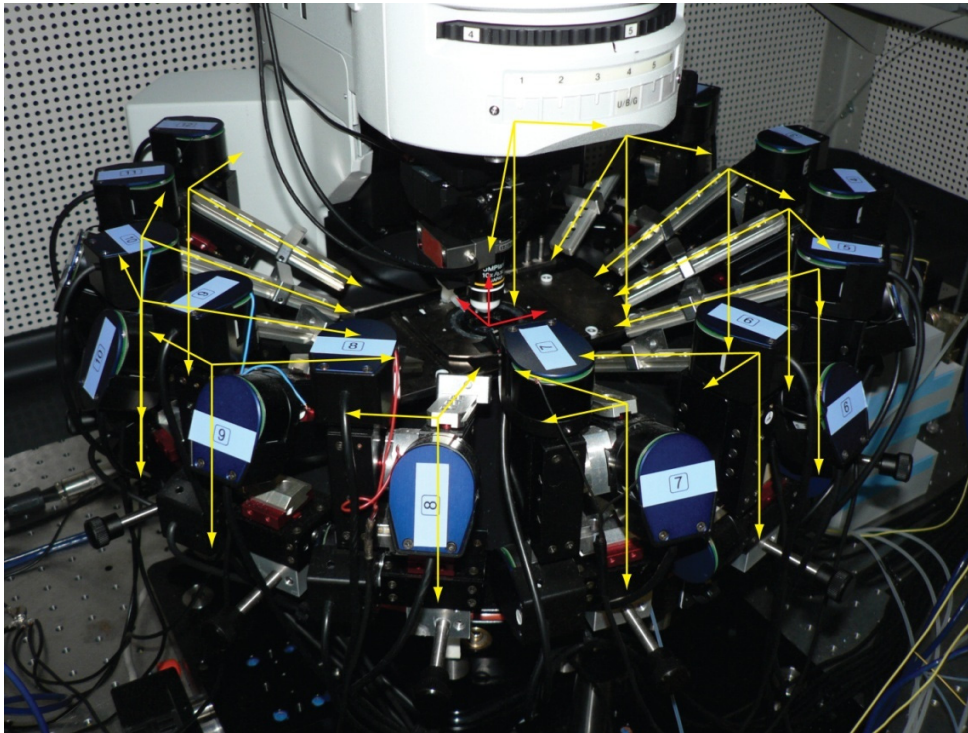


Figure 2-6 Twelve electrode setup and its coordinate systems. The yellow arrows indicate the coordinate systems of the manipulators and the red arrows represent the coordinate system of the microscope.

Amplifier Control

Our setup employed six Multiclamp amplifiers 700B from Axon Instruments. Each amplifier reads out current and voltage while it accepts a command voltage that will be converted into currents or smaller potentials according to the selected mode of operation. Axon Instruments provides a software library (DLL - Dynamically Linked Library) available for interfacing with their amplifiers. We used this library to enable control of the amplifiers from the input device and graphic interface. The greatest advantages of this development are the faster and more convenient adjustment of the amplifier settings and, most importantly, the reduction of the probability of human error by addressing the wrong amplifier or channel, which can often lead to

the death of recorded cell. Besides, amplifier setting can be programmatically changed, from a different computer through a network or serial port connection if necessary, to respond to demanding stimulation protocols that require changes in multiple settings as is the case when switching from voltage- to current-clamp with specific holding currents or potentials.

Oscilloscope Control

Many oscilloscopes such as the Tektronix TDS 2014 can be equipped with serial port communication which is extremely simple to use. It is convenient to have the oscilloscope display automatically scaled to the input the experimenter expects to observe or switch the appropriate channel from AC to DC coupling along with changes in amplifier settings without additional commands, thus increasing the speed and reliability of experimental procedures.

Pressure Control

Pressure control for multi-electrode patch-clamp can be a demanding and delicate operation and constitutes a surprisingly important step. Providing positive pressure for a pipette in patch-clamp procedures with few electrodes does not require much effort, it suffices to gently push the plunger of a syringe coupled to the pipette and lock the air, compressed in the tubing, with the turn of a stopcock. This pressure will slowly drop but the experimenter usually has enough time to finish all necessary steps before this becomes a problem. As the number of electrodes grows the task of maintaining constant positive pressure in each pipette consumes increasingly more time and effort. Worse, if there is no positive pressure for as little as a minute, the tip of a pipette is likely to accumulate impurities that will reduce the quality of the recording. A diaphragm pump (Schego Optimal, Schego, Offenbach, Germany) coupled to a system of valves (SMC S070C-6BG-32, SMC, Noblesville, Indiana) and pressure sensors (4DF6G, Honeywell) can provide constant air pressure and releasing the experimenter from a simple but crucial task. Buffers for positive and negative air pressure help stabilize the pressure before it is actually provided to the pipettes.

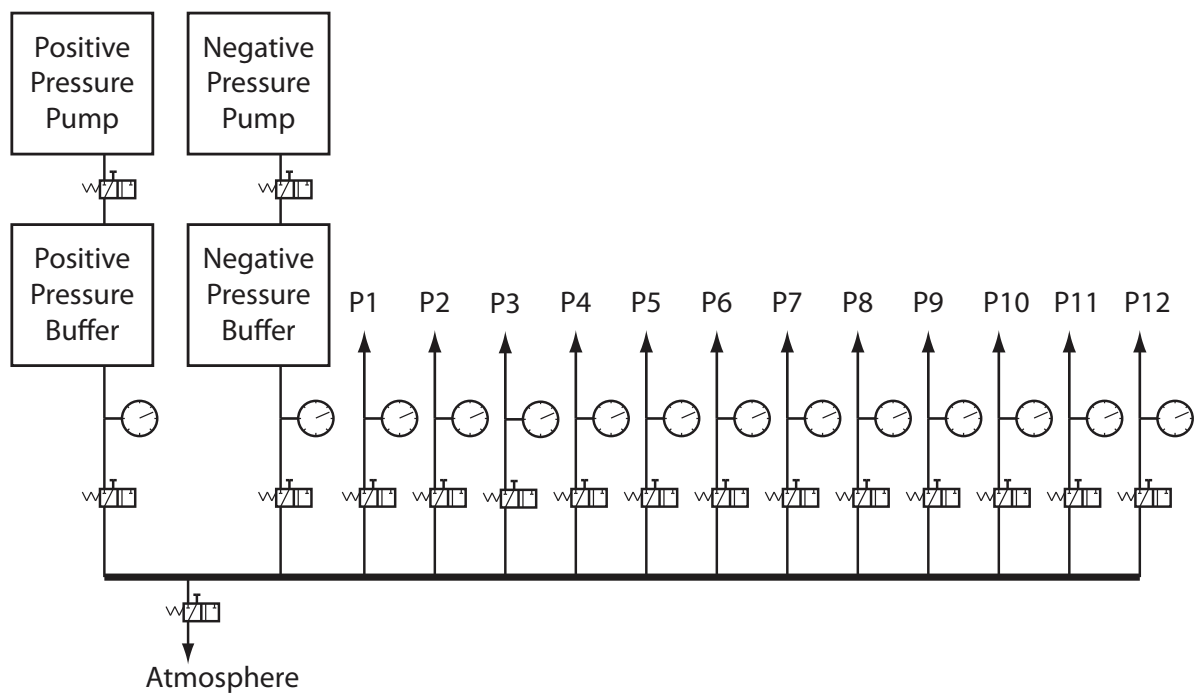


Figure 2-7 Schematic diagram of pressure controller pneumatics

To establish the control system a simple data acquisition system has to read the signal from the sensors and command the valves accordingly. A National Instruments PCI-6221 card was employed to that end. Libraries provided by National Instruments were integrated into the interface code and managed data input and output for the pressure system. Good performance was obtained by keeping positive pressure close to 70 mbar. Additionally, a second pump was modified to aspirate air providing negative pressure that was used to form seals. Finally, pressure control commands were integrated in the input device. The final pressure control system greatly increases the number of successful recordings in experiments but most importantly helps to avoid common mistakes such as applying positive pressure to a pipette that is already in cell-attached configuration, disrupting the cell membrane.

Video Acquisition and Display

Patch-clamp setups are usually equipped with an infrared camera coupled to a monitor by a coaxial cable. In order to integrate visual information to the interface, we acquire the camera

signal with a simple frame grabber board (Data Translation DT3120). Data Translation provides a library of functions to perform video acquisition and overlay. Overlays provide the possibility to add invaluable visual information to the video being displayed such as surrounding selected cells with circles or indicating which pipette will be used to record that cell and what path it will take in its approach. This overlaid visual information is constantly updated based on the coordinates of each axis.

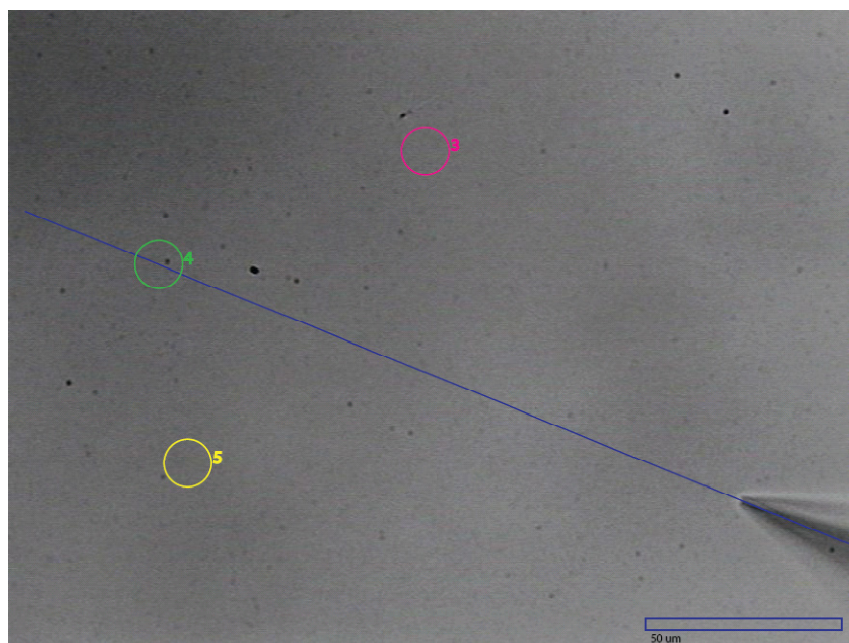


Figure 2-8 User view of pipette automatically positioned above the slice in order to start approach towards its assigned cell (green) several μm lower. Notice horizontal projection of positions of other cells of interest also displayed (magenta and yellow).

Experimental Data Acquisition

A programmable stimulation and recording interface is necessary when large numbers of electrodes are employed in order to efficiently design and apply stimulation protocols. At EPFL such an interface (PulseQ) was developed by Raphael Holzer, Rodrigo Perin and Luca Gambazzi in IGOR Pro 6 (Wavemetrics). This interface was optically linked to a low-noise data acquisition board ITC-1600 (Instrutech) which in turn was connected to the amplifiers.

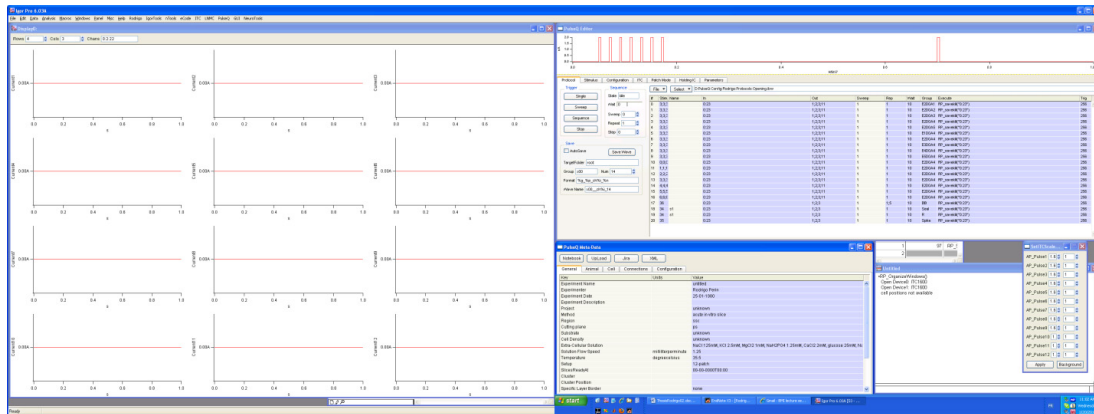


Figure 2-9 PulseQ interface

The documentation of experiments was designed to include substantial information on each experiment including for example animal data, experimental conditions, protocols and connectivity information. For ease of access the documentation was translated into XML format according to the Blue Brain Project schema definitions.

DISCUSSION

There is a large number of potential applications for the developed system as well as many possible improvements. Although the innovations described previously definitely simplify the task of performing multiple simultaneous whole-cell recordings it is important to keep in mind that this remains a complex task that requires much concentration and attention to detail.

Tissue Distortion

The most serious limiting factor to large-scale patch-clamp recordings is probably tissue distortion. The more pipettes are inserted into the tissue, the greater the chance of compromising a previously established seal, thus the importance of minimizing movement of the pipettes within the tissue. Electrodes are ideally inserted into the tissue along their longitudinal axes straight towards the cell of interest. In practice, it is very difficult to avoid minor adjustments. Computer assisted positioning represents a very large step towards minimizing such adjustments. Another

important step towards increasing the success rate is to approach cells according to decreasing depth relative to the slice surface, since approaches towards deep-seated cells are the most likely to cause tissue distortion. When recordings from neurons situated deeper in the slice are required a compromise must be found between pipette resistance and the increasing transversal section of the pipette that comes in contact with the tissue. Very thin or long-tapered pipettes cause minimal tissue distortion but have very large resistances, which hinders the quality of recordings. On the other hand thick pipettes, especially ones with short tapers, become almost impossible to use. In practice pipettes with openings of about 1 μm and long tapers yielded the best results with resistances of about 8 $\text{M}\Omega$.

Micro and Nano-electrode Technology

The development of new types of electrodes is clearly a field of much interest for the future of multiple-electrode intracellular recording systems and constitutes a domain of some activity (Schrlau, Dun et al. 2009). Unfortunately most carbon or metallic electrodes still face a great challenge in the reduction of the interface impedance. In a solution electricity is conducted by ions, in metals, by electrons. Traditional electrophysiology with micropipettes uses macroscopic silver-chloride electrodes which greatly minimize the interface impedance. Novel electrode technologies will therefore need to overcome this hindrance in order to provide substantial contributions to intracellular electrophysiology. Recent developments have shown, however, that progress is imminent in this domain (Edward D. de Asis, Leung et al. 2009). Single multiwalled carbon nanotubes have been used to perform whole-cell voltage-clamp recordings of muscle cells with 10 times lower impedance than patch electrodes whose tips were two orders of magnitude larger. Given their diameter, under 50 nm, such nanotubes can even improve recordings of small compartments such as thin dendrites and certainly cause less tissue distortion than patch pipettes. It remains to be seen if the assembly of such electrodes can be made simple enough for widespread use in electrophysiology or if they can be reused. An additional advantage of CNT electrodes is the fact that they do not interfere with the composition of the cytoplasm. Unfortunately, this also means the diffusion of dyes to stain recorded neurons is compromised. Advances in the field of micro and nano-electrodes are, nonetheless, extremely promising for the further development of large-scale electrophysiology studies.

Near Future Perspective for Multi-electrode Patch-clamp

Glass patch-clamp electrodes may still allow the number of simultaneously recorded neurons to double or triple. To that end two main developments must be achieved: the improvement of positioning reliability and the reduction of the cost per recording channel, both of which are well within reach of current technologies. The most cost-effective solution to the positioning issue is probably the development of a high-precision manipulator, with optically encoded position feedback, capable of addressing different electrodes instead of the direct motorization of every moving axis. In this case a precise locking system would be necessary whenever axes are not coupled to the manipulator but this remains a simple mechanical detail.

The intense popularization of data acquisition systems currently allows the design of low-cost electronics capable of recording membrane potentials with sufficient resolution. Custom data acquisition systems will probably constitute a central feature of future large-scale patch-clamp setups.

In multi-electrode experiments the average number of successful recordings can be estimated from a binomial distribution given an individual recording success probability. If we assume that in ideal conditions the success probability of an individual recording is 0.9 we obtain, for twelve and thirty electrodes respectively the distributions shown in Figure 2-10.

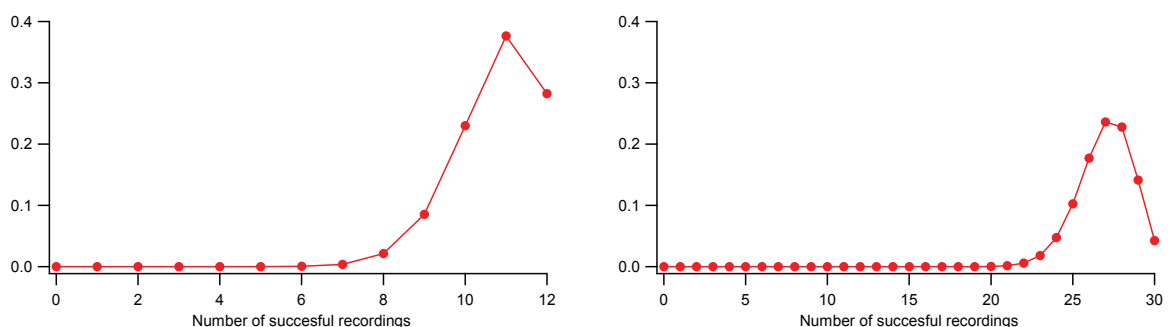


Figure 2-10 Calculated number of successful recordings for 12 and 30 multi-electrode recordings

Calculation of the average expected number of successfully employed electrodes from such distributions yields the values of 10.8 ± 1.1 , 18 ± 1.8 and 27 ± 2.7 , for 12, 20 and 30 electrodes respectively. In fact, these are optimistic values given that each electrode inserted into the tissue can, with a certain probability, interfere with previous recordings. With an estimated interference probability of 1% we obtain that the more realistic average value of 10.1 neurons successfully recorded when using 12 electrodes, and 16.1 when employing 20, which reinforces the importance of a reliable recording procedure and minimizing tissue distortion.

One of the most important issues in large scale simultaneous patch-clamp experiments is dealing with the time consumed by the approach procedure. Performing the approach of the electrodes towards multiple cells simultaneously is the most promising solution to the time problem but this requires the imaging of distinct regions simultaneously. Moreover, a simultaneous approach towards multiple cells requires multiple experimenters working in parallel or advanced image processing to reliably detect contact of the pipette with the membrane on a satisfactory site. Imaging distinct regions simultaneously can be achieved with fast optical components with which each site of interest should be imaged at a minimum of 10 frames per second. Recently the use of graphical processing units (GPUs) became much simpler and the computer vision algorithms already used in our system have been translated for use with GPUs which can perform image processing one to two orders of magnitude faster than traditional processors.

An additional important issue is the replacement and initial localization of pipettes. Most systems nowadays do not allow safe replacement of pipettes without risk of disrupting recordings in progress. This is a very limiting feature in the sense that each manipulator provides the experimenter with a single attempt at recording from a cell. For larger numbers of electrodes this becomes a much more severe limitation. Smooth replacement of pipettes has an even more pressing reason to be performed: the more pipettes there are in the bath gently diffusing intracellular solution over the slice, the more cells in the slice will be depolarized due to the perturbation of the bath solution composition. Minimizing the number of pipettes in the bath at a given time is the best practice to avoid the depolarization of neurons and to keep the pipette tips clean in order to ensure good quality recordings. The most effective solution to these issues is the

development of a mechanically smooth, automatic pipette placement system which would also represent a significant reduction in preparation time. Incorporating such a feature onto a manipulator constitutes a feasible task with considerable benefits.

In conclusion, multi-electrode patch-clamp systems constitute a technology that is ripe for use at academic level and that could become more widespread with the reduction of equipment cost. The applications in the study of neuronal microcircuitry are numerous; every different brain region is bound to have circuit properties relevant to information processing that have not yet been uncovered. The development of large-scale systems with further degrees of automation could be of great interest, not only at academic level, but also to pharmaceutical companies interested in screening circuit-level effect of drugs which so far are investigated only at the level of single cells or synapses.

Chapter 3 Clustered Connectivity in the Neocortex

In this chapter an introduction to the analytical techniques used to describe clustered connectivity in the neocortex is provided, followed by the presentation of the main experimental findings in the form of a manuscript.

INTRODUCTION

Employing the twelve electrode patch-clamp system described in the previous chapter, we simultaneously recorded from groups of pyramidal cells (PCs) in Layer V in somatosensory cortex slices in order to determine network properties of their connectivity. Tight synaptically-coupled groups of neurons, commonly called Hebbian assemblies, are believed to subserve memories because patterned stimulation is assumed to result, through activity-dependent plasticity, in patterned synaptic connectivity. Such assemblies have been theorized for decades (Hebb 1949), but never actually observed.

We found that clustered synaptic connectivity becomes highly evident when recording from at least six neurons. The underlying structure of clustered connectivity is based on the fact that two neurons synaptically connected to a common neighbor are also more likely to be interconnected to each other. We also show that the average synaptic strength grows as a function of the number of connections in groups of neurons.

Inspection of the spatial distribution of clusters of neurons show maximal clustering involved neurons about 125 μm apart, suggesting that assemblies are overlaid and interlaced within the same neural space. Hebbian assemblies therefore do exist, but the synaptic weights within assemblies are surprisingly predictable, paradoxically indicating that patterning synaptic weights within assemblies might be too constrained to serve as a mechanism for storing memories. We therefore hypothesize Hebbian assemblies as universal elementary building blocks formed during development and that acquiring memories may rather involve patterning weights between assemblies to shape the way assemblies are combined.

Several studies have shown that the cortical network connectivity is not random (Song, Sjöström et al. 2005; Yu, Bultje et al. 2009). Different neuron types are bound to exhibit different connectivity properties due to different morphologies. However, even within a given neuron type, there are rules governing the organization of synaptic circuits, one of the most conclusive indications being provided, although indirectly, in (Yoshimura, Dantzker et al. 2005).

Distance-dependent connection probabilities

Traditionally neuronal networks are described in terms of connection probabilities between and within cell types (Markram, Lübke et al. 1997; Brown and Hestrin 2009; Lefort, Tómm et al. 2009). Experimentalists are well-aware of the effects of increasing intersomatic distances on such connection probabilities and attempt, whenever possible, to restrict the intersomatic distance in experimental measurements to a narrow range, usually within 50 or 100 μm . Morphological estimates of connectivity predict an effect of distance on the expected connectivity (Kalisman, Silberberg et al. 2003; Chklovskii 2004; Stepanyants, Hirsch et al. 2008). Morphology definitely provides one of the most important constraints to connectivity, since cells whose axonal and dendritic arborizations do not overlap cannot be monosynaptically connected.

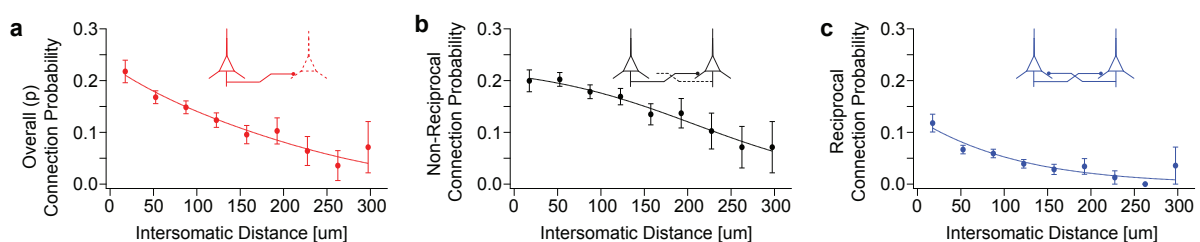


Figure 3-1 Connection probability as a function of distance. (a) Overall connection probability irrespective of pairwise configuration. **(b)** Non-reciprocal connection probability. **(c)** Reciprocal connection probability.

In order to test whether intersomatic distance alone is a good parameter for describing the connection probabilities of Layer V pyramidal neurons we measured connection probabilities at different intersomatic orientations and found that the differences were not statistically

significant. The functions of intersomatic distance fitting the connection probability profile can now be used for testing hypotheses concerning the organization of connections in groups of neurons.

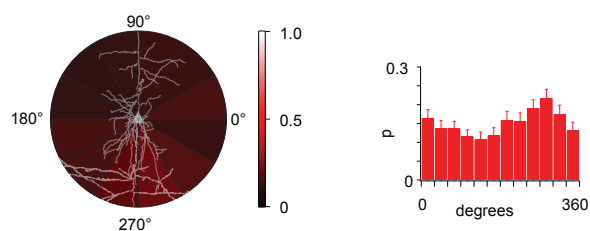


Figure 3-2 Connection probability as a function of intersomatic orientation

Assembly of pseudo-random networks

Having determined mathematical functions to describe connectivity probabilities as a function of distance and pairwise configuration, it is possible to assemble pseudo-random networks that follow these properties and in this way examine if such properties are sufficient to describe the experimental data. In order to represent neuronal networks where a single cell-type is present, directed graphs are the alternative of choice. A directed graph can be represented by a square matrix with as many rows and columns as there are neurons. Each position in the matrix $m(i,j)$ can assume either the value 1 or 0 indicating respectively that a connection exists or not from neuron i to neuron j , as traditionally done in graph theory (Erdos and Renyi 1960).

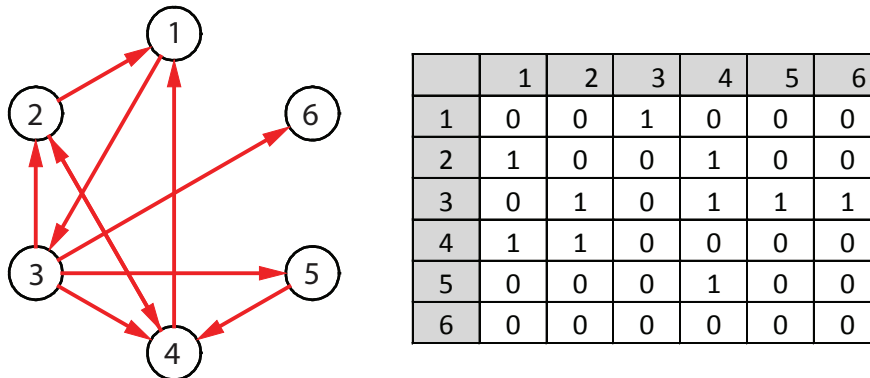


Figure 3-3 Example of random network and corresponding connectivity matrix

Entirely random networks are easily constructed, having as their only parameter a connection probability. A single line of code such as `net = rand(n) < p;` can produce a random network of any size in MATLAB. However, to produce networks with different probabilities of connection according to pairwise configuration more steps are necessary. In these networks the value in $m(i,j)$ is no longer independent from $m(j,i)$ and consequently, single random value must be generated to define the condition at symmetric positions in the matrix and four outcomes are possible instead of two. Let pr and pnr be the probability of a pair of neurons being reciprocally connected and non-reciprocally connected, respectively. For each position in the matrix where j is greater than i a random r number is generated. The outcomes are defined as follows which means that with a probability pr the pair will be reciprocally connected. With a probability $pnr/2$ the pair will be non-reciprocally connected from i to j . The same probability will apply to a non-reciprocal connection from j to i . In the remaining cases the pair is simply not connected.

To incorporate the distance relationship into the assembly of the matrix it suffices to express pr and pnr as a function of distance and apply the appropriate values for each pair. To this end a matrix $d(i,j)$ of the same size as m containing the pairwise distances has to be assembled beforehand. This is an important procedure that has been used numerous times in many of our analyses and simulations.

$$m(i, j) = \begin{cases} 1, & r < pr + pnr/2 \\ 0, & r \geq pr + pnr/2 \end{cases}$$

$$m(j, i) = \begin{cases} 1, & r < pr \\ 0, & pr \leq r < pr + \frac{pnr}{2} \\ 1, & pr + \frac{pnr}{2} \leq r < pr + pnr \\ 0, & r \geq pr + pnr \end{cases}$$

Equation 3-1 Pseudo-random network construction which accounts for high reciprocity tendency

Single cell connectivity

In a network described exclusively by the connection probability p , the sampling of an infinite number of neurons within groups of a given size yields a binomial distribution of numbers of connections per neuron. In such a scenario let us suppose experiments are performed where twelve cells are recorded in each experiment and that a probability of connection of 0.15 describes the network. In that case each neuron can project to any one of the eleven remaining neurons with probability 0.15 and receive a connection from any of those neurons with equal probability. Both incoming and outgoing connection distributions can be represented by Figure 3-4.

In this situation one third of the cells receive only one of the experimentally observed connections and the vast majority (93%) receives less than four. However, in the previous section, we have determined that connection probabilities depend on distance and pairwise configuration. Under such constraints we can calculate, using the same somatic positions obtained experimentally and the connectivity profiles determined previously, the expected number of connections that each cell should receive. Unfortunately this approach tells us little about the variability of the results. An alternative is to generate several instances of pseudo-random networks using the experimentally obtained somatic positions and connectivity profiles. Assembling a large number of such networks, i.e. 1000, we can extract a standard deviation for the distribution of incoming synaptic connections in the simulations. This variability allows us to determine the probability with which the experimental outcome would take place under the assumption that our parameters suffice to describe the network connectivity.

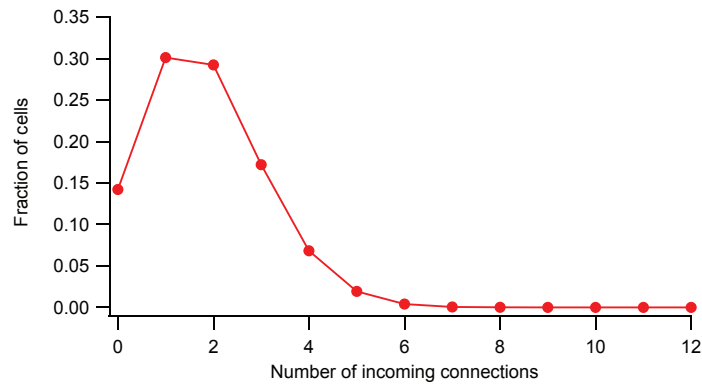


Figure 3-4 Distribution of number of incoming connections per cell

Mathematical description of connectivity patterns

In order to analyze connectivity patterns of any size a mathematical formulation is necessary. At the simplest level, the information that is required is the presence or absence of a connection at a specific location. As discussed graphs can be represented in matrix form by an adjacency matrix, which we will often refer to as connectivity matrix.

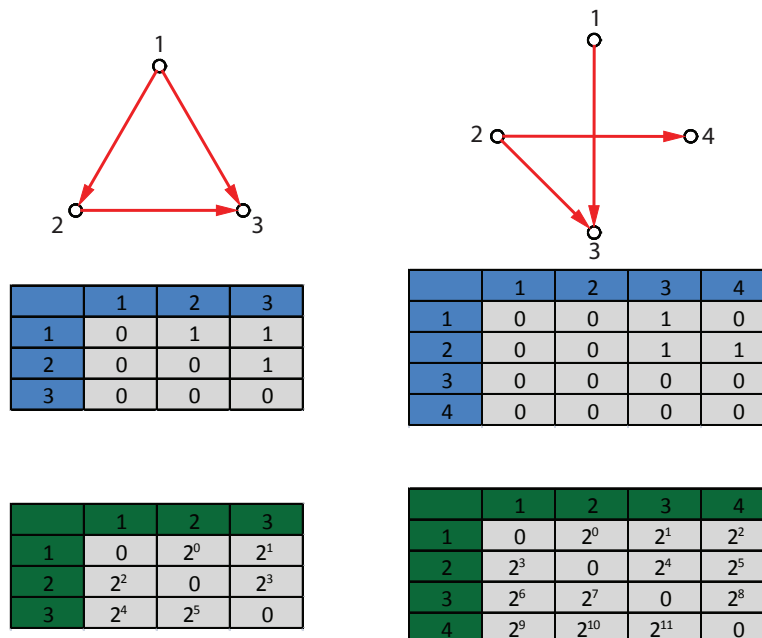


Figure 3-5 Examples of connectivity matrices

The matrix form is convenient for visualizing data but it can also be useful to obtain a representation that fully defines a pattern with a single and unique value, especially when classifying patterns into different classes. In order to obtain a unique integer code for each connectivity pattern involving a given number of neurons we can number each of the relevant positions in the connectivity matrix, ignoring the diagonal since autapses are not of interest for the current analysis. The actual code is given by the sum of the values obtained from the multiplication of the value at the given position (0 or 1) by 2 to the power of the position number.

	1	2	3	
1	0	2^0	2^1	
2	2^2	0	2^3	
3	2^4	2^5	0	

	1	2	3	4
1	0	2^0	2^1	2^2
2	2^3	0	2^4	2^5
3	2^6	2^7	0	2^8
4	2^9	2^{10}	2^{11}	0

Figure 3-6 Determination of pattern codes

Therefore the corresponding values for the examples provided in Figure 3-5 are $2^0 + 2^1 + 2^3 = 11$ for the three-neuron pattern and $2^1 + 2^4 + 2^5 = 50$ for the four-neuron pattern according to the convention described (Figure 3-6). It is important to be able to describe every possible outcome, especially if one wants to consider differences in the connectivity patterns. However, in order to compare patterns established among cells of the same type, it is useful to simplify similar patterns. Equivalent patterns are obtained by simultaneous permutations of the order of rows and columns of the connectivity matrix. This is the case only because we assume that the cells are of the same type. In this case the same pattern is represented when cell 1 projects to cells 2 and 3 as compared to cell 2 projecting to cells 1 and 3, (Figure 3-7, pattern number 2). In Figure 3-7 are illustrated the different patterns with the same simplification into one of the 16 possible outcomes.

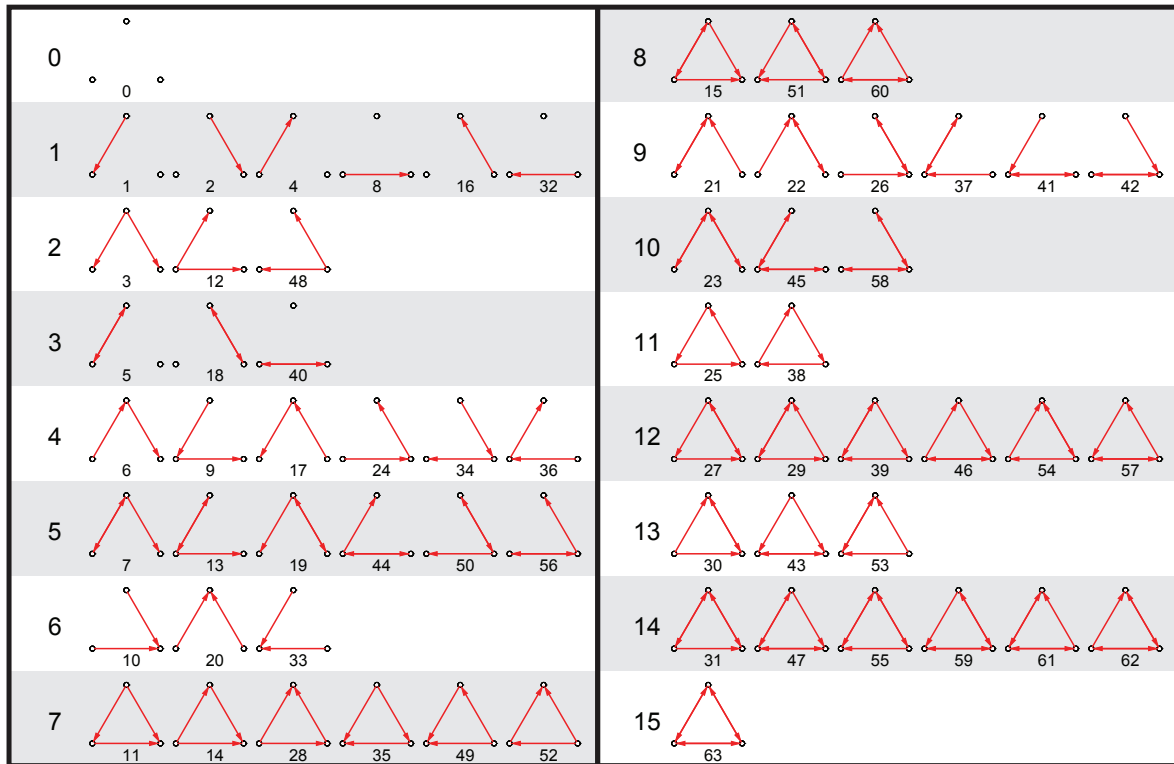


Figure 3-7 Simplification of three-neuron connectivity patterns

The same logic can be applied to groups of four or more neurons although the number of possible patterns grows extremely fast, according to the binomial coefficient ${}_n C_k$. The number of possible connections c within a group of n neurons is given by $c = n(n-1)$. The number of possible patterns is calculated with the formula $p = 2^c$. Thus for four-neuron groups the number of possible connectivity patterns is 4096 and for five-neuron groups it is above one million. Four-neuron patterns can be simplified into 218 classes just as three-neuron patterns can be simplified into 16 classes. Larger groups not only present a much greater challenge for simplification but it also becomes more difficult to interpret the possible meaning of a given pattern. For groups of five to eight neurons we grouped patterns according to the number of connections they contain. To extract the number of connections in a given pattern it suffices to count the non-zero elements of the connectivity matrix or decompose the pattern code in powers of 2 and count the non-zero values.

Clustering Algorithms

In this section we will discuss clustering as the process of separating a network or graph into sub-graphs according to its underlying structure. Usually the properties that are sought for a cluster are:

- a larger than average density of connections in the cluster
- a lower than average number of connections from the cluster to nodes external to the cluster
- the nodes in the cluster must all be connected, in few steps, by edges internal to the cluster.

In the literature clustering is also known as the identification of community structure in networks given a history of applications to social sciences. Two general approaches can be applied to the formation of clusters: divisive and agglomerative. Agglomerative clustering starts from a node and identifies adjacent nodes forming strongly linked groups. Such algorithms are usually efficient in identifying strongly linked cores of communities but tend to leave out peripheral vertices that clearly belong to a community. Divisive algorithms start from the entire network and progressively identify edges to remove, thus separating the network in clusters. The division is stopped when criteria that reflect ideal results are satisfied.

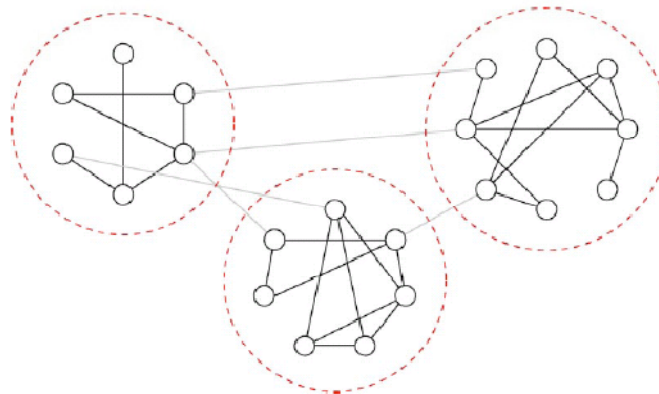


Figure 3-8 Example of graph with clear community structure (Newman and Girvan 2004)

An established algorithm for clustering (CNM) was presented by Clauset, Newman and Moore (Clauset, Newman et al. 2004) and is based on the concept of modularity. The modularity of a cluster can be defined as the difference between its number of edges and its expected number of edges based on the connection probability in the network. The algorithm starts from the whole network and iteratively eliminates an edge and recalculates the modularity for the underlying clusters. The edges are eliminated based on maximal edge-betweenness, a measure which corresponds to the number of shortest paths linking each neuron pair in the network that use the given edge. If many paths exist linking a pair of nodes the edge receives a value corresponding to the fraction of those paths in which it participates. Edges with high edge-betweenness link more densely connected groups of neurons.

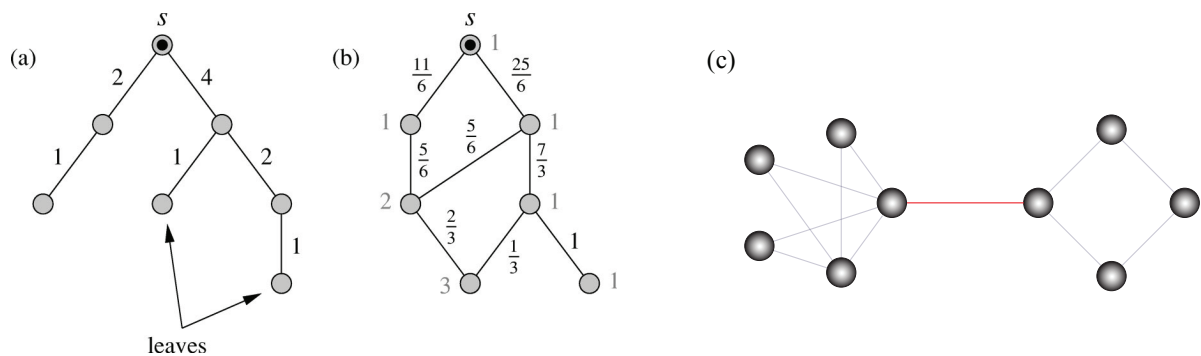


Figure 3-9 Edge-betweenness. (a,b) Step of calculation of edge-betweenness for paths starting from the marked nodes (Newman and Girvan 2004). (c) Edge with highest edge-betweenness in an example network marked in red.

The main difficulty when applying clustering algorithms to the neuronal networks modeled in the current work is the sensitivity of the algorithms to moderate numbers of connections between clusters. In most clustering applications such as social networks, the world-wide-web or protein interaction networks are more segregated and hierarchical structures are often apparent, i.e. few nodes concentrate many connections. The organization of a network with neurons of the same type and similar morphological features, such as the number of spines and varicosities, is unlikely to yield hierarchical organization, characterized by an uneven distribution of connections per node (Barabasi and Oltvai 2004). As a consequence the identification of clustering in neocortical networks may require very sensitive analytical methods.

Recently some authors have been faced with networks which required more refined techniques for clustering because traditional algorithms such as CNM's often yielded nearly trivial or trivial solutions encompassing all nodes in a network. In order to identify densely connected clusters Moussiades and Vakali (Moussiades and Vakali 2010) propose an agglomerative algorithm to maximize the intra-cluster connection ratio (AICR). The ICR of a cluster c is equal to the sum of the connection degree between cluster c and each of its vertices divided by the sum of the degrees of all vertices in c .

$$ICR(c) = \frac{\sum_{v \in c} d(c, v)}{\sum_{v \in c} d(v)} = \frac{2I_c}{2I_c + X_c}$$

Equation 3-2 Intra-cluster connection ratio (ICR)

I_c corresponds to the number of connections internal to the cluster and X_c , to the number of connections linking cluster c to the remaining network.

Traditional algorithms yield clusters where each node is more strongly connected to its cluster than with the remaining network. The AICR algorithm yields refined clusters that are more strongly connected to their cluster than any other cluster, a property of interest when considering neuronal networks. To illustrate the different results of CNM's well-established algorithm and the new AICR algorithm consider Figure 3-10 where the CNM algorithm yields clustering [0, 1, 2, 3, 4, 5] whereas ICR maximization yields the refined clusters [0, 1, 2], [3, 4, 5].

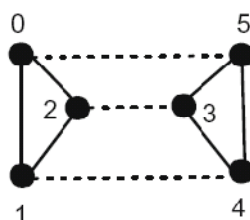


Figure 3-10 Different results for CNM and AICR algorithms (Moussiades and Vakali 2010).

The AICR algorithm can also be adapted to directed graphs, where Equation 2-1 still holds. In fact, it could possibly be adapted to account for the strength of interactions as well. Here, however we concentrate on the directed graph approach. Figure 3-11 illustrates clusters identified with the directed graph version of AICR.

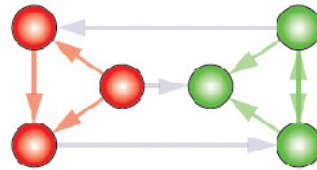


Figure 3-11 Results of the adaptation of AICR to directed graphs

Using Equation 3-2 we obtain that the red cluster has an *ICR* value of $6/(6+3) = 0.67$, just as the example clusters in the undirected case, while the green cluster has an *ICR* of $8/(8+3) = 0.73$. It is interesting to notice that the trivial clustering with all nodes belonging to the same cluster yields an *ICR* value of 1 while the obtained solution yields 1.4. The search for clusters in the AICR algorithm starts from a situation where each node constitutes a cluster. The merging of two clusters that yields the greatest increase in *ICR* is then performed. If more than a single option exists, one is selected randomly. The algorithm returns the clustering with largest *ICR* value identified. The algorithm may not always return the same solution for a dataset which is why it should be run several times.

RESULTS

Here the concepts explained in the introduction are employed to describe the organization of neocortical connectivity. The results are presented in the form of a manuscript.

Hebbian-like assemblies in the local neocortical circuits

Rodrigo Perin¹, Thomas K. Berger^{1,†} and Henry Markram¹

¹*Laboratory of Neural Microcircuitry, EPFL, Lausanne, Switzerland*

[†] Present address: Department of Molecular & Cell Biology, University of California, Berkeley.

Tightly-coupled groups of neurons, commonly called Hebbian assemblies, are believed to subserve memories by undergoing experience-dependent modifications in their patterns of synaptic interconnectivity. Such assemblies are also thought to contribute to the cortex's functional architecture. There is considerable evidence for functionally collaborating neurons, but direct observation of synaptically connected assemblies requires recording from many neurons simultaneously. We therefore developed a twelve-electrode patch-clamp system to simultaneously record from groups of pyramidal cells in neocortical slices in order to search for these elusive Hebbian assemblies. We found highly significant clustering of synaptic connectivity when analyzing groups of at least six recorded neurons. Maximal clustering was surprisingly dispersed suggesting that many separate assemblies can be overlaid and interlaced in the same local neural space. Paradoxically, however, both connectivity and synaptic weights between neurons can be analytically computed from the number of their common neighbors, suggesting that the functional architecture of these assemblies is significantly predetermined. We therefore demonstrate that Hebbian-like assemblies do exist in local circuits, but hypothesize that these assemblies may develop as universal, elementary and innate pre-representations and that acquired memories may better develop by modifying the weights between assemblies to build supra-assemblies.

Donald Hebb's profound insight over 50 years ago, that "neurons which fire together also wire together" (Hebb 1949) implies that when groups of neurons are co-activated, they tend to become more tightly synaptically-coupled to each other than with non-activated neurons. Such assemblies of tightly coupled neurons, formed by experience, are commonly called Hebbian

assemblies and are thought to be the neural substrate for acquired memories. An enormous body of work has since verified the long-lasting plasticity of synapses when synaptic pathways are activated and when two neurons are co-activated (Bliss and Lomo 1973; Kirkwood, Dudek et al. 1993; Singer 1995; Malenka and Nicoll 1999; McNaughton 2003; Holtmaat and Svoboda 2009). This synaptic phenomenon has important implications for the formation of memories as it implies that patterned stimulation is imprinted in the brain as patterned synaptic connectivity. The clustering of synaptic connectivity in particular is thought to bind together multiple facets of a stimulus in such a way that even when a remotely similar stimulus is subsequently presented, the same group of neurons would be more easily activated (Martin, Grimwood et al. 2000; Dudai 2002; Kandel 2006). Hebb's insight went further to suggest that persistent reverberations of activity within these assemblies could serve to hold and retrieve memories (Hebb 1949; Fuster and Alexander 1971; Kubota and Niki 1971; Goldman-Rakic 1995; Compte, Brunel et al. 2000). This is an intriguing and powerful concept that has shaped research on learning and memory mechanisms for decades. Hebbian assemblies could exist at different scales with elementary assemblies coupled to larger assemblies to form supra-assemblies. While topographically targeted projections between local circuits clearly create functional clustering across brain regions, it has still not been possible to conclusively prove that Hebbian assemblies exist at the most elementary level of the local microcircuitry and that they can indeed be the location for the storage of acquired memories.

Numerous functional studies have provided indirect evidence supporting the existence of local Hebbian assemblies. *In vivo* multi-unit recordings in multiple brain regions can show many spatiotemporal patterns (Fuster and Alexander 1971; Kubota and Niki 1971; Gray, Konig et al. 1989; Abeles, Bergman et al. 1993; Nicolelis, Baccala et al. 1995; Stopfer, Bhagavan et al. 1997; Ji and Wilson 2007; Pastalkova, Itskov et al. 2008) and *in vitro*, calcium imaging of multiple neurons has demonstrated correlated activity of groups of neurons (Ikegaya, Aaron et al. 2004). The nature of the circuits that support such patterned activity is however not clear. Neurons also participate in synchronous assemblies that have been proposed to bind features in perceptions, but it is believed that their participation is transient, as well as phase and stimulus dependent and it is also not clear whether these are due to local or more distributed interactions (Abeles, Bergman et al. 1993; Singer and Gray 1995; Maurer, Cowen et al. 2006). Momentary clustering

of activity can be caused by many functional mechanisms, including habituation and sensitization of synapses, recruitment of additional neurons in a network, ongoing network activity, stimulus priming, and the pattern of input stimuli (Compte, Brunel et al. 2000; Tsodyks, Uziel et al. 2000; Fellous and Sejnowski 2003). Theoretical models have shown that plasticity processes can generate Hebbian assemblies, which could have compelling information processing and memory storage capabilities (Hopfield 1982; Amit, Gutfreund et al. 1987), however questions remain about the stability of such assemblies since subsequent stimuli pose limitations on the capacity to store acquired memories (Parisi 1986; Amit, Brunel et al. 1994; Fusi and Abbott 2007; Rubin and Fusi 2007). Cortical circuits are also profoundly shaped by both learning and sleep (Sejnowski and Destexhe 2000; Kali and Dayan 2004; Ji and Wilson 2007), but the nature of the resulting circuitry is also not yet clear.

Hebbian assemblies, which we consider as clusters of neurons statistically more densely connected to each other than with other surrounding neurons, have been difficult to find because they require recording from large groups of neurons simultaneously. Paired recordings of cortical neurons in brain slices were pioneered with sharp-electrodes (Thomson, Deuchars et al. 1993) followed by multi-neuron patch-clamp recordings (Markram, Lubke et al. 1997), which allowed experiments that began revealing non-random local connectivity (Markram 1997; Markram, Lubke et al. 1997). Many intricate rules started to be revealed such as synaptic mapping between neurons that govern cell-type to cell-type target preferences (Thomson, Bannister et al. 2002; Thomson and Morris 2002; Thomson, West et al. 2002; Watts and Thomson 2005; West, Mercer et al. 2006) and the numbers and distributions of synapses formed, all factors that point towards Hebbian assemblies. One study showed that some patterns of synaptic connectivity occur more often than expected by chance among triplets of neurons (Song, Sjöström et al. 2005), while other studies found different connection probabilities reflected sub-networks for processing information from a different neocortical layer (Yoshimura, Dantzker et al. 2005; Kampa, Letzkus et al. 2006) or providing outputs to different brain regions (Le Be, Silberberg et al. 2007; Brown and Hestrin 2009). These studies inspired us to broaden the search for Hebbian assemblies with a large number of simultaneous patch-clamp recordings. Importantly, at the spatial scale of our experiments (around 30-300 μm), expected probabilities change rapidly with intersomatic

distance and hence the search for assemblies must account for distances between neurons otherwise clustering of the closest neurons may appear more significant than it actually is.

We developed a new multi-neuron patch-clamp system that is capable of 12 simultaneous whole-cell patch-clamp recordings of neurons located anywhere in a space spanning a few hundred micrometers in a neocortical slice. Using infrared differential interference contrast microscopy, we could select the same type of cortical neuron for all the experiments and obtain the exact XYZ position of each neuron relative to each other. We recorded exclusively from the thick tufted layer 5 pyramidal neurons in the neocortex of young rats (postnatal days, 14 – 16) since these neurons have been extensively studied at this age and have served as a model system for many cortical connectivity studies (Stuart and Sakmann 1994; Markram 1997; Kalisman, Silberberg et al. 2005; Song, Sjöström et al. 2005; Frick, Feldmeyer et al. 2007; Krieger, Künner et al. 2007).

Non-Random, Non-Lattice Connectivity

We performed whole-cell patch-clamp recordings in somatosensory cortical slices (300 μm) of Wistar rats (Fig. 1a-c) and determined connectivity of the neurons by applying trains (5 – 15 spikes at 20 – 70 Hz) of brief current steps (~ 2 nA for 2.5 – 4 ms) and recording the synaptic response in each of the other neurons in current-clamp mode (typically 20 trials) (Fig. 1d). Synaptic connections are readily revealed and the average amplitudes across multiple trials provide a reliable measurement of synaptic connections that produce microvolt-range postsynaptic responses. Twelve patch-clamp recordings allow capturing on average 20 synaptic pathways per experiment (Fig. 1d-e).

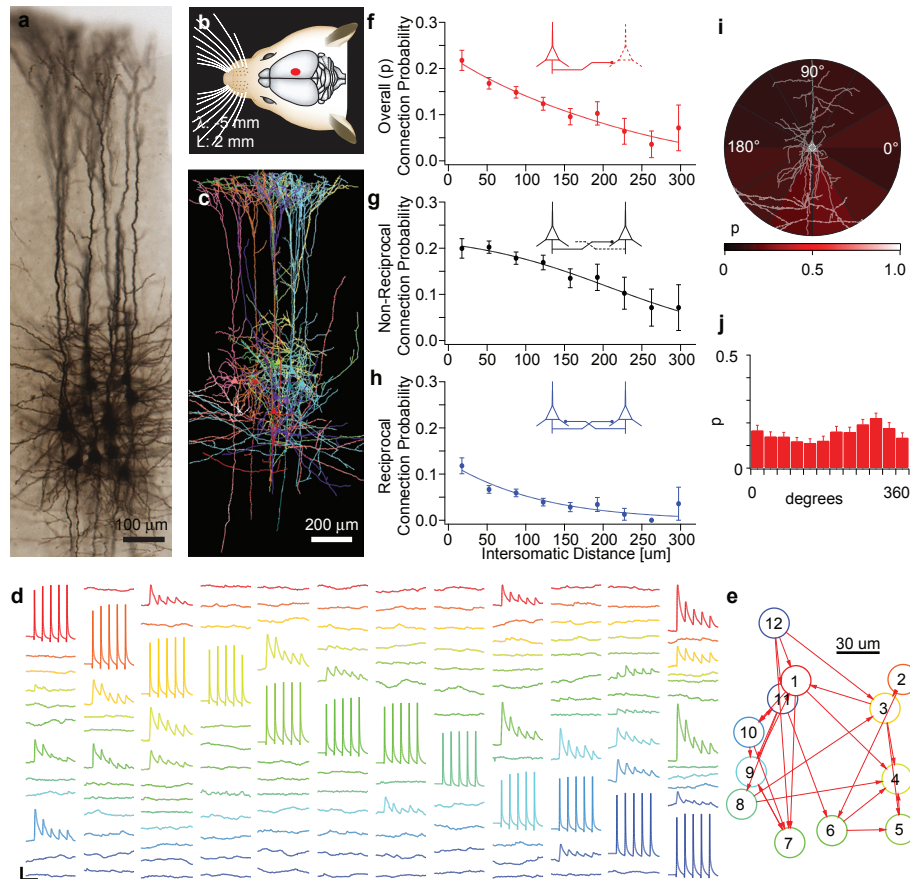


Figure 1 Pairwise connectivity. **(a)** Morphological staining of a cluster of twelve cells recorded simultaneously. **(b)** Region of the somatosensory cortex where recordings were done. **(c)** Example of morphologically reconstructed cluster. **(d)** Example of recorded traces in an experimental session. A different neuron is stimulated in each column and the responses of the remaining neurons are shown in the corresponding columns. Scale bars: horizontal 100 ms; vertical 1 mV (15 mV for action-potentials). **(e)** Connectivity diagram of neurons in **d**. **(f, g, h)** Connection probability profiles as a function of distance. **(i)** Intensity plot of outgoing connection probability at different intersomatic orientations, brighter regions have higher connection probability. **(j)** Bar plot of connection probabilities at different orientations.

The tridimensional (XYZ) coordinates of the somatic position of each recorded neuron were obtained and used to determine the distance-dependent profiles of connection probability (Fig. 1f-h). The number of occurrences of connections divided by the number of tested pathways yielded an estimate of the connection probability p as a function of distance between neurons. As expected, p decreases with distance ($P < 0.02$, Kruskal-Wallis test) (Fig 1e). The non-reciprocal and reciprocal connection probability profiles describe, in terms of intersomatic distance, the probability with which pairs of neurons ($n = 3237$) form uni- or bi-directional connections, respectively. Bi-directionally connected pairs occurred above chance level (Markram 1997), that

is, with probabilities greater than p^2 and thus estimates of the different pairwise configurations need to be considered to describe connectivity (Song, Sjöström et al. 2005). As expected, both probabilities decrease with distance (Fig. 1g-h), but unidirectional connection probability decays less abruptly reflecting some non-random overall organization of the connectivity. Bi-directional connection probability was also over 2 fold higher than expected, further supporting the previous notion that the microcircuitry is non-randomly organized. Connection probability p as a function of intersomatic orientation was not significantly different ($P = 0.23$, Kruskal-Wallis test) (Fig 1i-j) suggesting that there is no obvious lattice-like connectivity.

Distributed and Interlaced Assemblies

Using the distance-dependent profiles for reciprocal and non-reciprocal connections, we assigned to each recorded neuron pair ($n = 1468$ pairs in experiments involving at least eight neurons) the probabilities associated with each of the four possible connectivity graphs given their intersomatic distance. For example, given a pair of neurons A and B separated by $100\ \mu\text{m}$, the probability that these neurons connect reciprocally is ~ 0.05 . The probability that A projects to B while B does not project to A is ~ 0.09 . The same value describes the opposite relationship. The probability of the absence of any monosynaptic connections between neurons A and B is ~ 0.77 . From these probabilities, we derived expected values (see also Supplementary Methods) for the connectivity graphs within groups of neurons.

The number of groups that can be obtained from one experiment are given by the binomial coefficient ${}_n C_k$ where n is the number of recorded neurons in the experiment and k is the group size. We first assembled every possible subgroup of three neurons in each experiment ($n = 4199$) and counted the number of connections in each of these groups. These experimental counts were compared to the calculated distribution. We then repeated the operation for groups of four to eight neurons (Fig. 2a; $n = 8202, 11544, 12012, 9306, 5319$, respectively). Using this analysis we found that the number of groups with connectivity above chance level steadily increased as larger groups of neurons were examined (Fig 2). The difference between overall observed and expected distributions of the number of connections per group were not significant (i.e. the observed and expected samples could have come from the same underlying distribution) for

groups of three or four neurons ($P=0.7$ and 0.6 respectively, Two-sample Kolmogorov-Smirnov test), but highly significant for groups of six neurons or more ($P<0.001$ Two-sample Kolmogorov-Smirnov test). These data provide direct evidence of statistically significant clustered connectivity and further indicate that evidence for highly significant clustering within the network requires sampling at least 6 of the neurons simultaneously. When expected values are calculated with the experimentally obtained profiles (Fig 1g, h), the overall distribution of the number of connections for groups of three and four neurons is not significant, but some specific connectivity patterns are significantly overrepresented ($P<0.01$, z-test and Bonferroni correction for multiple hypothesis), consistent with a previous study (Song, Sjöström et al. 2005). The listing of specific over-represented patterns involving three and four neurons is shown in the Supplementary Methods.

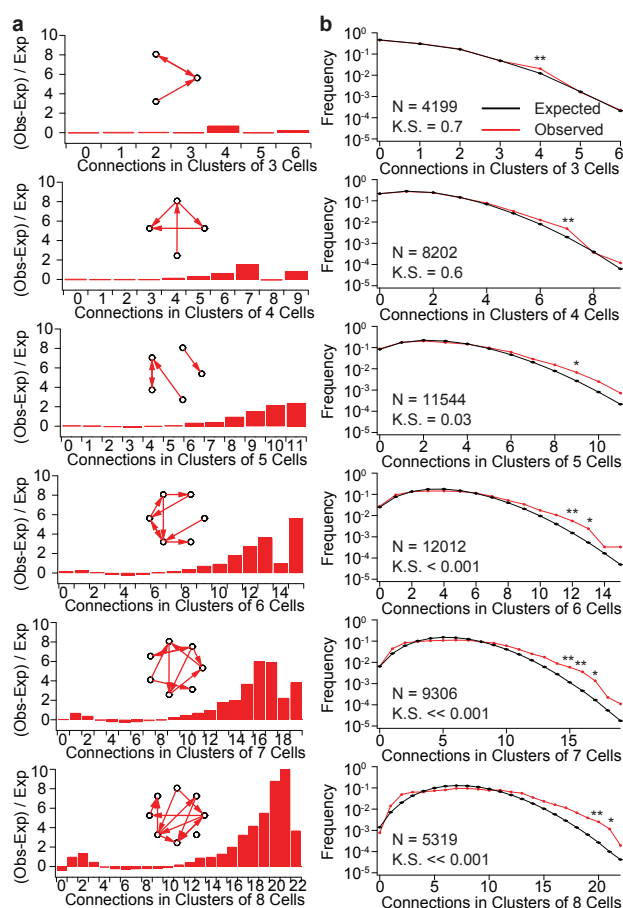


Figure 2 Higher order connectivity. (a) Difference between the observed and expected values in panel a divided by the expected values ($(Observed-Expected)/Expected$). Inset: schematic examples of possible patterns. Notice the increasingly larger disparity for clusters with many connections. (b) Comparison of observed (red) and expected (black) prevalence of given numbers of connections in clusters of three to eight cells.

Clusters of synaptically-coupled neurons could result from a few individual neurons systematically forming a large number of connections, thus acting as hubs. Highly connected neurons were, however, not observed above chance level ($P = 0.6$ Two-sample Kolmogorov-Smirnov test, Supplementary Fig 3a). Even considering separately incoming and outgoing connections, we did not find significant differences (Supplementary Fig 3b, c). These data therefore do not support the existence of hub-like connectivity among neurons of the same type in this neocortical microcircuit. A more distributed connectivity principle would seem to underlie clustered connectivity.

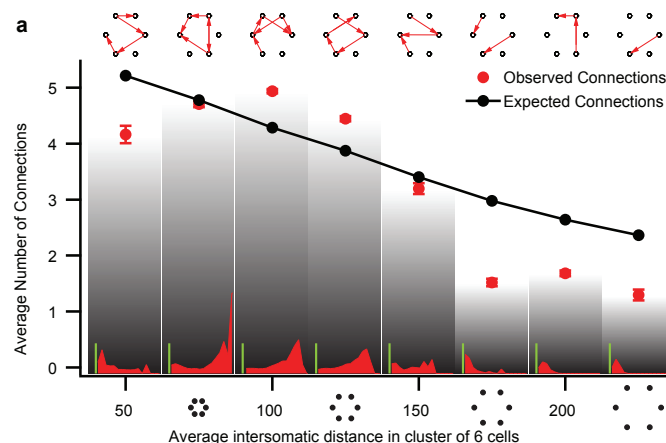


Figure 3 Clustering effect. (a) Average number of connections in clusters of six cells grouped according to cluster dimension. Inset: Difference over expected profiles as in Fig 2b for different cluster dimensions.

To examine the spatial spread of clustered connectivity across the microcircuit, we studied how connectivity changes when the neurons within groups of six neurons are progressively further apart. We used the average intersomatic distance as an indicator of the compactness of neuron groups and noticed that, quite contrary to expectations, the average number of connections in a group of neurons does not monotonically decrease with average intersomatic distance (Fig 3a, $P < 0.01$ Two-sample Kolmogorov-Smirnov test). In fact, groups with the

average intersomatic distance of 100 - 125 μm displayed the highest average number of interconnections, rather than those groups of closely packed neurons. Consequently, clusters of highly connected neurons are not confined to minicolumns (around 30-50 μm), but are rather spread out within the dimensions of a neocortical column (around 300-500 μm).

Common Neighbors Predict Connection Probability

Inspired by Watts and Strogatz's clustering coefficient (Watts and Strogatz 1998), a measure of the average interconnectivity among all the nodes in a network that connect to a given node, we proceeded to study the effect of clustering onto connection probabilities. We thus measured the average interconnectivity within pairs of neurons according to the number of common neighbors the pair shared. For simplicity, let us denote neurons connected by reciprocal or non-reciprocal connections, irrespective of direction, as neighbors. We found, according to the connection probability profiles and assuming approximately homogeneous density of pyramidal neurons that the neurons with the highest number of common neighbors are also located 100-125 μm apart (Fig 4a), the same range as for maximal clustering. These data suggested that connection probability between neurons is related to the number of common neighbors. We then observed that, at each intersomatic distance bin, the probability of connection is higher between neurons that share at least one common neighbor than between neurons that have no common neighbor (Fig 4b). Without knowing the complete network connectivity, our sampling was apparently representative enough to allow the observation of a clear tendency towards higher connection probabilities as the number of common neighbors that were recorded increased (Fig. 4c). The expected values are calculated based on the pairwise distance-dependent profile applied to the intersomatic distance of each tested pair (see Supplementary Methods).

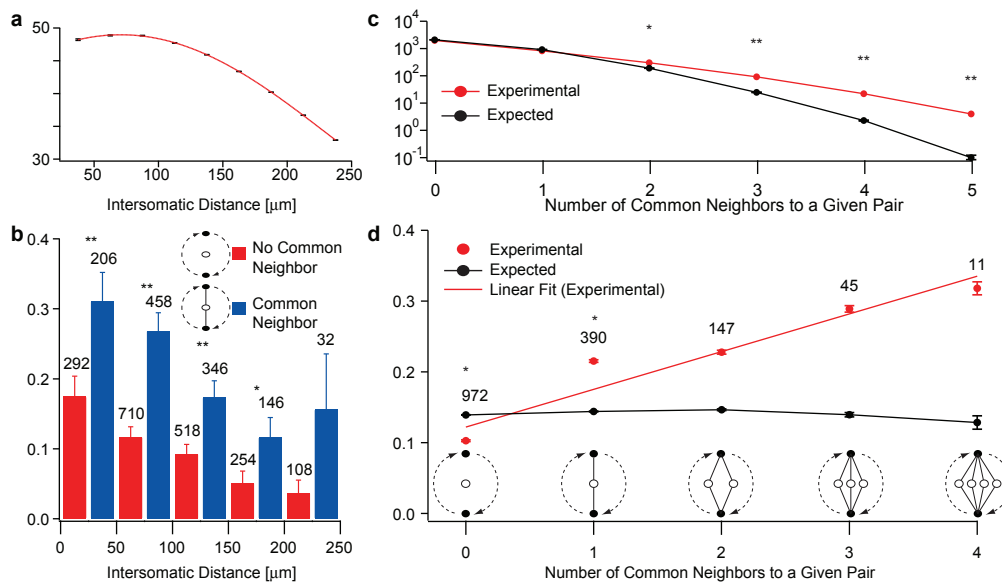


Figure 4 Common neighbor effect. (a) Estimated average number of common neighbors for Layer V as a function of distance based on connectivity profiles of Figure 1 g and h with a cell density of 21400 cells/mm³. Notice that clusters with highest number of connections fall in the region where neurons are expected to share most neighbors. (b) Connection probability as a function of distance comparing pairs that share a common neighbor against those that do not. (c) Occurrences of pairs of neurons sharing more than two common neighbors were significantly more numerous than expected by chance. (d) Connection probability between neurons experimentally observed as a function of the number of common neighbors.

Connectivity Predicts Synaptic Weights

The notion of imprinting sensory experiences onto synaptic landscapes implies the freedom for synaptic weights to change according to prior stimuli. Hebbian theory drove the notion of strengthening connections in assemblies, but later theoretical work showed that weakening connections is equally important in the storage of memories (Stent 1973). Indeed, long-term depression was subsequently demonstrated and has been observed in many brain regions and is implicated in memory formation (Ito 1986; Kirkwood, Dudek et al. 1993; Kirkwood and Bear 1994). The precise dependency on spike timing of pre and postsynaptic neurons can also drive connections within assemblies in both directions (Markram, Lubke et al. 1997; Bi and Poo 1998; Sjostrom, Turrigiano et al. 2001; Li, Lu et al. 2004). Thus, while a Hebbian assembly may be a highly physically connected cluster of neurons, the landscape of synaptic weights in the connections is expected to be shaped by the history of stimulation. We found that the probability

of synaptic coupling between any two neurons is proportional to the number of common neighbors the pair of neurons shares and therefore asked whether there is any relationship between the connectivity architecture and the synaptic weights of these connections.

We measured the average synaptic strength of the connections within groups of six neurons. Surprisingly, we found that the average strength as a function of distance followed closely the average number of connections as a function of distance (Fig 5a) suggesting a relationship between the number of connections in a cluster and the average strengths of these connections. Indeed, we found a striking relationship between the average amplitude of EPSPs and the level of interconnectivity within groups of neurons (Fig 5b, c). In order to confirm that this observation is not due to chance, we kept the same connectivity matrix for each experiment while the corresponding amplitudes were randomly assigned a value from the pool of recorded connections that was subsequently removed from the pool to avoid repetitions. We performed one hundred such amplitude redistributions over the entire set of experiments. Each time, the positive correlation was lost to constant average connection amplitudes, independent of the number of connections in a group. The synaptic weights recorded are unexpected, because they seem highly prescribed by the connectivity and are progressively stronger as the cluster density increases. To further explore this constraint, we performed a comparison of the distributions of synaptic strengths according to the number of common neighbors. We found a progressive shift in the distribution towards stronger connections as the number of common neighbors increased (Supplementary Fig. 4). Furthermore, synaptic weights follow a different slope of increase depending on whether the common neighbors are defined as common input or output neurons (Supplementary Fig 5).

The remarkably exact relationship between the average synaptic strength and the number of connections in general and the number and source of the common neighbors in particular, further suggests that not only the configuration of synaptic connectivity, but also the mean synaptic strength is to a large extent predetermined for any cluster of neurons, even across different animals of the same species. For groups of six neurons with any given number of connections, the amplitudes were significantly different from randomly assigned values (Two-sample Kolmogorov-Smirnov test Bonferroni corrected).

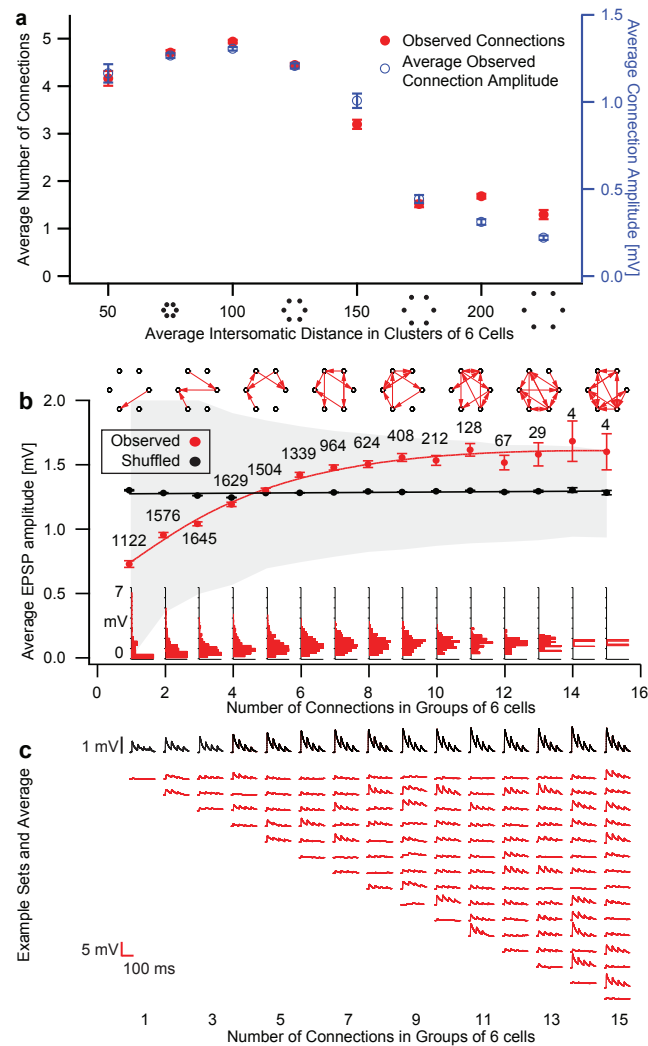


Figure 5 Clustering effect. (a) Average number of connections in clusters of six cells grouped according to cluster dimension (red) and corresponding average connection amplitude (blue). Inset: Difference over expected profiles as in Fig 2b for different cluster dimensions. (b) Connection amplitude as a function of number of connections in a cluster (red) and results after random shuffling of connection amplitudes (black). Inset: Distributions of average connection amplitude for groups with different numbers of connections. (c) Average amplitude and examples of the of connections recorded in corresponding clusters.

Construction of Hebbian Assemblies

In order to check whether the principles derived from these experiments are indeed sufficient to result in Hebbian-like assemblies, we connected a simulated network of 1000 “point neurons” (595 neurons/mm³) according to their pairwise connectivity profiles. We then applied a pairwise reorganization rule where connections occur with a probability that depends on the number of

common neighbors shared by the pair (see Supplementary Methods). The model assembly can be completed by assigning synaptic weights according to the number of common neighbors to yield synaptic clustering with proportional synaptic weights. We replicated the sampling and analysis performed in the experiments by “recording” from groups of twelve cells and analyzing all subgroups of three, six and eight neurons in each set of twelve neurons.

We found that this reorganization rule indeed leads to clustered networks whose connectivity properties are similar to those observed experimentally. Our algorithm successfully yields connection probabilities that are proportional to the number of common neighbors (Fig 6a) while respecting the overall, reciprocal and non-reciprocal pairwise connectivity as a function of distance (Fig 6 b-d). Similar tendencies to clustering as illustrated in Figure 2 are observed in the model (Fig 6 e, f). Finally, the model also yielded spatially distributed clusters (Fig 6g). In order to identify the most elementary clusters of neurons we applied a method of agglomerative maximization of intra-cluster connection ratio (AICR) described recently that provides refined clusters with large density of connections (Moussiades and Vakali 2010). We adapted the algorithm for directed graphs and applied it to 20 reorganized model networks. The algorithm successfully identifies groups of two to six neurons (2.4143 ± 0.6739) with interconnections significantly more numerous than expected and involving more neurons than in a purely random network. By definition neurons in these clusters are more interconnected within the cluster than with any other cluster. These results, similar to those obtained when applying the algorithm to experimentally obtained networks (Figure 6h, i), show that a simple common neighbor rule can result in Hebbian-like assemblies. Even if activity dependent plasticity during development drives changes in the circuit configuration and synaptic weights, the resulting configuration and synaptic weights must fall within the constraints of physical and functional architecture.

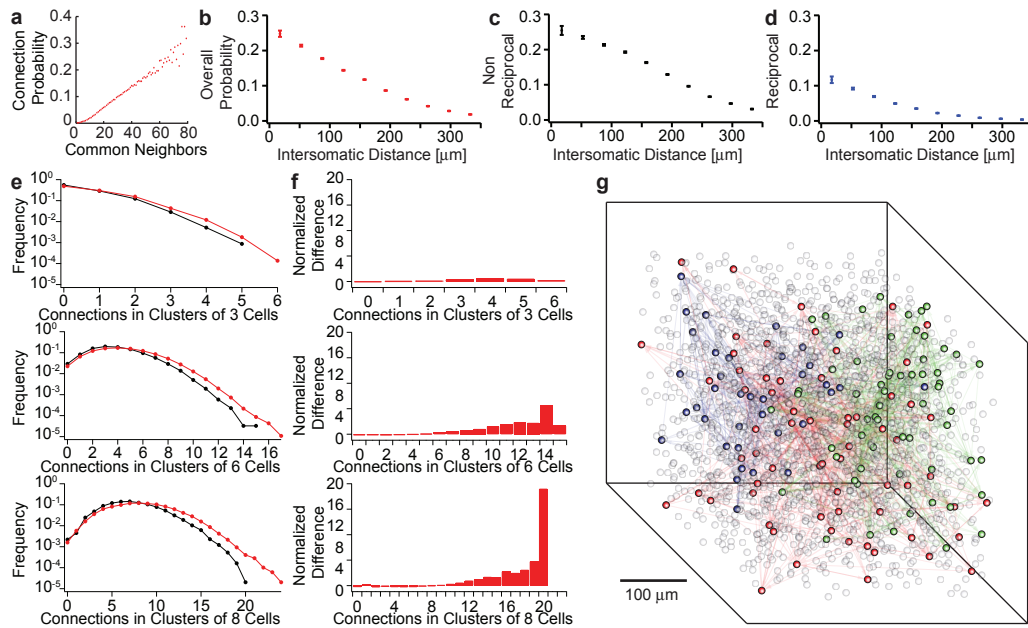


Figure 6 Simulation of Clustered Connectivity. (a) Linear increase of connection probability in simulated network as a function of the number of common neighbors. (b, c, d) Model connection probabilities that reflect the same function of distance as found in the experimental data. (e, f) Properties of simulated network of 1000 neurons that reflect experimental measurements shown in figure 2. (non-reorganized (black), reorganized (red)) (g) Connectivity diagram for the 0.5% strongest connections (involving roughly 10% of the simulated neurons). Neurons belonging to three given clusters shown in red, green and blue. Neurons that belong to other clusters shown in black.

Concluding remarks

We provide direct demonstration of the existence of elementary assemblies of neurons embedded at the level of the neural microcircuit. The assemblies are characterized by significantly higher densities of connections than expected by chance, which are also stronger the more clustered the neurons become. The neurons in these assemblies are related through sparser and weaker connections to neurons in different assemblies. The assemblies were surprisingly distributed allowing multiple assemblies to be overlaid and interlaced in the same neural space. The assemblies are not formed according to hub-like or lattice-like principles.

Many functional mechanisms are at play in neuronal circuits. Long-range efferent input and afferent outputs (Brown and Hestrin 2009; Petreanu, Mao et al. 2009) influence local connectivity, functional maps reorganize as a function of activity (Kilgard and Merzenich 1998;

Trachtenberg, Chen et al. 2002), neurons connect and disconnect to rewire the microcircuitry within hours (Le Be and Markram 2006), spines constantly and rapidly form and retract (Holtmaat and Svoboda 2009; Zito, Scheuss et al. 2009) and the precise relative timing between action potentials shapes synaptic strength (Markram, Lubke et al. 1997). However, it is likely that these plastic changes are occurring on a tightrope of innately determined constraints.

These findings do not discount that new experiences can shape synaptic weights within assemblies, but do indicate that these weights are significantly constrained. Weaker connections undergo much larger changes than stronger ones during plasticity protocols (van Rossum, Bi et al. 2000) which would further suggest that the connections within Hebbian assemblies are more difficult to change than those weaker ones between assemblies. Even if experiences can imprint a new connectivity configuration and shape a new landscape of synaptic weights within such local assemblies, the intense recurrent connectivity and strong synaptic connections, would tend to cause a collective response that may not necessarily be easily distinguishable from another configuration and/or landscape of synaptic weights hence limiting the scope for storage of many different memories.

Predetermined connectivity rules and synaptic weights pose the problem of how new experiences can be stored by microcircuit and synaptic plastic reorganization in general and by the reorganization of Hebbian assemblies in particular. One possibility is that assemblies are elementary building blocks for memories that hold innately prescribed representations. In such a scenario, microcircuit and synaptic plasticity within assemblies could serve to consolidate (and perhaps introduce subtle variations in) prescribed synaptic weights and connectivities to mature the neural substrate of innate representations. Circuit and synaptic plasticity of the weaker connections between assemblies, on the other hand, could serve to link assemblies into supra-assemblies in different sequences and combinations, depending on prior experiences, to form the neural substrate of acquired memories – a form of “lego memory”. The value of having predetermined assemblies may reside in providing a common genetically determined starting point to ensure similar perception and memory processes in animals of the same species. Indeed, some theories of memory have argued that memory formation from a tabula rasa is not possible without prior representations (Young 1979; Heidmann, Heidmann et al. 1984; Dudai 2002) that

hold a priori knowledge (Kant and Meiklejohn 1872). A recent study also proposed that consolidated spine changes could serve as a foundation for subsequent changes (Hofer, Mrsic-Flogel et al. 2009).

We therefore hypothesize that the most elementary Hebbian assemblies may constitute a key component of the neural substrate for innately determined pre-representations, while relationships between assemblies may form larger-scale Hebbian assemblies constituting a key component of the neural substrate for acquired memories.

METHODS SUMMARY

Electrophysiological recordings. Whole-cell recordings were made from pyramidal neurons at 35 °C in rat somatosensory cortex (λ -5, medio-lateral 2) slices from animals aged P14–16. Neuronal connectivity was established with trains of current pulses (5 to 15 pulses at 20 to 70 Hz).

Data analysis. Data was analyzed using IGOR (WaveMetrics), MATLAB (MathWorks) and C++. Clustering was performed using NodeXL (CodePlex). The cortical layer 5 neuron model was assembled with 1000 cells in a cube layout using MATLAB. Data are presented as mean \pm s.e.m.

Computer-assisted patch clamp. Recordings were achieved with custom C++ software that controlled manipulators, amplifiers, oscilloscopes, pipette pressure and video display.

REFERENCES

- Abeles, M., H. Bergman, et al. (1993). "Spatiotemporal firing patterns in the frontal cortex of behaving monkeys." *J Neurophysiol* **70**(4): 1629-1638.
- Amit, D. J., N. Brunel, et al. (1994). "Correlations of cortical Hebbian reverberations: theory versus experiment." *J Neurosci* **14**(11 Pt 1): 6435-6445.
- Amit, D. J., H. Gutfreund, et al. (1987). "Information storage in neural networks with low levels of activity." *Phys Rev A* **35**(5): 2293-2303.
- Bi, G. Q. and M. M. Poo (1998). "Synaptic modifications in cultured hippocampal neurons: dependence on spike timing, synaptic strength, and postsynaptic cell type." *J Neurosci* **18**(24): 10464-10472.

- Bliss, T. V. and T. Lomo (1973). "Long-lasting potentiation of synaptic transmission in the dentate area of the anaesthetized rabbit following stimulation of the perforant path." *J Physiol* **232**(2): 331-356.
- Brown, S. P. and S. Hestrin (2009). "Intracortical circuits of pyramidal neurons reflect their long-range axonal targets." *Nature*.
- Clauset, A., M. E. Newman, et al. (2004). "Finding community structure in very large networks." *Phys Rev E Stat Nonlin Soft Matter Phys* **70**(6 Pt 2): 066111.
- Compte, A., N. Brunel, et al. (2000). "Synaptic mechanisms and network dynamics underlying spatial working memory in a cortical network model." *Cereb Cortex* **10**(9): 910-923.
- Dudai, Y. (2002). *Memory from A to Z : keywords, concepts, and beyond*. Oxford, UK. ; New York, Oxford University Press.
- Dudai, Y. (2002). "Molecular bases of long-term memories: a question of persistence." *Curr Opin Neurobiol* **12**(2): 211-216.
- Fellous, J. M. and T. J. Sejnowski (2003). "Regulation of persistent activity by background inhibition in an in vitro model of a cortical microcircuit." *Cereb Cortex* **13**(11): 1232-1241.
- Frick, A., D. Feldmeyer, et al. (2007). "Postnatal development of synaptic transmission in local networks of L5A pyramidal neurons in rat somatosensory cortex." *J Physiol* **585**(Pt 1): 103-116.
- Fusi, S. and L. F. Abbott (2007). "Limits on the memory storage capacity of bounded synapses." *Nat Neurosci* **10**(4): 485-493.
- Fuster, J. M. and G. E. Alexander (1971). "Neuron activity related to short-term memory." *Science* **173**(997): 652-654.
- Goldman-Rakic, P. S. (1995). "Cellular basis of working memory." *Neuron* **14**(3): 477-485.
- Gray, C. M., P. Konig, et al. (1989). "Oscillatory responses in cat visual cortex exhibit inter-columnar synchronization which reflects global stimulus properties." *Nature* **338**(6213): 334-337.
- Hebb, D. O. (1949). "The Organization of Behavior - a Neuropsychological Theory." *Wiley, New York*.
- Heidmann, A., T. Heidmann, et al. (1984). "[Selective stabilization of neuronal representations by resonance between spontaneous prerepresentations of the cerebral network and percepts evoked by interaction with the outside world]." *C R Acad Sci III* **299**(20): 839-844.
- Hofer, S. B., T. D. Mrsic-Flogel, et al. (2009). "Experience leaves a lasting structural trace in cortical circuits." *Nature* **457**(7227): 313-317.
- Holtmaat, A. and K. Svoboda (2009). "Experience-dependent structural synaptic plasticity in the mammalian brain." *Nat Rev Neurosci* **10**(9): 647-658.
- Hopfield, J. J. (1982). "Neural networks and physical systems with emergent collective computational abilities." *Proc Natl Acad Sci U S A* **79**(8): 2554-2558.
- Ikegaya, Y., G. Aaron, et al. (2004). "Synfire chains and cortical songs: temporal modules of cortical activity." *Science* **304**(5670): 559-564.
- Ito, M. (1986). "Long-term depression as a memory process in the cerebellum." *Neurosci Res* **3**(6): 531-539.
- Ji, D. and M. A. Wilson (2007). "Coordinated memory replay in the visual cortex and hippocampus during sleep." *Nat Neurosci* **10**(1): 100-107.
- Kali, S. and P. Dayan (2004). "Off-line replay maintains declarative memories in a model of hippocampal-neocortical interactions." *Nat Neurosci* **7**(3): 286-294.
- Kalisman, N., G. Silberberg, et al. (2005). "The neocortical microcircuit as a tabula rasa." *Proc Natl Acad Sci U S A* **102**(3): 880-885.
- Kampa, B. M., J. J. Letzkus, et al. (2006). "Cortical feed-forward networks for binding different streams of sensory information." *Nat Neurosci* **9**(12): 1472-1473.
- Kandel, E. R. (2006). "In Search of Memory: The Emergence of a New Science of Mind."
- Kant, I. and J. M. D. Meiklejohn (1872). *Critique of pure reason*. London,, Bell & Daldy.
- Kilgard, M. P. and M. M. Merzenich (1998). "Cortical map reorganization enabled by nucleus basalis activity." *Science* **279**(5357): 1714-1718.
- Kirkwood, A. and M. F. Bear (1994). "Homosynaptic long-term depression in the visual cortex." *J Neurosci* **14**(5 Pt 2): 3404-3412.
- Kirkwood, A., S. M. Dudek, et al. (1993). "Common forms of synaptic plasticity in the hippocampus and neocortex in vitro." *Science* **260**(5113): 1518-1521.
- Krieger, P., T. Kuner, et al. (2007). "Synaptic connections between layer 5B pyramidal neurons in mouse somatosensory cortex are independent of apical dendrite bundling." *J Neurosci* **27**(43): 11473-11482.

- Kubota, K. and H. Niki (1971). "Prefrontal cortical unit activity and delayed alternation performance in monkeys." *J Neurophysiol* **34**(3): 337-347.
- Le Be, J. V. and H. Markram (2006). "Spontaneous and evoked synaptic rewiring in the neonatal neocortex." *Proc Natl Acad Sci U S A* **103**(35): 13214-13219.
- Li, C. Y., J. T. Lu, et al. (2004). "Bidirectional modification of presynaptic neuronal excitability accompanying spike timing-dependent synaptic plasticity." *Neuron* **41**(2): 257-268.
- Malenka, R. C. and R. A. Nicoll (1999). "Long-term potentiation--a decade of progress?" *Science* **285**(5435): 1870-1874.
- Markram, H. (1997). "A network of tufted layer 5 pyramidal neurons." *Cereb Cortex* **7**(6): 523-533.
- Markram, H., J. Lubke, et al. (1997). "Physiology and anatomy of synaptic connections between thick tufted pyramidal neurones in the developing rat neocortex." *J Physiol* **500** (Pt 2): 409-440.
- Markram, H., J. Lubke, et al. (1997). "Regulation of synaptic efficacy by coincidence of postsynaptic APs and EPSPs." *Science* **275**(5297): 213-215.
- Martin, S. J., P. D. Grimwood, et al. (2000). "Synaptic plasticity and memory: an evaluation of the hypothesis." *Annu Rev Neurosci* **23**: 649-711.
- Maurer, A. P., S. L. Cowen, et al. (2006). "Organization of hippocampal cell assemblies based on theta phase precession." *Hippocampus* **16**(9): 785-794.
- McNaughton, B. L. (2003). "Long-term potentiation, cooperativity and Hebb's cell assemblies: a personal history." *Philosophical Transactions of the Royal Society of London Series B-Biological Sciences* **358**(1432): 629-634.
- Newman, M. E. and M. Girvan (2004). "Finding and evaluating community structure in networks." *Phys Rev E Stat Nonlin Soft Matter Phys* **69**(2 Pt 2): 026113.
- Nicolelis, M. A., L. A. Baccala, et al. (1995). "Sensorimotor encoding by synchronous neural ensemble activity at multiple levels of the somatosensory system." *Science* **268**(5215): 1353-1358.
- Parisi, G. (1986). "A Memory Which Forgets." *Journal of Physics a-Mathematical and General* **19**(10): L617-L620.
- Pastalkova, E., V. Itskov, et al. (2008). "Internally generated cell assembly sequences in the rat hippocampus." *Science* **321**(5894): 1322-1327.
- Peteanu, L., T. Mao, et al. (2009). "The subcellular organization of neocortical excitatory connections." *Nature*.
- Rubin, D. D. and S. Fusi (2007). "Long memory lifetimes require complex synapses and limited sparseness." *Front Comput Neurosci* **1**: 7.
- Sejnowski, T. J. and A. Destexhe (2000). "Why do we sleep?" *Brain Res* **886**(1-2): 208-223.
- Singer, W. (1995). "Development and plasticity of cortical processing architectures." *Science* **270**(5237): 758-764.
- Singer, W. and C. M. Gray (1995). "Visual feature integration and the temporal correlation hypothesis." *Annu Rev Neurosci* **18**: 555-586.
- Sjostrom, P. J., G. G. Turrigiano, et al. (2001). "Rate, timing, and cooperativity jointly determine cortical synaptic plasticity." *Neuron* **32**(6): 1149-1164.
- Song, S., P. J. Sjostrom, et al. (2005). "Highly nonrandom features of synaptic connectivity in local cortical circuits." *PLoS Biol* **3**(3): e68.
- Stent, G. S. (1973). "A physiological mechanism for Hebb's postulate of learning." *Proc Natl Acad Sci U S A* **70**(4): 997-1001.
- Stopfer, M., S. Bhagavan, et al. (1997). "Impaired odour discrimination on desynchronization of odour-encoding neural assemblies." *Nature* **390**(6655): 70-74.
- Thomson, A. M., A. P. Bannister, et al. (2002). "Target and temporal pattern selection at neocortical synapses." *Philos Trans R Soc Lond B Biol Sci* **357**(1428): 1781-1791.
- Thomson, A. M., J. Deuchars, et al. (1993). "Large, deep layer pyramid-pyramid single axon EPSPs in slices of rat motor cortex display paired pulse and frequency-dependent depression, mediated presynaptically and self-facilitation, mediated postsynaptically." *J Neurophysiol* **70**(6): 2354-2369.
- Thomson, A. M. and O. T. Morris (2002). "Selectivity in the inter-laminar connections made by neocortical neurones." *J Neurocytol* **31**(3-5): 239-246.
- Thomson, A. M., D. C. West, et al. (2002). "Synaptic connections and small circuits involving excitatory and inhibitory neurons in layers 2-5 of adult rat and cat neocortex: triple intracellular recordings and biocytin labelling in vitro." *Cereb Cortex* **12**(9): 936-953.
- Trachtenberg, J. T., B. E. Chen, et al. (2002). "Long-term in vivo imaging of experience-dependent synaptic plasticity in adult cortex." *Nature* **420**(6917): 788-794.

- Tsodyks, M., A. Uziel, et al. (2000). "Synchrony generation in recurrent networks with frequency-dependent synapses." *J Neurosci* **20**(1): RC50.
- van Rossum, M. C., G. Q. Bi, et al. (2000). "Stable Hebbian learning from spike timing-dependent plasticity." *J Neurosci* **20**(23): 8812-8821.
- Wakita, K. and T. Tsurumi (2007). "Finding Community Structure in Mega-scale Social Networks." *CoRR abs/cs/0702048*.
- Watts, D. J. and S. H. Strogatz (1998). "Collective dynamics of 'small-world' networks." *Nature* **393**(6684): 440-442.
- Watts, J. and A. M. Thomson (2005). "Excitatory and inhibitory connections show selectivity in the neocortex." *J Physiol* **562**(Pt 1): 89-97.
- West, D. C., A. Mercer, et al. (2006). "Layer 6 cortico-thalamic pyramidal cells preferentially innervate interneurons and generate facilitating EPSPs." *Cereb Cortex* **16**(2): 200-211.
- Yoshimura, Y., J. L. Dantzker, et al. (2005). "Excitatory cortical neurons form fine-scale functional networks." *Nature* **433**(7028): 868-873.
- Young, J. Z. (1979). "Learning as a process of selection and amplification." *J R Soc Med* **72**(11): 801-814.
- Zito, K., V. Scheuss, et al. (2009). "Rapid functional maturation of nascent dendritic spines." *Neuron* **61**(2): 247-258.

Acknowledgements

We thank Michele Pignatelli, Yadin Dudai, Idan Segev and Sean Hill for discussions and comments. RP was supported by an *EU Synapse* grant. TKB was supported by an *EU Synapse* grant. This study was also carried out as part of the FACETS program.

Authors' Contributions.

H.M and R.P. designed the 12-patch system. R.P built the system. R.P. and T.K.B. performed the electrophysiology experiments. R.P. conducted the analysis and simulations. H.M. guided the development of the concepts and manuscript. All authors contributed to the writing of the article.

Correspondence and requests for materials should be addressed to Henry Markram

(henry.markram@epfl.ch).

SUPPLEMENTARY METHODS

Slice preparation. Experiments were carried out according to the Swiss national and institutional guidelines. Fourteen- to sixteen-day-old, non-anaesthetized Wistar rats were quickly decapitated and their brains carefully removed and placed in iced artificial cerebrospinal fluid (ACSF). Slices (300 μm) were cut on an HR2 vibratome (Sigmann Elektronik, Heidelberg, Germany). Parasagittal slices, approximately 1.7–2.2mm lateral to the midline, were cut to access primary somatosensory cortex (SSC, above the anterior extremity of the hippocampus \pm 1 mm). Slices were incubated at 37°C for 30–60 min and then left at room temperature until recording. Cells were visualized by infrared differential interference contrast video microscopy utilizing a VX55 camera (Till Photonics, Gräfeling, Germany) mounted on an upright BX51WI microscope (Olympus, Tokyo, Japan). Thick-tufted layer 5 PCs were selected according to their large soma size (15–25 μm) and their apparent large trunk of the apical dendrite. Care was taken to use only ‘parallel’ slices, i.e. slices that had a cutting plane parallel to the course of the apical dendrites and the primary axonal trunk. This ensured sufficient preservation of both the PCs’ axonal and dendritic arborizations.

Chemicals and solutions. Slices were continuously superfused with ACSF containing (in mM) 125 NaCl, 25 NaHCO₃, 2.5 KCl, 1.25 NaH₂PO₄, 2 CaCl₂, 1 MgCl₂, and 25 D-glucose, bubbled with 95% O₂–5% CO₂. The intracellular pipette solution contained (in mM) 110 potassium gluconate, 10 KCl, 4 ATP-Mg, 10 phosphocreatine, 0.3 GTP, 10 N-2-hydroxyethylpiperazine-N-2-ethanesulfonic acid (Hepes), and 13 biocytin, adjusted to pH 7.3–7.4 with 5 M KOH. Osmolarity was adjusted to 290–300 mosmol l⁻¹ with D-mannitol (25–35mM). The membrane potential values given were not corrected for the liquid junction potential, which was approximately –14 mV. Chemicals were from Sigma Aldrich (Steinheim, Germany) or Merck (Darmstadt, Germany).

Electrophysiological recordings. Multiple somatic whole cell recordings (6–12 cells simultaneously) were performed with Multiclamp 700B amplifiers (Molecular Devices, Union City, CA, USA) in the current clamp mode at 34 \pm 1°C bath temperature. Data acquisition was

performed via ITC-1600 board (Instrutech Co., Port Washington, NY, USA), connected to a PC running a custom-written routine under IGOR Pro (Wavemetrics, Portland, OR, USA). Sampling rates were 5kHz, and the voltage signal was filtered with a 2 kHz Bessel filter. Patch pipettes were pulled with a Flaming/Brown micropipette puller P-97 (Sutter Instruments Co., Novato, CA, USA) or a DMZ puller (Zeitz Instruments, Martinsreid, Germany) and had an initial resistance of 3–8M Ω .

Stimulation protocols. Monosynaptic, direct excitatory connections were identified by stimulation of a presynaptic cell with a 20-70 Hz train of 5 to 15 strong and brief current pulses (1–2 nA, 2–4 ms), followed by a so-called recovery test response 0.5 s after the end of the train, all precisely and reliably eliciting action potentials (APs).

Final somatic positions. The soma positions were recorded relative to an arbitrary reference point, the Z-axis was oriented perpendicular to the surface of the slice. Once morphological stainings were ready the Y-axis was rotated around the Z-axis to match the orientation of the apical dendrites. The X-axis was rotated by the same amount and remained orthogonal to the other two axes.

Connection amplitude measurement. The amplitude of EPSPs (excitatory post-synaptic potentials) was measured for events that followed a resting period of at least 15s during which the presynaptic neurons were not stimulated to produce action-potentials

Analysis of number of connections in groups of neurons. Two calculation methods were applied, for most analyses. The two methods converge to the same result. The first calculation consisted of applying directly the pairwise configuration probabilities as a function of distance. This analytic solution represents the expected results of an infinite number of simulated connectivity instances. The other method was to build 1000 instances of connectivity for the soma positions experimentally observed. These methods allowed us to confirm the statistical significance non-randomness assumption. The simulation of 1000 networks additionally allowed us to assess the standard deviation of the expected values.

To determine the probability of a given connectivity pattern we first extracted all possible groups of a given number of neurons in each experiment. In each group, each pair of neurons has a probability of occurring in one of four possible patterns that we described in binary terms. Whenever a connection is present the corresponding digit equals one otherwise it corresponds to zero. Thus a reciprocal connection is represented by the code 11 and a non-reciprocal connection can take place as 10 or 01 whereas a completely disconnected pair is represented by 00. In groups of three neurons three pairs exist. Therefore the representation of a given pattern will be comprised of six binary digits. With this representation all the possible outcomes can be attributed a probability that depends on pairwise relationships and intersomatic distances by simply. The total number of patterns is given by 2^{nc} where nc is the number of possible connections in a group of n neurons and is given by $nc = n * (n-1)$. There will be one pattern with no connections, one with nc connections and multiple patterns with intermediate numbers of connections. For each pattern we counted the number of connections and added its probability to that of a group of neurons displaying that exact number of connections (Supplementary Fig 1).

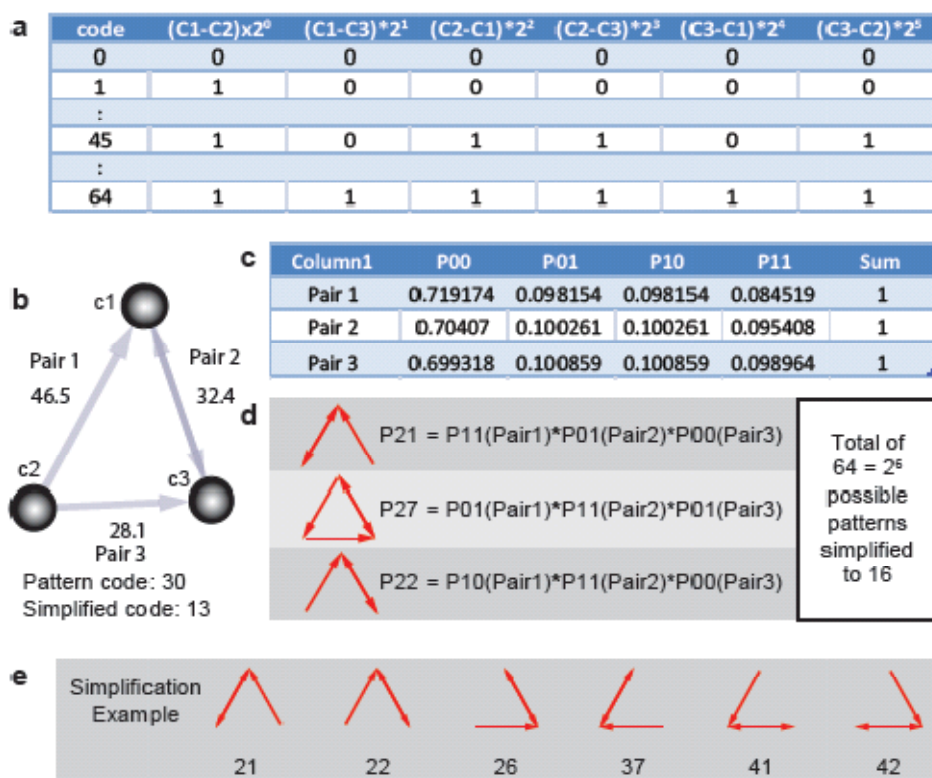


Figure S1 Three-neuron pattern calculations. (a) determination of all possible outcomes. (b) determination of experimentally observed patterns and distances. (c) calculation of probabilities of pairwise connectivity as a function of distance for analytic solution and simulated patterns. (d) Calculation of probabilities of each outcome based on step c. (e) simplification of equivalent patterns.

Specific pattern analysis. Specific patterns are much more varied than the number of connections in a group of neurons. Three-neuron groups where all neurons are identical can establish 16 different connectivity patterns. In order to identify overrepresented patterns we performed z-tests of the number of experimentally observed occurrences of each pattern with respect to the mean and standard deviation of 1000 randomly assembled connectivity instances of the experimental set. The tests were corrected for multiple hypotheses according to the Bonferroni method (Supplementary Fig 2).

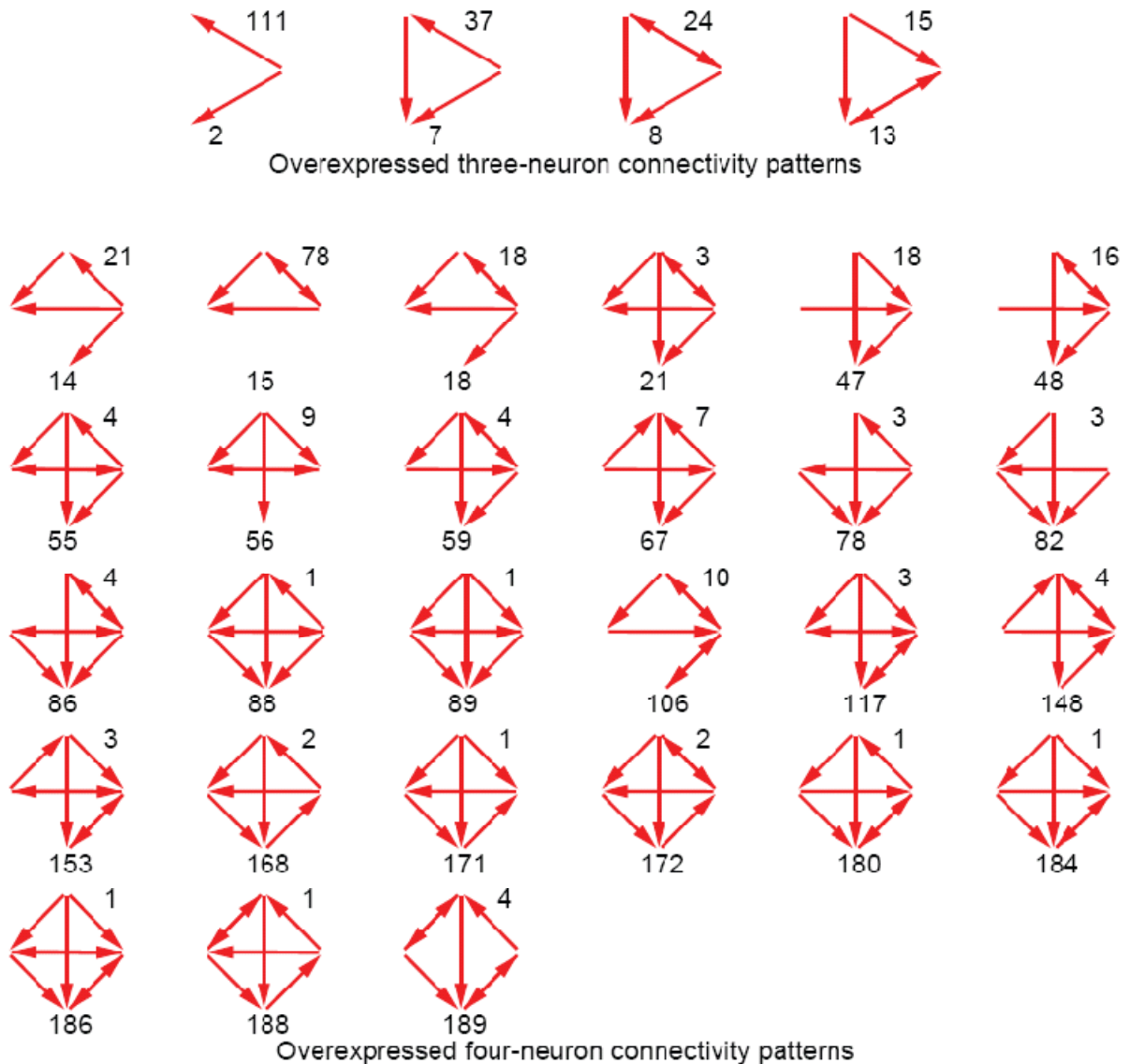


Figure S2 Overexpressed three- and four-neuron connectivity patterns. The numbers below the patterns indicate their code in our classification. The numbers on the top right indicate the number of occurrences of such patterns.

MinP-based statistical analysis yielded the similar overrepresented patterns as the z-test without multiple hypotheses correction. Applying an additional false discovery rate correction according to the Simes procedure yielded the same overrepresented patterns as the corrected z-test. The simulated connectivity patterns occur with a bell-shaped density distribution, closely resembling a normal distribution even if they fail strict normality tests such as the Lilliefors test. We repeated the same analysis for four neuron patterns. The total number of patterns with four

cells is considerably larger, 218, and several patterns never occurred which was expected and not statistically significant.

Number of connections per cell. The distribution of number of connections per cell found experimentally is similar to what could be expected in a network defined exclusively by the profiles of figure 1 (Supplementary Fig 3).

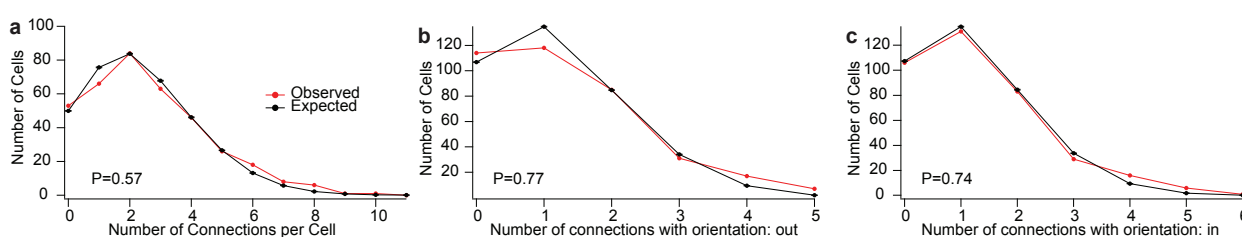


Figure S3 (a) Number of connections per cell. **(b)** Distribution of the number of connections projected from a cell. **(c)** Distribution of numbers of connections onto a cell.

Common Neighbors. The analysis to investigate the effect of common neighbors on the connection probability was also performed with two methods; simulations of 1000 cases and the analytical solution with probabilities. Both methods converged to the same values. The differences in connection probability were significant for zero and one common neighbor. The simulated network had much fewer cases of three or more common neighbors than the experimental networks. In fact the very number of occurrences of circuits with 2 to 5 common neighbors was significantly greater in the experimental data.

The number of common neighbors strongly influenced the synaptic strength distribution (Supplementary Fig 4). Weaker connections progressively give place to stronger ones as the number of common neighbor increases.

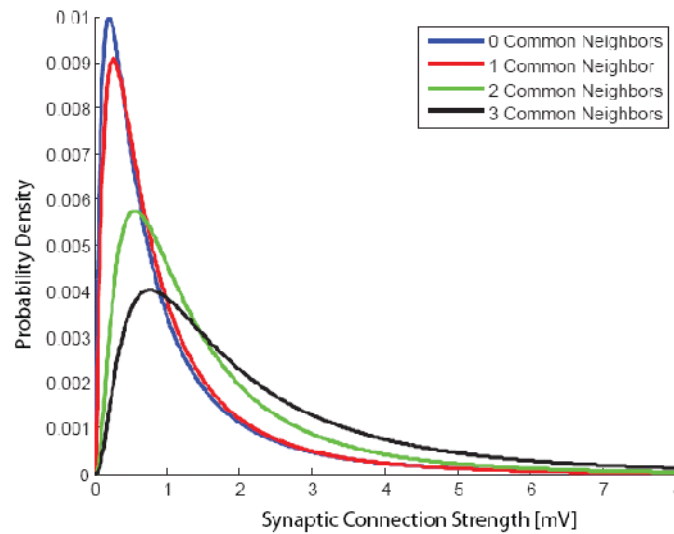


Figure S4 Synaptic strength amplitude distribution for pairs with increasing numbers of common neighbors.

Network Organization. Our model of network organization is built in two steps. The first step is to assign positions and initial connectivity to the neurons. To approximate experimental conditions 1000 cells were placed on average $36 \mu\text{m}$ apart with a jitter of $30 \mu\text{m}$ in x , y and z . The initial connectivity is established randomly while respecting the distance-dependent profiles for reciprocal and non-reciprocal connectivity.

The second step is to subject the assembled network to a reorganization algorithm applied to each possible pair according to three steps. First the probability of an incoming connection is set to be proportional to the number of common neighbors between the pair. Second, the sum of all probabilities of connection to a neuron is normalized to the expected number of connections received by that neuron. Finally the connection probabilities obtained based on the previous steps are divided in reciprocal and non-reciprocal configurations the respect the reciprocity tendency according to intersomatic distance.

MATLAB code of the network assembly function used to model networks with higher than chance reciprocity.

```
function [cells,conn,dist,p,pr,pnr]=RP_AssembleNet(d,nx,ny,nz,pair)
%'d' is the average distance between adjacent cells (36 usually)
%'nx' is the number of rows (10 usually)
%'ny' is the number of columns (10 usually)
%'nz' is the number of layers (10 usually)
%'pair' relevance of pairwise patterns (0-no, 1-yes)

acc=1; %initialize counter variable
nc=nx*ny*nz; %calculate total number of cells
pr=0; %initialize reciprocal connection probability
pnr=0; %initialize non-reciprocal connection probability
cells=zeros(nc,6); %initialize cell information matrix
for(i=1:nx) %for each row
    for(j=1:ny) %for each column
        for(k=1:nz) %for each layer
            cells(acc,1)=i*d; %define base x position
            cells(acc,2)=j*d; %define base y position
            cells(acc,3)=k*d; %define base z position
            acc=acc+1; %increase counter for next cell
        end
    end
end
end
r=rand(nc,3)*30; %create random matrix in range 0-30
cells(:,1:3)=cells(:,1:3)+r; %add jitter to cell positions in x,y and z
r=rand(nc)+eye(nc); %define random matrix with ones in diagonal
% (to ignore autapses)
dist=zeros(nc,nc); %initialize distance matrix
for(i=1:nc)
    for(j=i+1:nc) %for every possible pair
        dx=cells(i,1)-cells(j,1); %calculate dx
        dy=cells(i,2)-cells(j,2); %calculate dy
        dz=cells(i,3)-cells(j,3); %calculate dz
        dist(i,j)=sqrt(dx*dx+dy*dy+dz*dz); %calculate distance
        dist(j,i)=dist(i,j); %distance is symmetric
    end
end
pr=RP_DistprobPair(dist,2); %reciprocal connection probability matrix
pnr=RP_DistprobPair(dist,1)/2; %0.5*non-reciprocal connection prob. matrix
p=pnr+pr; %probability of connection matrix
if(pair==0) %if pairwise connectivity is not relevant
    conn=r<p; %connectivity is defined by p
else %if pairwise relationship is relevant
    r=triu(r,1)+tril(ones(nc)); %define upper triangular random matrix
    cr=r<pr; %define reciprocal connections
    cnr1=(r<(pr+pnr)).*(r>=pr); %define non reciprocal one-way
    cnr2=(r<(pr+2*pnr)).*(r>=pr+pnr); %define non reciprocal other-way
    conn=cr+cr'+cnr1+cnr2'; %final connectivity
end
```

MATLAB code of the network reorganization function used to model the effects of common neighbors.

```
function conn2=Reorganize(conn,iter,r,m,p,pr,pnr,dist)
% 'conn' is the initial binary connectivity matrix (nxn)
% 'iter' is the number of iterations to perform (scalar)
% 'r' is the power given to the reorganization matrix to (scalar)
% 'm' mean weight factor before applying power (scalar)
% 'p' is the probability of connection as a function of distance applied to
%each pair (nxn)
% 'pr' is the reciprocal probability of connection as a function of distance
%applied to each pair (nxn)
% 'pnr' is the non-reciprocal probability of connection as a function of
%distance applied to each pair (nxn)
% 'dist' is the distance between the neurons in each pair (nxn)

n=length(conn);           %number of cells
ins=sum(conn);           %array of column sums to determine
                          %number of inputs per cell

pc=n*(n-1);              %number of possible connections
nc=sum(sum(conn));       %number of actual connections
conn0=conn;              %storing initial connectivity

conn2=conn;              %allocating final connectivity
pp=p;                    %storing p

for(i=1:iter)
    conn=double(conn2); %to operate on results of last iteration
    cn=getNCN(conn);    %get common neighbors

    for(j=1:n)
        cn(:,j)=cn(:,j)/(m*mean(cn(:,j))); %divide common neighbors by
                                             %the weighted mean
        cn(:,j)=cn(:,j).^r;                %apply power

        cn(:,j)=cn(:,j).*pp(:,j);          %keep distance relations
        cn(:,j)=cn(:,j)./sum(cn(:,j));     %normalize to 1
        cn(:,j)=cn(:,j)*ins(j);           %to keep total inputs constant
    end

    pi=(cn+cn')/2;        %extract connection probability weight in each pair
    cpnr=pnr./p.*pi;     %define non-reciprocal connection probability
    cpr=pr./p.*pi;       %define reciprocal connection probability

    rnd=rand(n);         %define random matrix
    rnd=triu(rnd,1)+tril(ones(n)); %make it upper triangular
    cr=rnd<cpr;          %reciprocal connections
    cnr1=(rnd<(cpr+cpnr)).*(rnd>=(cpr)); %non-reciprocal one way
    cnr2=(rnd<(cpr+2*cpnr)).*(rnd>=(cpr+cpnr)); %non-reciprocal other way
    conn2=cr+cr'+cnr1+cnr2'; %final connectivity
end
```

MATLAB code for extraction of common neighbors, common input and common output neurons

```
function cneigh=getNCN(conn)
%this function returns a matrix with the number of cells that connect
%simultaneously, irrespective of direction, the two cells defined by the
%row and column in the result matrix

nc=size(conn,1);           %get size of matrix
neigh=double((conn+conn')&1); %make direction irrelevant
cneigh=neigh*neigh.*(1-eye(nc)); %get common neighbors and ignore diagonal
end

function cneigh=getncnIn(conn)
%this function returns a matrix with the number of cells that send
%connections simultaneously to the two cells defined by the
%row and column in the result matrix

nc=size(conn,1);           %get size of matrix
cneigh=conn*conn.*(1-eye(nc)); %get common inputs and ignore diagonal
end

function cneigh=getncnOut(conn)
%this function returns a matrix with the number of cells that receive
%connections simultaneously from the two cells defined by the
%row and column in the result matrix

nc=size(conn,1);           %get size of matrix
cneigh=conn*conn'.*(1-eye(nc)); %get common outputs and ignore diagonal
end
```

SUPPLEMENTARY MATERIAL

As an overview of the Layer V pyramidal network we display the 0.5% strongest connections in a simulated network built according to our algorithm (Supplementary Fig 5). Three different clusters are shown in red, green and blue. Connections to or from neurons in a cluster receive the same color as the cluster. If a connection goes from one cluster to another the color of the receiving neuron is assigned to the connection. It is interesting to note how these strong connections remain mainly within the same cluster. Weaker connections are distributed in a much more indiscriminate way linking different clusters.

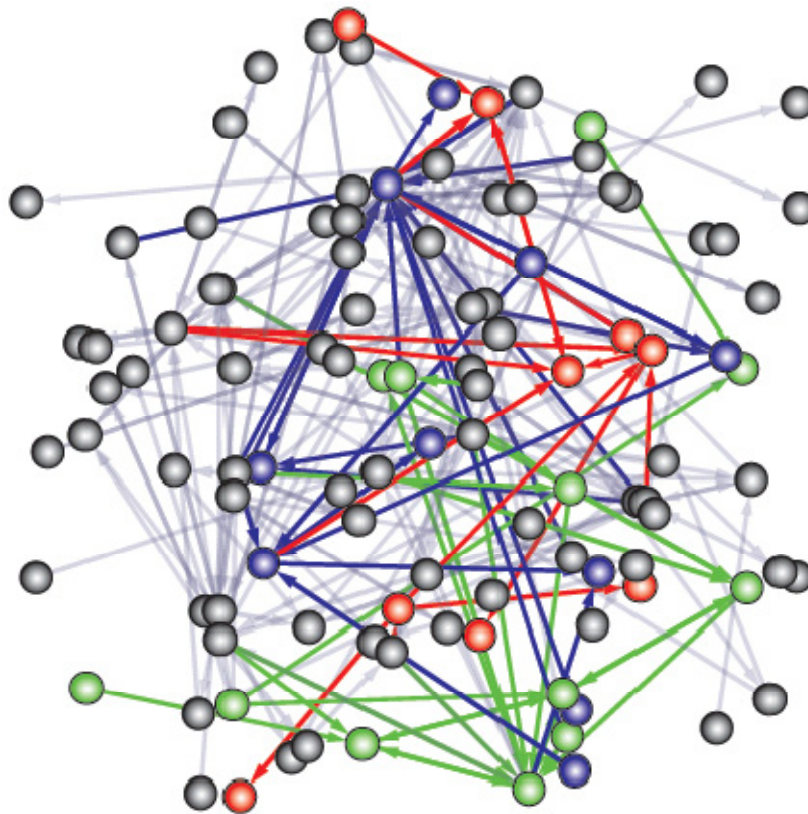


Figure S5 Clustered connectivity of strongest synapses (CNM algorithm).

Applying the clustering algorithm that identified clusters in the model network to individual experiments yields interesting results where the numbers of common neighbors are well above average, as expected.

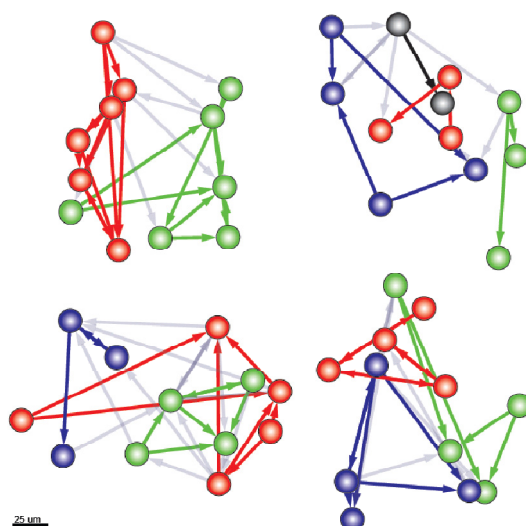


Figure S6 Clustered connectivity in individual experiments according to the CNM algorithm.

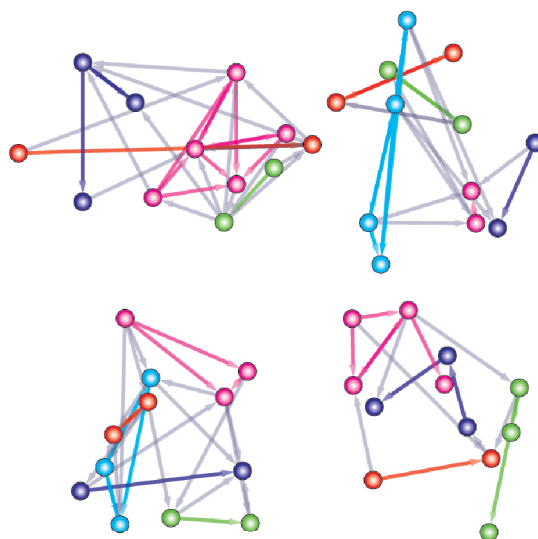


Figure S7 Clustered connectivity in individual experiments according to the AICR algorithm.

Chapter 4 Ephaptic Coupling of Neurons

Costas A. Anastassiou^{1,2,4}, Rodrigo Perin^{3,4}, Henry Markram³ & Christof Koch¹

¹*Division of Biology, California Institute of Technology, Pasadena, California*

²*Department of Bioengineering, Imperial College, London*

³*Laboratory of Neural Microcircuitry, EPFL, Lausanne, Switzerland*

⁴These authors contributed equally to the experimental work

INTRODUCTION

Communication among neurons in the brain is traditionally thought to occur at localized chemical or electrical synapses. The resultant electrical activity in pre- and post-synaptic structures gives rise to measurable low-frequency extracellular electric field and voltage fluctuations often referred to as local field potential (LFP) that typically extends hundreds of μm away (Bragin, Jando et al. 1995; Ylinen, Bragin et al. 1995; Logothetis, Pauls et al. 2001; Logothetis, Kayser et al. 2007; Katzner, Nauhaus et al. 2009). Such events, in turn, feed back onto the membrane potential itself, inducing so-called ephaptic coupling (Jefferys 1995). In mammals, the LFP is usually regarded as an epiphenomenon of coordinated neural activity and is recorded for diagnostic purposes. The extent to which ephaptic coupling between the LFP and individual neurons or neural populations alters their subthreshold and suprathreshold activity under physiological conditions has remained speculative (Arvanitaki 1942; Chan and Nicholson 1986; Chan, Hounsgaard et al. 1988; Ghai, Bikson et al. 2000; Francis, Gluckman et al. 2003; Bikson, Inoue et al. 2004; Deans, Powell et al. 2007; Radman, Su et al. 2007; Anastassiou, Montgomery et al. 2010). To address this question, we stimulated and recorded both extracellularly and intracellularly neocortical pyramidal neurons in slice. We show that very weak extracellular perturbation of the somatic membrane potential (less than 0.2 mV peak-to-peak) of neurons receiving strong suprathreshold intracellular input substantially entrains action

potential activity. Such entrainment is particularly effective for low extracellular stimulation frequencies (less than 8 Hz) leading to coordinated firing of spatially proximal neurons experiencing similar extracellular potential fluctuations in the absence of synaptic communication. These findings demonstrate that endogenous brain activity giving rise to a measurable extracellular signal such as slow cortical activity or hippocampal theta and sharp waves can impact neural population activity through ephaptic coupling under physiological conditions.

Neural communication occurring via spatially localized synaptic inputs gives rise to detections of the membrane potential (V_m) from rest that travel along neural processes giving rise to a number of subthreshold and suprathreshold events. Such events do not only affect the state and function of an individual neuron (Koch 1998; Stuart, Spruston et al. 2007) but may also dictate the modus operandi of neural populations (Li, Poo et al. 2009) and, under circumstances, even result in behaviorally distinguishing effects (Vallbo, Olsson et al. 1984; Brecht, Schneider et al. 2004; Houweling and Brecht 2008). Nevertheless, the neural membrane is susceptible not only to direct and spatially localized inputs but also to the presence of extracellular fields (E) giving rise to spatiotemporal changes of the extracellular potential (V_e) which, in turn, lead to changes in V_m through ephaptic coupling (Arvanitaki 1942; Traub, Dudek et al. 1985; Chan and Nicholson 1986; Jefferys 1995; Radman, Su et al. 2007; Anastassiou, Montgomery et al. 2010). For instance, the presence of imposed extracellular electric fields has been shown to affect the spike timing of individual neurons (Chan and Nicholson 1986; Radman, Su et al. 2007) and neural populations in models of pathological activity (Jefferys and Haas 1982; Taylor and Dudek 1982). Moreover, application of relatively modest whole-brain extracellular current stimulation was shown to result in measurable changes in the performance of a learning task in humans (Marshall, Helgadottir et al. 2006). While the extracellular signature from individual neurons such as extracellular action potentials remains modest and spatially confined (Gold, Henze et al. 2006), coordinated synaptic input within a specific brain region, for instance during cortical slow waves (Steriade, Nunez et al. 1993; Steriade, Nunez et al. 1993) hippocampal theta (Vanderwolf 1969; Buzsaki 2002; Lubenov and Siapas 2009) or sharp waves (Buzsaki, Horvath et al. 1992; Ylinen, Bragin et al. 1995), gives rise to more prominent spatiotemporal E - and V_e -fluctuations, the latter often being referred to as the LFP. While robust relationships between the LFP and

spiking activity have been shown to arise during a number of brain states and areas (O'Keefe and Recce 1993; Fries, Reynolds et al. 2001; Womelsdorf, Schoffelen et al. 2007) these have been solely attributed to synaptic communication. Here we tested whether and to which extent ephaptic coupling to LFP-like fluctuations alters the subthreshold and suprathreshold response of neurons and neural populations and, thus, provide an alternative form of neural communication.

METHODS

Slice preparation and cell identification. 14 – 20 days old Wistar rats were quickly decapitated according to the Swiss national and institutional guidelines. The brain was carefully removed and placed in iced artificial cerebrospinal fluid (ACSF). 300 μm thick parasagittal slices of the primary somatosensory cortex (hindlimb area) were cut on a HR2 vibratome (Sigmund Elektronik, Heidelberg, Germany). Slices were incubated at 37°C for 30 – 60 min and then left at room temperature until recording. Cells were visualized by infrared differential interference contrast videomicroscopy utilizing a VX55 camera (Till Photonics, Gräfeling, Germany) mounted on an upright BX51WI microscope (Olympus, Tokyo, Japan). Thick tufted layer 5 PCs were selected according to their large soma size (15 – 25 μm) and their apparent large trunk of the apical dendrite. Care was taken to use only “parallel” slices, i.e. slices that had a cutting plane parallel to the course of the apical dendrites and the primary axonal trunk. This ensured to have sufficient preservation of both the PCs' axonal and dendritic arborizations.

Chemicals and solutions. Slices were continuously superfused with ACSF containing (in mM) 125 NaCl, 25 NaHCO₃, 2.5 KCl, 1.25 NaH₂PO₄, 2 CaCl₂, 1 MgCl₂, and 25 D-glucose, bubbled with 95% O₂ – 5% CO₂. The intracellular pipette solution (ICS) contained (in mM) 110 K-gluconate, 10 KCl, 4 ATP-Mg, 10 phosphocreatine, 0.3 GTP, 10 N-2-hydroxyethylpiperazine-N9-2-ethanesulfonic acid (HEPES), and 13 biocytin, adjusted to a pH 7.3 – 7.4 with 5 M KOH. Osmolarity was adjusted to 290 – 300 mosmol l⁻¹ with D-mannitol (25 – 35 mM). The membrane potential values given were not corrected for the liquid junction potential, which was approximately –14 mV. SR 95531 Hydrobromide (Gabazine) was bought from TOCRIS, CNQX disodium salt was bought from BIOTREND and D-2-Amino-5-Phosphonovaleric-acid (APV)

and 1(S),9(R)-(-)-Bicuculline methiodide (Bicuculline) were bought from Sigma Aldrich. All experiments were performed under 20 μ M Gabazine or 20 μ M Bicuculline, 40 μ M APV and 10 μ M CNQX in order to avoid synaptic transmission from interfering with ephaptic signals.

Electrophysiological recordings. Multiple somatic whole cell recordings (1 – 4 cells simultaneously) were performed with Multiclamp 700B amplifiers (Molecular Devices, Union City, CA) in the current clamp mode. The temperature was $35 \pm 0.5^\circ\text{C}$ during recording. Data acquisition was performed via an ITC-1600 board (Instrutech Co, Port Washington, NY), connected to a PC running a custom written interface (PulseQ) under IgorPro (Wavemetrics, Portland, OR). Sampling rates were 10 kHz, and the voltage signal was filtered with a 1.2 kHz Bessel filter. Patch pipettes were pulled with a Flaming/Brown micropipette puller (DMZ Universal Puller, Zeitz-Instrumente GmbH, Munich, Germany) and had an initial resistance of 4 – 8 M Ω for patch recordings and 1 – 3 M Ω for extracellular recordings. 3D morphological reconstruction of biocytin-labeled cells was done under an Olympus BX 51 W microscope fitted with a water-immersion 60x (numerical aperture (NA) 0.9) or an oil-immersion 100x (NA 1.35) objective using Neurolucida software (MicroBrightField, Magdeburg, Germany). Intracellular stimulation was provided via MultiClamp 700B amplifiers whereas extracellular stimulation was provided either by MultiClamp 700B (up to 200 nA) or via an Isolated pulse stimulator (A-M Systems 2100, Sequim, USA) for higher currents in characterization experiments.

Electrode positioning. Using multiple electrodes, whose positions were carefully determined with 40x magnification, we applied extracellular stimulation and recorded several extracellular sites as well as one to three neurons intracellularly (Figure 1). The stimulation electrode was placed 50-100 μ m from the somata of the recorded neurons. The extracellular recording electrodes were arranged around the neurons at various distances while at least one electrode was placed immediately next to each soma to precisely measure the potential difference across the membrane. The requirement for an extracellular electrode for measuring the membrane potential across the membrane stems from the fact that the usual reference electrode, a silver chloride pellet, is several millimeters away, too far to register the fluctuations induced by the extracellular stimulation.

RESULTS

The question whether, in principle, endogenous electric field activity (LFP-activity typically induces E -amplitude < 5 mV/mm and V_e -amplitude < 0.5 mV, (Buzsaki, Horvath et al. 1992; Bragin, Jando et al. 1995; Kamondi, Acsady et al. 1998; Buzsaki 2004)) can alter neural activity has remained unanswered mainly due to experimental restrictions: intracellular and extracellular stimulation of individual neurons while concurrently accurately monitoring the induced extracellular field at a specific neural compartment (such as the soma) requires the ability to position and individually control multiple pipettes within a confined space. For this reason, we developed a 12-pipette setup that allows independent positioning of each pipette under visual control with μm accuracy (Fig. 1a) offering the flexibility of using an arbitrary number of them as patching, extracellularly stimulating or extracellular recording pipettes (Fig. 1b, c). To unravel the effect of extracellular electric fields on neurons, we performed experiments where we stimulated layer 5 neocortical pyramidal neurons while recording both inside and outside their cell bodies (Fig. 1d). Typically, a single extracellular stimulation electrode (S1) was positioned at a distance of 50-150 μm from the soma (Fig. 1d). The cell soma was patched by an intracellular electrode (I1) and surrounded by a number of extracellular pipettes monitoring the extracellular voltage (V_e) fluctuations. V_m was determined by subtracting the intracellular potential (V_i) from the V_e of the extracellular recording site most proximal to the soma, typically within 15 μm (Fig. 1e, f). The induced electric field as a function of distance from S1, was estimated through the spatial gradient of the best fit of all V_e -traces (least-squares fitting; Fig. 1f and S1) assuming the point-source approximation (Logothetis, Kayser et al. 2007). For all experiments, synaptic activity was always pharmacologically silenced in the slice (silenced synaptic type (drug): NMDA (APV), GABA (gabazine/bicuculine) and AMPA (CNQX); (Bikson, Inoue et al. 2004; Deans, Powell et al. 2007)) to ensure changes in subthreshold and suprathreshold activity were purely attributed to the impact of the field and not synaptically mediated from other neurons. Also, the extracellular stimuli applied in this study were always (at least) 50-fold weaker than the lowest reported stimulation amplitude required to directly stimulate cortical neurons (Stoney, Thompson et al. 1968; Moore and Fallah 2004; Tehovnik, Tolia et al. 2006; Histed, Bonin et al. 2009).

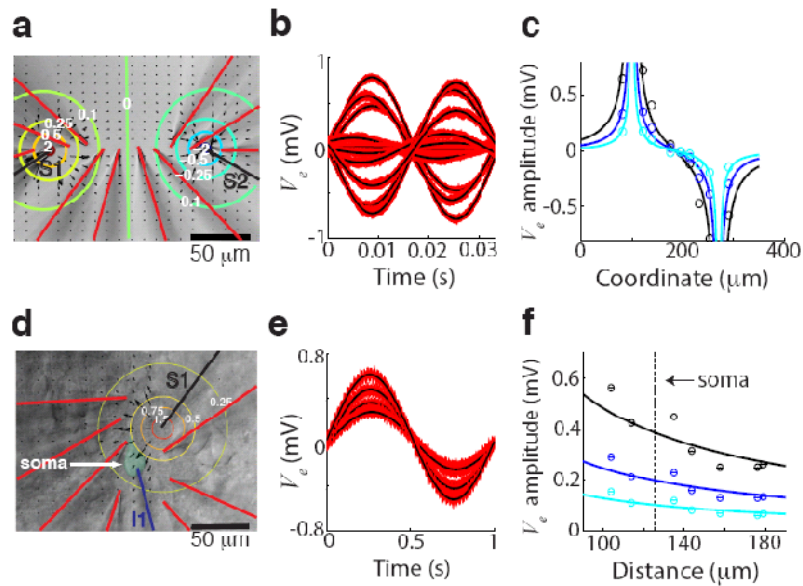


Figure 1 Experimental setup allowing massively parallel intra- and extracellular recordings from individual neurons during intra- and extracellular stimulation. (a) Line-arrangement of 12 pipettes in saline (inter-pipette distance: 15 μm). **(b)** Bipolar anti-phase stimulation ($I_0=200$ nA, $f=30$ Hz; S1, S2 stimulation pipettes) in saline and measurement of spatiotemporal V_e -profile from 10 pipettes (red traces: V_e -recordings, black traces: mean waveform after 9 s stimulation). **(c)** V_e -amplitude as a function of pipette location for $I_0=50$ (cyan), 100 (blue) and 200 (black) nA bipolar anti-phase stimulation. Circles designate V_e -amplitude and lines the theoretical estimate based on the point-source approximation (medium conductivity $\rho=1$ m; isopotentials are shown in (a)). **(d)** Unipolar stimulation ($I_0=200$ nA, $f=1$ Hz) in slice using an extracellular stimulation pipette (S1) near the soma of a patched pyramidal neuron (I1). **(e)** 7 extracellular pipettes are positioned proximally to the soma to monitor V_e (red traces: V_e -recordings, black traces: mean waveform after 9 s stimulation). **(f)** V_e -amplitude as a function of pipette location in slice for $I_0=50$ (cyan), 100 (blue) and 200 (black) nA (circles: mean; error bars: std). Distance is calculated from the tip of the extracellular stimulating electrode S1. Solid lines show the point-source approximation (the value of ρ is determined using least squares fitting; typically $\rho=2.0\text{-}3.5$ Ωm).

What are the characteristics of V_m -entrainment to spatiotemporal E - and V_e -fluctuations? In what we refer to as the 'subthreshold' analysis, we quantified the characteristics of subthreshold V_m -entrainment to a number of electric field configurations. More specifically, the oscillatory current injected through the extracellular stimulation electrode S1, $I = I_0 \sin(2\pi ft)$, was varied in strength (I_0) and frequency (f) while V_e , V_i and V_m were monitored (5 s duration, 1-2 repetitions, $n=23$ cells; Fig. 1d-f and Fig. 2a). I_0 was chosen such as to induce relatively weak E - and V_e -fluctuations of the same characteristics as the LFPs measured in vivo so that $I_0=25, 50, 100, 200$ nA resulted in V_e -amplitude= $0.07\pm 0.04, 0.14\pm 0.08, 0.28\pm 0.16, 0.55\pm 0.32$ mV and E -amplitude= $0.74\pm 0.53, 1.49\pm 1.06, 2.96\pm 2.11, 5.86\pm 4.25$ mV/mm, respectively (mean \pm standard deviation; Fig. S1) for $f=1$ Hz with V_e recorded from the most proximal somatic extracellular

pipette. Larger f did not alter the induced E - and V_e -characteristics (Fig. 2b, c and S1)(Logothetis, Kayser et al. 2007). Given that in the living animal pyramidal neurons constantly receive synaptic input we also tested whether the characteristics of ephaptic coupling persist for different levels of hyperpolarization and depolarization of neurons by injecting a subthreshold intracellular dc stimulus I_{inj} ($n=17$ cells; Fig. 2a, c). We found that the anti-phase relationship between V_e (and V_i) and V_m was observed for all field configurations (I_0, f) and cells as measured with mean properties (Fig. 2b, c) and cross-correlation analyses (Fig. 2d, e)(Holt and Koch 1999). The characteristics (mean \pm s.e.m.) of ephaptic coupling remained broadly unaltered for $f=1-100$ Hz (for $f=1$ Hz: V_m -amplitude= $0.16\pm 4\times 10^{-4}$ mV, V_m -phase= $164^\circ\pm 4^\circ$; for $f=100$ Hz: V_m -amplitude= 0.11 ± 0.01 mV and V_m -phase= $178^\circ\pm 2^\circ$; Fig. 2b, d) as well as varying levels of hyperpolarization and depolarization ($I_{inj}=-150$ pA: V_m -amplitude= 0.13 ± 0.01 mV, V_m -phase= $170^\circ\pm 4^\circ$; for $I_{inj}=100$ pA: V_m -amplitude= 0.13 ± 0.01 mV and V_m -phase= $151^\circ\pm 5^\circ$; Fig. 2c, e). Markedly, we observed that ephaptic coupling has different characteristics than direct intracellular (subthreshold) current injections such as chirps (Fig. 2b). Thus, we conclude that LFP-like extracellular field activity can readily entrain subthreshold V_m -activity.

In a subsequent step, we examined the impact of ephaptic coupling on the 'suprathreshold', i.e. spiking activity of neurons ($n=25$ cells). To do so, we applied a 9 second dc intracellular somatic current that induced spiking activity (typically 2-4 Hz; see Fig. S2). We divided the experiments into two groups, 'control' experiments where only the intracellular stimulus was applied in the absence of the extracellular stimulus and 'extracellular stimulation' experiments where both intracellular and extracellular stimuli were applied concurrently (Fig. 3a). To assess the effect of the field on spiking activity we performed the control experiments immediately before each extracellular stimulation experiment using the same intracellular dc input. We repeated each pair of experiments (control, extracellular stimulation) 4-6 times for each field configuration (I_0, f) and $f=1, 8, 30$ Hz. We observed an impact of the field on the cross-correlation between V_i and V_e , V_m and V_e (Fig. 3b) as well as the spike triggered average (STA) of individual neurons (Fig. 3c).

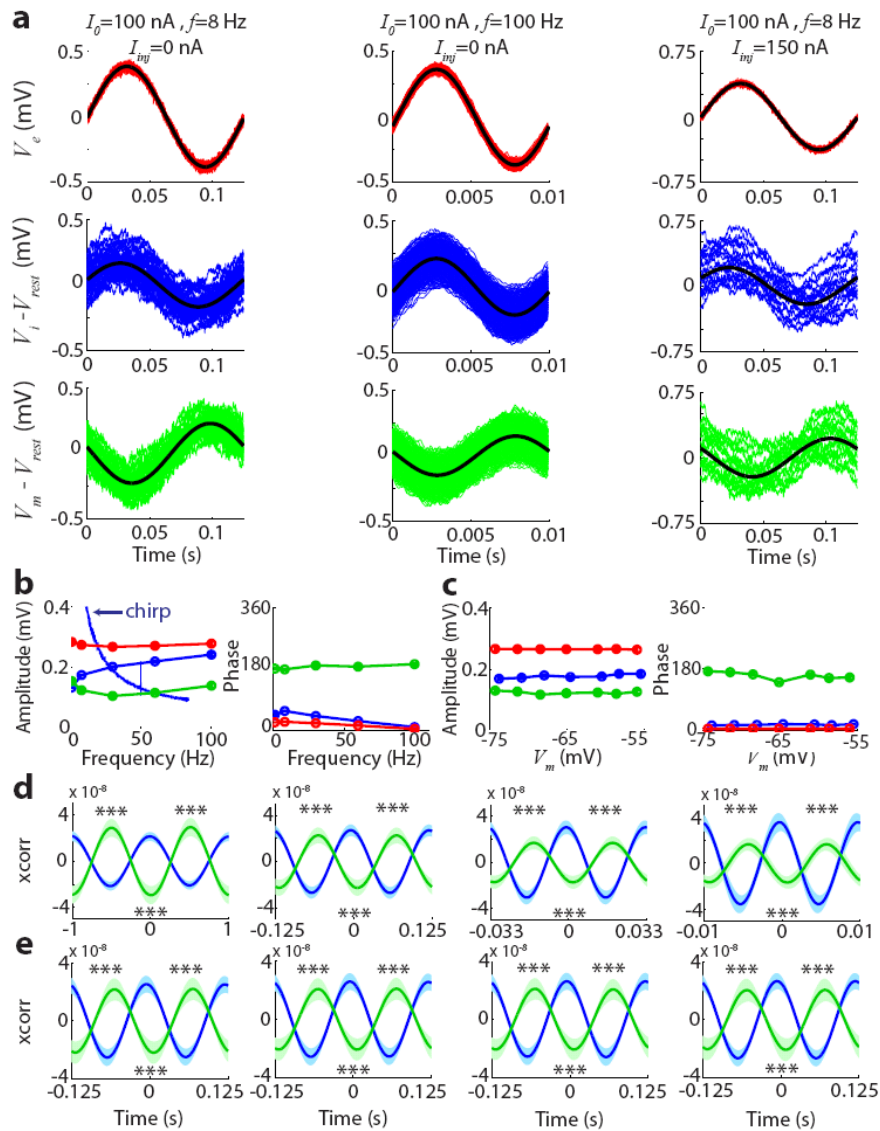


Figure 2: Subthreshold extracellular field entrainment. (a) V_e (first row; traces shown in red, mean in black), V_i (second row; traces shown in blue, mean in black) and V_m (third row; traces shown in green, mean in black) are shown for an individual neuron for three cases of stimulation: slow frequency/no depolarization (left column), high frequency/no depolarization (middle column), and low frequency/depolarized V_m (right column). (b) The amplitude and phase (circles: mean, error bars: s.e.m.) of the V_e (red), V_i (blue) and V_m (green) fluctuations for increasing extracellular stimulation frequency $f=1-100$ Hz and constant $I_0 = 100$ nA ($n=23$ cells). The strong attenuation of intracellular stimuli with increasing f is shown by plotting the V_i resulting by intracellular chirp stimulation in the absence of an extracellular field. (c) The characteristics of subthreshold V_e - (red), V_i - (blue) and V_m - (green) entrainment to the extracellular field are preserved as a function of hyperpolarization and depolarization ($n=17$ cells; circles: mean; error bars: s.e.m.) (d) Cross correlation (xcorr) between V_i and V_e (blue) as well as V_m and V_e (green) of the data shown in b (line: mean; shadowed area: s.e.m.) for (from left to right) $f=1, 8, 30$ and 100 Hz reveals the persistence of the phase-relationship between V_e , V_i and V_m for $f=1-100$ Hz. Stars indicate the statistical significance of the difference between $\text{xcorr}(V_i, V_e)$ and $\text{xcorr}(V_m, V_e)$ for each f calculated through paired t -test (Bonferroni corrected for multiple comparisons) at $t=T/4$, $T=2$ and $3T=4$ with $T=1/f$. (e) Cross correlation between V_i and V_e (blue) as well as V_m and V_e (green) of the data shown

in (c) (line: mean; shadowed area: s.e.m.) for (from left to right) $I_{inj} = -150, 0, 50, 100$ pA reveals the persistence of the phase-relationship for different hyperpolarization and depolarization levels.

Given that the cross-correlation and STA also depend on the V_e -amplitude we applied the population vector (PV) analysis (Fig. 3d, Fig. S3-S5) and the spike field coherence (SFC) measure, a modified version of the spike-triggered average (STA) analysis to quantify the relationship between spiking activity and the extracellular stimulus (Fries, Reynolds et al. 2001; Womelsdorf, Schoffelen et al. 2007). In the case of the PV-analysis, we used the Rayleigh test to examine whether the presence of the extracellular field led to spikes being elicited non-uniformly along the phase-space $[0^\circ, 360^\circ]$. We found that increasing field strength led to spikes being elicited non-uniformly with the preferred spiking-phase, as expressed through the mean direction of the PV, being $266^\circ, 250^\circ, 242^\circ$ and 242° for $f=1$ Hz and $I_0=25, 50, 100$ and 200 nA, respectively (Fig. 3d, Fig. S3-S5), i.e. similar to the phase of the V_e -trough and the V_m -peak as determined in the subthreshold analysis (Fig. 2)(Holt and Koch 1999).

To quantify the STA of all neurons (Fig. 3c), we calculate its power spectrum that gives the magnitude of all frequency components of the STA as a function of frequency (Fig. 3d). Increased STA power at a specific frequency is interpreted as increased phase-locking of spikes to that particular frequency. We found that increasing the strength of the extracellular stimulus resulted in an increasing phase-locking of the spikes to f . In order to examine whether the increase in phase-locking is solely attributed to the presence of the field we also included the control experiments in this analysis by assuming a (virtual) V_e identical to the subsequent extracellular stimulation experiment so that phases could be ascribed to spike times of the control experiments. The increase in STA spectrum at f of the extracellular stimulation experiments was always greater than that of the control experiments (Fig. 3e).

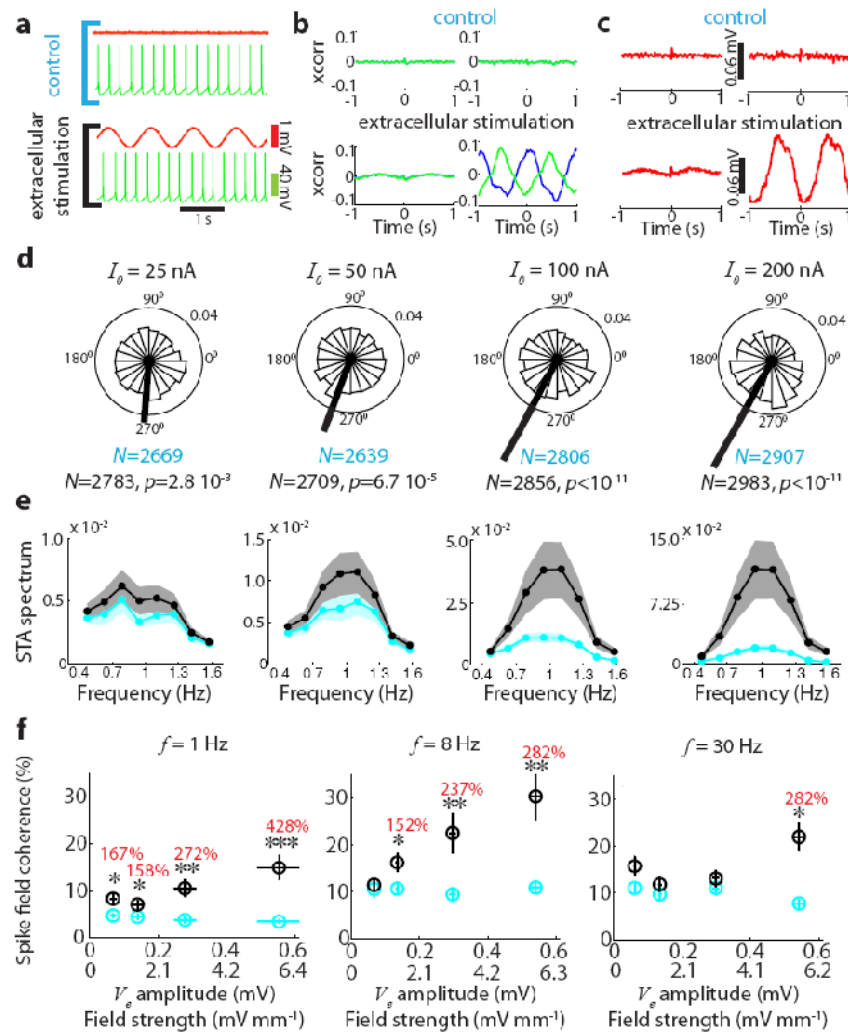


Figure 3: Weak electric fields entrain spiking activity of individual neurons. (a) The presence or absence of the extracellular stimulation during the intracellular dc stimulus differentiates between control and extracellular stimulation experiments, respectively (red trace, extracellular voltage; green trace; transmembrane voltage). (b) Cross correlation (xcorr) between V_i and V_e (blue) as well as V_m and V_e (green) of the low-pass (<100 Hz) suprathreshold data of an individual neuron for the control (upper part) and extracellular stimulation (lower part) experiments. Extracellular stimulation parameters are $I_0=25$ nA, $f=1$ Hz (left) and $I_0=200$ nA, $f=1$ Hz (right). (c) Entrainment of spiking activity assessed through STA analysis with control experiments resulting in at STAs while the presence of an extracellular field gives rise to a non-zero STA. (d) Effect of increasing field strength on the entrainment of the spiking phase for all ($n=25$) neurons when stimulation frequency $f=1$ Hz and amplitude $I_0=25, 50, 100, 200$ nA (from left to right). For the extracellular stimulation experiments, each spike was attributed a phase based on the time of spike initiation and its relationship to the harmonic V_e -signal (see panel a). Increasing population vector length $|R|$ indicates the increasing entrainment of suprathreshold activity to the external field ($|R|=0.045$ for $I_0=25$ nA, $|R|=0.11$ for $I_0=200$ nA). The entrainment increase is attributed to field entrainment resulting in non-uniform spike-phase distribution (p -values calculated using the Rayleigh test) and not changes in number of spikes (N (cyan): control; N (black): extracellular stimulation). (e) The STA spectrum (circles: mean; shadowed areas: s.e.m.) calculated for the same cases as in (d) while for the control experiments a (virtual) V_e identical to the subsequent extracellular stimulation experiment was assumed (black: extracellular stimulation; cyan: control). (f) Spike field coherence (circles: mean; error bars: s.e.m.) for extracellular stimulation (black) and control (cyan) experiments at the stimulation frequency $f=1, 8$ and 30 Hz (from left to right) as a function of stimulation strength (x-axis: first row, circles: mean V_e -amplitude at

the soma, error bars: s.e.m.; second row: circles: mean E -amplitude at the soma, error bars: s.e.m.) Statistical significance of the difference between control and extracellular stimulation experiments for each field configuration (I_0, f) calculated through paired t -test, fdr-corrected for multiple comparisons. Slow extracellular stimuli ($f=1$ Hz) entrain spiking activity even at low amplitudes (V_e -amplitude ≈ 0.07 mV and E -amplitude ≈ 0.74 mV/mm). The ratio (in percent) between the mean extracellular stimulation SFC experiments and control SFC for each field configuration inducing statistically significant SFC-changes is indicated by the numbers in red.

The SFC defined as the STA spectrum normalized by the power spectrum of all power spectra of all V_e -segments that were averaged to obtain the STA (Fries, Reynolds et al. 2001), ranges between 0 and 100 %, with 0 % indicating no phase relationship between spikes and the imposed field and 100 % the phase-locking of all spikes to a particular phase of the extracellular stimulus. Due to its normalization, the SFC is an accurate indicator of the magnitude of stereotypy in spike time relative to V_e -fluctuations of a particular frequency (Fries, Reynolds et al. 2001). Based on the fact that ephaptic coupling led to an increase of the STA spectrum at f , we compared the SFC between extracellular stimulation and control experiments at f for each field configuration (Fig. 3f and S3-S5). We found that while increases in field strength led to increases of suprathreshold ephaptic coupling, the strength of the coupling as expressed through the statistical significance (paired t -test, fdr-corrected for multiple comparisons) of SFC changes relative to control decreased for increasing stimulus frequency f with the lowest V_e - (E -) amplitude of statistically significant entrainment being 0.07 mV (0.74 mV/mm) for $f=1$ Hz while 0.54 mV (5.58 mV/mm) for $f=30$ Hz. Thus, we conclude that phase-locking of spiking activity to the extracellular stimulus through ephaptic coupling is more effective (and occurs for lower field strengths) for slow rather than fast modulations of E and V_e . This is a single-neuron response to electric fields in the absence of synaptic transmission, population responses in vivo may depend more strongly on base firing frequencies of different neuron types (Knight 1972).

Notably, the increased phase-locking of spikes to the V_e -modulation was not attributed to altered spiking frequency but to the emergence of a preferred spiking phase. This was confirmed by comparing the number of spikes and the spike frequency between extracellular stimulation and control experiments (Fig. 3d and S2; paired t -test Bonferroni-corrected for multiple comparisons) as well as by comparing the spike triggered power (STP; Fig. S3-S5; paired t -test Bonferroni-corrected for multiple comparisons) for all field configurations (I_0, f). The STP quantifies the oscillations which are present in the V_e -signal regardless of whether they are

related to the occurrence of spikes or not and is calculated by averaging each individual V_e -segment centered on each spike (Fries, Reynolds et al. 2001) (The SFC is defined as the STA spectrum divided by the STP spectrum). While the average STP of all neurons indicated the strong presence of oscillations at f (Fig. S3-S5), the power of the STP at f did not distinguish between extracellular stimulation and control experiments (paired t -test Bonferroni-corrected for multiple comparisons) indicating that phase-locking is indeed attributed to ephaptic entrainment of spiking activity.

Our results show that even modest E - and V_e -fluctuations can entrain both subthreshold and suprathreshold activity of individual neurons. Given that LFP-signals extend over hundreds of μm (Bragin, Jando et al. 1995; Katzner, Nauhaus et al. 2009), can such fields lead to the cooperative entrainment of neurons that under other circumstances would operate independently? To address this question we simultaneously patched 3 proximally located neurons and positioned the extracellular stimulation electrode S1 close so that all 3 neurons experienced a simultaneous and similar V_e -fluctuation at their somata. 6 extracellular recording electrodes served to monitor V_e close to the somata of the 3 neurons and the space between them (Fig. 4a). During experiments we applied a simultaneous suprathreshold intracellular dc input (duration 9 s) to all neurons in the presence (extracellular stimulation) or absence (control) of an extracellular stimulus (Fig. 4b). Cross-correlation between V_i and V_e (low pass portion of the signal, <100 Hz) revealed the correlation between the V_i of all neurons and the common V_e (Fig. 4c). While the extent to which the activity of each cell was modulated by the field stimulation was differential (mainly due to the differential distance from S1; Fig. S6), the spiking activity of the neural population (and each cell individually) was entrained in the presence of the extracellular field as defined by the deviation of spike phases from uniformity for increasing extracellular field strength (p -values calculated using the Rayleigh test). In agreement with the outcomes of the subthreshold and suprathreshold studies, extracellular stimulation experiments resulted in a preferred spiking-phase (from left to right) 286° , 277° , 272° , 275° and 273° . The observed phase preference was attributed to the simultaneous entrainment of spiking activity of all neurons to the extracellular field and not to spike rate changes between extracellular stimulation and control experiments (paired t -test fdr -corrected for multiple comparisons). In another experiment with 2 (simultaneously patched) neurons the outcomes were similar (Fig. S7).

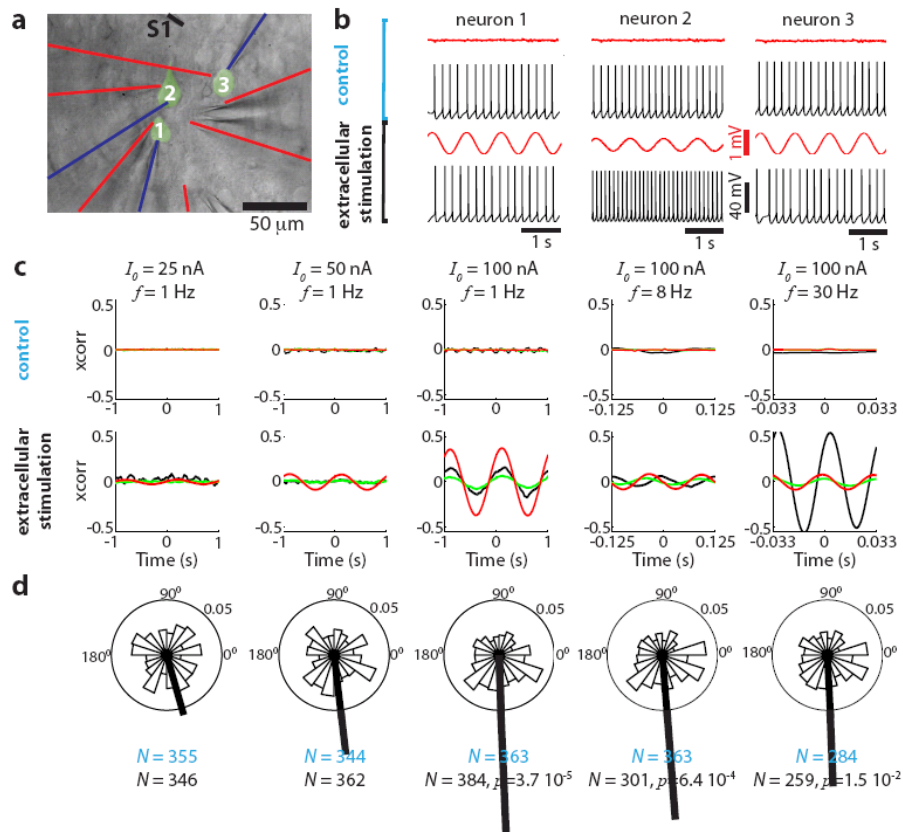


Figure 4 Ephaptic communication leads to coordinated spiking activity between proximally located neurons. **(a)** Three neurons whose somata are located within $50\ \mu\text{m}$ were patched with intracellular electrodes (blue lines). Six extracellular electrodes were used to monitor V_e -fluctuations (red lines). The extracellular stimulation electrode (S1, black line) was positioned approx. $50\ \mu\text{m}$ from cells 1-3. **(b)** Intracellular (black) and extracellular (red) activity during concurrent intracellular application of suprathreshold dc input to the three neurons (control: top rows; extracellular stimulation experiment: bottom rows). **(c)** Cross correlation between the low-pass portion ($<100\ \text{Hz}$) of the V_f and V_e -signal (as recorded from the closest somatic electrode) for neuron 1 (black), 2 (green) and 3 (red) for control (top row) and extracellular stimulation (bottom row) experiments for (from left to right) (I_0, f)=(25 nA, 1 Hz), (50 nA, 1 Hz), (100 nA, 1 Hz), (100 nA, 8 Hz) and (100 nA, 30 Hz). Extracellular stimulation results in (from left to right): V_e -amplitude= 0.09 ± 0.03 , 0.24 ± 0.12 , 0.40 ± 0.12 , 0.39 ± 0.12 and $0.50\pm 0.21\ \text{mV}$; E -amplitude= 0.99 ± 0.47 , 2.07 ± 0.99 , 4.06 ± 1.96 , 3.87 ± 1.79 , $3.77\pm 1.69\ \text{mV/mm}$ (mean \pm std, among the 3 neurons). **(d)** PV analysis of all spikes from neurons 1-3 for the extracellular stimulation conditions shown in (c). As the field strength increases spikes from all neurons cluster at 270° and the phase-distribution significantly deviates from uniformity (p -values calculated using the Rayleigh test). As indicated by the total number of spikes from all neurons (control: N(cyan); extracellular stimulation: N(black)) spike-clustering at 270° is attributed to spike phase re-shuffling due to field entrainment (see c) and not due to differential spiking rate.

DISCUSSION

We showed that weak electric fields of the same magnitude and spatial characteristics as measured in vivo readily entrain both subthreshold and suprathreshold (spiking) activity of pyramidal neurons. While subthreshold V_m -activity can be easily entrained up to 100 Hz, spiking activity is mainly affected by slower E - and V_e -modulations. The implications of such observations are many.

At the Single neuron level, a number of computations have been attributed to the integration of subthreshold synaptic input (Kamondi, Acsady et al. 1998; Poirazi, Brannon et al. 2003; Polsky, Mel et al. 2004) and oscillatory membrane currents. We showed here that V_m is entrained by LFP-like fluctuations and importantly, that the entrainment is frequency-independent. These subthreshold fluctuations can be of importance to single-neuron computations. Considering suprathreshold activity, when comparing the SFC-changes we observed (Fig. 3f) with typical SFC-changes reported in the literature during performance of cognitive tasks it becomes evident that the presence of even weak extracellular fields may, under certain circumstances, give rise equal or even stronger correlations between field and spiking activity through ephaptic coupling (compare to (Fries, Reynolds et al. 2001; Womelsdorf, Schoffelen et al. 2007)) than correlations attributed to cognitive processing. It follows therefore that ephaptic interactions may play an important role during sparse coding in deeper cortical layers as well as the hippocampus where endogenous synaptic activity gives rise to measurable field activity. The influence of ephaptic interactions in sparse coding may be directly manifested by altering the correlation between spiking and field activity that is known to impact biophysical aspects of computation (Holscher, Anwyl et al. 1997; Markram, Lubke et al. 1997; Hyman, Wyble et al. 2003) as well as behavior (O'Keefe and Recce 1993) (Skaggs, McNaughton et al. 1996; Harris, Henze et al. 2002; Huxter, Burgess et al. 2003; Kreiman, Hung et al. 2006).

At the neural population level ephaptic coupling can be regarded as a possible mechanism to perform computations involving proximally located neurons. Even if our population experiments (Fig. 4 and S7) illustrate that ephaptic coupling can lead to cooperative spiking activity of neurons that otherwise act independently, all neurons within a specific volume (designated by similar E - and V_e -characteristics) will be rhythmically hyperpolarized and depolarized due to ephaptic coupling. While our work suggests that such coupling can be important for pyramidal neurons this will also be the case for fast-spiking inhibitory neurons. Therefore, both excitation and inhibition at a given brain area will be affected through ephaptic coupling suggesting that a common LFP does not merely synchronize neural populations. Much more, ephaptic coupling could be regarded as a mechanism providing 'windows of opportunity' by rhythmically organizing cell assemblies in potentiated (depolarized) and depressed (hyperpolarized) V_m -states. Such states may contribute to synchronization of spiking activity but concurrently also enable sparse-coding (for example, winner-take-all networks or (Poulet and Petersen 2008)). Notably, ephaptic coupling can be regarded as an energetically-cheap mechanism since they alter the state and function of neurons based on their location with no added energy cost.

REFERENCES

- Anastassiou, C. A., S. M. Montgomery, et al. (2010). "The effect of spatially inhomogeneous extracellular electric fields on neurons." *J Neurosci* **30**(5): 1925-1936.
- Arvanitaki, A. (1942). "Effects evoked in an axon by the activity of a contiguous one." *Journal of Neurophysiology* **5**(2): 89-108.
- Bikson, M., M. Inoue, et al. (2004). "Effects of uniform extracellular DC electric fields on excitability in rat hippocampal slices in vitro." *J Physiol* **557**(Pt 1): 175-190.
- Bragin, A., G. Jando, et al. (1995). "Gamma (40-100 Hz) oscillation in the hippocampus of the behaving rat." *J Neurosci* **15**(1 Pt 1): 47-60.
- Brecht, M., M. Schneider, et al. (2004). "Whisker movements evoked by stimulation of single pyramidal cells in rat motor cortex." *Nature* **427**(6976): 704-710.
- Buzsaki, G. (2002). "Theta oscillations in the hippocampus." *Neuron* **33**(3): 325-340.
- Buzsaki, G. (2004). "Large-scale recording of neuronal ensembles." *Nat Neurosci* **7**(5): 446-451.
- Buzsaki, G., Z. Horvath, et al. (1992). "High-frequency network oscillation in the hippocampus." *Science* **256**(5059): 1025-1027.
- Chan, C. Y., J. Hounsgaard, et al. (1988). "Effects of electric fields on transmembrane potential and excitability of turtle cerebellar Purkinje cells in vitro." *J Physiol* **402**: 751-771.
- Chan, C. Y. and C. Nicholson (1986). "Modulation by applied electric fields of Purkinje and stellate cell activity in the isolated turtle cerebellum." *J Physiol* **371**: 89-114.
- Deans, J. K., A. D. Powell, et al. (2007). "Sensitivity of coherent oscillations in rat hippocampus to AC electric fields." *J Physiol* **583**(Pt 2): 555-565.
- Francis, J. T., B. J. Gluckman, et al. (2003). "Sensitivity of neurons to weak electric fields." *J Neurosci* **23**(19): 7255-7261.

- Fries, P., J. H. Reynolds, et al. (2001). "Modulation of oscillatory neuronal synchronization by selective visual attention." *Science* **291**(5508): 1560-1563.
- Ghai, R. S., M. Bikson, et al. (2000). "Effects of applied electric fields on low-calcium epileptiform activity in the CA1 region of rat hippocampal slices." *J Neurophysiol* **84**(1): 274-280.
- Gold, C., D. A. Henze, et al. (2006). "On the origin of the extracellular action potential waveform: A modeling study." *J Neurophysiol* **95**(5): 3113-3128.
- Harris, K. D., D. A. Henze, et al. (2002). "Spike train dynamics predicts theta-related phase precession in hippocampal pyramidal cells." *Nature* **417**(6890): 738-741.
- Histed, M. H., V. Bonin, et al. (2009). "Direct activation of sparse, distributed populations of cortical neurons by electrical microstimulation." *Neuron* **63**(4): 508-522.
- Holscher, C., R. Anwyl, et al. (1997). "Stimulation on the positive phase of hippocampal theta rhythm induces long-term potentiation that can be depotentiated by stimulation on the negative phase in area CA1 in vivo." *J Neurosci* **17**(16): 6470-6477.
- Holt, G. R. and C. Koch (1999). "Electrical interactions via the extracellular potential near cell bodies." *J Comput Neurosci* **6**(2): 169-184.
- Houweling, A. R. and M. Brecht (2008). "Behavioural report of single neuron stimulation in somatosensory cortex." *Nature* **451**(7174): 65-68.
- Huxter, J., N. Burgess, et al. (2003). "Independent rate and temporal coding in hippocampal pyramidal cells." *Nature* **425**(6960): 828-832.
- Hyman, J. M., B. P. Wyble, et al. (2003). "Stimulation in hippocampal region CA1 in behaving rats yields long-term potentiation when delivered to the peak of theta and long-term depression when delivered to the trough." *J Neurosci* **23**(37): 11725-11731.
- Jefferys, J. G. (1995). "Nonsynaptic modulation of neuronal activity in the brain: electric currents and extracellular ions." *Physiol Rev* **75**(4): 689-723.
- Jefferys, J. G. and H. L. Haas (1982). "Synchronized bursting of CA1 hippocampal pyramidal cells in the absence of synaptic transmission." *Nature* **300**(5891): 448-450.
- Kamondi, A., L. Acsády, et al. (1998). "Theta oscillations in somata and dendrites of hippocampal pyramidal cells in vivo: activity-dependent phase-precession of action potentials." *Hippocampus* **8**(3): 244-261.
- Katzner, S., I. Nauhaus, et al. (2009). "Local origin of field potentials in visual cortex." *Neuron* **61**(1): 35-41.
- Knight, B. W. (1972). "The relationship between the firing rate of a single neuron and the level of activity in a population of neurons. Experimental evidence for resonant enhancement in the population response." *J Gen Physiol* **59**(6): 767-778.
- Koch, C. (1998). *Biophysics of Computation: Information Processing in Single Neurons (Computational Neuroscience)*, Oxford University Press, USA.
- Kreiman, G., C. P. Hung, et al. (2006). "Object selectivity of local field potentials and spikes in the macaque inferior temporal cortex." *Neuron* **49**(3): 433-445.
- Li, C. Y., M. M. Poo, et al. (2009). "Burst spiking of a single cortical neuron modifies global brain state." *Science* **324**(5927): 643-646.
- Logothetis, N. K., C. Kayser, et al. (2007). "In vivo measurement of cortical impedance spectrum in monkeys: implications for signal propagation." *Neuron* **55**(5): 809-823.
- Logothetis, N. K., J. Pauls, et al. (2001). "Neurophysiological investigation of the basis of the fMRI signal." *Nature* **412**(6843): 150-157.
- Lubenov, E. V. and A. G. Siapas (2009). "Hippocampal theta oscillations are travelling waves." *Nature* **459**(7246): 534-539.
- Markram, H., J. Lubke, et al. (1997). "Regulation of synaptic efficacy by coincidence of postsynaptic APs and EPSPs." *Science* **275**(5297): 213-215.
- Marshall, L., H. Helgadottir, et al. (2006). "Boosting slow oscillations during sleep potentiates memory." *Nature* **444**(7119): 610-613.
- Moore, T. and M. Fallah (2004). "Microstimulation of the frontal eye field and its effects on covert spatial attention." *J Neurophysiol* **91**(1): 152-162.
- O'Keefe, J. and M. Recce (1993). "Phase relationship between hippocampal place units and the EEG theta rhythm." *Hippocampus* **3**(3): 317-330.
- Poirazi, P., T. Brannon, et al. (2003). "Arithmetic of subthreshold synaptic summation in a model CA1 pyramidal cell." *Neuron* **37**(6): 977-987.
- Polsky, A., B. W. Mel, et al. (2004). "Computational subunits in thin dendrites of pyramidal cells." *Nat Neurosci* **7**(6): 621-627.

- Poulet, J. F. and C. C. Petersen (2008). "Internal brain state regulates membrane potential synchrony in barrel cortex of behaving mice." *Nature* **454**(7206): 881-885.
- Radman, T., Y. Su, et al. (2007). "Spike timing amplifies the effect of electric fields on neurons: implications for endogenous field effects." *J Neurosci* **27**(11): 3030-3036.
- Skaggs, W. E., B. L. McNaughton, et al. (1996). "Theta phase precession in hippocampal neuronal populations and the compression of temporal sequences." *Hippocampus* **6**(2): 149-172.
- Steriade, M., A. Nunez, et al. (1993). "Intracellular analysis of relations between the slow (< 1 Hz) neocortical oscillation and other sleep rhythms of the electroencephalogram." *J Neurosci* **13**(8): 3266-3283.
- Steriade, M., A. Nunez, et al. (1993). "A novel slow (< 1 Hz) oscillation of neocortical neurons in vivo: depolarizing and hyperpolarizing components." *J Neurosci* **13**(8): 3252-3265.
- Stoney, S. D., Jr., W. D. Thompson, et al. (1968). "Excitation of pyramidal tract cells by intracortical microstimulation: effective extent of stimulating current." *J Neurophysiol* **31**(5): 659-669.
- Stuart, G., N. Spruston, et al. (2007). *Dendrites*. Oxford ; New York, Oxford University Press.
- Taylor, C. P. and F. E. Dudek (1982). "Synchronous neural afterdischarges in rat hippocampal slices without active chemical synapses." *Science* **218**(4574): 810-812.
- Tehovnik, E. J., A. S. Tolias, et al. (2006). "Direct and indirect activation of cortical neurons by electrical microstimulation." *J Neurophysiol* **96**(2): 512-521.
- Traub, R. D., F. E. Dudek, et al. (1985). "Simulation of hippocampal afterdischarges synchronized by electrical interactions." *Neuroscience* **14**(4): 1033-1038.
- Vallbo, A. B., K. A. Olsson, et al. (1984). "Microstimulation of single tactile afferents from the human hand. Sensory attributes related to unit type and properties of receptive fields." *Brain* **107** (Pt 3): 727-749.
- Vanderwolf, C. H. (1969). "Hippocampal electrical activity and voluntary movement in the rat." *Electroencephalogr Clin Neurophysiol* **26**(4): 407-418.
- Womelsdorf, T., J. M. Schoffelen, et al. (2007). "Modulation of neuronal interactions through neuronal synchronization." *Science* **316**(5831): 1609-1612.
- Ylinen, A., A. Bragin, et al. (1995). "Sharp wave-associated high-frequency oscillation (200 Hz) in the intact hippocampus: network and intracellular mechanisms." *J Neurosci* **15**(1 Pt 1): 30-46.

SUPPLEMENTARY FIGURES

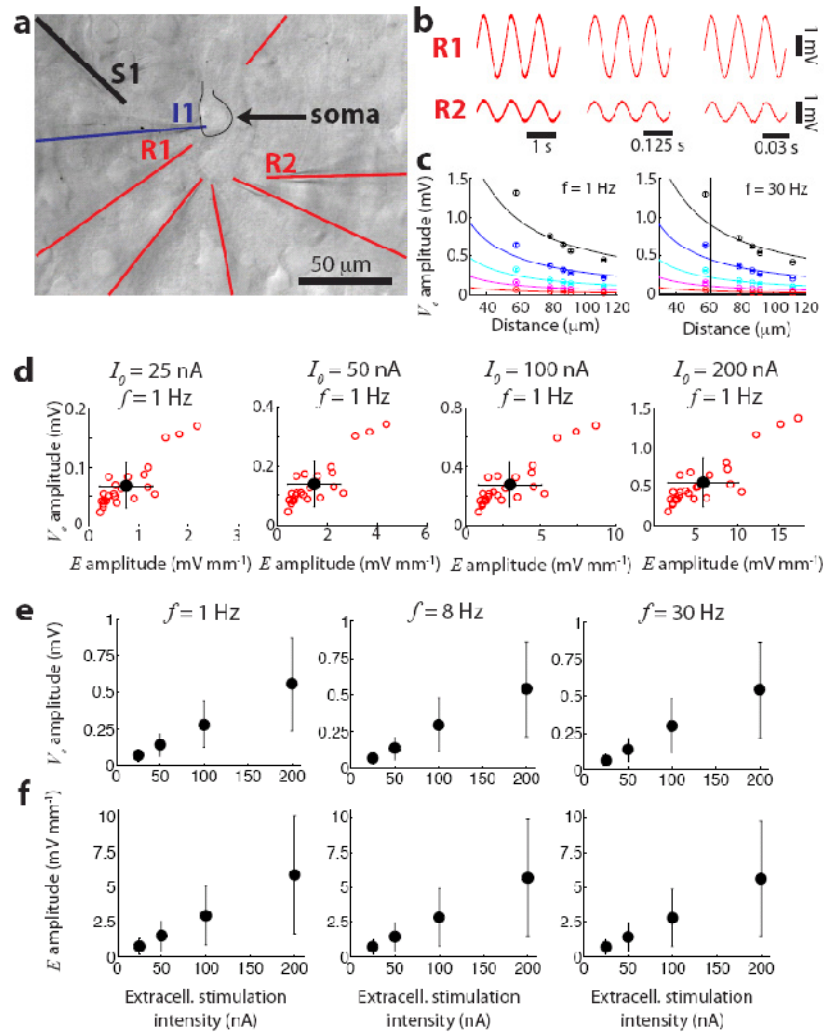


Figure S1 Characteristics of the externally imposed spatiotemporal E - and V_e -fluctuations. (a) A typical experimental configuration with an extracellular stimulation electrode (S1, black line), an intracellular patching electrode (I1, blue line) and 6 extracellular recording pipettes monitoring V_e close to the cell soma (circumference designated by the thin black line). (b) V_e as measured by two extracellular recording site R1 and R2 for extracellular stimulation amplitude $I_\sigma = 200$ nA and stimulation frequency (from left to right) $f = 1, 8$ and 30 Hz. (c) The relationship between the V_e -amplitude (circles: mean, error bars: standard deviation) and the distance from S1 for five stimulus intensities $I_\sigma = 10$ (red), 25 (magenta), 50 (cyan), 100 (blue) and 200 nA (black) and two stimulus frequencies, $f = 1$ (left) and 30 Hz (right). Solid lines indicate the best fit (least-squares) of the point-source approximation using the extracellular medium conductance ρ as a variable. The values of ρ determined through this procedure were typically $\rho = 1.5\text{--}3.0$ Ωm in agreement with (1). (d) The V_e - and E -amplitude (red circles: data from $n = 25$ experiments, black circles: mean, error bars: std) induced by the harmonic extracellular stimulation for (from left to right) $I_\sigma = 25, 50, 100$ and 200 nA for $f = 1$ Hz as measured by the extracellular electrode closest to the soma (R1 in panel a). (e, f) The V_e - and E -amplitude (black circles: mean, error bars: std, $n = 25$ experiments) induced by the harmonic extracellular stimulation for (from left to right) $f = 1, 8$ and 30 Hz as measured by the extracellular electrode closest to the soma (R1 in panel a).

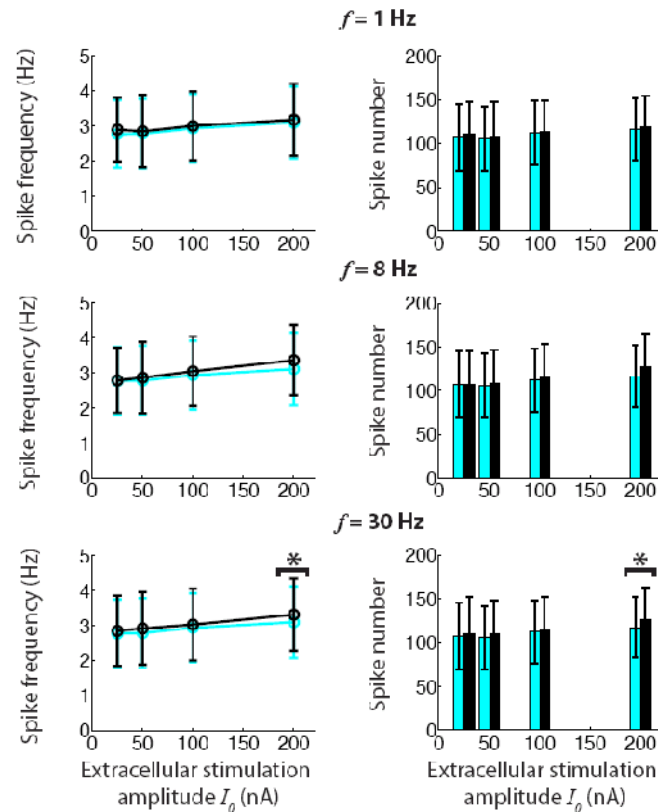


Figure S2 Spiking frequency and number of spikes for all neurons and field configurations (see Fig. 3). A suprathreshold dc intracellular stimulus induced spiking activity of the patched neuron (duration: 9 s). The experiment was conducted in the absence (control experiment) and presence (extracellular stimulation experiment) of the extracellular stimulus (identical intracellular stimulus was used in both cases) for 3-6 repetitions. Spiking activity as expressed in the spiking frequency and total number of spikes elicited for a specific field configuration (I_0 , f) remained unaltered compared to the control experiments (cyan: control experiments, black: extracellular stimulation experiments; bars: mean, error bars: std) as assessed through the paired t -test (Bonferroni-corrected for multiple comparisons). Only in one case for $(I_0, f) = (200 \text{ nA}, 30 \text{ Hz})$ did we observe a statistically difference in frequency and number of spikes between control and extracellular stimulation experiments.

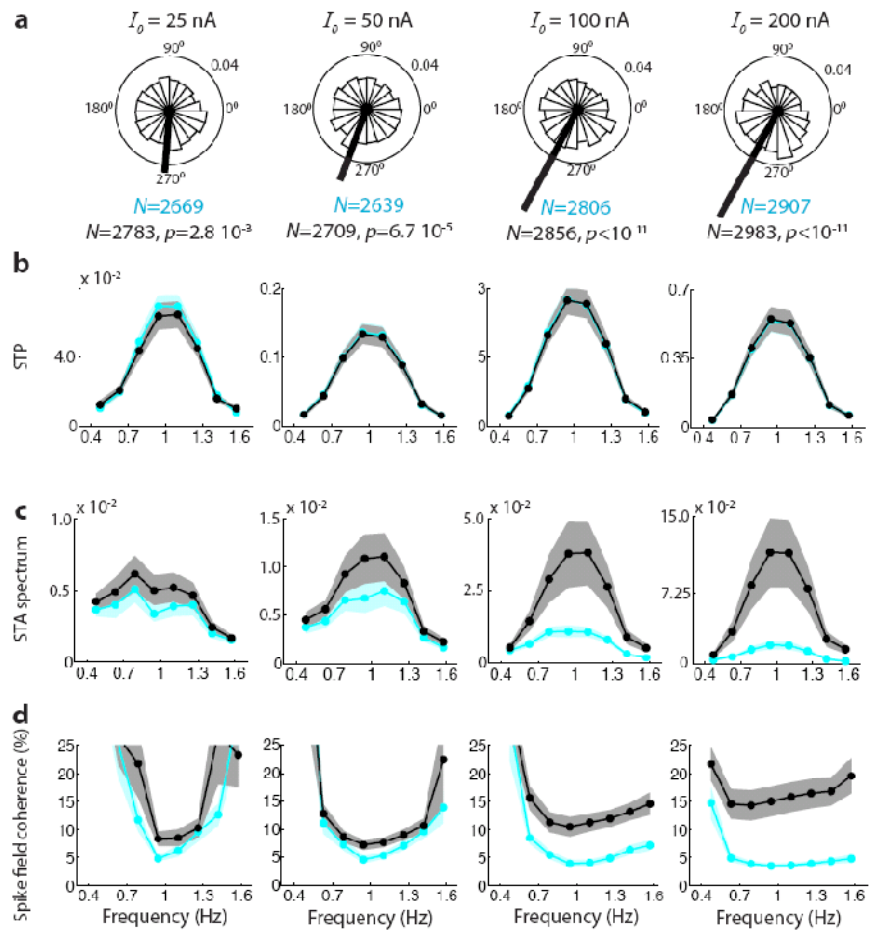


Figure S3 Entrainment characteristics of spiking activity of individual neurons for $f=1$ Hz. (a) Effect of increasing field strength on the entrainment of the spiking phase for all ($n=25$) neurons for $f=1$ Hz and amplitude (from left to right) $I_0=25, 50, 100, 200$ nA as quantified through the population vector (PV) analysis (black: extracellular stimulation experiments; thick black line: PV). Increasing PV length $|R|$ indicates increasing entrainment of suprathreshold activity to the external field ($|R|=0.045$ for $I_0=25$ nA, $|R|=0.11$ for $I_0=200$ nA). Same data as in Fig. 3d. The entrainment increase is attributed to field entrainment resulting in non-uniform spike-phase distribution (p -values calculated using the Rayleigh test) and not by changes in number of spikes (see N (cyan): control; N (black): extracellular stimulation; see also Fig. S2). (b) Spike triggered power (STP) remains constant (paired t -test fdr -corrected for multiple comparisons) between control and extracellular stimulation experiments (line: mean, shaded area: s.e.m.) with control experiments being attributed a 'virtual' V_e -signal identical to the subsequent extracellular stimulation experiment in order to define a spiking-phase. (c) The spike-triggered average (STA) spectrum of the extracellular stimulation experiments increases with respect to control experiments for increasing I_0 (circles: mean, shaded area: s.e.m.) (d) The spike field coherence (SFC) defined through the ratio of the STA and the STP spectrum is used as a measure of quantifying the entrainment of spiking activity to the extracellular field. The results reported in Fig. 3f (left panel) are based on the difference between control and extracellular stimulation SFC at $f=1$ Hz.

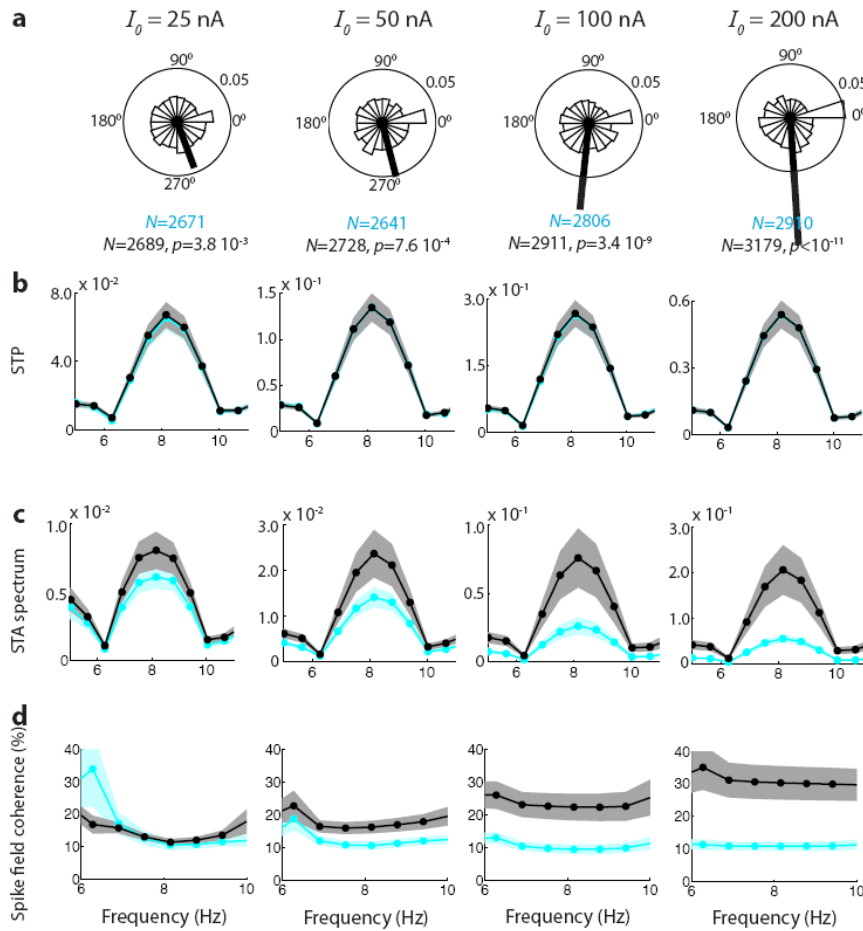


Figure S4 Entrainment characteristics of spiking activity of individual neurons for $f=8$ Hz. (a) Effect of increasing field strength on the entrainment of the spiking phase for all ($n=25$) neurons for $f=8$ Hz and amplitude (from left to right) $I_0=25, 50, 100, 200$ nA (black: extracellular stimulation experiments) as quantified through the PV analysis. Increasing PV length $|R|$ indicates the increasing entrainment of suprathreshold activity to the external field ($|R|=0.046$ for $I_0=25$ nA, $|R|=0.118$ for $I_0=200$ nA). The entrainment increase is attributed to field entrainment resulting in non-uniform spike-phase distribution (p -values calculated using the Rayleigh test) and not by changes in number of spikes (see N(cyan): control; N(black): extracellular stimulation; see also Fig. S2). (b) Spike triggered power (STP) remains constant (paired t -test fdr -corrected for multiple comparisons) between control and extracellular stimulation experiments (line: mean, shaded area: s.e.m.) with control experiments being attributed a 'virtual' V_e -signal identical to the subsequent extracellular stimulation experiment in order to define a spiking-phase. (c) The spike-triggered average (STA) spectrum of the extracellular stimulation experiments increases with respect to control experiments for increasing I_0 (circles: mean, shaded area: s.e.m.) (d) The spike field coherence (SFC) defined through the ratio of the STA and the STP spectrum is used as a measure of quantifying the entrainment of spiking activity to the extracellular field. The results reported in Fig. 3f (middle panel) are based on the difference between control and extracellular stimulation SFC at $f=8$ Hz.

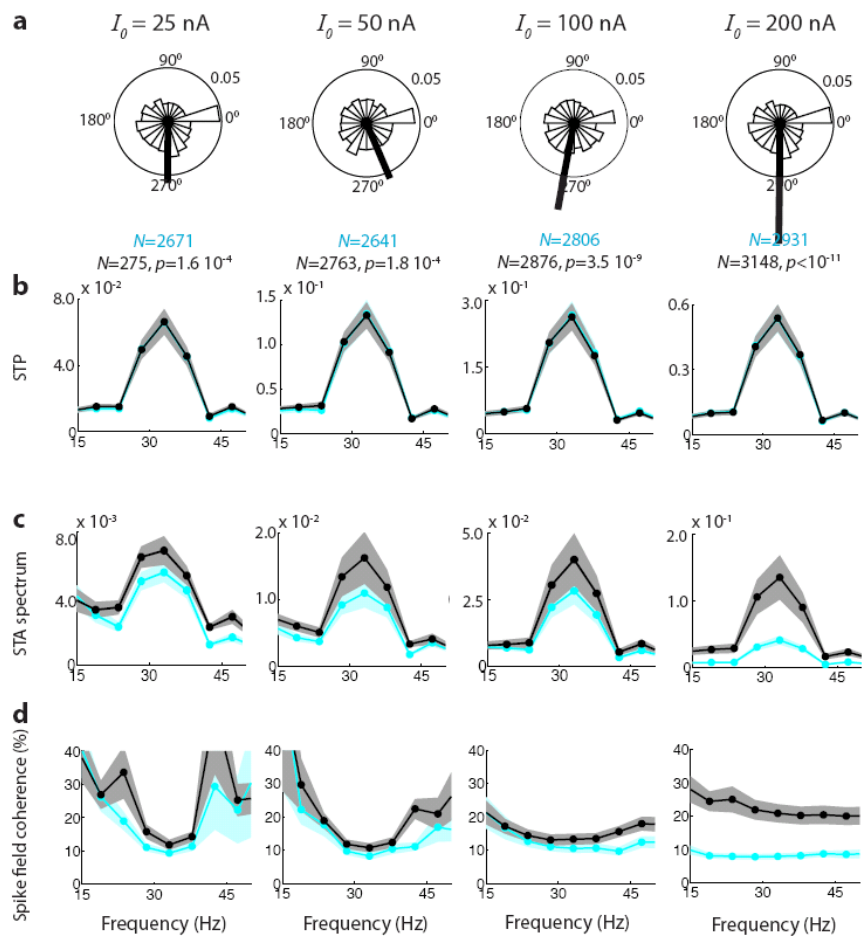


Figure S5 Entrainment characteristics of spiking activity of individual neurons for $f=30$ Hz. (a) Effect of increasing field strength on the entrainment of the spiking phase for all ($n=25$) neurons for $f=30$ Hz and amplitude (left to right) $I_0=25, 50, 100, 200$ nA (cyan: control experiments; black: extracellular stimulation experiments) as quantified through the PV analysis. Increasing PV length $|R|$ indicates the increasing entrainment of suprathreshold activity to the external field ($|R|=0.084$ for $I_0=25$ nA, $|R|=0.252$ for $I_0=200$ nA). The entrainment increase is attributed to field entrainment resulting in non-uniform spike phase distribution (p -values calculated using the Rayleigh test) and not by changes in number of spikes (see N (cyan): control; N (black): extracellular stimulation; see also Fig. S2). (b) Spike triggered power (STP) remains constant (paired t -test fdr -corrected for multiple comparisons) between control and extracellular stimulation experiments (line: mean, shaded area: s.e.m.) with control experiments being attributed a 'virtual' V_e -signal identical to the subsequent extracellular stimulation experiment in order to define a spiking-phase. (c) The spike-triggered average (STA) spectrum of the extracellular stimulation experiments increases with respect to control experiments for increasing I_0 (circles: mean, shaded area: s.e.m.) (d) The spike field coherence (SFC) defined through the ratio of the STA and the STP spectrum is used as a measure of quantifying the entrainment of spiking activity to the extracellular field. The results reported in Fig. 3f (right panel) are based on the difference between control and extracellular stimulation SFC at $f=30$ Hz.

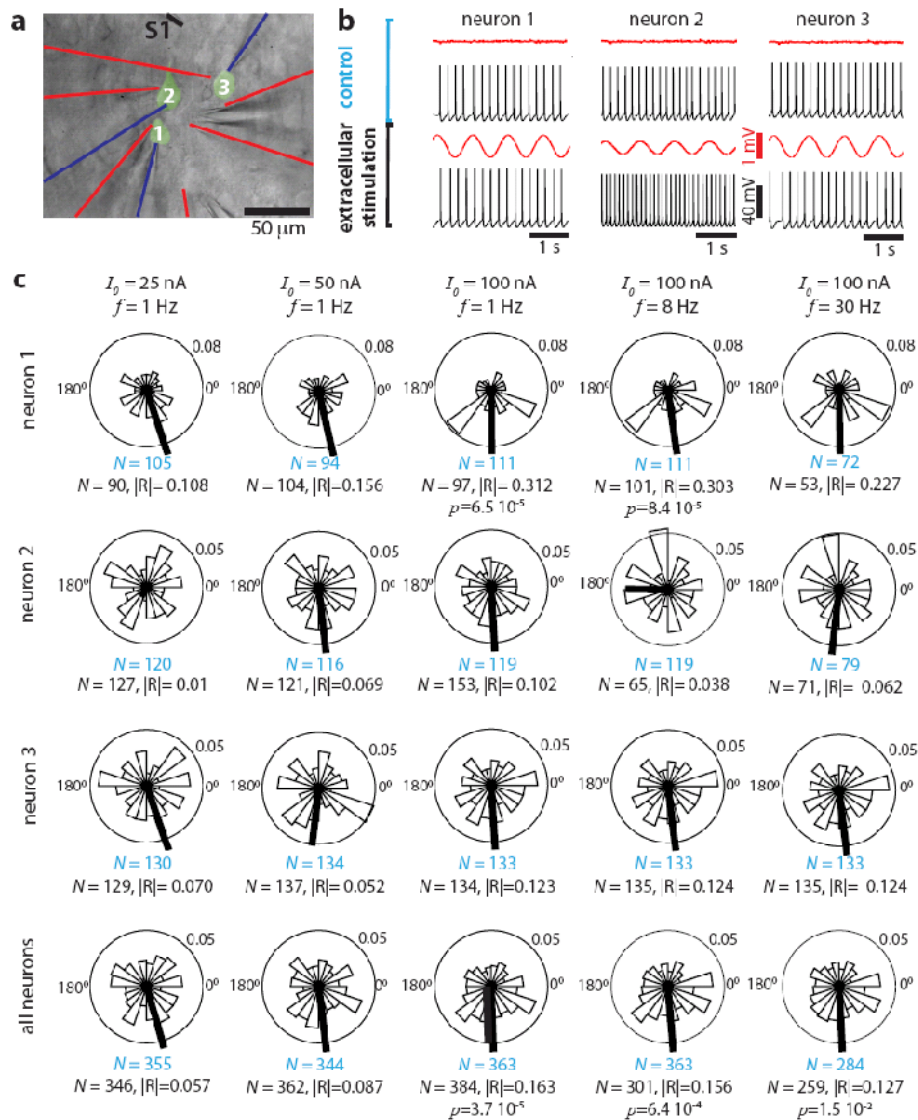


Figure S6 Analysis of the suprathreshold activity of each neuron of the neural population experiment (Fig. 4). (a) Three neurons whose somata are located within 50 μm were patched with intracellular electrodes (blue lines). Six extracellular electrodes were used to monitor V_e -fluctuations (red lines). The extracellular stimulation electrode (S1, black line) was positioned approx. 50 μm from cells 1-3. (b) Intracellular (black traces) and extracellular (red traces) activity during concurrent intracellular application of suprathreshold dc input to the three neurons (control: top rows; extracellular stimulation experiment: bottom rows). (c) PV analysis for each individual neuron (first row: neuron 1; second row: neuron 2; third row: neuron 3; fourth row: all neurons) for (from left to right) $(I_0, f) = (25 \text{ nA}, 1 \text{ Hz})$, $(50 \text{ nA}, 1 \text{ Hz})$, $(100 \text{ nA}, 1 \text{ Hz})$, $(100 \text{ nA}, 8 \text{ Hz})$ and $(100 \text{ nA}, 30 \text{ Hz})$. The number of spikes N for each field configuration is shown (cyan: control experiments; black: extracellular stimulation experiments) as well as $|R|$. p -values were calculated by the Rayleigh test and are reported when statistically significant ($p < 0.05$). As observed, increasing I_0 results in (differential) entrainment of all neurons and increasingly coordinated spiking activity in the absence (due to pharmacological silencing) of any synaptic communication.

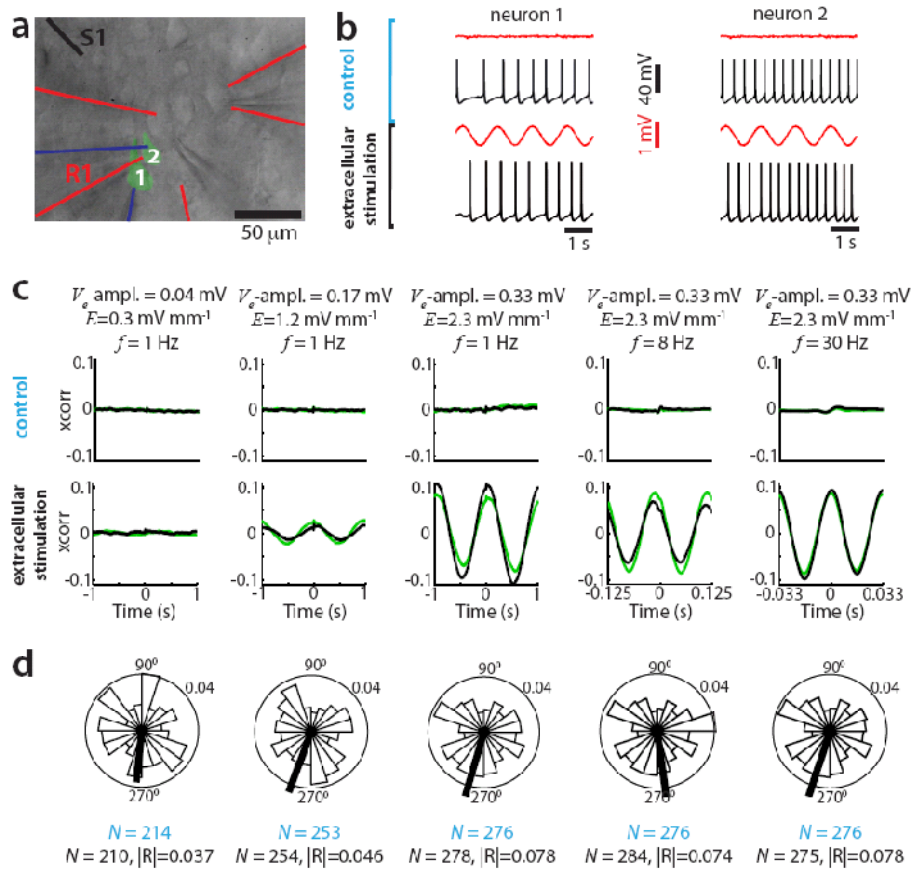


Figure S7 Ephaptic communication leads to coordinated activity between proximately located neurons. (a) Two neurons whose somata are located within 20 μm were patched with intracellular electrodes (blue lines). Six extracellular electrodes were used to monitor V_e -fluctuations (red lines). The extracellular stimulation electrode (S1, black line) was positioned approx. 70 μm from the somata. (b) V_i (black traces) and V_e (red traces) during concurrent intracellular application of suprathreshold dc input to both neurons (control: top rows; extracellular stimulation experiment: bottom rows). (c) Cross correlation between the low-pass portion (<100 Hz) of the V_i and V_e -signal (as recorded from the closest somatic electrode) for neuron 1 (black) and 2 (green) for control (top row) and extracellular stimulation (bottom row) experiments for (from left to right) (I_0, f) = (50 nA, 1 Hz), (100 nA, 1 Hz), (200 nA, 1 Hz), (200 nA, 8 Hz) and (200 nA, 30 Hz). The V_e - and E -amplitude induced for each (I_0, f) are shown on the top (because the distance between the somata is small compared to their distance to S1, the V_e - and E -amplitudes are very similar). (d) PV analysis of all spikes from neurons 1 and 2 for the extracellular stimulation conditions shown in (c). Increasing I_0 leads to spikes from both neurons to cluster around 270° as expressed by the mean PV angle (from left to right: $264^\circ, 250^\circ, 254^\circ, 252^\circ$) and the increasing $|R|$. As indicated by the total number of spikes from all neurons (control: N(cyan); extracellular stimulation: N(black)) the spike clustering is attributed to spike phase re-shuffling due to field entrainment (see c) and not to differential spiking rate (paired t -test fdr -corrected for multiple comparisons).

Chapter 5 Frequency-dependent disynaptic inhibition in the pyramidal network – a ubiquitous pathway in the rodent neocortex

Frequency-dependent disynaptic inhibition in the pyramidal network – a ubiquitous pathway in the rodent neocortex

Thomas K. Berger¹, Rodrigo Perin¹, Gilad Silberberg², Henry Markram¹

¹ Laboratory of Neural Microcircuitry, Brain Mind Institute, Ecole Polytechnique Fédérale de Lausanne, Lausanne (EPFL), CH-1015, Switzerland

² Department of Neuroscience, Karolinska Institute, Stockholm 17177, Sweden.

Correspondence:
Henry Markram
Laboratory of Neural Microcircuitry
Brain Mind Institute
Ecole Polytechnique Fédérale de Lausanne
Lausanne (EPFL)
CH-1015
Switzerland
Email: henry.markram@epfl.ch

SUMMARY

The general structure of the mammalian neocortex is remarkably similar across different cortical areas. Despite certain cytoarchitectural specializations and deviations from the general blueprint, the principal organization of the neocortex is relatively uniform. It is not known, however, to what extent stereotypic synaptic pathways resemble each other between cortical areas, and how far they might reflect possible functional uniformity or specialization. Here, we show that frequency-dependent disynaptic inhibition (FDDI) is a generic circuit motif that is present in all neocortical areas we investigated (primary somatosensory, auditory and motor cortex, secondary visual cortex and medial prefrontal cortex of the developing rat). We did find, however, area-specific differences in occurrence and kinetics of FDDI and the short-term dynamics of monosynaptic connections between pyramidal cells (PCs). Connectivity between PCs, both monosynaptic and via FDDI, is higher in primary cortices. The long-term effectiveness of FDDI is likely to be limited by an activity-dependent attenuation of the PC–interneuron synaptic transmission. Our results suggest that the basic construction of neocortical synaptic pathways follows principles that are independent of modality or hierarchical order within the neocortex.

INTRODUCTION

The mammalian neocortex consists of dozens of functional areas that are engaged in a variety of different tasks, ranging from the integration of primary sensory information to memory storage and high-level cognitive processing. Given this wide range of functions, its general design is relatively homogeneous between different cortical areas. In its standard form, the mammalian neocortex is a continuous six-layered structure, and shows, depending on the specific area, a more or less pronounced modular organization termed the cortical column. The ratio between excitatory (spiny stellate and pyramidal) neurons and inhibitory (local circuit) neurons is relatively constant (~80 to 20%) (Braitenberg & Schüz, 1998), and the distribution of many though not all visualizable molecular markers is relatively homogeneous (Dong, 2007). Neuron types are layer-specific rather than area-specific, and as a consequence cortical areas have been mainly defined according to their interconnections with other cortical or subcortical regions. Another aspect that distinguishes cortical areas quantitatively is the thickness of the individual layers and correspondingly the cell density per layer and column (DeFelipe *et al.* 2002), and the neocortical cytoarchitectural specializations have also been used to classify different areas for over 100 years (Brodmann, 1909).

Much less is known about the area-specific physiology and dynamics of specific synaptic pathways, and to what extent they might reflect or define the function of a cortical area. Thick-tufted layer 5 pyramidal cells (PCs) are one of the principal output neurons of the cortex and are among the cortical cell types that are investigated in greatest detail (Markram *et al.* 1997; Spruston, 2008). They are interconnected with glutamatergic synapses that are mainly formed on basal and oblique dendrites and display depressing short-term dynamics in juvenile rodents. Recently, the direct recruitment of inhibitory synaptic potentials from intermediate interneurons induced by PC activity has received special attention (Kapfer *et al.* 2007; Ren *et al.* 2007; Silberberg & Markram, 2007; Molnár *et al.* 2008). Frequency-dependent disynaptic inhibition (FDDI) has been shown to be an important dynamic and activity-dependent synaptic pathway in layer 5 and layer 2/3 of the primary somatosensory cortex (Kapfer *et al.* 2007; Silberberg & Markram, 2007). High frequency spiking (~70 Hz) in a single PC can lead, via a strongly facilitating synapse, to suprathreshold activity in specific nearby interneurons, e.g. the Martinotti

cell. These cells in turn project back to the pyramidal cell population and preferentially inhibit the apical and tufted dendrites (Silberberg & Markram, 2007).

In the present study we investigate five different cortical areas in juvenile rats by comparing their monosynaptic excitatory (direct EPSPs) and FDDI connectivity between large layer 5 pyramidal cells. We show that FDDI is a generic inhibitory pathway existing in all investigated cortical areas, with a prevalence which is more than double that of monosynaptic excitatory connections and with kinetics that exhibit area-specific differences. FDDI has a lateral extent comparable to monosynaptic excitatory connectivity, and also drops in amplitude in a similar way. FDDI becomes weaker or disappears after repetitive high frequency stimulation, with the fatigue of the PC–interneuron synapse as one possible reason.

METHODS

Slice preparation. Experiments were carried out according to the Swiss national and institutional guidelines and comply with *The Journal's* policies and regulations (Drummond, 2009). Fourteen- to 18-day-old, non-anaesthetized Wistar rats were quickly decapitated and their brains carefully removed and placed in iced artificial cerebrospinal fluid (ACSF). Slices (300 μm) were cut on an HR2 vibratome (Sigmann Elektronik, Heidelberg, Germany). Parasagittal slices, approximately 1.7–2.2mm lateral to the midline, were cut to access primary somatosensory cortex (SSC, above the anterior extremity of the hippocampus \pm 1 mm), primary motor cortex (MC, 2–4mm anterior to the hippocampus), or secondary visual cortex (VC2, 3–5mm posterior) (Fig. 1A) (Sherwood & Timiras, 1970; Paxinos & Watson, 1998). Slices of primary auditory cortex (AC, approximately 2mm dorsal to the rhinal fissure) and also VC2 (\sim 4mm lateral to the midline) were obtained by coronal slices, rostrocaudally positioned where the corpus callosum (CC) joins the two hemispheres and the hippocampus completely ‘encloses’ subcortical structures (around bregma – 4.8 mm). Slices of medial prefrontal cortex (mPFC) were coronally cut, rostrocaudally positioned where the CC was already visible but not yet joined (around bregma+2.5 mm). Slices were incubated at 37°C for 30–60 min and then left at room temperature until recording. Cells were visualized by infrared differential interference

contrast videomicroscopy utilizing either a C2400-03 camera (Hamamatsu, Hamamatsu City, Japan) mounted on an upright Axioscope FS microscope (Zeiss, Oberkochen, Germany), or a VX55 camera (Till Photonics, Gräfeling, Germany) mounted on an upright BX51WI microscope (Olympus, Tokyo, Japan). Thick-tufted layer 5 PCs were selected according to their large soma size (15–25 μm) and their apparent large trunk of the apical dendrite. Care was taken to use only ‘parallel’ slices, i.e. slices that had a cutting plane parallel to the course of the apical dendrites and the primary axonal trunk. This ensured sufficient preservation of both the PCs’ axonal and dendritic arborizations.

Chemicals and solutions. Slices were continuously superfused with ACSF containing (in mM) 125 NaCl, 25 NaHCO₃, 2.5 KCl, 1.25 NaH₂PO₄, 2 CaCl₂, 1 MgCl₂, and 25 D-glucose, bubbled with 95% O₂–5% CO₂. The intracellular pipette solution contained (in mM) 110 potassium gluconate, 10 KCl, 4 ATP-Mg, 10 phosphocreatine, 0.3 GTP, 10 *N*-2-hydroxyethylpiperazine-*N'*-2-ethanesulfonic acid (Hepes), and 13 biocytin, adjusted to pH 7.3–7.4 with 5 M KOH. Osmolarity was adjusted to 290–300 mosmol l⁻¹ with D-mannitol (25–35mM). The membrane potential values given were not corrected for the liquid junction potential, which was approximately –14 mV. Chemicals were from Sigma Aldrich (Steinheim, Germany) or Merck (Darmstadt, Germany). The endocannabinoid receptor antagonist AM251 was from Tocris (Ellisville,MO, USA).

Electrophysiological recordings. Multiple somatic whole cell recordings (2–12 cells simultaneously) were performed with Axopatch 200B or Multiclamp 700B amplifiers (Molecular Devices, Union City, CA, USA) in the current clamp mode at 34±1°C bath temperature. Data acquisition was performed via an ITC-18 or ITC-1600 board (Instrutech Co., Port Washington, NY, USA), connected to a PC or Macintosh running a custom-written routine under IGOR Pro (Wavemetrics, Portland, OR, USA). Sampling rates were 5–10 kHz, and the voltage signal was filtered with a 2 kHz Bessel filter. Patch pipettes were pulled with a Flaming/Brown micropipette puller P-97 (Sutter Instruments Co., Novato, CA, USA) and had an initial resistance of 3–8M Ω .

Stimulation protocols. Monosynaptic, direct excitatory connections were identified by stimulation of a presynaptic cell with a 20 Hz train of eight strong and brief current pulses (1–3.5

nA, 2–4 ms), followed by a so-called recovery test response 0.5 s after the end of the train, all precisely and reliably eliciting action potentials (APs). Disynaptic connections (FDDI) were characterized by the same protocol but at a higher frequency (70 Hz) and 15 APs. Occasionally, postsynaptic PCs were slightly depolarized from a potential of ~ -62 mV to -58 to -60 mV to increase the driving force for inhibitory connections. This resulted in slightly larger amplitudes, but was usually not necessary to detect FDDI. It has been previously shown that FDDI is based on a GABA_A conductance (Silberberg & Markram, 2007). Although the intracellular and extracellular chloride concentrations amount to a reversal potential of ~ -68.6 mV, we observed hyperpolarizing somatic currents. This was probably due to the location of the interneuron–PC synapses at distant locations of the apical dendrite, which has been reported to have a more depolarized membrane potential (Stuart & Spruston, 1998; Berger *et al.* 2001).

Data analysis. Connectivity ratios, both for monosynaptic excitatory and FDDI, were calculated as the ratio between observed *versus* tested connections between a pair of cells. A pair of cells could therefore maximally have two connections (both directions), a triplet could have six connections, and a cluster of n neurons could potentially have $n(n - 1)$ connections. The error bars of the connectivity ratios express, based on the binomial distribution, the standard error of the mean (S.E.M.) estimate according to $S.E.M. = (P(1 - P)/(n - 1))^{1/2}$, with P being the observed (estimated) connectivity ratio (probability of connection) and n the number of tested connections (Zar, 1999). For analysis of the kinetics of FDDI and monosynaptic excitation (EPSPs), the membrane potential baseline V_{bl} was calculated as the average membrane potential V_m 1–99 ms prior to stimulation onset (see Figs 4C and 5C). Both FDDI and EPSPs were detected visually based on the mean response of 10–50 repetitions, corresponding roughly to a crossing of V_{bl} plus 3–7 times the standard deviation of V_{bl} . Due to noise, extraction of kinetic parameters for events equal to or smaller than 0.1–0.15 mV was barely possible and those results were then not included in the analysis. They were, however, taken into account for estimation of the connectivity ratios. Some experiments in the SSC were also used in a different context for a study on summation properties of disynaptic connections (unpublished observations), and not all SSC connections were used for the kinetic analysis of EPSPs and FDDIs (260 out of 667 monosynaptic excitatory and 679 out of 1383 FDDI connections). FDDI ‘contaminated’ with monosynaptic excitatory connections were also excluded from the kinetic analysis. FDDI

amplitude was extracted as the difference between the minimal voltage V_{peak} 0.06–0.4 s after stimulation onset t_{stim} and V_{bl} . The slope of the rising phase of FDDI was calculated linearly between 20 and 80% of the amplitude. The intersection of this line and the baseline was taken as the response onset time t_{onset} . The slope of the decaying phase and FDDI offset were calculated accordingly. FDDI symmetry, describing the position of the V_{peak} relative to onset and offset, was calculated as $(t_{\text{peak}} - t_{\text{onset}})/(t_{\text{onset}} - t_{\text{offset}})$. The overshoot was the maximal voltage reached within 0.2 s after t_{peak} , relative to V_{bl} . EPSP amplitude was extracted as the difference between the maximal voltage V_{peak} 3–18 ms after stimulation onset and V_{bl} (Fig. 5C). Stimulation onset t_{stim} was defined as the time of the peak of the presynaptic AP. For the 2nd to 8th EPSPs, V_{bl} was calculated from 1 to 2 ms prior to t_{stim} . The EPSP rising phase was calculated between 20 and 80% of the amplitude, τ_{rise} was a single exponential fit between 0 and 100%. Time to peak was the difference between t_{peak} and t_{stim} . Paired pulse ratio (PPR) was defined as the ratio between second and first EPSP amplitude. All analysis on synaptic kinetics was performed with IGOR Pro. Synaptic short-term dynamics were fitted with a phenomenological model (Markram *et al.* 1998), giving estimates for release probability: utilization (U), absolute synaptic efficacy (A_{se}), recovery from depression (D), and synaptic facilitation (F). Statistical analysis and model fitting were performed with MATLAB using the Kruskal–Wallis test followed by Dunn’s method for multiple comparisons with a significance level of $\alpha=0.01$ or 0.05 (Zar, 1999). Distance-dependent connectivity ratios were fitted with a Gaussian with the standard deviation σ as the only free parameter since it gave better results than an exponential fit (FDDI, Gaussian fit with $\sigma=290 \mu\text{m}$, $\chi^2_{\text{Gauss}}=0.53$, as compared with single exponential fit with $\lambda=221 \mu\text{m}$, $\chi^2_{\text{exp}}=0.76$; EPSPs, Gaussian fit with $\sigma=265 \mu\text{m}$, $\chi^2_{\text{Gauss}}=0.58$, as compared with single exponential fit with $\lambda=211 \mu\text{m}$, $\chi^2_{\text{exp}}=0.60$). Distance-dependent amplitudes were fitted with single exponentials.

RESULTS

We recorded from 1584 PCs (SSC, 1193; MC, 40; AC, 56; VC2, 170; mPFC, 125) in 367 slices of 163 rats aged between 14 and 18 days (mean 15 days). Two to 12 thick-tufted/large layer 5 PCs were patched simultaneously, with one cell stimulated and the other remaining cells passively recorded in order to observe possible synaptic connections. In some cases step currents

(1.5 s, \sim -300 to 500 pA) were injected to characterize the intrinsic properties of the cells (Figure 1B). All cells were continuous or sometimes burst-regular spiking, and showed a typical sag in response to a hyperpolarizing step current. Two different protocols were applied to investigate synaptic connectivity between PCs (exemplified in Fig. 1). A 20 Hz train revealed short-term dynamics and kinetics of the excitatory connection between two directly connected PCs (Fig. 1C). FDDI, mediated via an intermediate interneuron such as the Martinotti cell, was triggered and analysed with a 70 Hz train of 15 APs (Fig. 1D). Biphasic responses were seen when both pathways were present and stimulation frequency was sufficiently high (Fig. 1E). These cases were not analysed any further in the current study, although they were still included in the FDDI connectivity count.

Table 1. Kinetics of FDDI

	SSC ($n = 363$)	MC ($n = 41$)	AC ($n = 46$)	VC2 ($n = 119$)	mPFC ($n = 67$)	KW test, Dunn $P < 0.01$	KW test, Dunn $P < 0.05$
Amplitude (mV)	-0.718 ± 0.488	-0.651 ± 0.427	-1.518 ± 0.787	-0.971 ± 0.796	-0.558 ± 0.271	3-1,2,4,5 4-5	3-1,2,4,5 4-5
Onset (s)	0.107 ± 0.043	0.193 ± 0.062	0.190 ± 0.032	0.195 ± 0.053	0.185 ± 0.030		1-5
Slope rise (mV ms^{-1})	-0.010 ± 0.008	-0.009 ± 0.006	-0.023 ± 0.015	-0.012 ± 0.011	-0.009 ± 0.006	3-1,2,4,5	3-1,2,4,5
Slope decay (mV ms^{-1})	0.007 ± 0.005	0.006 ± 0.005	0.012 ± 0.007	0.006 ± 0.006	0.004 ± 0.003	3-1,2,4,5 1-5	3-1,2,4,5 1-4,5
Symmetry	0.448 ± 0.114	0.426 ± 0.124	0.396 ± 0.098	0.379 ± 0.133	0.374 ± 0.137	1-4,5	1-3,4,5
Overshoot (mV)	0.083 ± 0.116	0.101 ± 0.122	0.107 ± 0.107	0.017 ± 0.179	0.066 ± 0.088	4-1,3	4-1,2,3

Kinetic parameters of FDDI for SSC, MC, AC, VC2 and mPFC as displayed in Fig. 4 (means \pm s.d.). Statistically significant differences between individual areas, tested with Kruskal-Wallis (with $\alpha < 0.01$ and $\alpha < 0.05$ significance level) followed by Dunn's method for multiple comparisons, are shown in the two rightmost columns.

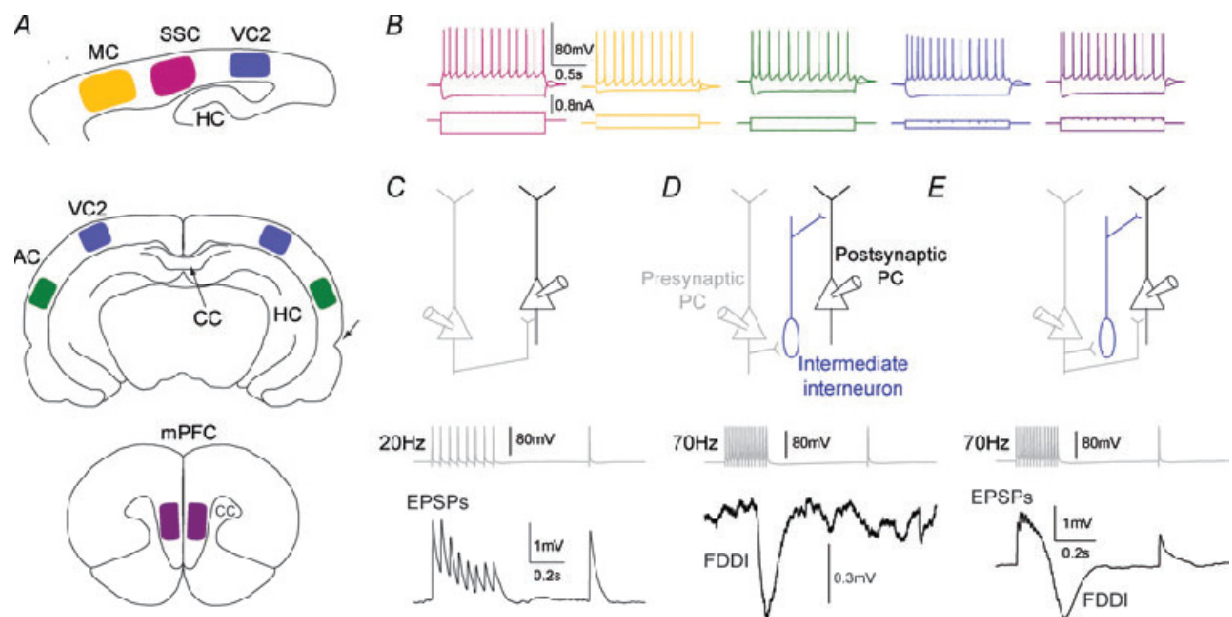


Figure 1 Cortical areas and stimulation protocols. (A) cortical areas that have been investigated. Top, parasagittal slice with primary motor cortex (yellow, MC), primary somatosensory cortex (pink, SSC), and secondary visual cortex (blue, VC2). Hippocampus abbreviated as HC. Middle, coronal slice with VC2 and primary auditory cortex (green, AC). Intact corpus callosum (CC) and rhinal fissure are indicated by arrows. Bottom, coronal slice with medial prefrontal cortex (purple, mPFC). (B) firing pattern and hyperpolarizing voltage response to de- and hyperpolarizing step currents. All cells were continuous or burst-regular spiking. (C) two pyramidal cells (PCs), directly interconnected. The presynaptic cell was stimulated with an 8 spike–20 Hz train plus recovery test pulse 0.5 s later in order to determine EPSP kinetics and short-term dynamics. (D) two PCs interconnected via a single (or multiple) interneuron(s). High frequency stimulation in the presynaptic PC (15 spikes, 70 Hz) elicits suprathreshold activity in a nearby interneuron, which in turn gives rise to FDDI in a neighbouring PC. (E) two PCs connected with both monosynaptic EPSPs and FDDI.

FDDI is a generic sub-circuit of the neocortex

FDDI was present between large layer 5 PCs in all investigated cortical areas (Fig. 2A; SSC, MC, AC, VC2 and mPFC). The dynamics of excitatory connections between PCs were always dominated by synaptic depression, with the exception of responses in the mPFC that had a facilitatory component as well (Fig. 2B). The connectivity rate (ratio between observed connections and tested connections) of disynaptic inhibition ranged between 21% (mPFC) and 40.6% (AC), and was always more than double the monosynaptic excitatory connectivity ratio in each area, which ranged between 5.4 and 18% (Fig. 2C and D).

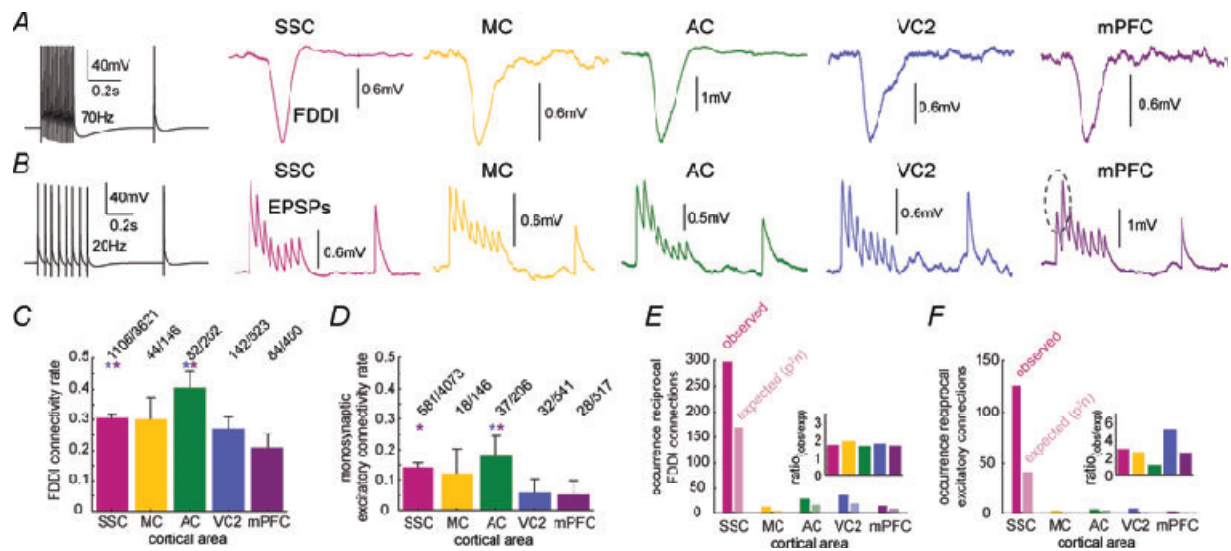


Figure 2 Connectivity ratios of FDDI and EPSPs in different cortical areas. (A) high frequency stimulation (70 Hz) of a PC and examples of responses in a postsynaptic PC in SSC, MC, AC, VC2 and mPFC. (B) 20 Hz stimulation of a PC and examples of responses in a postsynaptic PC in the same cortical areas as in A. (C) FDDI connectivity rate between PCs in the investigated cortical areas. Highly significant differences were found between some areas (PSSC–AC = 0.0027, PSSC–mPFC = 7.24×10^{-5} , PAC–VC2 = 4.44×10^{-4} , PAC–mPFC = 3.78×10^{-7} , two-sided χ^2 test). (D) monosynaptic excitatory connectivity between PCs in the investigated cortical areas. Significant differences were found between primary (SSC, MC, AC) and non-primary (VC2, mPFC) cortices (PSSC–VC2 = 7.6×10^{-8} , PSSC–mPFC = 2.3×10^{-8} , PMC–VC2 = 0.0081, PMC–mPFC = 0.0037, PAC–VC2 = 3.74×10^{-7} , PAC–mPFC = 1.02×10^{-7} , two-sided χ^2 test). (E) occurrence of reciprocal FDDI connections between PCs in the investigated cortical areas. Expectancy was calculated as P^2n . Inset shows the ratio between observed and expected occurrences. (F) occurrence of reciprocal monosynaptic excitatory connections between PCs in the investigated cortical areas. Color code as in Fig. 1. Error bars in C and D denote S.E.M.

Interestingly, several monosynaptic excitatory connectivity ratios were significantly higher in primary areas such as SSC and AC than in VC2 or mPFC (two-sided χ^2 test of a contingency table followed by Tukey-type multiple comparison testing for proportions (Zar, 1999); $P < 0.01$ for SSC–mPFC, SSC–VC2, AC–mPFC, AC–VC2). There were also highly significant differences between some areas for FDDI connections ($P < 0.01$ for SSC–mPFC, AC–mPFC, and AC–VC2; $P < 0.05$ for AC–SSC). We did not find significant differences between MC and any other cortical area, which is possibly due to the relatively small sampling size in MC. Reciprocal connections, that is, cell A projecting to cell B and vice versa, are displayed in Fig. 1E and F. Given the observed connectivity rates for single connections one can estimate how many reciprocal connections one expects to find assuming random network statistics (expected). For example, monosynaptic excitatory reciprocal connections between PCs have

been reported to be more frequent than expected in SSC and VC (Markram *et al.* 1997; Song *et al.* 2005; but see Lefort *et al.* 2009). The actual observed reciprocal FDDI connectivity rates were 1.68–1.96 times higher than expected. For excitatory connections, the discrepancy in connectivity rates between observed and expected and also between the different areas was higher (ranging from 1.2 in AC to 5.28 in VC), possibly also due to a smaller sampling size.

The remarkably high connectivity rates in the auditory cortex are illustrated in Fig. 3. The example shows a seven-cell cluster that featured 4 monosynaptic excitatory and 30 disynaptic inhibitory connections (Fig. 3A). Thus, in this particular cluster, the connectivity ratios were $4/42=9.5\%$ and $30/42=71.4\%$, respectively. Interestingly, the FDDI connectivity between cells 1–6 is complete, that is, each cell is connected to each other (Fig. 3A and B). Cell 7 was not involved in this inhibitory circuit with the stimulation protocol used. As can be seen in the connectivity matrix, FDDI responses varied considerably in amplitude and kinetics, and these parameters are illustrated in Fig. 4 and summarized in Table 1 for the different investigated areas.

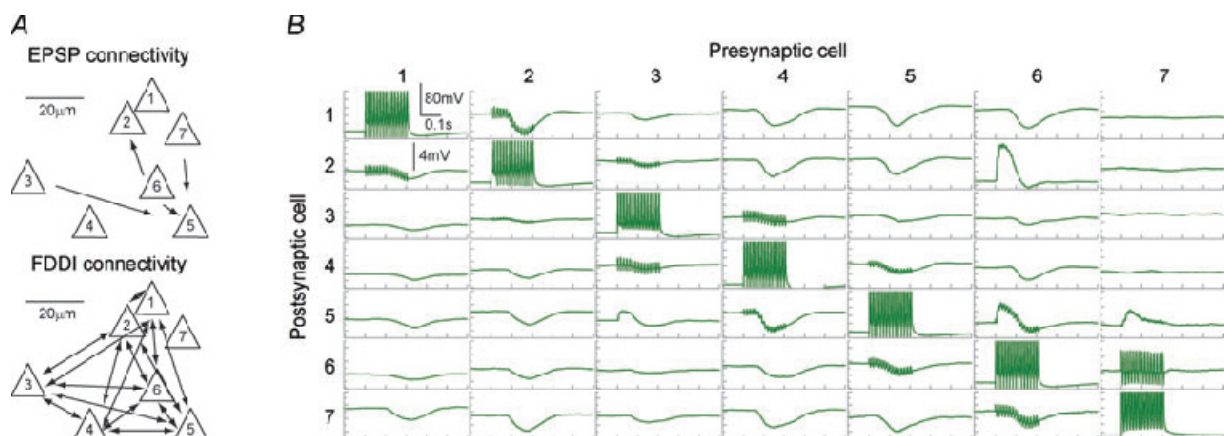


Figure 3 Seven-cell cluster example in AC. (A) relative somatic positions of seven simultaneously patched cells and their connectivity in the AC. Cell 5 received monosynaptic excitatory input from cells 3, 6 and 7, and cell 2 received input from cell 6. Cells 1–6 were all interconnected with FDDI. **(B)** matrix of the membrane potentials of all seven cells in response to high frequency stimulation. Postsynaptic voltage response to a presynaptic stimulation (on the diagonal) is shown in the corresponding row. Electrodes (cells) next to the stimulated electrode (on the secondary diagonals in the matrix) show stimulation artifacts in the voltage trace.

Fifteen APs at 70 Hz were elicited in a presynaptic PC, and the FDDI response was recorded in the postsynaptic cell (Fig. 4A and B). Note that the exact number of interneurons mediating this response is not known. Six different parameters have been extracted from this compound inhibitory potential (Fig. 4C; see also Methods). FDDI in the auditory cortex seems to stand out. Here, we find the largest average amplitudes (-1.52 ± 0.79 mV), and the fastest rise and decay slopes (-0.02 ± 0.02 mV ms⁻¹ and 0.01 ± 0.01 mV ms⁻¹, Fig. 4D, F and G), rendering the response properties of auditory PCs most transient. A possible explanation for large amplitudes could be a more negative chloride reversal potential in PCs of the auditory cortex compared with other areas. We therefore determined the reversal potential of FDDI in auditory cortex by current clamping the postsynaptic PC to various hyperpolarized potentials while stimulating a FDDI-mediating PC. We found an average reversal potential in AC of -76.04 ± 7.72 mV ($n = 5$), which is remarkably similar to values obtained in the SSC by Silberberg and colleagues using the same intra and extracellular solutions (-78.9 ± 10.3 mV, $n = 55$; Silberberg & Markram, 2007). Thus, it is unlikely that a larger chemical gradient of chloride ions is responsible for large FDDI amplitudes in AC.

The onset (Fig. 4E) was remarkably homogeneous between all areas, indicating that the excitability of the intermediate interneurons by PCs is likely to be relatively similar. Alternatively, excitability and the kinetics of the participating synaptic pathways could vary between the different areas while being tuned to match certain onset timing. The symmetry of FDDI represents the relative position of the peak response with regard to its onset and offset. A perfectly symmetrical response would have a symmetry value of 0.5. But a typical postsynaptic potential (PSP), for example, has a much faster rise time constant than decay time constant, and therefore its response peak is very close to the beginning of the PSP, giving symmetry values of close to 0. On the contrary, FDDI is in general in all areas far more symmetric, yielding values between 0.37 ± 0.14 (mPFC) and 0.45 ± 0.11 (SSC), with the SSC significantly different from VC2 and mPFC. These high values can be explained by the abundance of the cationic H-current (I_h) in the apical and tufted dendrites in PCs, leading to a fast depolarization, milliseconds after stimulus onset (Silberberg & Markram, 2007). The same current is also responsible for the overshoot, a depolarization following the hyperpolarizing FDDI signal. It does not occur in every

connection, and especially in VC2 it seems to be frequently lacking (0.02 ± 0.18 mV), showing highly significant differences from SSC and mPFC (0.08 ± 0.12 mV and 0.07 ± 0.09 mV).

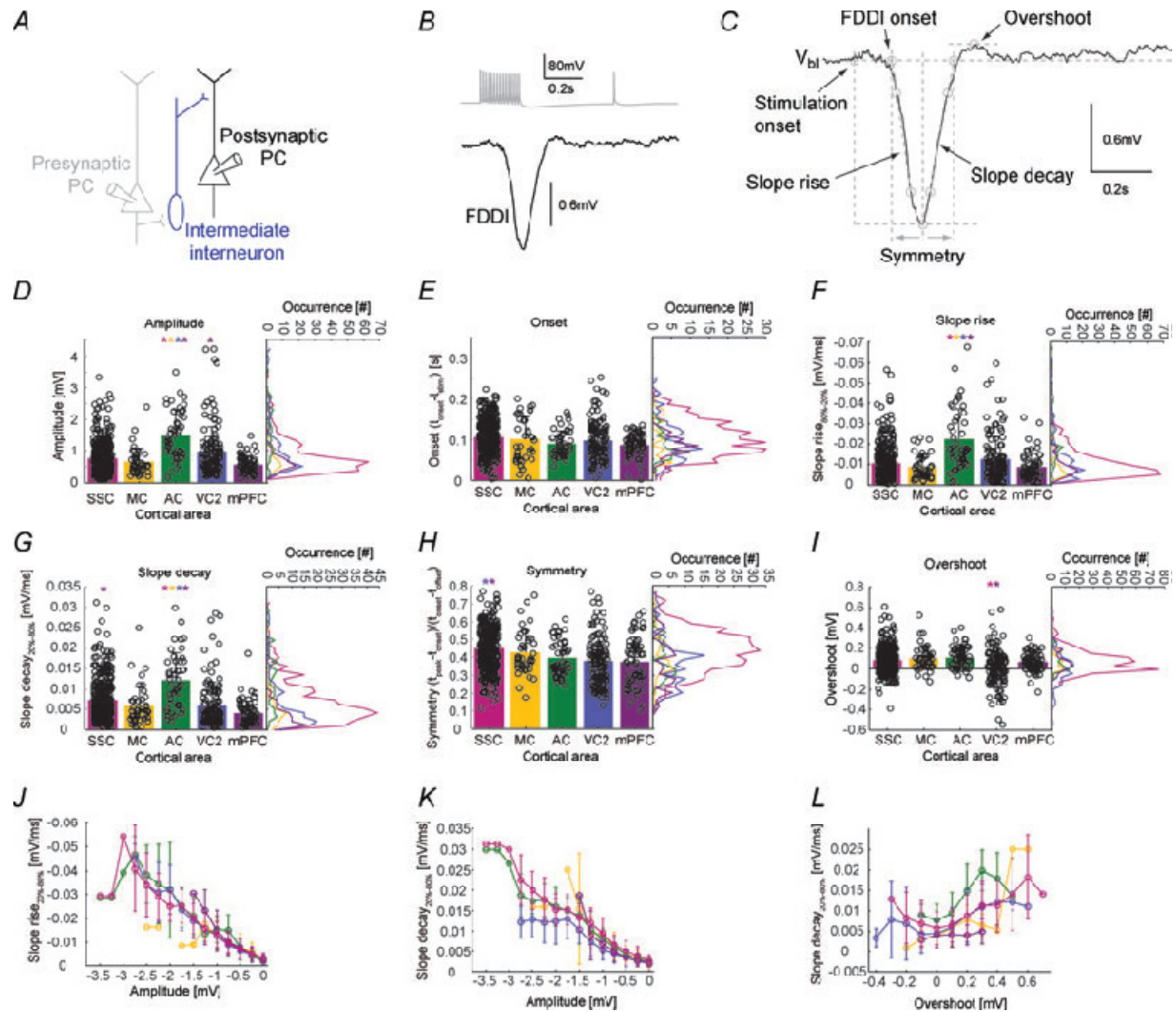


Figure 4 Area-specific kinetics of FDDI. (A) a presynaptic PC (grey), connecting to an interneuron (blue), in turn innervating a postsynaptic PC (black). (B) stimulation of the presynaptic PC leading to FDDI in the postsynaptic PC. (C) parameters extracted from the disynaptic inhibitory response. (D–I) amplitude, onset time ($t_{\text{onset}} - t_{\text{stim}}$), slopes of the rising and decaying phases, symmetry ($(t_{\text{peak}} - t_{\text{onset}})/(t_{\text{onset}} - t_{\text{offset}})$) and overshoot of the FDDI response. Colour code corresponds to areas depicted in Fig. 1. Bar graphs show the mean, black circles individual data points (scattered for better illustration). Vertical histograms contain 31 equally spaced bins. See Methods for a detailed description of the parameter extraction. Error bars denote standard deviation. Only highly significant differences ($P < 0.01$), colour coded (in one direction for a pair) are marked with an asterisk (Kruskal–Wallis test followed by Dunn’s method for multiple comparisons, see Table 1). (J) slope rise time as a function of FDDI amplitude. (K) slope decay time as a function of FDDI amplitude. (L) slope decay time as a function of overshoot. For J–L, abscissa was

divided into 15 (J and K), or 12 (L) equally spaced bins. Colour coding for the different areas as in the histograms.

FDDI with large amplitudes had fast rise and decay times in all investigated cortical areas (Fig. 4J and K). The mean correlation coefficients were -0.82 ± 0.06 and 0.73 ± 0.15 , respectively. Therefore, the multiple differences found between AC and other cortices might reflect a single specialization of this circuitry in AC, e.g. larger unitary IPSPs produced by the interneuron–PC synapse. We also find dependence between decay time and overshoot (Fig. 4L, correlation coefficient 0.40 ± 0.20). Decay time and overshoot depend on I_h (Silberberg & Markram, 2007), so the expression of this current should have a similar impact on both of them.

Similar kinetics but different short-term dynamics of EPSPs between PCs

The properties of monosynaptic excitatory connections between PCs were elucidated using 8 APs–20Hz stimulation trains (Fig. 5A and B). Four kinetic parameters of the first EPSP were extracted (Fig. 5C). Amplitude, 20–80% rise time, and time to peak do not show a strong area specificity (Fig. 5D and E, Table 2). Only the single exponential fit to the rising phase, τ_{rise} , shows significant differences (mPFC vs. SSC and MC, VC2 vs. MC, Table 2). In contrast, short-term dynamics show some more diversity between the areas, especially regarding connections in the mPFC. The paired pulse ratio (PPR) between the second and the first EPSP is significantly higher ($P < 0.01$) in mPFC (0.97 ± 0.41) compared to all other areas (SSC, 0.62 ± 0.23 ; AC, 0.66 ± 0.41 ; MC, 0.55 ± 0.08 ; and VC2, 0.58 ± 0.24 ; Figs 2B and 5F, Table 2).

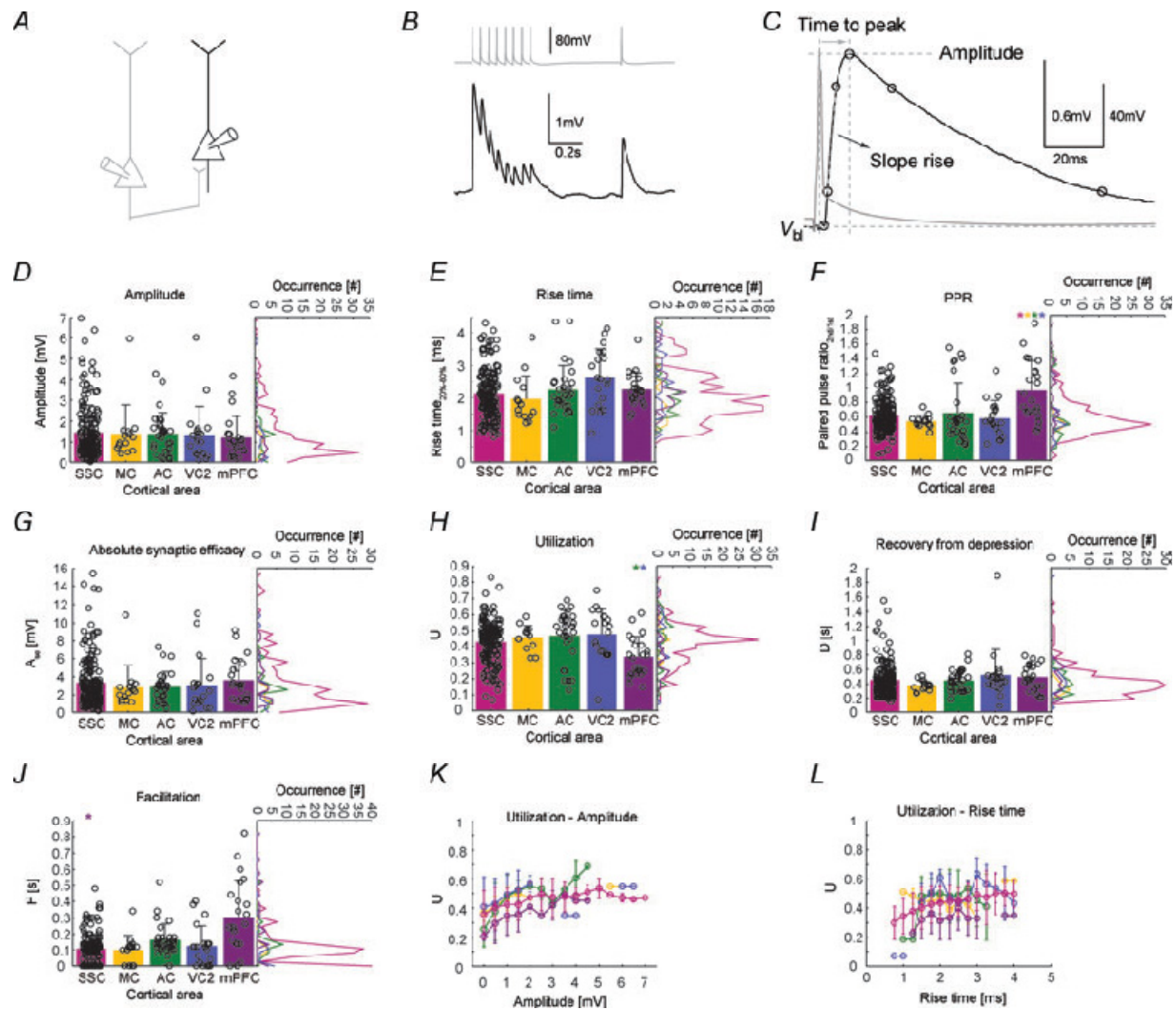


Figure 5 Area-specific kinetics of EPSPs and short term dynamics of EPSP trains (A) a presynaptic PC (grey) connecting to a postsynaptic PC (black). **(B)** stimulation of the presynaptic PC leading to EPSPs in the postsynaptic PC. **(C)** parameters extracted from the monosynaptic excitatory response. **(D)** and **(E)** amplitude and 20–80% rise time of the first EPSP in the train. **(F)** paired pulse ratio of 2nd over 1st EPSP amplitude. **(G–J)** parameters extracted from a fit to a model of synaptic dynamics: bar graphs show the mean, black circles individual data points (scattered for better illustration). Vertical histograms contain 31 equally spaced bins. See Methods for a detailed description of the parameter extraction. Error bars denote standard deviation. Only highly significant differences ($P < 0.01$), colour coded (in one direction for a pair) are marked with an asterisk (Kruskal–Wallis test followed by Dunn’s method for multiple comparisons, see Table 2). **(K–L)** utilization as a function of amplitude and rise time. Abscissa was divided into 15 (K) or 17 (L) equally spaced bins. Colour coding for the different areas as in the histograms.

The increased PPR in mPFC is caused by a reduced release probability, reflected in the low utilization (U) value of the model fit of synaptic dynamics (mPFC, 0.34 ± 0.13) compared to

most other areas ($P < 0.01$ with AC, 0.47 ± 0.16 , and VC2, 0.48 ± 0.16 ; $P < 0.05$ with SSC, 0.43 ± 0.13 , Fig. 5H). Further, the facilitation time constant F is significantly higher in mPFC (mPFC, 0.301 ± 0.230 s) compared with other areas ($P < 0.01$, with SSC, 0.110 ± 0.086 s; $P < 0.05$, with MC, 0.102 ± 0.089 s, and VC2, 0.125 ± 0.125 s, Fig. 5J). F is also different between SSC and AC ($P < 0.05$, 0.110 ± 0.086 s and 0.165 ± 0.097 s, respectively). Recovery from depression (Fig. 5I) and absolute synaptic efficacy (Fig. 5G) show no significant differences between the areas. Thus, the synaptic dynamics of direct connections in the mPFC seem to be most dissimilar due to their low initial release probability. We find some dependencies between kinetics and short-term dynamics parameters as illustrated by Fig. 5K and L. Large-amplitude synapses also had a high utilization parameter (Fig. 5K), which is reflected in a positive correlation coefficient in all areas (0.38 ± 0.16 ; for SSC, 0.29). This indicates that large-amplitude synaptic connections are not only strong *per se*, but they also have a high release probability (which is equivalent to the utilization parameter in the synaptic dynamics model). We also find a correlation between 20–80% rise time and utilization (Fig. 5L, correlation coefficient 0.16 ± 0.17 , for SSC, 0.33) which was unexpected.

Table 2. Kinetics and short-term dynamics of monosynaptic EPSPs

	SSC ($n = 171$)	MC ($n = 14$)	AC ($n = 29$)	VC2 ($n = 20$)	mPFC ($n = 22$)	KW test, Dunn, $P < 0.01$	KW test, Dunn, $P < 0.05$
Amplitude (mV)	1.460 ± 1.291	1.399 ± 1.373	1.397 ± 1.011	1.346 ± 1.352	1.223 ± 1.028		
Rise time (ms)	2.122 ± 0.751	1.952 ± 0.743	2.249 ± 0.757	2.628 ± 0.882	2.262 ± 0.521		
τ_{rise} (ms)	2.377 ± 0.860	1.932 ± 0.525	2.675 ± 0.988	3.034 ± 0.972	3.163 ± 0.856	2–4,5 1–5	2–4,5 1–4,5
Time to peak (ms)	8.072 ± 2.286	7.993 ± 3.125	8.288 ± 1.965	8.930 ± 2.807	8.309 ± 2.022		
PPR	0.623 ± 0.228	0.545 ± 0.082	0.659 ± 0.411	0.583 ± 0.243	0.970 ± 0.407	5–1,2,3,4	5–1,2,3,4
A_{se} (mV)	3.340 ± 2.857	2.818 ± 2.428	2.865 ± 1.687	3.064 ± 2.932	3.624 ± 2.352		
U	0.431 ± 0.126	0.460 ± 0.075	0.470 ± 0.157	0.479 ± 0.155	0.337 ± 0.126	5–3,4	5–1,3,4
D (s)	0.452 ± 0.217	0.374 ± 0.072	0.446 ± 0.140	0.518 ± 0.353	0.491 ± 0.178		
F (s)	0.110 ± 0.086	0.102 ± 0.089	0.165 ± 0.097	0.125 ± 0.125	0.301 ± 0.230	5–1	5–1,2,4 1–3

Kinetic parameters of direct EPSPs for SSC, MC, AC, VC2 and mPFC as displayed in Fig. 5 (means \pm s.d.). Statistically significant differences between individual areas, tested with Kruskal–Wallis (with $\alpha < 0.01$ and $\alpha < 0.05$ significance level) followed by Dunn's method for multiple comparisons, are shown in the two rightmost columns. PPR, paired pulse ratio. A_{se} , absolute synaptic efficacy; U , utilization; D , recovery from depression; F , synaptic facilitation (see methods).

Distance-dependent drop of connectivity

The SSC connectivity data presented so far include only cell pairs that are of equal or less than $150\ \mu\text{m}$ intersomatic distance. In order to investigate the spatial extent of FDDI and monosynaptic excitatory connectivity, we recorded from laterally spread PCs in SSC and investigated the distance dependence of synaptic parameters. Figure 6A and B show the distance-dependent occurrence of FDDI and monosynaptic excitatory connections, respectively. As can be seen in the insets, the connectivity rates are relatively stable for the first $100\text{--}150\ \mu\text{m}$ (binning was $25\ \mu\text{m}$), and then drop towards zero.

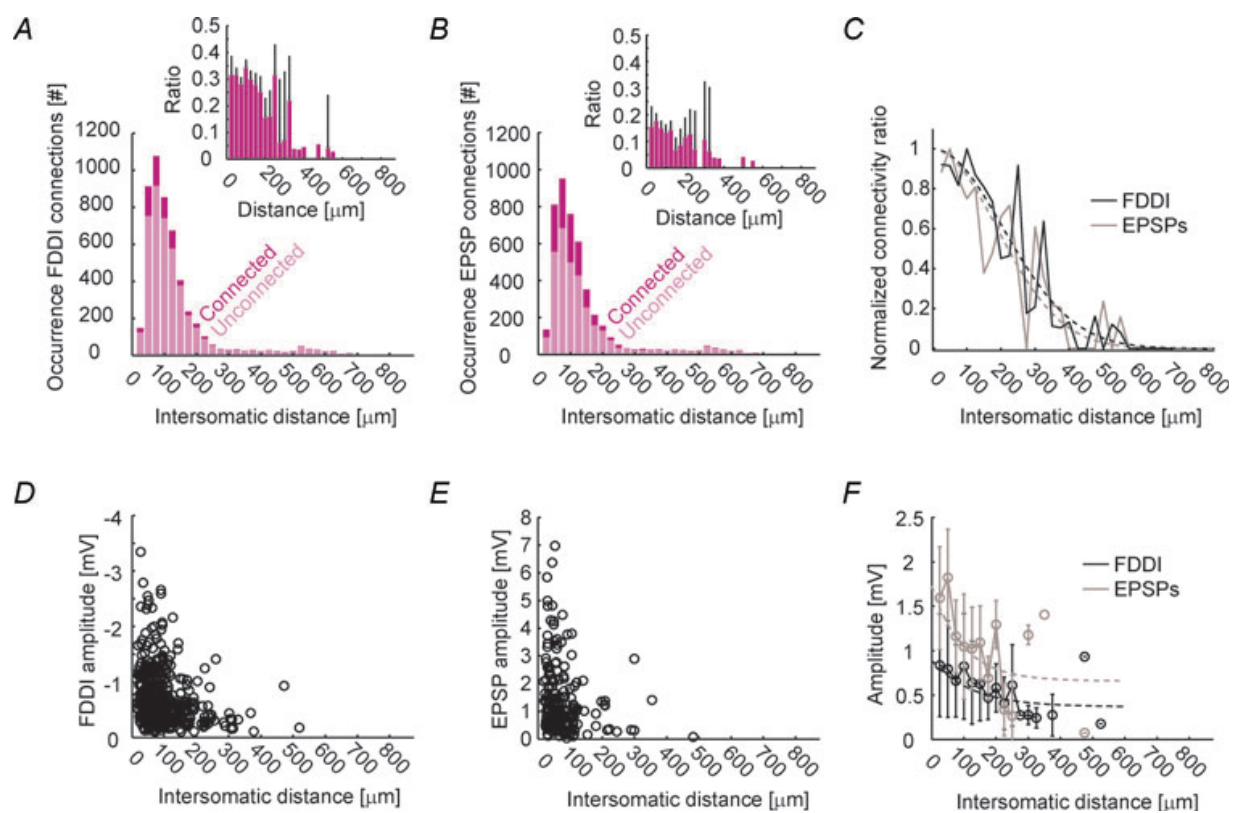


Figure 6 Distance-dependent drop of connectivity (A) occurrence of FDDI connections as a function of the intersomatic distance of two PCs. Light pink shows the number of unconnected pairs, dark pink the number of connected pairs. Inset shows the ratio of connected over unconnected pairs. Binning was in $25\ \mu\text{m}$ steps. **(B)** occurrence of monosynaptic connections as a function of the intersomatic distance of two PCs. Labelling and binning as in (A). **(C)** normalized connectivity ratio as a function of the intersomatic distance of two PCs (black, FDDI; grey, EPSPs). Dashed lines are Gaussian fits (FDDI, $\lambda = 290\ \mu\text{m}$; EPSPs, $\lambda = 265\ \mu\text{m}$). Binning as in (A). **(D)** FDDI amplitude as a function of intersomatic distance. **(E)** EPSP amplitudes as a function of intersomatic distance. **(F)** FDDI and EPSP amplitudes as a function of intersomatic distance, binned in $25\ \text{mm}$ steps. Dashed lines are exponential fits (FDDI, black, $\lambda = 97\ \mu\text{m}$; EPSPs, grey, $\lambda = 126\ \mu\text{m}$). Error bars denote S.E.M. (A and B) or standard deviation (F).

In Fig. 6C, FDDI and monosynaptic excitatory connectivity rates are normalized in order to better compare their relative extent. Both graphs were reasonably fitted with Gaussians and show a very similar course ($\sigma_{\text{FDDI}} = 290 \mu\text{m}$, $\sigma_{\text{EPSPs}} = 265 \mu\text{m}$). FDDI and monosynaptic excitation were found between cells with an intersomatic distance of up to $526.7 \mu\text{m}$. We also tested several kinetic parameters for their distance dependence. The only striking effect we could observe was for FDDI and EPSP amplitudes (Fig. 6D and E). Using a binning of $25 \mu\text{m}$, we could fit the distance dependence with single exponentials ($\lambda_{\text{FDDI}} = 97 \mu\text{m}$, $y^{(\infty)}_{\text{FDDI}} = 0.66 \text{ mV}$, $\lambda_{\text{EPSPs}} = 126 \mu\text{m}$, $y^{(\infty)}_{\text{EPSPs}} = 0.37 \text{ mV}$).

Fatigue of the PC–interneuron synapse

Screening the connectivity pattern within a multi-cell cluster requires multiple repetitive stimulation of all cells in order to obtain sufficiently good and noise-free average responses (see Methods). Long waiting periods of tens of seconds were interleaved with repetitive stimulation of a given cell. FDDI was especially prone to disappear when the waiting times were too short, and reappeared when inter-stimulation intervals (ISIs) were long enough, as shown in Fig. 7. The presynaptic cell of a pair of PCs connected via a non-patched intermediate interneuron (Fig. 7A) was stimulated with 70 Hz (15 APs) (Fig. 7B). The first 30 repetitions were interrupted with very short ISIs of 1 s, leading to a disappearance of FDDI after the 11th stimulation. Repetitions of 30–60 were interleaved with 30 s ISIs, and FDDI reappeared after 8 stimulations (Fig. 7B and C). In this specific example, the inhibitory response did not seem to regain the reliability that it used to have, expressed in FDDI failures in multiple repetitions with 30 s ISIs. Figure 7D summarizes the data of seven cases with three alternating short and long ISI periods. With this protocol, FDDI does recover from 1 s ISIs, but never reaches the initial amplitudes. The reason might be that even 30 s ISIs are not long enough to enable full recovery of the participating biophysical processes. What is causing this strong activity-dependent effectiveness of FDDI? As seen in the traces in Fig. 7B, FDDI seems to be present or not present, and disappears *ad hoc*, without a pronounced gradual decline. Thus, neurotransmitter pool depletion in the interneuron–PC synapse is an unlikely reason for FDDI vanishing, since this would be expected to happen in a more gradual way.

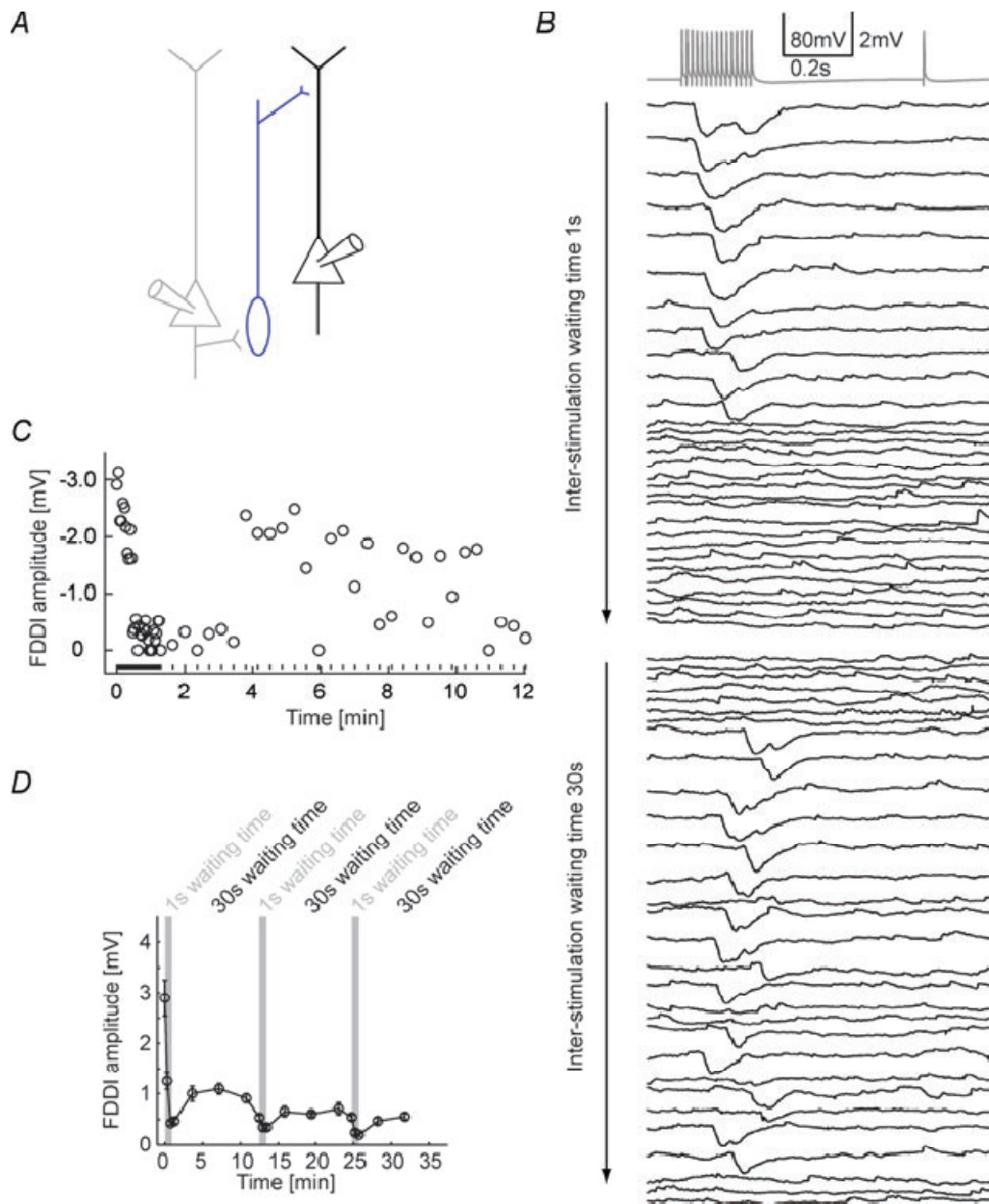


Figure 7 Stability of FDDI after repetitive stimulation. **(A)** a PC (grey) connecting via an interneuron (blue) to a postsynaptic PC (black). **(B)** high frequency stimulation of the presynaptic PC (grey) with the individual responses of the postsynaptic PC (black). The first 30 repetitions were applied with only 1 s waiting time between each stimulus application, the last 30 repetitions were done with 30 s waiting time. **(C)** FDDI amplitude as a function of time and inter-stimulation interval (waiting time). Circles denote the amplitude, lines at the bottom of the graph the time of stimulation. **(D)** FDDI amplitude as a function of time, with a binning of 10 repetitions. Grey background illustrates the epochs of 'fast' stimulation with small inter-stimulation intervals (1 s waiting time). Error bars denote S.E.M.

The (possibly only) FDDI-mediating interneuron is the Martinotti cell (Silberberg & Markram, 2007), which is likely to be part of the low threshold spiking (LTS) neuron population. LTS neurons have been shown to hyperpolarize upon repetitive suprathreshold stimulation, and this hyperpolarization has been shown to be dependent on an intracellular signaling pathway via endocannabinoid receptors (Bacci *et al.* 2004). The disappearance of FDDI could therefore be attributed to a somatic hyperpolarization of the interneurons, making discharge, which is essential for FDDI signaling, less likely. We blocked this endocannabinoid pathway by applying 10 μ M AM251, but this did not prevent FDDI from disappearing during 1 s ISI stimulation, though the recovery of the amplitude is slightly improved ($n=3$, Fig. 8A). Thus, spiking-induced hyperpolarization of interneurons is also probably not the main reason for FDDI disappearance.

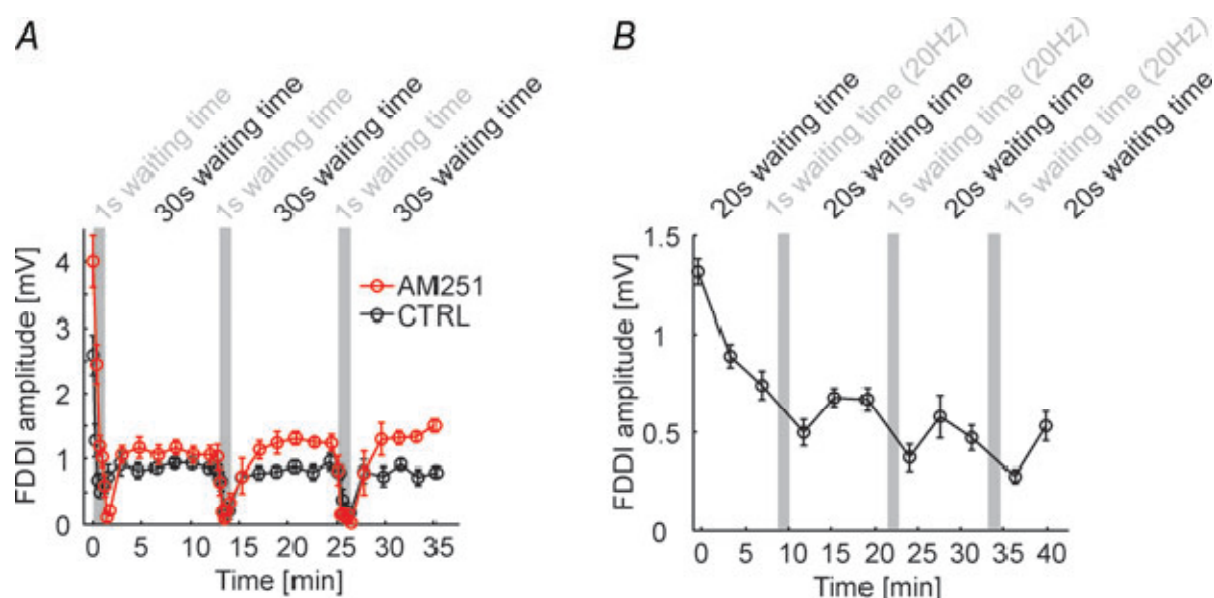


Figure 8. The PC–interneuron synapse limits FDDI stability. (A) FDDI amplitude as a function of time and inter-stimulation interval in control conditions (black) and in the presence of the endocannabinoid receptor antagonist AM251 (10 μ M, red). (B) FDDI amplitude as a function of time and inter-stimulation interval, with ‘fast’ stimulation (small waiting time) of 20 instead of 70 Hz. Stimulation of 20 Hz does not usually trigger suprathreshold activity in the interneuron, therefore allowing the isolation of synaptic- from spike-evoked effects. Error bars denote S.E.M.

Finally, we replaced the 70Hz–1 s ISI stimulation protocol with a 20Hz–0.3 s ISI stimulation (Fig. 8B). With this protocol the number of presynaptic APs stays the same, but we do not elicit any spikes in the intermediate interneuron since the frequency is not high enough.

Thereby, we isolate spiking-dependent effects in the interneuron from effects in the PC–interneuron synapse. And indeed, we always find a decrease in FDDI amplitude after the 20 Hz stimulation phases ($n = 6$), indicating that FDDI disappearance might be due to an activity-dependent weakening of the PC–interneuron synapse. This reversible weakening might cause a delay of recovery from short-term depression, or, as described earlier, synaptic fatigue as it is reversible and inducible with relatively low frequencies (Abrahamsson *et al.* 2005).

DISCUSSION

The current study reveals properties of disynaptic inhibitory and monosynaptic excitatory connections in five different cortical areas. We characterized the kinetics of both signaling pathways and synaptic short-term dynamics of excitatory connections. We thereby show that cortical areas of different modalities resemble one another in terms of the existence of FDDI, but show differences in connectivity rates and some kinetic parameters. In addition, we show the distance dependence of connectivity rates and synaptic parameters, and the activity-dependent drop of FDDI connections in the SSC.

FDDI as a functionally relevant generic neocortical sub-circuit motif

FDDI has been recently described between layer 5 and between layer 2/3 PCs of the primary somatosensory cortex of rats (Kapfer *et al.* 2007; Silberberg & Markram, 2007). It is mediated via somatostatin-positive interneurons, i.e. the Martinotti cell and perhaps other interneurons that receive strongly facilitating input from PCs. In the above studies as well as the present one long and high frequency trains, which are not very likely to happen during sparse neocortical activity *in vivo*, were used to observe the inhibitory response. The number of APs as well as the train frequency necessary to trigger FDDI is, however, greatly reduced by synchronous activation of a few PCs (unpublished observations). *In vivo* studies showed the occurrence of high frequency bursts in layers 5 and 2/3 (de Kock & Sakmann, 2008), therefore the necessary conditions for FDDI signalling appear to exist under physiological conditions. Another recent study found evidence for modulation of dendritic Ca^{2+} spikes by deep-layer interneurons, both *in vitro* and *in vivo* (Murayama *et al.* 2009).

We show that FDDI exists in all investigated areas, thus suggesting that frequency-dependent feed-forward and feedback projections are a fundamental microcircuit motif in the cortex.

Area-specific specializations

Regarding monosynaptic excitatory connections between PCs, the mPFC has previously been shown to feature specialized synaptic properties in ferrets (Wang *et al.* 2006). Subpopulations of PCs seem to interconnect with more facilitating synapses, and also display morphological heterogeneities, namely an early branching of the apical dendrite. Intrinsic response properties of mPFC PCs have been reported to show wide-range sensitivity to input fluctuations (Arsiero *et al.* 2007), and together with the observed synaptic facilitation their relevance for persistent working memory has been stressed. Although not the focus of our study, we did not observe morphological differences such as a very early branching apical dendrite in mPFC PCs. We did find, however, compared to the other cortical areas, significantly elevated paired pulse ratios and a reduced initial release probability.

Disynaptic inhibition was most frequent, and was strongest and fastest in the auditory cortex. This might reflect the nature of auditory processing, requiring a high temporal precision for the encoding of fast events. It should be considered, however, that our analysis of FDDI kinetics is based on average responses, and that two synapses are involved in the synaptic response. A large jitter in the spike timing of the intermediate interneuron can lead to widely distributed IPSP onsets in the postsynaptic PC, which is expressed in slow rising and decay times in the average response. Therefore, a fast average FDDI response could also reflect precise triggering of interneuron spiking. Another aspect that should be considered when comparing different (primary) cortical areas in juvenile rats is the onset time of functioning of the sense concerned. In rats, the eyes open at around postnatal day P14 (authors' observations), whereas the hearing onset is around P12 (Uziel *et al.* 1981), and somatosensory sensing is even earlier. Therefore, the maturation of neurons and synaptic circuits, especially the formation of experience-dependent processes, may substantially vary depending on the specific area, which would result in different synaptic properties at a given, young age. Even during adolescence,

biophysical properties of central synapses do substantially change. Synaptic connections in the primary somatosensory cortex, for example, undergo a developmental switch from dominating depressing to facilitating responses between P14 to young adulthood (Reyes & Sakmann, 1999; Williams, 2005). It remains to be tested whether PC–PC connections in the mPFC are just advanced in their maturation and not functionally different because of different purposes. Therefore, it would be essential to investigate whether synaptic differences between cortical areas become stronger in more mature animals.

An aspect that is very likely to have caused some variability to our data is the diversity of the pyramidal cell population. We chose the largest PCs for recording, which might be a relatively homogeneous under infra-red videomicroscopy identifiable cell population in the primary SSC (thick-tufted PCs; Le Bé *et al.* 2007), but more diverse in frontal cortex regions (Morishima & Kawaguchi, 2006). It has recently been shown that cortical sub-networks in layer 5 and also in layer 6 exist, with preferred connectivity between pyramidal cells targeting the same (subcortical) regions (Mercer *et al.* 2005; Morishima & Kawaguchi, 2006, Le Bé *et al.* 2007, Brown & Hestrin, 2009). Therefore, some measured connectivity rates may underestimate connectivity within subnetworks, since PCs from different populations tend to be less connected to each other. Whether a heterogeneous population of PCs is also the reason for the relatively low connectivity rates in ‘higher’ cortical areas like VC2 and mPFC remains to be elucidated. It should be considered, however, that the slice preparations of the investigated cortical areas required different cutting planes, which might have differentially lowered the observed connectivity rates. We therefore took care to only choose slices with a cutting plane parallel to the apical dendrite and principal axonal branch, which usually preserves the cells’ arborizations best.

The overrepresented reciprocity that we and also several previous studies in layers 2/3 and 5 observed (Markram *et al.* 1997; Sjöström *et al.* 2001; Holmgren *et al.* 2003; Song *et al.* 2005) might stem from relatively separated, non-identified subnetworks with high intrinsic connectivity. One recent thorough study in the mouse barrel cortex, however, did not observe an overrepresentation of reciprocity in any of the six investigated layers (Lefort *et al.* 2009). They distinguished layer 5A and B and found connectivity ratios of 19.1% and 7.2% between PCs,

respectively. These are between our and previously found estimates that are based on connectivity rates between somato-dendritically defined cells (Markram *et al.* 1997; Sjöström *et al.* 2001; Song *et al.* 2005). One possible explanation for Lefort's different reciprocity could be the separate treatment of layer 5A and B, the extraordinary specialization of the barrel cortex, or general differences between mouse and rat neocortex. More research is necessary for finding out more about non-random distributions in different cortical areas and animals.

Lateral extent of connectivity

Most paired recording studies that mention the intersomatic distance between the recorded cells did not find a very prominent drop of connectivity ratio for the first tens of micrometres distance, either between layer 2/3 or layer 5 PCs in somatosensory or visual cortex (Holmgren *et al.* 2003; Song *et al.* 2005). This is in agreement with our data: both FDDI and EPSP connectivity were relatively stable for the first 100–150 μm . The connectivity started to drop thereafter, and was best fitted with Gaussians with a standard deviation of 265–290 μm . It needs to be considered that any connectivity rates obtained from acute slices suffer from bias in the estimates due to cut dendrites and axon along the slicing plane. This bias can be reduced if the recorded cells are located as deep as possible in the slice but will always be a source of error in slice experiments. Moreover, this uncertainty might be larger for large intersomatic distances. Likewise, amplitude drops of EPSP might be explained by a higher likelihood of cut synaptic contacts for distant cells. Some of the synaptic contacts between Martinotti cells and PCs are located at the dendritic tuft, electrotonically remote from the soma. It may be that due to the dendritic spread of PCs and the axonal spread of Martinotti cells in layer 1, FDDI also occurs at larger distances, but is mediated only by those distal synapses that might escape detection by somatic recordings.

Activity dependence of FDDI signaling

We found FDDI to be a very sensitive pathway that would disappear rapidly upon fast high frequency repetitive stimulation if the inter-stimulation intervals were too short. This decay can probably be attributed to a loss of strength of the PC–interneuron synapse, since this decay was

also present for lower, 20 Hz stimulation frequency that did not elicit spikes in the interneuron. Repetitive suprathreshold activity in LTS cells is known to lead to slow self-inhibition, mediated by the endocannabinoid 2-arachidonoylglycerol (Bacci *et al.* 2004; Marinelli *et al.* 2008). We did not find evidence for an involvement of this pathway since the endocannabinoid receptor antagonist AM251 could not prevent FDDI decline. The investigated PC–interneuron pathway, which might be exclusively composed of the PC–Martinotti cell synapse, has a strongly facilitating response for short (~8–15 spikes) train protocols (Silberberg & Markram, 2007). It remains to be determined whether this synapse becomes fatigued after repetitive high-frequency stimulation. If so, this pathway might be relatively inactive during epileptiform activity in diseased brain tissue, though it might be able to prevent the onset of seizures.

In this study we have shown that FDDI between layer 5 pyramidal neurons, which has been previously described in the SSC (Silberberg & Markram, 2007), is a common and robust microcircuit feature across the entire rat neocortex, including granular, agranular, sensory and motor regions. In all tested areas, the occurrence of FDDI was higher than that of monosynaptic excitation between PCs, yet the prevalence as well as kinetic properties varied between areas. We also quantified the lateral spatial extent of FDDI (and monosynaptic connections), as well as its use-dependent fatigue. These findings add to our knowledge about the diverse role of inhibitory interneurons in the neocortical microcircuitry and provide a quantitative description of spatial and temporal properties of a specific inhibitory sub-circuit. Further experimental and theoretical studies are still required in order to understand the role of FDDI in the intact brain and at different cortical states.

REFERENCES

- Abrahamsson T, Gustafsson B & Hanse E (2005). Synaptic fatigue at the naive perforant path–dentate granule cell synapse in the rat. *J Physiol* **569**, 737–750.
- Arsiero M, Lüscher H-R, Lundström BN & Giugliano M (2007). The impact of input fluctuations on the frequency current relationships of layer 5 pyramidal neurons in the rat medial prefrontal cortex. *J Neurosci* **27**, 3274–3284.
- Bacci A, Huguenard J & Prince D (2004). Long-lasting self-inhibition of neocortical interneurons mediated by endocannabinoids. *Nature* **431**, 312–316.
- Berger T, Larkum ME & Lüscher HR (2001). High I_h channel density in the distal apical dendrite of layer V pyramidal cells increases bidirectional attenuation of EPSPs. *J Neurophysiol* **85**, 855–868.
- Braitenberg V & Schüz A (1998). *Cortex: Statistics and Geometry of Neuronal Connectivity*, 2nd edn. Springer, Berlin, Heidelberg, New York.

- Brodman K (1909). *Vergleichende Lokalisationslehre der Grosshirnrinde in ihren Prinzipien dargestellt auf Grund des Zellenbaues*. Barth, Leipzig.
- Brown SP & Hestrin S (2009). Intracortical circuits of pyramidal neurons reflect their long-range axonal targets. *Nature* **457**, 1133–1136.
- DeFelipe J, Alonso-Nanclares L & Arellano JI (2002). Microstructure of the neocortex: comparative aspects. *J Neurocytol* **31**, 299–316.
- de Kock CPJ & Sakmann B (2008). High frequency action potential bursts (~ 100 Hz) in L2/3 and L5b thick tufted neurons in anaesthetized and awake rat primary somatosensory cortex. *J Physiol* **586**, 3353–3364.
- Dong HW (2007). *The Allen Atlas: A Digital Color Brain Atlas of the C57BL/6J Male Mouse*. Wiley & Sons.
- Drummond GB (2009). Reporting ethical matters in *The Journal of Physiology*: standards and advice. *J Physiol* **587**, 713–719.
- Holmgren C, Harkany T, Svennenfors B & Zilberter Y (2003). Pyramidal cell communication within local networks in layer 2/3 of rat neocortex. *J Physiol* **551**, 139–153.
- Kapfer C, Glickfeld LL, Atallah BV & Scanziani M (2007). Supralinear increase of recurrent inhibition during sparse activity in the somatosensory cortex. *Nat Neurosci* **10**, 743–753.
- Le Bé J, Silberberg G, Wang Y & Markram H (2007). Morphological, electrophysiological, and synaptic properties of corticocollateral pyramidal cells in the neonatal rat neocortex. *Cereb Cortex* **17**, 2204–2213.
- Lefort S, Tomm C, Floyd Sarria J-C & Petersen CCH (2009). The excitatory neuronal network of the C2 barrel column in mouse primary somatosensory cortex. *Neuron* **61**, 301–316.
- Marinelli S, Pacioni S, Bisogno T, Marzo VD, Prince DA, Huguenard JR & Bacci A (2008). The endocannabinoid 2-arachidonoylglycerol is responsible for the slow self-inhibition in neocortical interneurons. *J Neurosci* **28**, 13532–13541.
- Markram H, Lübke J, Frotscher M, Roth A & Sakmann B (1997). Physiology and anatomy of synaptic connections between thick tufted pyramidal neurones in the developing rat neocortex. *J Physiol* **500**, 409–440.
- Markram H, Wang Y & Tsodyks M (1998). Differential signalling via the same axon of neocortical pyramidal neurons. *Proc Natl Acad Sci U S A* **95**, 5323–5328.
- Mercer A, West DC, Morris OT, Kirchhecker S, Kerkhoff JE & Thomson AM (2005). Excitatory connections made by presynaptic cortico-cortical pyramidal cells in layer 6 of the neocortex. *Cereb Cortex* **15**, 1485–1496.
- Molnár G, Oláh S, Komlósi G, Füle M, Szabadics J, Varga C, Barzó P & Tamás G (2008). Complex events initiated by individual spikes in the human cerebral cortex. *PLoS Biol* **6**, e222.
- Morishima M & Kawaguchi Y (2006). Recurrent connection patterns of corticostriatal pyramidal cells in frontal cortex. *J Neurosci* **26**, 4394–4405.
- Murayama M, Pérez-García E, Nevian T, Bock T, Senn W & Larkum ME (2009). Dendritic encoding of sensory stimuli controlled by deep cortical interneurons. *Nature* **457**, 1137–1141.
- Paxinos G & Watson C (1998). *Theoretical Rat Brain in Stereotaxic Coordinates*, 4th edn. Academic Press.
- Ren M, Yoshimura Y, Takada N, Horibe S & Komatsu Y (2007). Specialized inhibitory synaptic actions between nearby neocortical pyramidal neurons. *Science* **316**, 758–761.
- Reyes A & Sakmann B (1999). Developmental switch in the short-term modification of unitary EPSPs evoked in layer 2/3 and layer 5 pyramidal neurons of rat neocortex. *J Neurosci* **19**, 3827–3835.
- Sherwood N & Timiras P (1970). *A Stereotaxic Atlas of the Developing Rat Brain*. University of California Press, Berkeley, CA, USA.
- Silberberg G & Markram H (2007). Disynaptic inhibition between neocortical pyramidal cells mediated by Martinotti cells. *Neuron* **53**, 735–746.
- Sjöström PJ, Turrigiano GG & Nelson SB (2001). Rate, timing, and cooperativity jointly determine cortical synaptic plasticity. *Neuron* **32**, 1149–1164.
- Song S, Sjöström PJ, Reigl M, Nelson S & Chklovskii DB (2005). Highly nonrandom features of synaptic connectivity in local cortical circuits. *PLoS Biol* **3**, e68.
- Spruston N (2008). Pyramidal neurons: dendritic structure and synaptic integration. *Nat Rev Neurosci* **9**, 206–221.
- Stuart G & Spruston N (1998). Determinants of voltage attenuation in neocortical pyramidal neuron dendrites. *J Neurosci* **18**, 3501–3510.
- Uziel A, Romand R & Marot M (1981). Development of cochlear potentials in rats. *Audiology* **20**, 89–100.
- Wang Y, Markram H, Goodman PH, Berger TK, Ma J & Goldman-Rakic PS (2006). Heterogeneity in the pyramidal network of the medial prefrontal cortex. *Nat Neurosci* **9**, 534–542.
- Williams SR (2005). Encoding and decoding of dendritic excitation during active states in pyramidal neurons. *J Neurosci* **25**, 5894–5902.

Zar JH (1999). *Biostatistical Analysis*, 4th edn. Prentice Hall.

Author contributions

T.K.B., G.S., and H.M. designed the experiments, T.K.B. and R.P. performed the experiments, T.K.B. analysed the data. T.K.B. and G.S. wrote the manuscript. All authors discussed the results and commented on the manuscript.

Acknowledgements

We thank the LNMC members.

Chapter 6 Brief bursts self-inhibit and correlate the pyramidal network

Brief bursts self-inhibit and correlate the pyramidal network

Thomas K. Berger¹, Gilad Silberberg², Rodrigo Perin¹, Henry Markram¹

¹ Laboratory of Neural Microcircuitry, Brain Mind Institute, Ecole Polytechnique Fédérale de Lausanne, Lausanne (EPFL), CH-1015, Switzerland

² Department of Neuroscience, Karolinska Institute, Stockholm 17177, Sweden.

Correspondence:
Henry Markram
Laboratory of Neural Microcircuitry
Brain Mind Institute
Ecole Polytechnique Fédérale de Lausanne
Lausanne (EPFL)
CH-1015
Switzerland
Email: henry.markram@epfl.ch

SUMMARY

Inhibitory pathways are an essential component in the function of the neocortical microcircuitry. Despite the relatively small fraction of inhibitory neurons in the neocortex, these neurons are strongly activated due to their high connectivity rate and the intricate manner in which they interconnect with pyramidal cells (PCs). One prominent pathway is the frequency-dependent disynaptic inhibition (FDDI) formed between layer 5 PCs and mediated by Martinotti cells (MCs). Here, we show that simultaneous short bursts in 3 - 4 PCs are sufficient to exert FDDI in all neighboring PCs within the dimensions of a cortical column. This powerful inhibition is supported by a high degree of both divergence and convergence in PC-MC interconnectivity, leading to strongly correlated membrane fluctuations and synchronous spiking between PCs simultaneously receiving FDDI. Somatic integration of such inhibition is independent and electrically isolated from monosynaptic excitation formed between the same PCs. FDDI is strongly shaped by $I(h)$ in PC dendrites, which determines the effective integration time window for inhibitory and excitatory inputs. We propose a key disynaptic mechanism by which brief bursts generated by a few PCs can synchronize the activity in the pyramidal network.

INTRODUCTION

The mammalian neocortex consists of neurons that form an intricate network of recurrent circuits (Thomson et al., 2002, Douglas and Martin, 2004, Somogyi et al., 1998). The synaptic wiring between cells follows a number of stereotypic rules including targeting specific domains of neurons, specific connection probabilities, target neuron preferences, and specific short-term synaptic dynamics (Thomson et al., 2002, Douglas and Martin, 2004, Somogyi et al., 1998, Markram et al., 1998, Reyes et al., 1998). Revealing these rules is essential to understand the mechanisms that generate the response of a cortical column (or functional unit) to any external input. In particular, it is crucial to tease apart the synaptic pathways that enable the neocortex to appropriately respond to all possible environmental stimuli.

Neocortical neurons receive excitatory and inhibitory inputs over a variety of different network activity states (Shu et al., 2003, Monier et al., 2003). Balanced E-I activity is remarkable since the large majority of cells in the neocortex are pyramidal (excitatory) cells (PCs), only around 25 % are inhibitory GABAergic interneurons (White, 1989, Ren et al., 1992), and almost 90 % of the neocortical synapses are presumably excitatory (DeFelipe et al., 2002). This relatively small population of interneurons is tasked to generate a precisely matched inhibition for a variety of cortical network states. One synaptic principle for dynamically adjusting the level of excitation within a neocortical column is the use of dynamically depressing excitatory synapses (Abbott et al., 1997, Tsodyks and Markram, 1997, Galarreta and Hestrin, 1998), but how inhibitory synaptic pathways ensure dynamic application of balanced inhibition as a function of the moment to moment excitation of the neocortical column is not clear.

A disynaptic pathway and dynamic circuit mechanism allowing an activity dependent recruitment of inhibition was recently reported: Frequency Dependent Disynaptic Inhibition (“FDDI”) is indeed a common pathway in the somatosensory cortex that is dynamically regulated by the firing rate and the number of presynaptic PCs (Silberberg and Markram, 2007, Kapfer et al., 2007, Silberberg, 2008). In response to high frequency stimulation of a PC, Martinotti Cells (MCs, (Wang et al., 2004)) are recruited via facilitating synapses, thus providing

a level of inhibition that depends on the previous excitation level in the network. MCs display a characteristic ascending axonal arborization up to layer 1, and they are the only interneurons that target the combination of oblique, apical, and tuft dendrites of their neighboring PCs (Somogyi et al., 1998, Silberberg and Markram, 2007). FDDI has so far been explored mainly as a pairwise interaction between PCs and MCs, but little is known about how this synaptic pathway could operate to dynamically apply inhibition to the microcircuit as a function of multi-cellular activity.

Here, we used multi-neuron whole cell recordings to characterize *summation properties* of FDDI between layer 5 thick tufted PCs within the dimensions of a neocortical column. FDDI tends to summate linearly with coincident EPSPs from neighboring PCs, but may also shunt some input arriving at the apical dendrite. 3 – 4 PCs firing simultaneously are sufficient to generate FDDI in all PCs within the dimensions of a cortical column and 8 – 9 PCs can saturate the amount of hyperpolarization recorded from their somata. A brief, high frequency burst in only a few PCs can therefore constitute a gating mechanism for further excitatory input to the apical dendrites of the entire column. This global inhibition induces strong subthreshold correlations in PCs. Functional implications for dynamically balanced EI, its saturation levels, and the importance of compartmentalization are discussed.

RESULTS

In order to study the network properties of FDDI, we obtained simultaneous whole-cell recordings from neighboring thick tufted layer 5 PCs and in some cases also layer 5 MCs. In total, 1086 PCs and 14 MCs in 264 clusters from 123 animals were recorded for this study. The average age of the rats was 15.0 days (range 14 – 18).

Components of FDDI

Figure 1 illustrates the basic components (**A-C**) that mediate FDDI (**D**). A presynaptic PC (red) projecting onto an MC (blue) excites the MC using a facilitating synapse, which in turn gives

rise to a delayed inhibition in another postsynaptic PC (black). A lower stimulation frequency (20 Hz instead of 70 Hz) usually results in subthreshold activity only, allowing a characterization of the dynamics of the PC-MC synaptic connection (Figure 1E). In agreement with previous publications, the PC-MC connection strongly facilitates, leading to an average 2.5-fold amplitude increase between the 1st and 8th EPSP in response to a 20 Hz train ($n = 8$, $\mu\text{EPSP}_1 = 0.58 \pm 0.97$ mV, $\mu\text{EPSP}_8 = 1.50 \pm 1.35$ mV (mean \pm standard deviation)). Likewise, a train stimulation of the MC reveals the synaptic dynamics of the MC-PC connection. In contrast to the PC-MC connection, the MC-PC connection is depressing ($n = 3$, $\mu\text{EPSP}_1 = 0.32 \pm 0.37$ mV, $\mu\text{EPSP}_8 = 0.12 \pm 0.12$ mV).

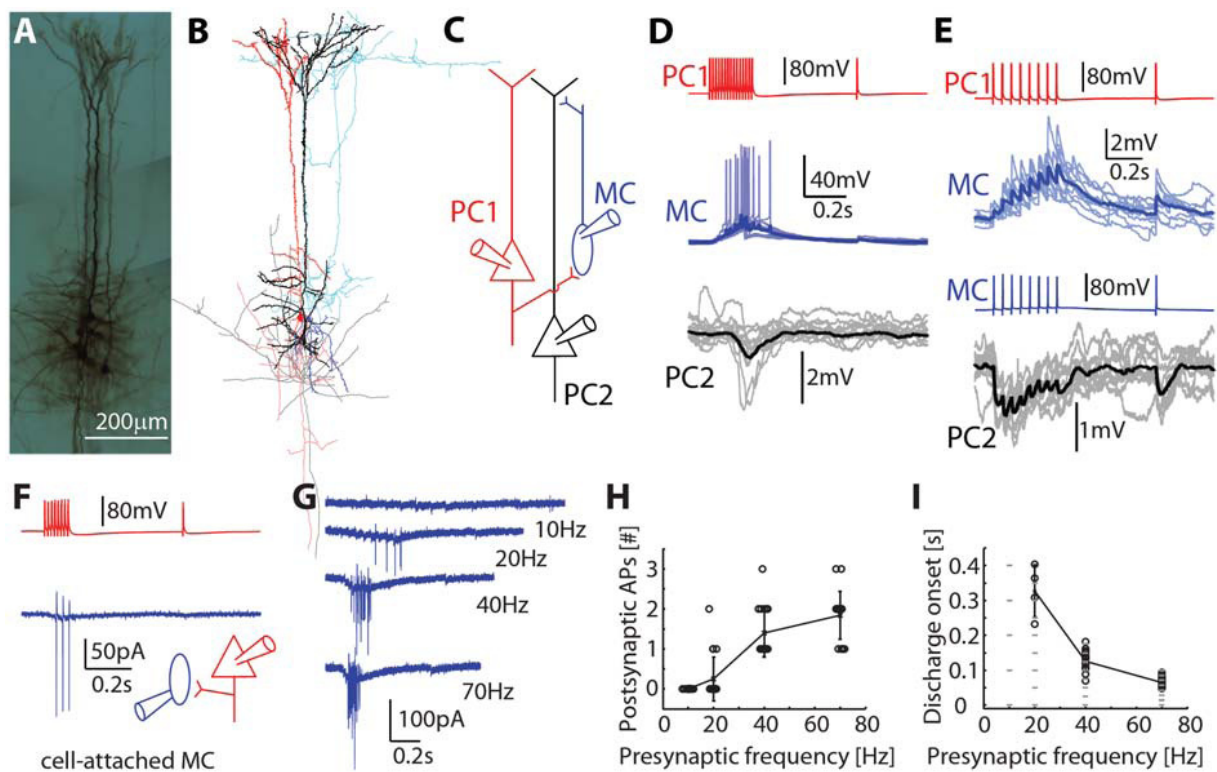


Figure 1. Components of frequency-dependent disynaptic inhibition (FDDI) and excitability of Martinotti cells (MCs). (A) Photomicrograph of a cluster of recorded cells (6 PCs, 1 MC). (B) Reconstruction of the complete pathway of disynaptic inhibition (2 PCs, 1 MC). (C) Sketch of the FDDI pathway. (D) Stimulation (70 Hz, 15 APs) of the presynaptic PC (in red) leads to delayed AP firing in the MC (in blue), giving in turn a hyperpolarizing inhibitory signal in the postsynaptic PC (in black). Single repetitions are in faint, means in full colors. (E) Stimulation (20 Hz, 8 APs) of the PC (red) or the MC (blue) reveals the short term dynamics of the PC-MC (blue) and MC-PC (black) connections, respectively. (F) Stimulation of a presynaptic PC (8 spikes at 70 Hz plus a single spike 0.5 s later, black) with the corresponding response of a postsynaptic MC in the cell-attached configuration (blue). (G) Average

responses of the postsynaptic MC in response to various presynaptic stimulation frequencies. **(H)** Number of postsynaptic APs as a function of the presynaptic stimulation frequency. Note that individual data points are slightly scattered for better visualization. **(I)** Delay of discharge onset ($t_{\text{postsynAP}} - t_{\text{presynAP}}$) as a function of the presynaptic stimulation frequency. The gray horizontal bars mark the timing of the presynaptic APs. Error bars **(H,I)** denote s.d.

Direct excitatory connections between PCs occurred in 14% of paired recordings ($p = 0.14$; 463 connected pairs out of 3342 tested pairs), while PC-MC connections occurred far more frequently ($p = 0.43$; 26/61) and MC-PC connections had a probability of occurring of 0.31 (18/58). The entire FDDI loop occurs with a probability of 0.283 (859/3041), which is more than double the monosynaptic connectivity between them.

Recruitment of MC firing strongly depends on the PC stimulation frequency (see also (Silberberg and Markram, 2007), Figure 1F-I). Here we demonstrate this by holding the MC in the cell-attached configuration while stimulating a presynaptic PC in the whole-cell mode (Figure 1F). By doing so the intracellular ion concentrations are not perturbed by the large volume of intracellular solution in the patch pipette. Action potentials (APs) are detected as fast inward currents, and even subthreshold depolarizations can be detected in averaged responses (Figure 1G). The number of MC action potentials increases (Figure 1H) and the MC discharge onset decreases (Figure 1I) with presynaptic stimulation frequency.

I_h in PCs spatiotemporally separates synaptic inputs

Silberberg and Markram (2007) previously showed a strong modulation of FDDI by I_h currents (Silberberg and Markram, 2007). Blocking I_h currents with extracellular application of zd7288 leads to larger amplitudes (average 75% increase, $n = 23$, $\mu_{\text{ctrl}} = 0.99 \pm 0.5$ mV, $\mu_{\text{zd7288}} = 1.73 \pm 0.99$ mV, $p = 0.0002$, paired t-test) and longer decay time constants (250% increase, $\mu_{\text{ctrl}} = 0.051 \pm 0.01$ s, $\mu_{\text{zd7288}} = 0.182 \pm 0.071$ s, $p = 7.64e-9$) of FDDI (Figure 2A, B). In some cases (3 out of 26) FDDI disappeared after I_h block. As zd7288 blocks I_h irreversibly (Williams et al., 1997) we do not know whether the disappearance is due to a drug action or a general rundown. On the other hand, I_h block never lead to FDDI appearance *de novo* ($n = 19$). In order to understand whether the effects of I_h are on the intermediate interneuron or postsynaptic PC, we recorded from the entire disynaptic pathway while I_h was blocked.

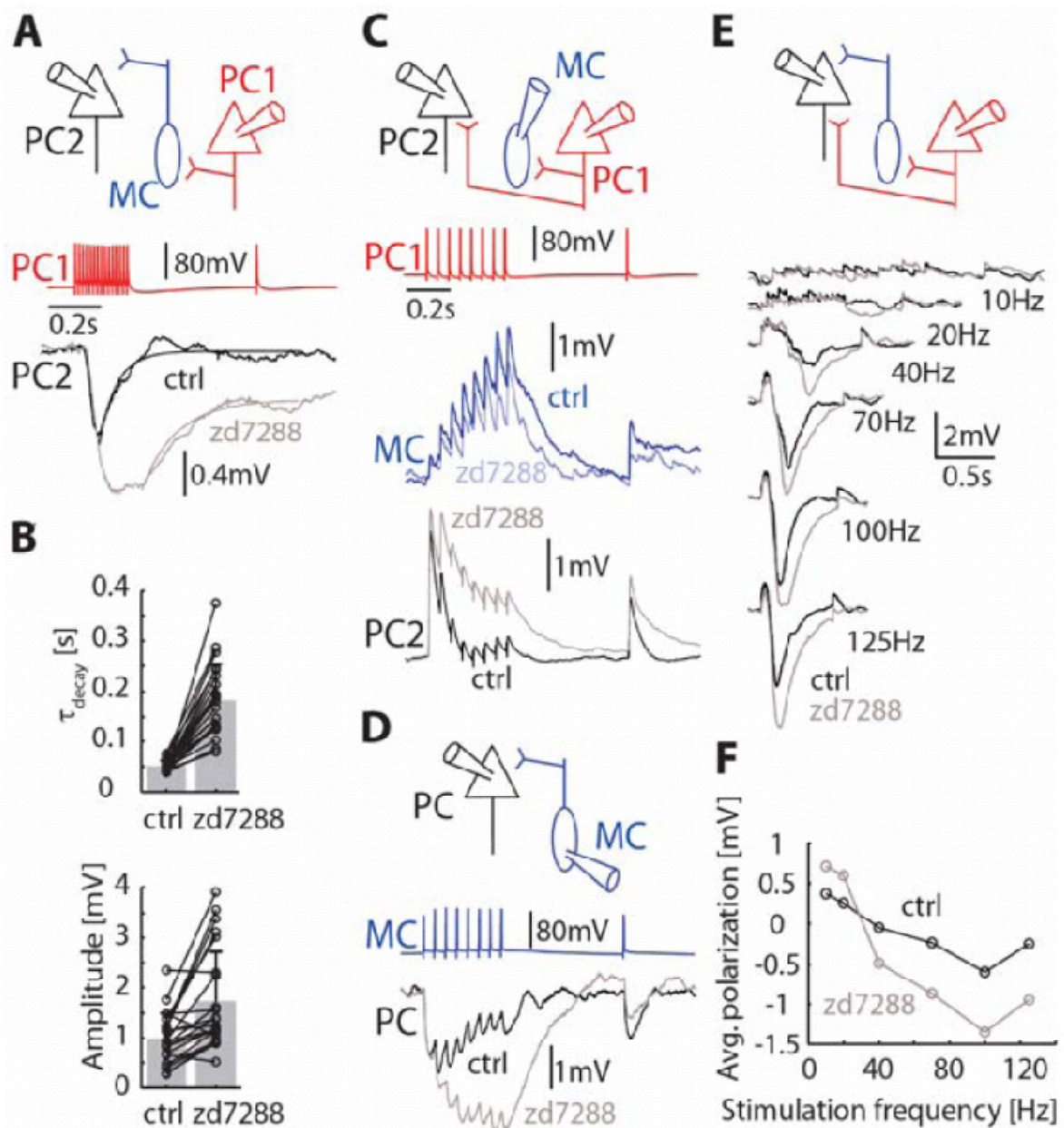


Figure 2. Ih current in PCs has a strong impact on FDDI. (A) Stimulation of a presynaptic PC (red) eliciting FDDI in a postsynaptic PC under control condition (black) and in the presence of 50 μM of the Ih blocker zd7288 applied to the bath (gray, same labeling for C-F). (B) Influence of zd7288 on the Results decay time constant and amplitude of the FDDI. (C) Stimulation of a presynaptic PC (8 APs at 20 Hz plus a single AP 0.5 s later) and the corresponding responses in a postsynaptic MC (blue) and a postsynaptic PC (black). (D) Stimulation of a presynaptic MC (parameters as in (C)) and the corresponding responses in a postsynaptic PC. (E) Stimulation of a PC that targets a postsynaptic PC with an excitatory direct connection as well as FDDI with (gray) or without (black) bath application of 50 μM zd7288. The overall polarization of the postsynaptic PC (measured by the integral from EPSP onset to 0.5 s after stimulation offset) depends on the stimulation frequency (stimulation train always contained 15 APs). (F) Ih block leads to a larger dynamic range of EPSP-FDDI balance with respect to the stimulation frequency. Error bars (B) denote s.d.

Facilitating EPSPs from PCs to MCs were only slightly changed in the presence of zd7288 (average 8% decrease of maximal depolarization; $n = 5$, $\mu_{\text{ctrl}} = 2.275 \pm 1.961$ mV, $\mu_{\text{zd7288}} = 2.431 \pm 1.825$ mV, $p = 0.384$, paired t-test), whereas input onto PCs, from MCs or another PC displayed increased synaptic summation (Figure 2C, D). Thus, the strong effect of zd7288 on FDDI can be attributed to I_h in PCs.

PCs receiving both disynaptic inhibition and monosynaptic excitation from their neighboring PCs display a frequency-dependent transition from a net depolarization to hyperpolarization (Figure 2E, F). Blockage of I_h resulted in an increased frequency dependence, enhancing both low-frequency depolarization and high-frequency hyperpolarization. Together with the observed shortening of synaptic events, this suggests that I_h in PCs acts to localize synaptic inputs, both spatially and temporally.

Selective non-linear summation of excitatory inputs with FDDI

Monosynaptic excitation between PCs mainly targets their basal dendrites (Markram et al. 1997) while FDDI mainly targets their apical and tuft dendrites (Silberberg & Markram, 2007). It is not clear to what extent these two inputs interact. We therefore activated both pathways simultaneously and quantified the linearity of summation. Clusters of 3 PCs, with a PC receiving FDDI from a neighboring PC and a direct excitatory connection from another PC, were stimulated in a way that FDDI and a direct EPSP coincided (Figure 3A).

We observed supra-, sub-, and linear amplitude summation in the soma (Figure 3B) in different experiments, and on average there was no significant difference in EPSP amplitude between control and coinciding FDDI (Figure 3C, $n = 21$, $\mu_{\text{ctrl}} = 1.885 \pm 1.334$ mV, $\mu_{\text{FDDI}} = 1.808 \pm 1.154$ mV, $p = 0.295$, paired t-test). Inhibition in the distal dendrites may not shunt the peak amplitude of fast AMPA-mediated EPSPs from the basal dendrites, but could reduce the total charge. We did not, however, observe any significant change in the integral of the EPSPs ($\mu_{\text{ctrl}} = 0.08 \pm 0.057$ mV*ms, $\mu_{\text{FDDI}} = 0.074 \pm 0.048$ mV*ms, $p = 0.15$, paired t-test).

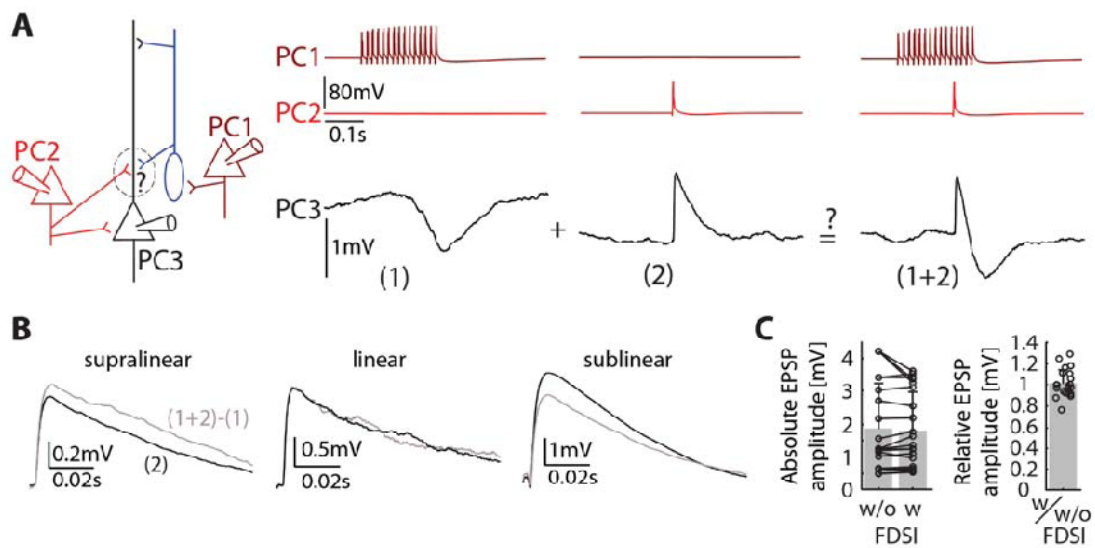


Figure 3. FDDI and EPSPs from neighboring PCs summate on average linearly. (A) Sketch of the experimental setup and stimulation protocol. PC 1 connects via an unpatched MC to PC 3, giving rise to FDDI upon high frequency stimulation (15 APs at 70 Hz). PC 2 is directly connected to PC 3 and triggers an EPSP upon stimulation (1 AP, timed to be between the onset and the half-amplitude of FDDI). High frequency stimulation in PC 1 (dark red) with corresponding FDDI in PC 3 (left column), single AP stimulation in PC 2 (red) with resulting EPSP in PC 3 (middle column), and synchronous stimulation (high frequency and single AP in PC 1 and 2, respectively) with the resulting response in PC 3. (B) Examples of supralinear, linear, and sublinear summation of EPSP and FDDI. The black traces show EPSPs triggered by an AP in PC 2, and the gray traces show a subtraction of the EPSP – FDDI trace (synchronous stimulation of PC 1 & 2) minus the FDDI trace (stimulation of PC 1 only). (C) Comparison of the absolute EPSP amplitudes, in control condition (w/o FDSI) and with synchronously activated FDDI (w FDSI), and relative EPSP amplitude (ratio of EPSP amplitude with FDSI activation divided by control EPSP amplitude). Error bars (C) denote s.d.

Next, we used the same protocol to investigate the summation of FDDI with excitatory input to the apical dendrite (Figure 4A, B). Instead of stimulating a neighboring PC, we synchronously injected a brief current (aEPSP) into the trunk of the apical dendrite that mimicked EPSP kinetics ($\tau_{\text{rise}} = 0.5$ ms, $\tau_{\text{decay}} = 2$ ms) and amplitude (200 – 500 pA, tuned to match a somatic voltage depolarization of 1 – 4 mV). The somatic amplitude and integral of dendritic aEPSPs was reduced by FDDI input in a distance dependent manner (Figure 4C, D) and as a function of the number of presynaptic PCs (Figure 4E).

These data suggest that FDDI is more effective in shunting synaptic input from the apical and tuft dendrites than input from the basal dendrites, revealing a dual and separable action between layer 5 PCs; direct excitation mostly onto basal dendrites, and indirect inhibition mostly

onto the apical and tuft dendrites. This finding is supported by the anatomical separation of the inputs (Figure 1A, see also (Somogyi et al., 1998, Silberberg and Markram, 2007, Markram et al., 1997a)).

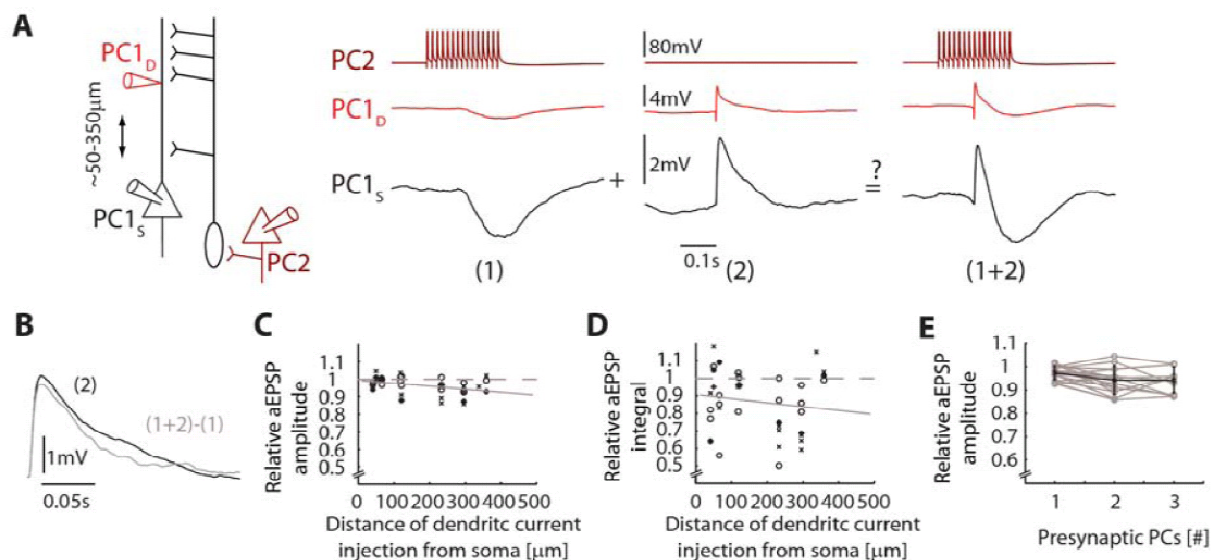


Figure 4. FDDI summates sublinearly artificial EPSP (aEPSP) evoked at the apical dendrite. (A) Sketch of the experimental setup and stimulation protocol. PC 2 connects via an unpatched MC to PC 1, giving rise to FDDI upon high frequency stimulation (15 APs at 70 Hz). Patch electrode 1 (labeled PC 1D, red) injects a current mimicking an aEPSP in the apical dendrite of PC 1 during the rising phase of the FDDI. High frequency stimulation of PC 2 (dark red) with corresponding FDDI in PC 1 (left column), aEPSP stimulation with electrode 1 with resulting “EPSP” in the soma of PC 1 (labeled PC 1S, black) (middle column), and synchronous stimulation (high frequency stimulation in PC 2 and aEPSP stimulation via PC 1D, respectively) with the resulting response in PC 1S (right column). **(B)** Example traces of sublinear summation of an aEPSP and FDDI. The black trace shows an aEPSP at the soma of PC 1 that was triggered by PC 1D, and the gray trace shows a subtraction aEPSP FDDI trace (synchronous stimulation of PC 2 & PC 1D) – FDDI trace (stimulation of PC 2). **(C)** Distance dependence (distance between dendritic patch electrode and the soma) of the relative aEPSP amplitude, calculated as the ratio of the aEPSP amplitude with FDDI activation divided by control aEPSP amplitude without FDDI activation. Linear fit was $A = -0.0001695x + 0.99329$ (A, relative amplitude; x, distance from soma). **(D)** Distance dependence (distance between dendritic patch Results electrode and the soma) of the relative aEPSP integral, calculated as the ratio of aEPSP integral with FDDI activation divided by control aEPSP integral without FDDI activation. Linear fit was $I = -0.00022643x + 0.90711$ (I, relative integral; x, distance from soma). **(E)** Relative aEPSP amplitude as a function of the number of PCs triggering FDDI. Note the broken ordinates for panels (C-E). Error bars (E) denote s.d.

FDDI mediated by few MCs

We performed a set of experiments to estimate the number of MCs that are required to activate the inhibition between any two PCs. We stimulated a presynaptic PC that synapses onto an MC, which in turn projects to another PC (Figure 5A). Every other iteration, the MC was prevented from discharge by a hyperpolarizing step current, thereby isolating the effect of this one MC on the FDDI recorded in the postsynaptic PC. FDDI amplitude was reduced to 47.5 ± 38.1 % (integral to 45.3 ± 35 %) when the single MC was prevented from participating (Figure 5B, $n = 7$, amplitude: $\mu_{wMC} = 0.692 \pm 0.417$ mV, $\mu_{w/oMC} = 0.460 \pm 0.446$ mV, $p = 0.0011$, integral: $\mu_{wMC} = 0.08 \pm 0.082$ mV*ms, $\mu_{w/oMC} = 0.053 \pm 0.049$ mV*ms, $p = 0.1148$, paired t-tests). These results show that, although on average multiple MCs participate in FDDI, a single MC can make a significant contribution to the overall FDDI produced in a target PC. The exact number of intermediate MCs is not straightforward to extrapolate. Assuming linear amplitude summation of the MCs' IPSPs, 3 MCs ($\mu_{wMC}/(\mu_{wMC} - \mu_{w/oMC})$) participate on average in FDDI upon stimulation of one layer 5 PC (range 1 – 28 MCs). By hyperpolarizing the recorded MC, however, we might have further prevented spiking in neighboring MCs due to electrical coupling. Figure 5C shows an example of two MCs coupled via gap junctions. Their coupling coefficient was 0.11 for hyperpolarizing step currents, which is within the range that has been found in previous studies (Gibson et al., 1999, Galarreta and Hestrin, 1999). Due to low pass filtering, miniature EPSPs in one MC do not pass to the other MC (arrows in Figure 5C). For the same reason, the coupling coefficient was only 0.02 for action potentials. Thus, gap junctions can only play a role in the communication in the FDDI network if synaptic summation is sufficiently slow.

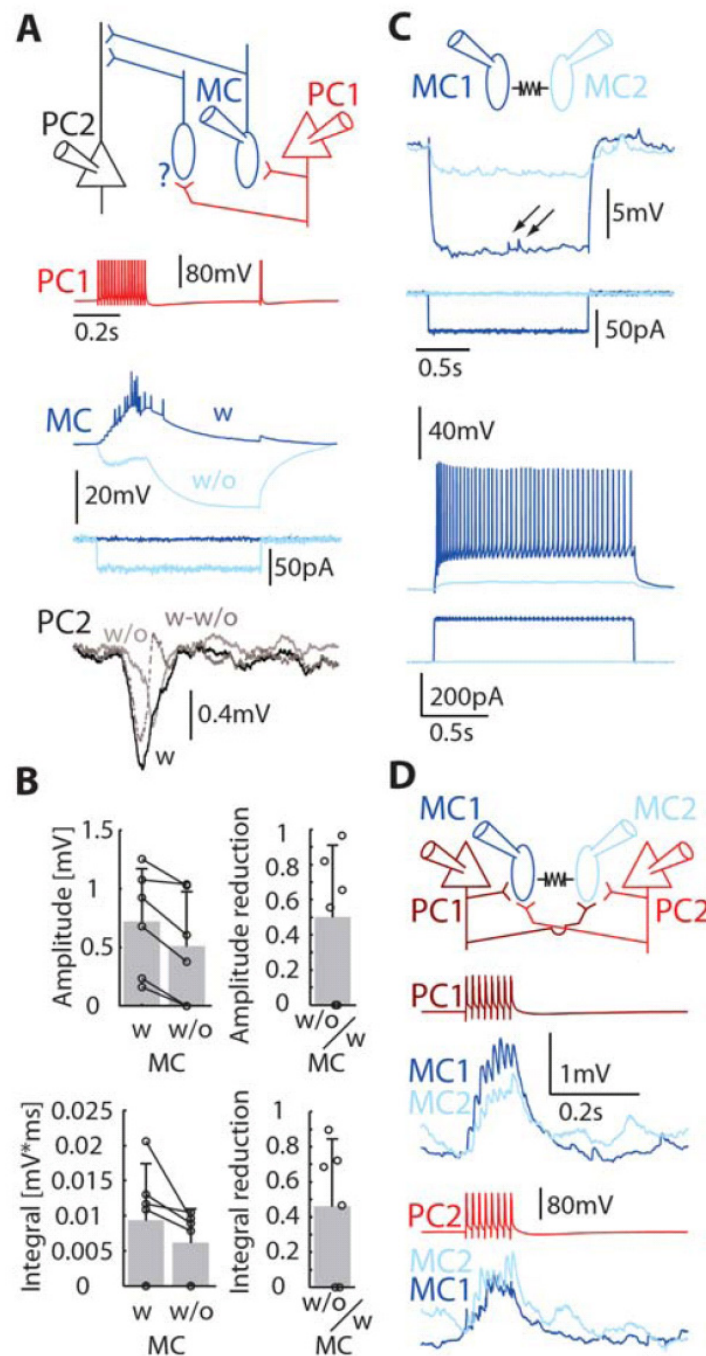


Figure 5. Few MCs mediate FDDI. (A) Sketch of the experimental setup and stimulation protocol. PC 1 connects to MC 2, which in turn inhibits PC 2. Possible other MCs (labeled with a question mark) might mediate FDDI between PC 1 and PC 3. High frequency stimulation (15 APs at 70 Hz) of PC 1 (red) results in spiking in the postsynaptic MC in control condition (blue trace, average of 12 iterations), but only if the MC is not inhibited by a hyperpolarizing current step (light blue trace, -40 pA). The resulting FDDI in PC 2 is depicted in the bottom panel, with the control condition (black), the recorded MC inhibited (light gray), and the subtraction control – inhibited (dashed gray). In this example there was/were (an)other MC(s) mediating FDDI. (B) Absolute (left bar graph) and subtractive (right bar graph)

comparison of FDDI amplitude (top panels) and integral (bottom panels) with and without the contribution of a FDDI-mediating MC. **(C)** 2 MCs connected with a gap junction. A hyperpolarizing step current was injected into one cell (blue), leading to a (weaker) hyperpolarization in the electrically coupled cell (light blue). The arrows mark EPSPs in the blue cell that do not pass through the gap junction. A depolarizing step current injected into one cell leads to spiking (blue trace), but to a very mild depolarization in the coupled cell only (light blue trace). APs do not pass efficiently through gap junctions. **(D)** The same 2 MCs were both postsynaptic to 2 PCs (top, sketch). Stimulation of PC1 (middle, dark red) or PC 2 (bottom, red) led to facilitating EPSPs in both of the MCs. Error bars **(B)** denote s.d.

The same two MCs were targeted by two PCs that were patched at the same time (Figure 5D) providing direct evidence for PC-MC divergent and PC-MC convergent connectivity. We also found multiple cases of MC-PC divergent connectivity (data not shown). Interconnectivity between PCs and MCs is the basis for the convergence/divergence ratio of FDDI between PCs. In Figure 6A, we compare these ratios for direct EPSPs and FDDI. For clusters of 3 or more simultaneously patched PCs we stimulated a single PC and determined the ratio of postsynaptic PCs that were connected (divergence, examples drawn in gray). Also, we calculated the ratio of how many presynaptic PCs from which a single PC got inputs (convergence, examples drawn in black). For direct EPSPs the distributions for convergence and divergence do not differ significantly (χ^2 -test, $p = 0.11$). In the case of FDDI we see a significant difference between convergence and divergence ($p < 0.00001$). For example, we saw a higher occurrence of PCs that get convergent input from only a fraction of PCs (black arrows) than PCs that give divergent input to only a ratio of simultaneously recorded PCs. Also, PCs had a far greater tendency to *transmit* inhibition to all recorded PCs than to *receive* inhibition from all PCs (gray arrow). Thus, divergence seems to be an all-or-none principle, whereas the ratio of connected PCs for convergence was more diffusely distributed. Therefore, FDDI seems to affect, once activated, the whole population of neighboring PCs in a global manner rather than only specific subsets of cells. A likely reason for this could be that the efficacy of the PC-MC connection constitutes the bottleneck of FDDI – it needs to be strong enough to cause spiking in the MCs. If it succeeds, then, due to the high MC-PC connectivity, most of the neighboring PCs are inhibited.

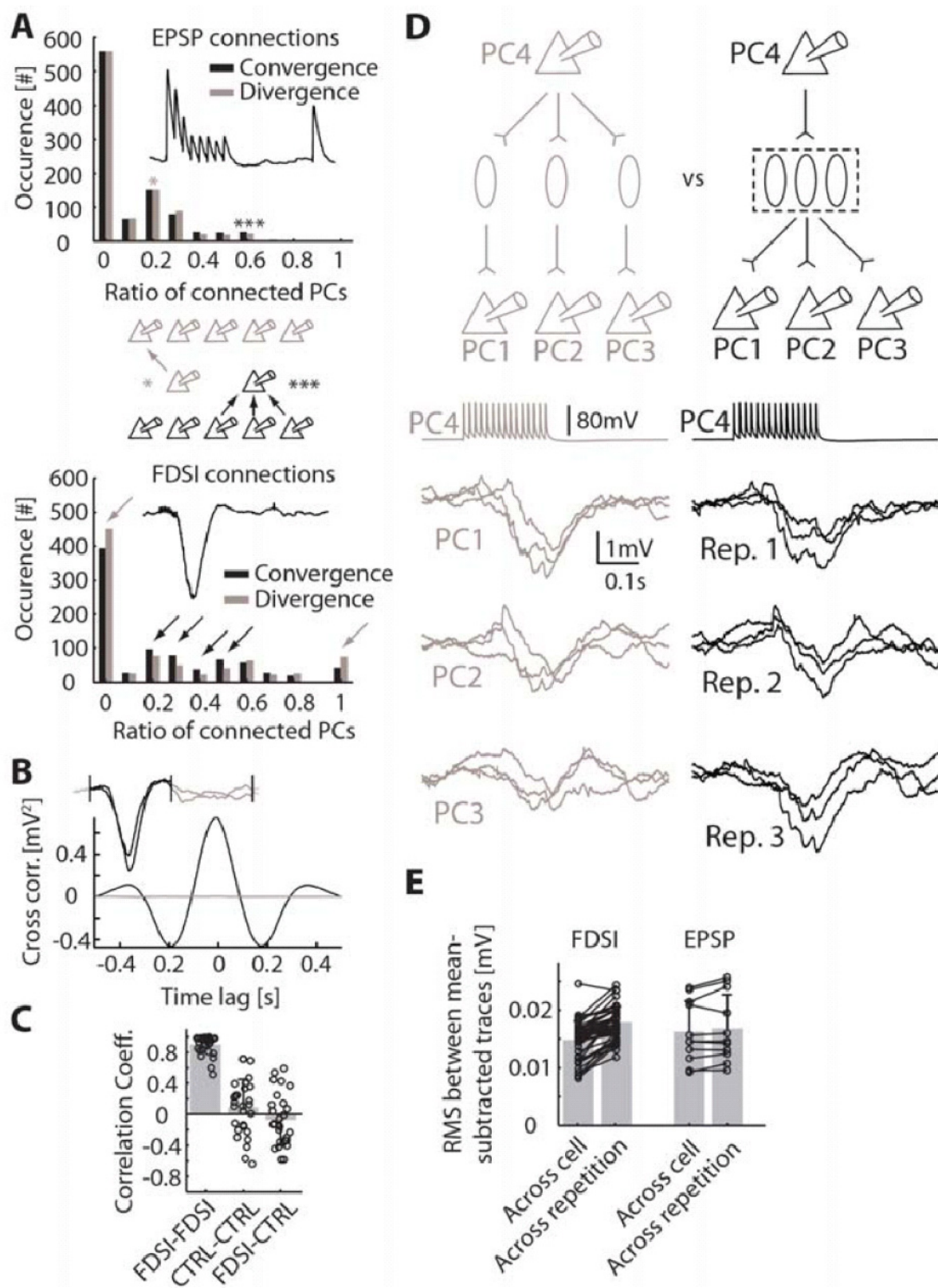


Figure 6. FDDI correlates subthreshold membrane potential in PCs. (A) Ratio of connected PCs that converged (black) or diverged (gray) to or from a post- or presynaptic PC. Top bar graph shows the ratios for EPSPs, bottom bar graph for FDDI. Arrows in the bottom bar graph indicate the combination of an absolute and relative occurrence difference of 10 and 10%, respectively. Below the top graph divergence (gray, one star, connectivity ratio 0.2) and convergence (black, 3 stars, connectivity ratio 0.6) examples are given. (B) Cross-correlation of averaged FDDI responses (black, time interval containing actual FDDI responses; gray, time interval 0.6 s after FDDI responses). Inset shows the averaged FDDI traces. (C) Correlation coefficient for simultaneously recorded FDDI responses in different PCs (FDDI-FDDI) and control conditions (CTRL-CTRL, correlation coefficient measured 0.6 s after FDDI response, see gray colored interval in the inset of (B); FDDI-CTRL, FDDI present in one PC but not in the other). (D) Sketch of experimental setup and stimulation protocol. Stimulation of PC 4 triggers FDDI in several postsynaptic PCs (1 – 3), which could be mediated in principle for each PC by a separate MC (PC-MC convergence, left, gray), or by one MC (or a pool acting as a functional unit) alone for all PCs (right, black). 3 responses following stimulation of PC 4, arranged according to the different cells (left, gray) and to the different repetitions (right, black). (E) Root mean square (RMS) between mean-subtracted traces for conditions across cell (different cells, same repetition) and across repetition (same cells, different repetition), showing for FDDI (left) higher trial-to-trial variability of identical PCs than PC-to-PC variability of the same trial. Divergent excitatory connections (EPSP, right) do not show this difference. Error bars (C,E) denote s.d.

FDDI correlates subthreshold activity between neighboring PCs

The high degree of interconnectivity between PCs and MCs results in subthreshold correlations between PCs (Figure 6B,C), showing a high correlation coefficient for simultaneous FDDI in different PCs ($n = 28$, $\mu_{\text{FDDI-FDDI}} = 0.892 \pm 0.125$), and significantly lower ones for control conditions ($n = 28$, $\mu_{\text{CTRL-CTRL}} = 0.085 \pm 0.364$, $n = 26$, $\mu_{\text{FDDI-CTRL}} = -0.070 \pm 0.331$, $p < 0.00001$, ANOVA with Scheffe correction). This correlation was calculated with average traces and is therefore based on mean responses. In order to estimate the similarity of FDDI in different PCs arising from stimulating a single PC, we further performed a trial-to-trial analysis of divergent FDDI responses. In principle, the high divergence of FDDI may be mediated by a high degree of divergence from PCs onto many different MCs and/or a high degree of divergence from MC to PCs (see Figure 6D for illustration). To quantify the amount of common FDDI input we defined a “Dissimilarity Index” (DI), which is the root mean squared of mean subtracted traces (see Methods). DI was calculated between pairs of single trial traces, either between simultaneous traces of different cells, or, as a control, between traces of the same (or different, data not shown) cells but from different trials. If each postsynaptic PC receives FDDI from a different set of interneurons (as illustrated in the left part of Figure 6D), the inhibitory response in the different postsynaptic PCs would not co-vary from trial to trial. In this scenario, single trials of FDDI between different PCs should be strongly dissimilar (high DI, as control). If each postsynaptic

PC received common input from the same set of interneurons (right part of Figure 6D), single-trial FDDI responses between different PCs should be more similar (low DI, smaller than control). In all tested cases except one, we found a lower DI of simultaneously acquired traces than that of non-simultaneously acquired traces, indicating a high degree of common input. The data of the illustrated example as well as 43 more cases suggest high MC to PC divergence (Figure 6F, $n = 44$, $\mu_{ac} = 0.0148 \pm 0.0033$ mV, $\mu_{ar} = 0.0178 \pm 0.0028$ mV, $p = 2e-12$, paired t-test). Direct connections diverging from a PC to 2 or more postsynaptic PCs did not have a significantly different DI ($n = 11$, $\mu_{ac} = 0.0162 \pm 0.0054$ mV, $\mu_{ar} = 0.0168 \pm 0.0058$ mV, $p = 0.1063$, paired t-test). These results show that divergent FDDI from a single PC onto multiple neighboring PCs is not because of a large set of MCs, but can be accounted for by a highly divergent MC-PC connectivity. Combined with these findings on the contribution of a single MC on FDDI (Figure 5A-C), we conclude that the high prevalence of FDDI is supported by both PC-MC divergence as well as a high degree of MC-PC divergent connectivity. This MC-PC divergence causes the inhibitory inputs onto neighboring PC to be precisely timed, and, together with the mean-based correlations (Figure 6B), enables FDDI to facilitate synchronization of PC activity.

Diversity of FDDI summation and cooperativity

Next, we investigated the spatial and temporal integration properties of FDDI in a single PC when multiple presynaptic PCs are stimulated at the same time. Figure 7A shows that an increased number of stimulated PCs lead to a reduced delay of MC firing. The MC was recorded in cell-attached mode so that the intracellular medium remained undisturbed. Not only the discharge onset is earlier by tens of milliseconds ($\mu_{3pre} = 0.114 \pm 0.021$ s, $\mu_{2pre} = 0.202 \pm 0.036$ s, $p = 0.000021$, two-sample t-test), also the number of APs fired by the MC increases (Figure 7B). Figure 7C shows the same type of experiment with the MC recorded in whole-cell mode. Stimulation of two PCs simultaneously can lead to earlier and more spikes (Rep. 1, black traces), a PC-MC convergence configuration, which would lead to earlier and larger FDDI in a PC postsynaptic to the MC (supralinear summation). On the other hand, simultaneous stimulation may also lead to earlier MC spiking only (Rep. 2, gray traces), which should lead to reduced FDDI amplitude in postsynaptic PCs (sublinear summation). In view of the latency shortening

and increased discharge in MCs, we analyzed both amplitudes and onset latencies of FDDI mediated by several presynaptic PCs onto a single postsynaptic one (Figure 7D-F, Figure 8).

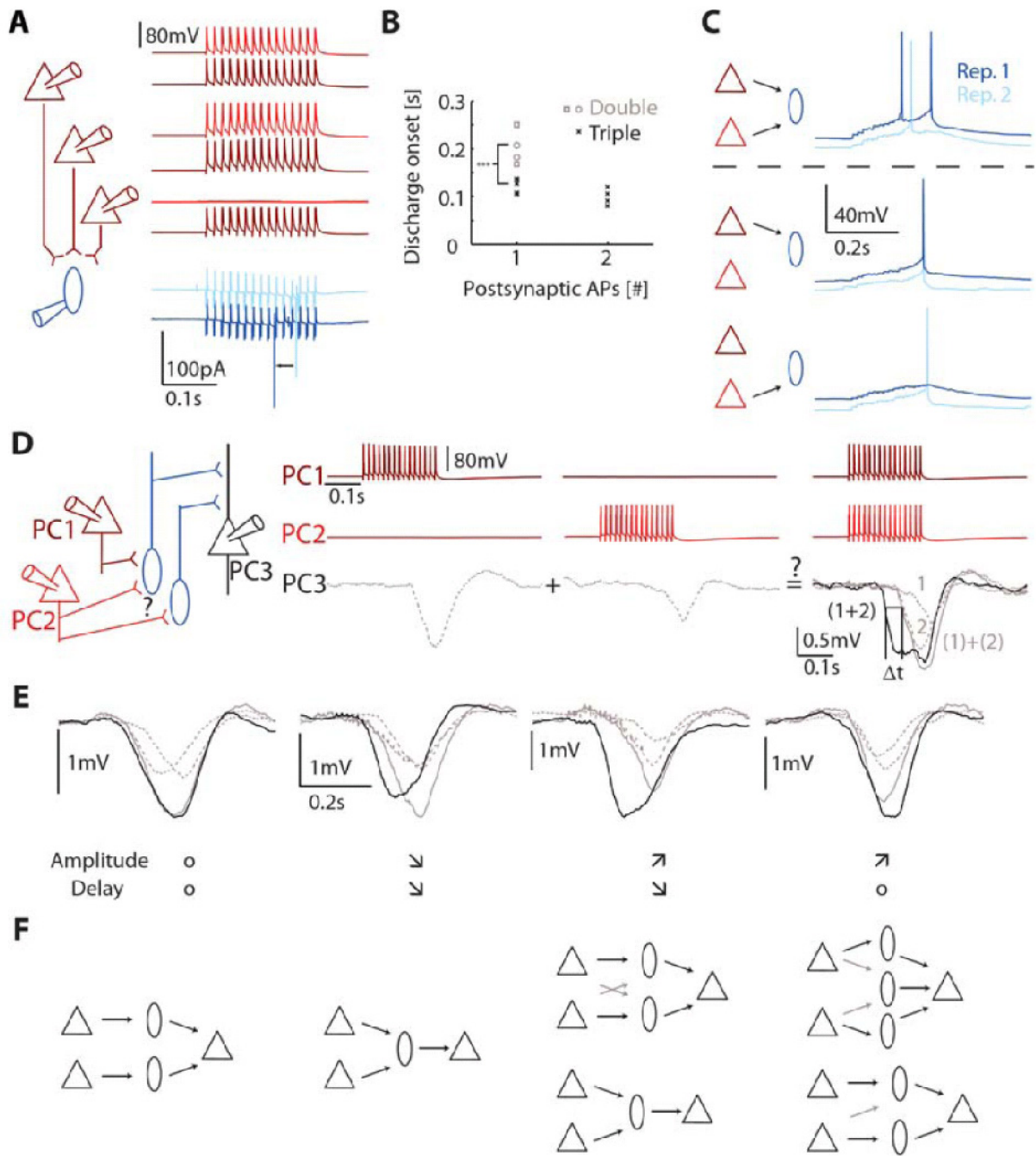


Figure 7. Summation properties indicate network configuration. (A,B) PC-MC convergence leads to a reduced latency of MC spiking and increases number of MC spikes. (A) 2 out of 3 (gray traces) or 3 out of 3 PCs (black), all presynaptic to an MC recorded in the cell-attached mode, were stimulated with a high frequency (15 APs at 70 Hz). Stimulation of 3 PCs led to a reduced delay in the spiking response of the MC. (B) Discharge onset during stimulation of 2 (gray, double) or 3 PCs (black, triple). Stimulation of 3 PCs occasionally led to 2 postsynaptic APs in the MC. (C) Stimulation of 2 PCs converging onto a postsynaptic MC (recorded in the whole-cell mode) can lead to more and earlier APs in the MC (black trace) or to an earlier single AP only (gray trace) as compared to single PC stimulation. (D-F) Summation properties of FDDI partially explain underlying connectivity pattern. (D) Sketch of experimental setup and stimulation protocol. High frequency stimulation (15 APs at 70 Hz) in PC 1 or PC 2 with corresponding FDDI in PC 3 (left or middle column), and simultaneous stimulation of PC 1 and PC 2 with FDDI response in PC 3 that has an earlier onset (right column). (E) Different scenarios of summation showing either no difference, reduced delay with reduced amplitude, or increased peak amplitude with and without reduced delay (same color code as in panel (D)). (F) Underlying connectivity patterns that can explain the summation properties. Note that these connectivity schemes show the simplest scenarios, with the minimal number of mediating MCs needed, see Results.

Similarly to the previous summation experiments we compared FDDI in response to synchronous stimulation of two PCs (Figure 7D, black traces in the right column) to the offline calculated sum of the separate stimulations (left and middle column, gray dashed traces, and gray traces in right column). As expected, a variety of different responses were found (Figure 7E), ranging from linear summation (left), reduced amplitude with reduced onset delay (left middle), increased amplitude with reduced onset delay (right middle), and increased amplitude with same delay (right). Possible underlying connectivity schemes are depicted in Figure 7F. In cases where the onset delay was shortened, it is very likely that the FDDI is mediated by MCs receiving convergent common excitation from both PCs. The common input decreases the discharge onset of the MC(s) and results in earlier onset of inhibition (see Figure 7A-C). Networks that did not exhibit a latency decrease following costimulation may also involve MCs receiving common input, but not exclusively (Figure 7F, right). The origin of amplitude summation is more complicated, since both supra- and sublinear summation can be explained by convergent PC-MC inputs: if an intermediate MC can be reliably activated only by convergent input, this will result in an average supralinear increase in amplitude (Figure 7F). However, if an MC discharges reliably following inputs from both PCs individually, such that co-activation does not significantly increase the number of APs, the result is sublinear amplitude summation. Our results show that on average the latency was shortened by 33.7 ± 35.8 ms ($n = 103$, $p < 0.0001$, two-tailed t-test), and the amplitude increase was supralinear ($\mu_{\text{sync}} = 1.232 \pm 0.723$ mV, $\mu_{\text{summed}} = 1.111 \pm 0.877$ mV, $n = 103$, $p = 0.00096$, paired t-test). These results indicate that co-stimulation

of presynaptic PC pairs increases FDDI in a supralinear manner due to the high degree of PC-MC convergence.

Few PCs saturate FDDI

How does FDDI summate when more than two neighboring PCs are active? We stimulated an increasing number of PCs and recorded FDDI in another PC (Figure 8A, gray shades of the traces according to the number of stimulated cells). FDDI monotonically increased in amplitude and voltage integral, which saturated when 8 – 9 PCs were simultaneously stimulated (Figure 8B). In order to compare the pooled data of many recorded clusters, we defined a nonlinearity index for amplitude and integral summation (Kapfer et al., 2007). FDDI summated on average supralinear for the amplitude as well as for the integral following stimulation of two presynaptic PCs (Figure 8C, $n = 103$, $p_{\text{amp}} = 1.977\text{e-}6$, $p_{\text{int}} = 2.710\text{e-}13$, one-sample t-test). Stimulation of 3 (Figure 8D) or more (Figure 8E and Figure S1 in the Supplemental Data available with this article online) presynaptic PCs increased the supralinearity of integral and amplitude of FDDI, and also decreased the onset delay. Saturation levels of amplitude and integral difference were reached at around 60% and 70% when 6 – 7 PCs were stimulated simultaneously (Figure 8E). A remarkable feature of FDDI was its abundance in the layer 5 network. Upon stimulation of 4 PCs simultaneously *all* recorded neighboring PC were inhibited (Figure 8F).

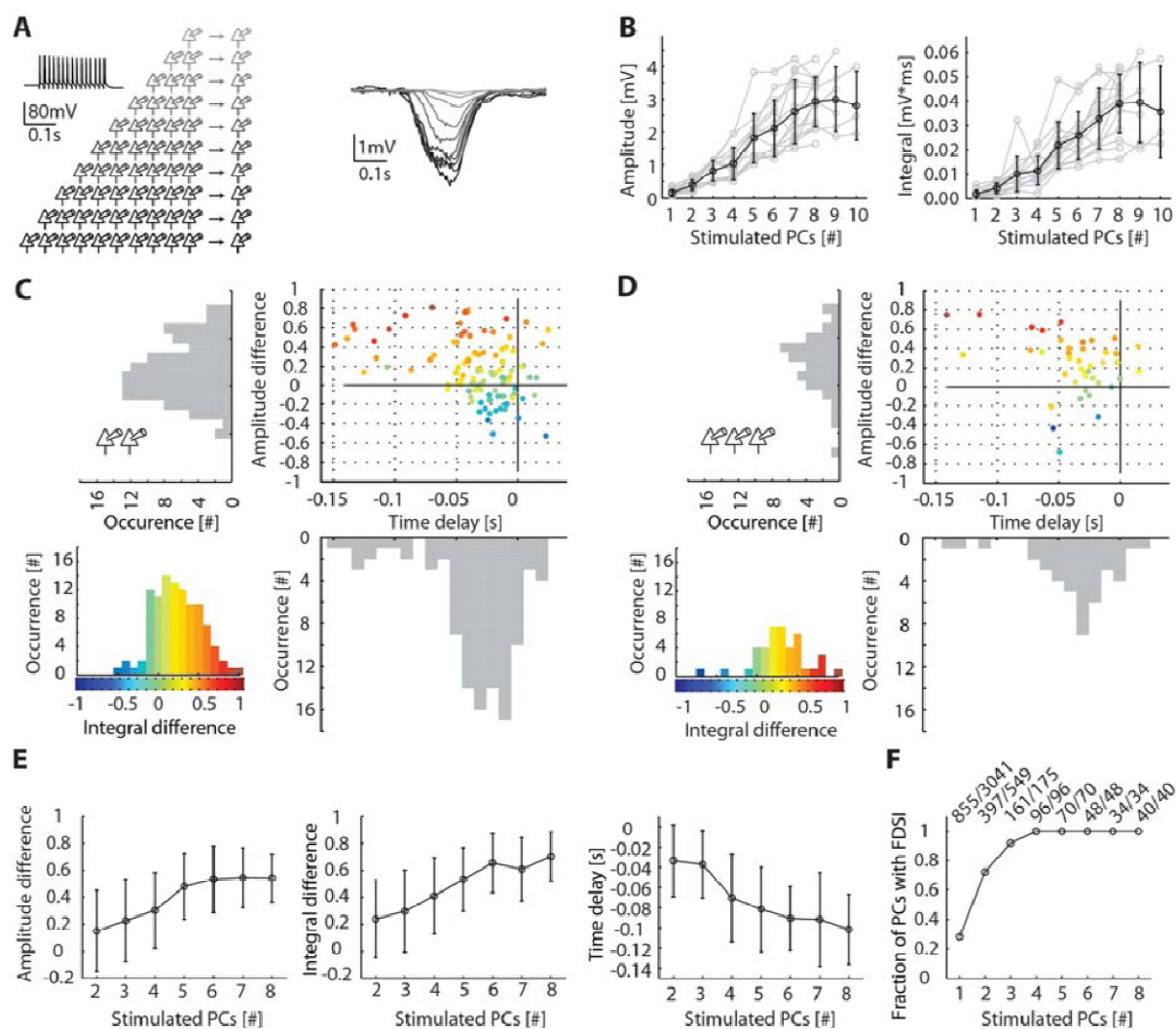


Figure 8. FDDI saturates at resting conditions with few stimulated PCs. (A) Sketch of experimental setup and example traces. Up to 10 cells were stimulated simultaneously (left). FDDI in response to 1 – 10 PCs stimulated (15 APs at 70 Hz, right). (B) FDDI amplitude and integral as a function of PCs stimulated. (C) Summation properties of FDDI elicited by 2 presynaptic PCs. Histograms show amplitude and integral difference as well as the time delay. A positive amplitude (integral) difference means that synchronous stimulation of the two PCs gave a larger FDDI amplitude than the offline summed response of the individually evoked FDDIs. A more negative time delay shows an earlier response of the synchronously evoked FDDI as compared to the summed response of the individually evoked FDDIs. (D) Summation properties of FDDI elicited by 3 presynaptic PCs. Same labeling as in (C). (E) Saturation of FDDI as a function of the number of stimulated PCs for amplitude and integral difference and time delay. (F) Fraction of PCs displaying FDDI as a function of number of PCs stimulated. Error bars (B,E) denote s.d.

Predicting FDDI amplitude from number and frequency of stimulated PCs

Finally, we varied the number of stimulated cells along with the stimulation frequency (Figure 9A, 1 – 4 cells stimulated with 15 APs at 10, 20, 40, 70, and 100 Hz, average data from 4 different experiments). Thereby, we found isoclines that revealed equivalent effectiveness of various numbers of stimulated cells and stimulation frequency. For example, the FDDI amplitude when stimulating 2 PCs with 70 Hz was similar when 4 PCs were stimulated with 40 Hz (Figure 9B). An extrapolation of these results, based on a linear 2D fit (Figure 9B), allow the prediction of the FDDI amplitude generated by a larger number of cells (Figure 9C). The linear extrapolation is not likely to hold for very high frequencies (due to refractoriness, synaptic depression, etc.) nor for a very large number of cells due to saturation of the disynaptic response (see Figure 7,8). The number of APs required to initiate FDDI is depicted in Figure 9D.

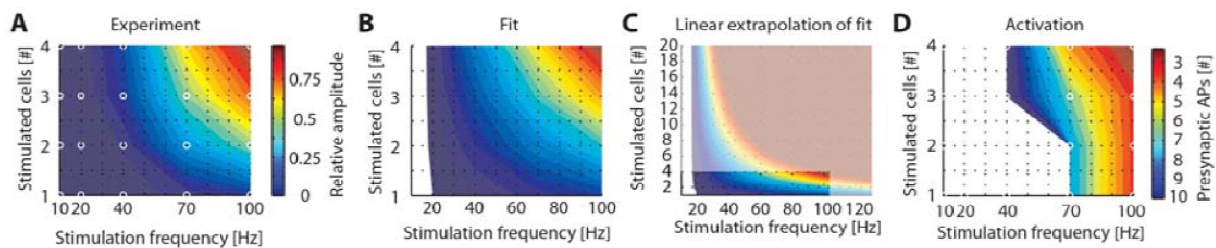


Figure 9. FDDI depending on stimulation frequency and number of stimulated cells. (A) 1 – 4 cells were stimulated with 10, 20, 40, 70, or 100 Hz (always 15 APs). The resulting FDDI amplitudes (white circles) were used to generate a color-coded contour plot, with the colors encoding the FDDI amplitudes. (B) Contour plot as in panel (A), but generated with a least square error fit according to $F = 0.0013x + 0.0558y - 0.0034xy - 0.0127$, where F is the amplitude, x the stimulation frequency, and y the number of stimulated cells. (C) Linear extrapolation of the least square error fit. (D) Number of presynaptic APs prior to FDDI onset.

DISCUSSION

This study reveals the key properties of one of the most physiologically and anatomically distinguished disynaptic inhibitory pathways in the neocortex, FDDI: the number of PCs required, divergent and convergent properties to and from MCs, spatio-temporal principles that govern the integration of the inhibition applied through this pathway, the dependency of this

form of inhibition on I_h currents, and its potential influence on the functioning of the network of thick tufted PCs in the somatosensory neocortex of juvenile rats.

Summation, saturation, and limits of FDDI recruitment

Previously, the summation properties for convergent FDDI have been investigated for 2 or 3 stimulated presynaptic PCs (Silberberg and Markram, 2007, Kapfer et al., 2007), and the activity dependent recruitment of MCs was extrapolated for the case of multiple active PCs (Kapfer et al., 2007). Here we show experimentally that every neighboring (~150 μm) thick tufted layer 5 PC is affected by FDDI when 4 or more PCs are stimulated with 70 Hz, and the FDDI amplitude saturates at the somatic recording site at resting condition when 8 – 9 PCs are stimulated simultaneously. Several reasons may underlie the observed FDDI saturation: limited recruitment of MC (due to limited connectivity or limited number of MCs), reduction in the driving-force of the inhibitory signal in the apical dendrite when it reaches the GABA_A reversal potential, saturating firing rates in MCs, and frequency dependent synaptic depression of the MC-PC connection. It is likely that all these factors contribute to this early saturation.

Summation properties as displayed in Figure 5-7 indicate that only a few MCs are actually recruited by a cluster of PCs. We cannot, however, state that MC *recruitment* is saturated by stimulation of 8 – 9 PCs since multiple MCs could mutually shunt their inhibitory signals in a postsynaptic PC and therefore mask the contribution of additional MCs to FDDI. Further, it should be considered that the saturation might not hold in different cortical activity states. A high level of excitatory synaptic input to the apical dendrite would require larger activation of the FDDI pathway in order to reach saturation.

Subthreshold correlations between PCs

Neighboring neocortical cells can show highly correlated activity patterns both *in vitro* (Sanchez-Vives and McCormick, 2000) and *in vivo* (Lampl et al., 1999, Okun and Lampl, 2008). Recently it has been shown that the synchrony of subthreshold membrane potential fluctuations depends

on the behavioural state of the animal (Poulet and Petersen, 2008). FDDI acts as a synchronizer of subthreshold membrane potential between PCs in two ways. Multiple PCs, targeted by the same MC, receive FDDI simultaneously, resulting in a high correlation coefficient (Figure 6B). This is supported by the high degree of divergence of FDDI signaling (Figure 6A). Moreover, due to the reliability of the MC-PC synapse, and its high divergence, the inter-trial variability is mainly due to the summation of the facilitating PC-MC synaptic response. A previous study has also shown that the synaptic dynamics from interneurons are virtually identical across postsynaptic neurons of the same class, which may also underlie the high subthreshold correlations mediated by MCs (Gupta et al., 2000). Simultaneous responses in different postsynaptic PCs are therefore more similar to each other than the responses of the same PC for different iterations. The high correlation in FDDI across PCs suggests that inhibitory inputs from MCs to PCs may contribute to subthreshold correlations observed between neighboring PCs under *in vivo* conditions (Lampl et al., 1999, Okun and Lampl, 2008). Photostimulation studies have suggested that interneurons with adapting firing pattern (like MCs) are less specific or selective concerning the targeting of their synaptic input and output (Yoshimura and Callaway, 2005), a finding which is in agreement with the high degree of FDDI divergence we report (Figure 6A).

FDDI targeting the apical dendrite

Several previous studies addressed the question whether two synaptic inputs of the same kind summate linearly (Urban and Barrionuevo, 1998, Schwindt and Crill, 1998, Cash and Yuste, 1999). The results depend on the location of the inputs, and most protocols resulted in a summation that was on average linear. Likewise, FDDI and EPSPs elicited from neighboring PCs summated on average linearly. On the other hand, FDDI was able to shunt inputs at the apical dendrite in a distance dependent manner. The effect was not very large (maximal reduction to 85% of the original amplitude), probably because of the distributed synaptic MCPC innervation on multiple locations of the apical and tufted dendrite (Silberberg & Markram, 2007). It is likely, however, that natural synaptic excitatory input to the apical dendrite is also distributed, and therefore prone to be affected in a non-linear manner by FDDI. Furthermore, the fact that we used fast AMPA kinetics for the aEPSPs leads to a strong underestimation of the

shunting effect by FDDI because slower kinetics, including NMDA components and EPSPs filtered by dendritic attenuation, would be more prone to shunting by FDDI.

It has been suggested previously that LTS interneurons in mice, which are presumably equivalent to MCs, control bursting in PCs (Goldberg et al., 2004). Thus, bursts in the network of layer 5 PCs might be followed by periods of insensitivity of the apical dendrite. This insensitivity does not seem to extend over inputs arriving at the basal dendrites, therefore allowing a specific gating of the apical dendrite with brief synchronous bursts of a few PCs. Thus, at certain network activity levels, associative (or top-down) input is minimized (Cauller, 1995), and the same might occur with thalamic input that is prone to delayed feed forward inhibition (Tan et al., 2008).

One speculation is that information transfer between cortical areas and between cortex and thalamus is generically modulated by a set of high-pass filters constituted by the MC population. When layer 5 PCs discharge output above a certain critical frequency, the column processes only local activity and is disconnected from more distal inputs. In contrast to other cellular filtering mechanisms like adaptive currents, the described mechanism is compartment specific. Interestingly, FDDI could also be activated by basal input only, and in this case it would not shunt its origin, but act in a feed-forward manner. It remains to be elucidated whether this is the case, or whether FDDI is mainly driven by bursts caused by calcium spikes at the apical and tuft dendrites.

I_h in PCs as a frequency-dependent gain modulator

I_h is a prominent current with increasing channel density along the dendrites of layer 5 PCs (Berger et al., 2001, Kole et al., 2006). It renders the apical (and presumably also the basal dendrites) disconnected from the soma (Berger et al., 2003) by counteracting any polarization deviating from the resting potential. The decay times of de- and hyperpolarizing inputs are substantially shortened, allowing for a higher temporal precision in the processing of information. Due to its increasing density along the dendrites it also renders EPSP shape and

time course site independent (Williams and Stuart, 2000). Here we showed that I_h can change the gain between excitation and inhibition for train stimulations, thus increasing the dynamic frequency range. A modulation of this channel conductance might be an approach to profoundly alter this inhibitory pathway (Kole et al., 2006, Berger et al., 2003). Studies showed I_h presence in MCs as well, but there seem to be exceptions to this finding, with not all MCs expressing the I_h mediated sag in response to hyperpolarizing step currents (Wang et al., 2004). We also did not find a prominent sag in MCs that participated in FDDI ($n = 3$, data not shown). It remains to be elucidated whether there are various, yet to be defined, populations of MCs, and what their relative contribution to FDDI is.

FDDI in other cell types

Several aspects of FDDI still remain to be elucidated. So far, layer 5 thick tufted PCs and layer 3 PCs have been shown to display FDDI (Silberberg and Markram, 2007, Kapfer et al., 2007). Cortical-callosal layer 5 PCs with a slender apical dendrite lacking tuft dendrites do not seem to feature this type of inhibition (Le Bé et al., 2007). Also, PCs in layer 6 do not show any measurable FDDI (Berger and Markram, unpublished data). It is however not clear whether these potential pathways require a larger number of active neurons to become observable. It remains to be shown whether other PC classes are inhibited in a similar manner, and whether this inhibition is mediated via the same MCs. Apart from the FDDI mediated within the same layer, it is possible that presynaptic activity in one layer will inhibit PCs in a different layer. Kapfer and colleagues (Kapfer et al., 2007) showed that MCs in layer 5 mediated FDDI between layer 3 PCs. It is not known, however, if these MCs also mediate FDDI onto layer 5 PCs, and whether they are recruited by layer 5 PCs. Subpopulations of SOM expressing interneurons are now GFP labeled in various mouse strains (Ma et al., 2006), facilitating future investigations of FDDI in different layers. A recent study described differences in monosynaptic excitatory connectivity between different types of layer 5 PCs (Brown and Hestrin, 2009), according to their long-range projections. It would be of great importance to determine the properties of disynaptic inhibition between these populations as well.

Modulation affecting FDDI

MCs can be modulated by various means. Acetylcholine receptor agonists lead to increased firing in MCs (Kawaguchi and Kondo, 2002), which might influence the plasticity rules at the apical dendrite of PCs (Couey et al., 2007). Compared to other cell types, they seem to be particularly susceptible to changes in the general cortical activity state (Fanselow et al., 2008). Spiking activity (in certain frequency ranges) in MCs can trigger intracellular endocannabinoid signaling that eventually leads to hyperpolarization, thus reduced excitability (Bacci et al., 2004). It remains to be elucidated which modulations play strong roles in physiological conditions, and to what extent FDDI properties presented in the present study are altered.

An aspect that is not covered in the present study is the dendritic calcium spike that emerges in older animals, above p28 (Zhu, 2000, Larkum et al., 1999, Murayama et al., 2009). FDDI could be perfectly suited both temporally and spatially to modulate or even prevent such spikes. Indeed, a recent study shows a high effectiveness of FDDI in preventing dendritic calcium spikes in behaving rodents (Murayama et al., 2009). Dendritic calcium spikes are reported to occur only after the third postnatal week in rats (Zhu, 2000), however, FDDI is already functional in younger animals, and therefore it may serve other purposes at different developmental stages.

METHODS

Slice preparation and cell identification. 14 – to 18 days old Wistar rats were quickly decapitated according to the Swiss national and institutional guidelines. The brain was carefully removed and placed in iced artificial cerebrospinal fluid (ACSF). 300 μm thick parasagittal slices of the primary somatosensory cortex (hindlimb area) were cut on a HR2 vibratome (Sigmund Elektronik, Heidelberg, Germany). Slices were incubated at 37°C for 30 – 60 min and then left at room temperature until recording. Cells were visualized by infrared differential interference contrast videomicroscopy utilizing either a C2400-03 camera (Hamamatsu, Hamamatsu City, Japan) mounted on an upright Axioscope FS microscope (Zeiss, Oberkochen, Germany), or a VX55 camera (Till Photonics, Gräfeling, Germany) mounted on an upright

BX51WI microscope (Olympus, Tokyo, Japan). Thick tufted layer 5 PCs were selected according to their large soma size (15 – 25 μm) and their apparent large trunk of the apical dendrite. Care was taken to use only “parallel” slices, i.e. slices that had a cutting plane parallel to the course of the apical dendrites and the primary axonal trunk. This ensured to have sufficient preservation of both the PCs’ and MCs’ axonal and dendritic arborizations. Some experiments included patching of MCs. They were targeted by their soma, which is oval and bitufted, and often oriented sideways.

Chemicals and solutions. Slices were continuously superfused with ACSF containing (in mM) 125 NaCl, 25 NaHCO₃, 2.5 KCl, 1.25 NaH₂PO₄, 2 CaCl₂, 1 MgCl₂, and 25 D-glucose, bubbled with 95% O₂ – 5% CO₂. The intracellular pipette solution (ICS) contained (in mM) 110 K-gluconate, 10 KCl, 4 ATP-Mg, 10 phosphocreatine, 0.3 GTP, 10 N-2-hydroxyethylpiperazine-N9-2-ethanesulfonic acid (HEPES), and 13 biocytin, adjusted to a pH 7.3 – 7.4 with 5 M KOH. Osmolarity was adjusted to 290 – 300 mosmol l⁻¹ with D-mannitol (25 –35 mM). The membrane potential values given were not corrected for the liquid junction potential, which was approximately –14 mV. 4-(*N*-ethyl-*N*-phenylamino)-1,2-dimethyl-6- (methylamino) pyridinium chloride (zd7288) was bought from Biotrend (Zurich, Switzerland), and all other drugs and chemicals were from Sigma-Aldrich (Steinheim, Germany) or Merck (Darmstadt, Germany).

Electrophysiological recordings. Multiple somatic whole cell recordings (2 – 12 cells simultaneously) were performed with Axopatch 200B or Multiclamp 700B amplifiers (Molecular Devices, Union City, CA) in the current clamp mode. In some experiments, MCs were first recorded in voltage clamp in the cell-attached configuration, leaving the intracellular medium unperturbed, and then in whole-cell mode, thus perfused with the ICS contained in the pipette. In experiments including dendritic recordings, dendrites were patched before the somata. Alexafluor594 (Invitrogen, Eugene, OR, USA) was sometimes included in the dendritic patch electrode, revealing the corresponding soma unambiguously. The temperature was $34 \pm 1^\circ\text{C}$ during recording. Data acquisition was performed via an ITC- 18 or ITC-1600 board (Instrutech Co, Port Washington, NY), connected to a PC or Macintosh running a custom written routine under IgorPro (Wavemetrics, Portland, OR). Sampling rates were 5 – 10 kHz, and the voltage signal was filtered with a 2 kHz Bessel filter. Patch pipettes were pulled with a Flaming/Brown

micropipette puller P-97 (Sutter Instruments Co, Novato, CA) and had an initial resistance of 3 – 8 M Ω (10 – 15 M Ω for dendritic patches). 3D morphological reconstruction of biocytin-labeled cells was done under an Olympus BX 51 W microscope fitted with a water-immersion 60x (numerical aperture (NA) 0.9) or an oil-immersion 100x (NA 1.35) objective using NeuroLucida software (MicroBrightField, Magdeburg, Germany).

Stimulation protocols and data analysis. Monosynaptic, direct connections were usually identified by stimulation of a presynaptic cell with a 20 Hz train of 8 strong and brief current pulses (1 – 3.5 nA, 2 – 4 ms), followed by a so-called recovery test response (RTR) 0.5 s after the end of the train, all precisely and reliably eliciting APs. Disynaptic connections were characterized by the same protocol but at a higher frequency (usually 70 Hz) and with longer trains (usually 15 APs). Postsynaptic PCs were slightly depolarized from a potential of ~ -62 mV to $-57 - -60$ mV to increase the driving force for inhibitory connections. This was usually not necessary to detect FDDI, but gave larger amplitudes occasionally. Due to the dendritic location and the resulting space clamp effect in layer 5 PCs, especially MC-PC synapses have a very hyperpolarized apparent somatic reversal potential, that deviates strongly from the calculated one (Silberberg and Markram, 2007). We did not find any depolarizing FDDI responses, possibly because we used rats older than 13 days (Khazipov et al., 2004). Connectivity ratios were calculated as the ratio between observed versus tested connections between a pair of cells. A pair of cells could therefore maximally have two connections (both directions), a triplet could have 6 connections, and a cluster of n neurons could potentially have $n * (n - 1)$ connections. Autaptic connections were not taken into consideration. The balance between de- and hyperpolarization due to FDDI and direct EPSPs as a function of stimulation frequency (Figure 2F) was calculated as the net polarization deviating from baseline in the time window starting from stimulation onset, and ending just before the RTR, i.e. 0.5 s after the stimulation train ended. Bath application of zd7288 resulted in a strong hyperpolarization of PCs ($\sim 10 - 12$ mV, (Silberberg and Markram, 2007)), which was counteracted by a positive holding current to reestablish resting membrane potential of around -60 mV. The waiting time between stimulations was 10 – 20 s. Especially for FDDI summation experiments (Figure 8,9) long waiting times were crucial as FDDI (not EPSP) amplitudes would decrease otherwise. Stimulations were given in an alternating manner (ABAB... instead of AABB...). For summation experiments in Figure 8,

linearity of amplitude (and likewise integral) was calculated as a normalized difference according to $L = (A_{\text{input}(1,2,\dots,n)} - (A_{\text{input}1} + A_{\text{input}2} + \dots + A_{\text{input}n})) / A_{\text{input}(1,2,\dots,n)}$, where $A_{\text{input}(1,2,\dots,n)}$ is the amplitude of the simultaneous stimulation, and $A_{\text{input}1} + A_{\text{input}2} + \dots + A_{\text{input}n}$ is the offline calculated sum of the separately stimulated presynaptic cells. For Figure 8C,D and S1, data were included if the FDDI evoked by synchronous stimulation exceeded 0.5 mV, as the signal-to-noise ratio was too high for the difference measures. The error bars in the figures denotes the standard deviation unless stated otherwise. All statistical analysis (paired and unpaired student's t-test, ANOVA) was done with MATLAB (The Mathworks, Natick, MA, USA). The "Dissimilarity Index" (DI) was defined as

$$DI = \left(\sum_{i=1}^n ((y_i - \hat{y}) - (z_i - \check{z}))^2 \right)^{0.5}$$

where y_i and z_i are single repetitions of different or identical cells and different or identical repetitions, and \hat{y} and \check{z} are mean responses. DI is therefore a pointwise root mean square (RMS) between mean-subtracted traces, calculated for every possible pair of traces, i.e. "across cells, same repetition", "same cell, across repetitions", and "across cells, across repetitions". It quantifies the deviation from the average response and shows whether noise coming along the FDDI signal co-varies between 2 cells or not. Given 1 stimulated presynaptic PC, 2 postsynaptic PCs receiving FDDI, and n repetitions of stimulation, one obtains n "across cells, same repetition" conditions, $n * (n + 1)/2$ "same cell, across repetitions" conditions, and $n * (n - 1)$ "across cells, across repetitions" conditions. For the latter two conditions the DI measure was nearly identical, therefore the "across cells, across repetitions" condition is not displayed in Figure 5E. DI was taken for the interval from 0 to 0.5 s after stimulation onset.

Acknowledgements

We are very grateful to Eulalie Sauthier for cellular reconstructions, the LNMC members for their continuous support, and the EUSynapse and FACETS project for funding.

REFERENCES

- Abbott, L. F., Varela, J. A., Sen, K., and Nelson, S. B. (1997). Synaptic depression and cortical gain control. *Science*, 275(5297):220–224.
- Bacci, A., Huguenard, J., and Prince, D. (2004). Long-lasting self-inhibition of neocortical interneurons mediated by endocannabinoids. *Nature*, 431:312–316.
- Berger, T., Larkum, M. E., and Lüscher, H. R. (2001). High I(h) channel density in the distal apical dendrite of layer V pyramidal cells increases bidirectional attenuation of EPSPs. *J Neurophysiol*, 85(2):855–868.
- Berger, T., Senn, W., and Lüscher, H.-R. (2003). Hyperpolarization-activated current Ih disconnects somatic and dendritic spike initiation zones in layer V pyramidal neurons. *J Neurophysiol*, 90:2428–2437.
- Brown, S. P. and Hestrin, S. (2009). Intracortical circuits of pyramidal neurons reflect their long-range axonal targets. *Nature*.
- Cash, S. and Yuste, R. (1999). Linear summation of excitatory inputs by CA1 pyramidal neurons. *Neuron*, 22:383–394.
- Cauler, L. (1995). Layer I of primary sensory neocortex: where top-down converges upon bottom-up. *Behav Brain Res*, 71(1-2):163–170.
- Couey, J., Meredith, R., Spijker, S., Poorthuis, R., Smit, A., Brussaard, A., and Mansvelder, H. (2007). Distributed network actions by nicotine increase the threshold for spike-timing dependent plasticity in prefrontal cortex. *Neuron*, 54:73–87.
- DeFelipe, J., Alonso-Nanclares, L., and Arellano, J. I. (2002). Microstructure of the neocortex: comparative aspects. *J Neurocytol*, 31(3-5):299–316.
- Douglas, R. J. and Martin, K. A. C. (2004). Neuronal circuits of the neocortex. *Annu Rev Neurosci*, 27:419–451.
- Fanselow, E. E., Richardson, K. A., and Connors, B. W. (2008). Selective, state-dependent activation of somatostatin-expressing inhibitory interneurons in mouse neocortex. *J Neurophysiol*, 100(5):2640–2652.
- Galarreta, M. and Hestrin, S. (1998). Frequency-dependent synaptic depression and the balance of excitation and inhibition in the neocortex. *Nat Neurosci*, 1(7):587–594.
- Galarreta, M. and Hestrin, S. (1999). A network of fast-spiking cells in the neocortex connected by electrical synapses. *Nature*, 402(6757):72–75.
- Gibson, J. R., Beierlein, M., and Connors, B. W. (1999). Two networks of electrically coupled inhibitory neurons in neocortex. *Nature*, 402(6757):75–79.
- Goldberg, J., Lacefield, C., and Yuste, R. (2004). Global dendritic calcium spikes in mouse layer 5 low threshold spiking interneurons: implications for control of pyramidal cell bursting. *J. Physiol. (Lond.)*, 558:465–478.
- Gupta, A., Wang, Y., and Markram, H. (2000). Organizing principles for a diversity of GABAergic interneurons and synapses in the neocortex. *Science*, 287(5451):273–278.
- Kapfer, C., Glickfeld, L. L., Atallah, B. V., and Scanziani, M. (2007). Supralinear increase of recurrent inhibition during sparse activity in the somatosensory cortex. *Nat Neurosci*, 10(6):743–753.
- Kawaguchi, Y. and Kondo, S. (2002). Parvalbumin, somatostatin and cholecystokinin as chemical markers for specific GABAergic interneuron types in the rat frontal cortex. *J. Neurocytol.*, 31:277–287.
- Khazipov, R., Khalilov, I., Tyzio, R., Morozova, E., Ben-Ari, Y., and Holmes, G. (2004). Developmental changes in GABAergic actions and seizure susceptibility in the rat hippocampus. *Eur. J. Neurosci.*, 19:590–600.
- Kole, M., Hallermann, S., and Stuart, G. (2006). Single Ih channels in pyramidal neuron dendrites: properties, distribution, and impact on action potential output. *J. Neurosci.*, 26:1677–1687.
- Lampl, I., Reichova, I., and Ferster, D. (1999). Synchronous membrane potential fluctuations in neurons of the cat visual cortex. *Neuron*, 22(2):361–374.
- Larkum, M., Zhu, J. J., and Sakmann, B. (1999). A new cellular mechanism for coupling inputs arriving at different cortical layers. *Nature*, 398(6725):338–341.
- Le Bé, J., Silberberg, G., Wang, Y., and Markram, H. (2007). Morphological, electrophysiological, and synaptic properties of corticocortical pyramidal cells in the neonatal rat neocortex. *Cereb. Cortex*, 17:2204–2213.
- Ma, Y., Hu, H., Berrebi, A., Mathers, P., and Agmon, A. (2006). Distinct subtypes of somatostatin-containing neocortical interneurons revealed in transgenic mice. *J. Neurosci.*, 26:5069–5082.
- Markram, H., Lübke, J., Frotscher, M., Roth, A., and Sakmann, B. (1997). Physiology and anatomy of synaptic connections between thick tufted pyramidal neurons in the developing rat neocortex. *J. Physiol. (Lond.)*, 500 (Pt 2):409–440.
- Markram, H., Wang, Y., and Tsodyks, M. (1998). Differential signaling via the same axon of neocortical pyramidal neurons. *Proc Natl Acad Sci U S A*, 95(9):5323–5328.

- Monier, C., Chavane, F., Baudot, P., Graham, L. J., and Frégnac, Y. (2003). Orientation and direction selectivity of synaptic inputs in visual cortical neurons: a diversity of combinations produces spike tuning. *Neuron*, 37(4):663–680.
- Murayama, M., Pérez-Garci, E., Nevian, T., Bock, T., Senn, W., and Larkum, M. E. (2009). Dendritic encoding of sensory stimuli controlled by deep cortical interneurons. *Nature*, 457(7223):1137–1141.
- Okun, M. and Lampl, I. (2008). Instantaneous correlation of excitation and inhibition during ongoing and sensory-evoked activities. *Nat Neurosci*, 11(5):535–537.
- Poulet, J. F. A. and Petersen, C. C. H. (2008). Internal brain state regulates membrane potential synchrony in barrel cortex of behaving mice. *Nature*, 454(7206):881–885.
- Ren, J. Q., Aika, Y., Heizmann, C. W., and Kosaka, T. (1992). Quantitative analysis of neurons and glial cells in the rat somatosensory cortex, with special reference to gabaergic neurons and parvalbumin-containing neurons. *Exp Brain Res*, 92(1):1–14.
- Reyes, A., Lujan, R., Rozov, A., Burnashev, N., Somogyi, P., and Sakmann, B. (1998). Target- cell-specific facilitation and depression in neocortical circuits. *Nat Neurosci*, 1(4):279–285.
- Sanchez-Vives, M. V. and McCormick, D. A. (2000). Cellular and network mechanisms of rhythmic recurrent activity in neocortex. *Nat Neurosci*, 3(10):1027–1034.
- Schwindt, P. and Crill, W. (1998). Synaptically evoked dendritic action potentials in rat neocortical pyramidal neurons. *J. Neurophysiol.*, 79:2432–2446.
- Shu, Y., Hasenstaub, A., and McCormick, D. A. (2003). Turning on and off recurrent balanced cortical activity. *Nature*, 423(6937):288–293.
- Silberberg, G. (2008). Polysynaptic subcircuits in the neocortex: spatial and temporal diversity. *Curr Opin Neurobiol*.
- Silberberg, G. and Markram, H. (2007). Disynaptic inhibition between neocortical pyramidal cells mediated by martinotti cells. *Neuron*, 53(5):735–746.
- Somogyi, P., Tamás, G., Lujan, R., and Buhl, E. H. (1998). Salient features of synaptic organisation in the cerebral cortex. *Brain Res Brain Res Rev*, 26(2-3):113–135.
- Tan, Z., Hu, H., Huang, Z., and Agmon, A. (2008). Robust but delayed thalamocortical activation of dendritic-targeting inhibitory interneurons. *Proc. Natl. Acad. Sci. U.S.A.*, 105:2187–2192.
- Thomson, A. M., West, D. C., Wang, Y., and Bannister, A. P. (2002). Synaptic connections and small circuits involving excitatory and inhibitory neurons in layers 2-5 of adult rat and cat neocortex: triple intracellular recordings and biocytin labelling in vitro. *Cereb Cortex*, 12(9):936–953.
- Tsodyks, M. V. and Markram, H. (1997). The neural code between neocortical pyramidal neurons depends on neurotransmitter release probability. *Proc Natl Acad Sci U S A*, 94(2):719–723.
- Urban, N. and Barrionuevo, G. (1998). Active summation of excitatory postsynaptic potentials in hippocampal CA3 pyramidal neurons. *Proc. Natl. Acad. Sci. U.S.A.*, 95:11450–11455.
- Wang, Y., Toledo-Rodriguez, M., Gupta, A., Wu, C., Silberberg, G., Luo, J., and Markram, H. (2004). Anatomical, physiological and molecular properties of Martinotti cells in the somatosensory cortex of the juvenile rat. *J. Physiol. (Lond.)*, 561:65–90.
- White, E. (1989). *Cortical Circuits. Synaptic Organization of the Cerebral Cortex*. Birkhäuser, Boston.
- Williams, S. R. and Stuart, G. J. (2000). Site independence of EPSP time course is mediated by dendritic I(h) in neocortical pyramidal neurons. *J Neurophysiol*, 83(5):3177–3182.
- Williams, S. R., Turner, J. P., Hughes, S. W., and Crunelli, V. (1997). On the nature of anomalous rectification in thalamocortical neurones of the cat ventrobasal thalamus in vitro. *J Physiol*, 505 (Pt 3):727–747.
- Yoshimura, Y. and Callaway, E. (2005). Fine-scale specificity of cortical networks depends on inhibitory cell type and connectivity. *Nat. Neurosci.*, 8:1552–1559.
- Zhu, J. (2000). Maturation of layer 5 neocortical pyramidal neurons: amplifying salient layer 1 and layer 4 inputs by Ca²⁺ action potentials in adult rat tuft dendrites. *J. Physiol. (Lond.)*, 526 Pt 3:571–587.

SUPPLEMENTARY MATERIAL

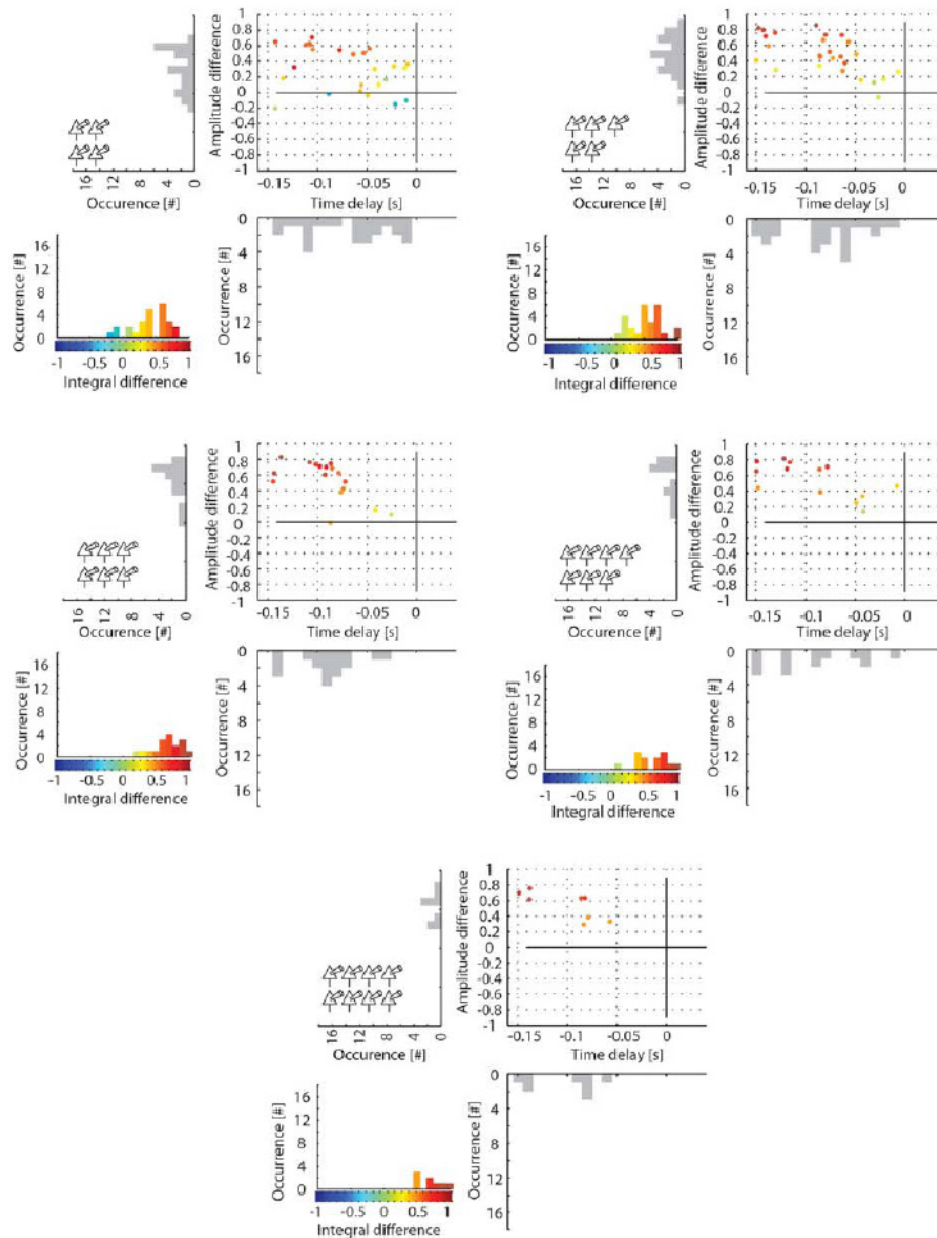


Figure S1. Summation properties of FDDI elicited by 4 – 8 presynaptic PCs. Histograms show amplitude and integral difference as well as the time delay. A positive amplitude (integral) difference means that synchronous stimulation of the two PCs gave a larger FDDI amplitude than the offline summed response of the individually evoked FDDIs. A more negative time delay shows an earlier response of the synchronously evoked FDDI as compared to the summed response of the individually evoked FDDIs.

Chapter 7 Interactions between synaptic connections and gap junctions in the olfactory bulb

Michele Pignatelli^{1,2}, Rodrigo Perin², Henry Markram² and Alan Carleton^{1,3,4}

¹*Flavour Perception Group, BMI, EPFL, Lausanne, Switzerland*

²*Laboratory of Neural Microcircuitry, BMI, EPFL, Lausanne, Switzerland*

³*Laboratory of Sensory Perception and Plasticity, Department of Neurosciences, Faculty of medicine, University of Geneva, Genève, Switzerland*

⁴*Geneva Neuroscience Center, University of Geneva, Switzerland*

INTRODUCTION

The olfactory bulb is the brain region that receives innervations from the olfactory nerve and first processes olfactory input from the olfactory receptors. It is organized in glomeruli, each receiving inputs from different groups of olfactory receptor neurons sensitive to distinct families of molecules. Each glomerulus is composed of the dendrites of mitral and tufted cells and the axons of olfactory neurons. In these dense and highly interconnected regions, many gap junctions and synapses occur among the dendrites of mitral cells. The organization of the glomeruli is such that the somatic position of each neuron has practically no influence on the connectivity of its tuft inside the glomerulus. According to their morphological properties, any two mitral cells projecting to the same glomerulus should have approximately the same probability of being connected. Experimental measures were obtained for the ratio of occurrence of gap junctions and synaptic connections in multi-electrode patch-clamp experiments. Interestingly, when comparing mitral cell connectivity to random networks some discrepancies become apparent, especially when considering the coincident reciprocal synaptic and electric connections. With such circuit properties in mind we investigated the possible effects of the overlap between synaptic connections and gap junctions. This overlap can be observed in many brain regions: cerebellum, inferior olivary nucleus, trigeminal nucleus, hippocampus, neocortex, striatum and olfactory bulb (Condorelli, Belluardo et al. 2000). Therefore the effect of the

interaction between synaptic connection and gap junctions on network topology is a fundamental issue that we address in this study.

RESULTS

Experimentally Measured Connectivity

We considered data exclusively extracted from mice older than 24 days in order to ensure stable gap-junction connectivity (Belluardo, Mudò et al. 2000). All the Mitral Cell (MC) pairs belonged anatomically to the same glomerulus (Fig. 1 A, B, C).

The probability of synaptic connection between $n = 79$ MC pairs was $P_s = 0.65$. Synaptic connections appeared to be randomly distributed. In fact, the distribution of reciprocal R ($P = 0.42$), non-reciprocal NR ($P = 0.47$), and no- connections N ($P = 0.11$), was matched by a randomly connected network (Fig. 1 D). Probability of gap junctions between $n = 67$ MC pairs was $P_e = 0.68$.

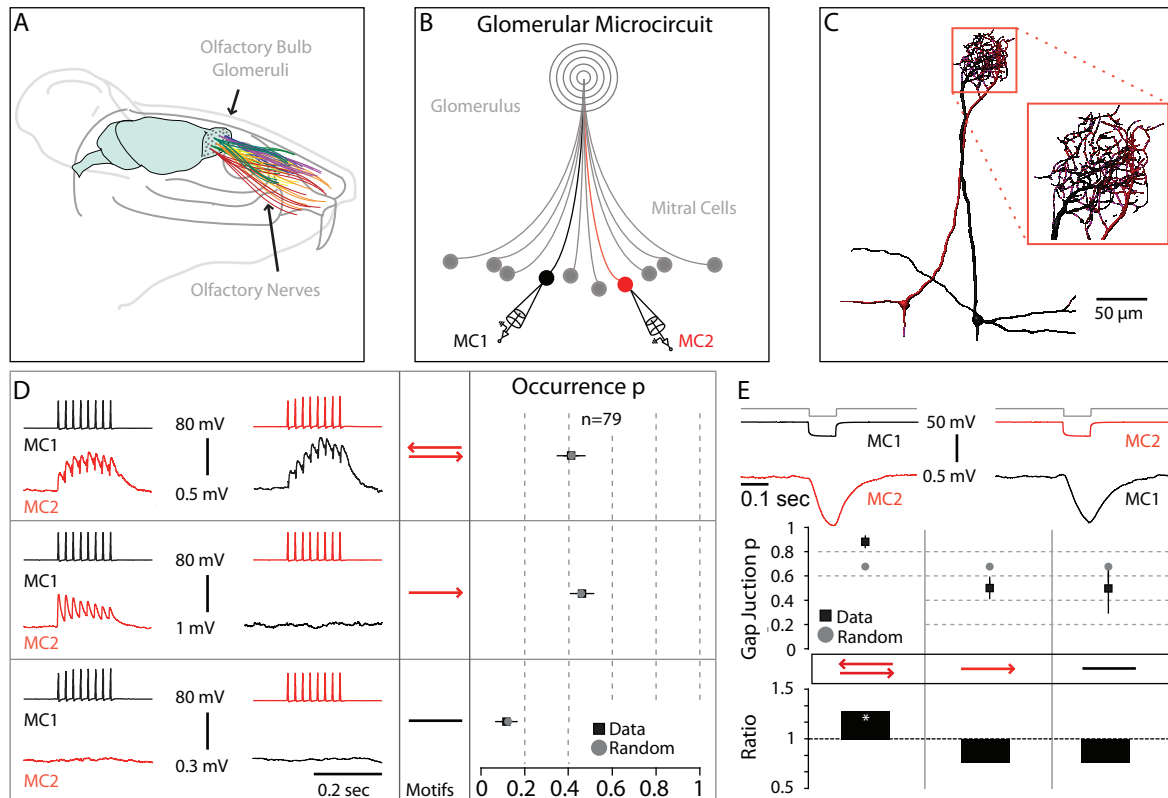


Figure 1 Intraglomerular connectivity. (A) Anatomic representation of the olfactory system. (B) Schematic diagram illustrating the sampling procedure used to estimate the microcircuit connectivity. (C) Two reconstructed Mitral cells affiliated to the same glomerulus. (D) Comparison between observed and expected synaptic connectivity. Note the close correspondence. (E) Probability of gap junction expression in relation to the synaptic connectivity patterns. Note the gap junctions are over expressed on reciprocal connections. Error bars are computed assuming binomial distribution.

However, gap junctions were not randomly distributed when related to synaptic connections (Fig. 1E). In fact, gap junctions were significantly over expressed on reciprocal connections when compared to the expected value ($n = 30$ pairs, $P_{observed} = 0.9$, $P_{expected} = 0.68$, χ^2 -test: $p < 0.05$). A model where the only form of synaptic interaction between MCs is self-excitation (SE) propagated by gap junctions (Schoppa and Westbrook 2002) could explain this over expression. Nevertheless, the same model cannot support the following experimentally observed patterns:

- 1) Gap junctions expressed on non-reciprocal synaptic connections
- 2) Gap junctions expressed on synaptically disconnected pairs
- 3) Reciprocal connections not expressing gap junctions.

If we consider how measurements are performed, at the somatic level, we must recognize that it can be extremely difficult to differentiate direct synaptic connections from self-excitation spreading through a gap junction although both forms of interaction are likely to exist.

Morphological interaction between Mitral cells

Morphological analysis of $n = 16$ reconstructed pairs revealed the presence of potential points of contact (Supplementary Fig. 1) accountable for synaptic transmission (Fig. 2 A, B and C). Morphological contacts (Fig. 2 B) were always located on a precise branching order of the tuft (average order position = 7 ± 1 , average branching order number = 14 ± 1 measured on $n = 21$ cells). The probability of a potential morphological contact between tufts of MC pairs was $p_m = 0.84$ while the average number of potential contact points between pairs was 1.8 ± 0.2 (Fig. 2 C). 3D overlap between glomerular tufts significantly affected the formation of a point of contact ($n = 24$ potential contact points). In fact, considering an overlap index $O < 1$ (see Methods), the resulting $p_m = 0.66$, while for an $O > 1$, $p_m = 0.33$ (χ^2 -test: $p < 0.05$). However, the physiological connections were independent from degree of overlap (Fig. 2 D).

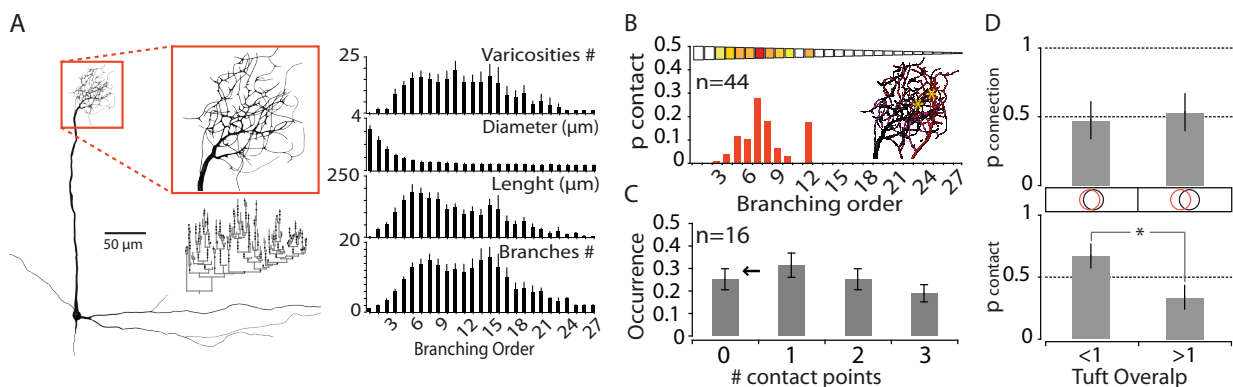


Figure 2 Morphological analysis of the dendrodendritic interactions among Mitral cells. (A) Anatomical analysis of the MC tufts. Inset: dendrogram of the enlarged glomerulus. Analysis of the number of varicosities, segments diameter and length and number of branches plotted as a function of the branching orders. **(B)** Location of potential contact points as a function of the tuft branching order. Note the clustering at the proximal branching orders. **(C)** Occurrence of the number of potential contact points between pairs of synaptically connected cells. Arrow: some pairs did not display any contact point. **(D)** Probability of synaptic connection and probability of morphological contact were plotted in function of the degree of 3D overlap between tufts. Note the lack of relation for synaptic connections. Error bars represent standard error of the mean.

Surprisingly, we found the occurrence of $n = 4$ physiologically connected pairs in the absence of morphological interaction (Fig. 3 A and B). The lack of contact was clear because the two tufts were located on different subfields of the same glomerulus, suggesting therefore, a different connectivity mechanism.

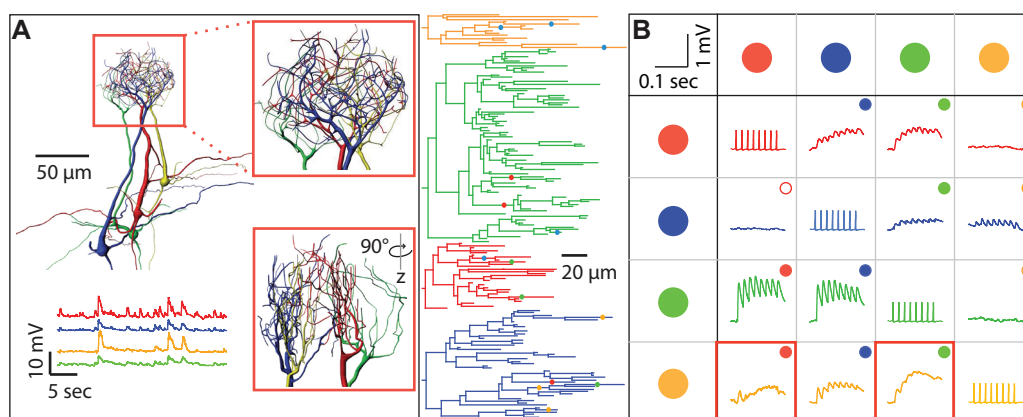


Figure 3 Physiological connections without morphological contacts. (A) Group of four reconstructed cells projecting the apical dendrite to the same glomerulus but segregated within the glomerulus (note the correlated spontaneous activity). The dendrogram of each tuft illustrates the position of the potential contact points. **(B)** Physiological connectivity matrix. Filled circles represent synaptic connections and empty circles represent lack of connection. Note the connections in the red boxes and their lack of morphological points of contacts on the dendrogram.

Functional interaction between synaptic and electric connections

The substantial overlap between reciprocal synaptic connections and gap junctions, and the lack of relationship between anatomical and physiological connectivity can be explained by a functional interaction between synaptic connections and gap junctions. We propose that if an action potential is triggered in a presynaptic compartment, it evokes a postsynaptic potential (PSP) in a first order postsynaptic compartment that can then propagate to a second order compartment through a gap junction. Consequently, a PSP is not only elicited in its direct postsynaptic target but propagates to the compartments electrically coupled to the direct postsynaptic target. Assuming the possibility of propagation of PSPs through gap junctions, the effective connectivity measured experimentally can be a consequence of the interaction between synaptic connections and gap junctions. Therefore, in order to estimate the direct synaptic

connection probability we developed a model, based on the interaction between synaptic connections and gap junctions (Fig. 4), in which we made the following assumptions:

- 1) Gap junctions filter out fast events such as action potentials.
- 2) All MCs display self-excitation.
- 3) Gap junctions are randomly distributed.
- 4) Synaptic connections are randomly distributed.

The propagation of PSP-like signals through gap junctions yields three important and non-trivial outcomes:

- 1) A direct synaptic connection followed by a direct gap junction is experimentally observed as a synaptic connection between the presynaptic compartment and its indirectly coupled compartment.
- 2) Due to the presence of self-excitation, each direct gap junction is experimentally observed as a reciprocal synaptic connection overlapped by a gap junction (Fig. 4B)
- 3) Experimental identification of gap junctions by negative current pulse injections may not allow distinction between a direct gap junction and two consecutive gap junctions. Thus, for modeling purposes two consecutive gap junctions yield a functional gap-junction.

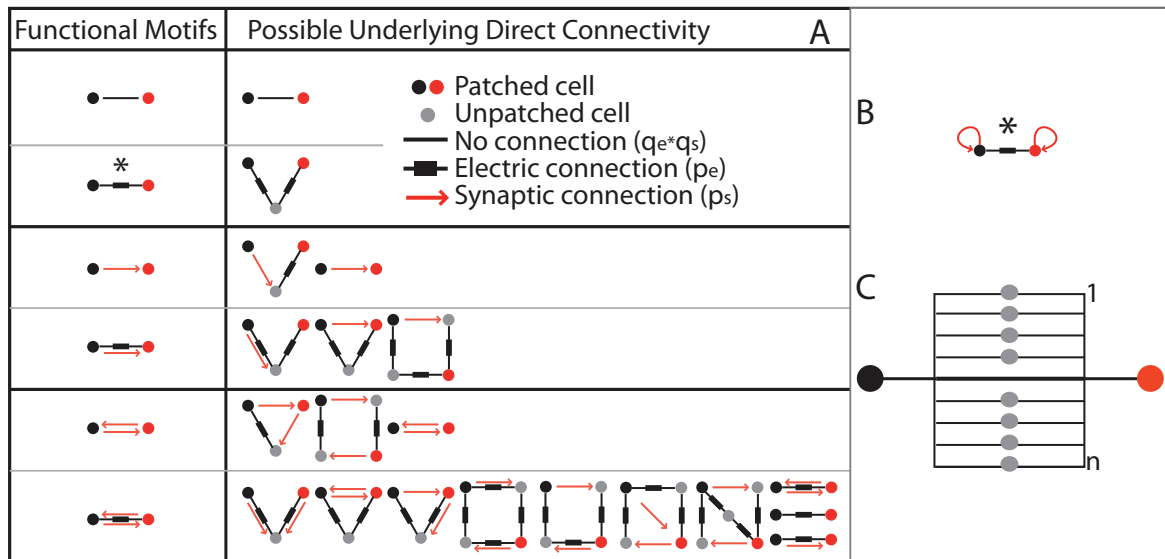


Figure 4 Measured interactions and underlying patterns (A) Schematic illustration describing the possible second order pathways and their respective underlying possible motifs. **(B)** Note that due to the self-excitation, gap junctions between synaptically disconnected cells (asterisk) will always result functionally in a reciprocal synaptic connection overlapped by gap junction. In this model experimentally observed gap junctions in NR or N connections are a result of indirect electrical coupling. **(C)** A PSP-like signal generated in the black cell is going to have n possible two-step pathways to reach the red cell in addition to one possible direct pathway.

Considering the experimentally measured probability of gap junctions $P_e = 0.68$ in a network of $n = 30$ MC (see Supplementary Fig. 2), and assuming that a test signal can propagate through up to two consecutive gap junctions, the estimated probability of occurrence of a direct gap junction is $p_e = 0.18$. We obtain the value of p_e from Equation 1:

The estimation of $(1 - P_e)$, the experimental probability of not observing a functional gap junction, is equal to the probability of the absence of a direct gap junction $(1 - p_e)$ multiplied by probability that none of the $n - 2$ possible pathways display two consecutive gap junctions $1 - p_e^2$.

Considering that the experimentally observed synaptic connectivity is constituted by either self-excitation transmitted by gap junctions, or direct synaptic connections, or direct synaptic connections propagated through at most one gap-junction, the resulting estimated probability of direct synaptic connection is $p_s = 0.15$, which represents the ratio between the

number of existing synaptic connections and the number of possible synaptic connections (See also Supplementary Equation 1).

$$(1 - P_e) = (1 - p_e) (1 - p_e^2)^{(n-2)}$$

Equation 1 Calculation of the direct gap junction probability

$$(1 - P_s) = (1 - p_s) (1 - p_e) (1 - p_s p_e)^{(n-2)}$$

Equation 2 Calculation of the direct synaptic connection probability

The estimation of $(1 - P_s)$, the experimental probability of not observing a synaptic connection, is equal to the probability of the absence of a direct synaptic connection $(1 - p_s)$ multiplied by the probability of absence of a direct gap junction $(1 - p_e)$, multiplied the probability that none of the $n-2$ possible paths display a synaptic connection followed by gap junction $1 - p_s p_e$. We then tested the values obtained for p_s and p_e assembling random networks of direct gap junctions (Figure 5A) and direct synaptic connections (Figure 5B) that interact according to the principles explained previously. As expected, the experimentally observed values of P_s and P_e were obtained in the final network (Figure 5C)

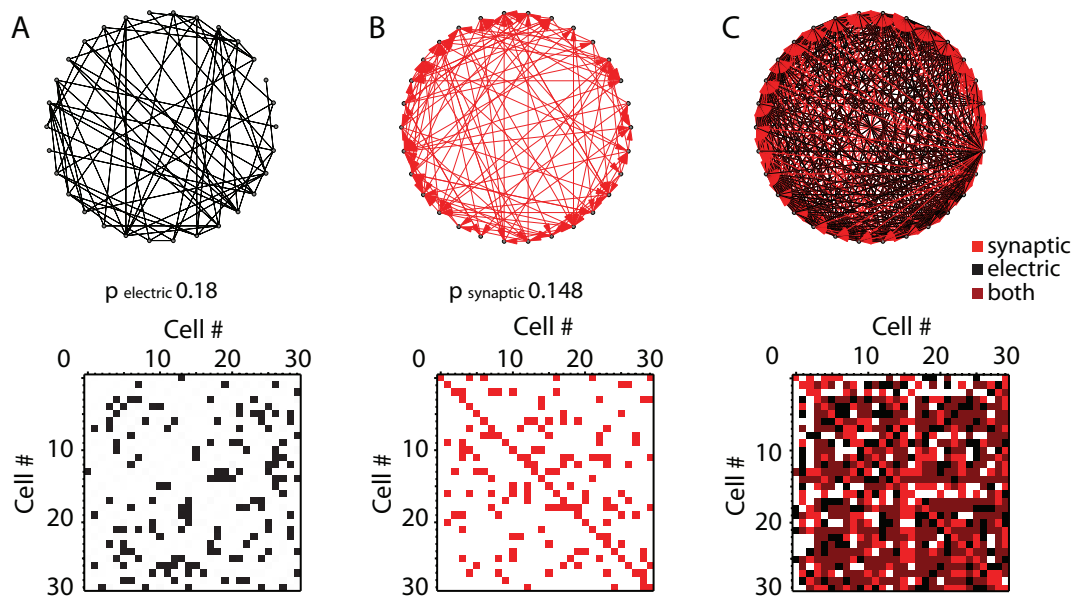


Figure 5 Modeling the functional interaction between gap junctions and synaptic connections. Schematic illustration, connectivity diagram and connectivity matrix showing the propagation of postsynaptic potentials (red) mediated by gap junctions (black). (A) Direct gap junctions. (B) Direct synaptic connections. (C) Interaction between gap junctions and synaptic connections. Note the dramatic expansion of the functional network connectivity compared to the direct connectivity of the two interacting networks.

Our model yields two predictions:

- 1) The coupling ratios (CR) displayed by the gap junctions expressed on the R synaptic connections should be on average stronger than the ones expressed on NR or N connections. CRs measured on R connections are constituted by direct and indirect coupling, while the CRs measured on NR and N are constituted by indirect coupling.
- 2) The estimated probability of direct synaptic connection p_s can be confirmed on a system where the gap junctions are abolished.

Experimental confirmation of the predictions

In support of the hypothesis that two consecutive gap junctions lead to a functional electrical coupling between the neurons involved we show that the distribution of $n = 80$ CR couldn't be

represented by a normal or log-normal distribution (KS test for normal or log-normal distribution). Instead, the CR distribution was characterized by few strong and many weak couplings (probability of a CR $< 0.03 = 0.54$) potentially reflecting signals passing through more than one gap junction. Given that reciprocal connections overlapped by gap junctions are likely to result from self-excitation propagated through gap junction, CR_R is more likely to be expression of a direct gap junction. In fact, comparing CR amplitudes across R connections ($n = 44$, $CR = 0.04 \pm 0.004$), NR ($n = 23$, $CR = 0.02 \pm 0.004$) and N ($n = 12$, $CR = 0.015 \pm 0.005$) connectivity patterns resulted in a significant overexpression of high amplitude CR on R connections (CR_R vs CR_{NR} , KS test: $p < 0.05$; CR_R vs CR_N , KS test: $p < 0.05$, CR_N vs CR_{NR} , KS test: $p > 0.05$). The CR expressed by NR and N connections can be attributed to indirect coupling. Furthermore each independent set of CR (CR_R , CR_{NR} , CR_N) was log-normally distributed (KS test for log-normal distribution) indicating that the total CR distribution may contain data from different groups such as direct and indirect gap junctions (Fig. 6A).

To confirm the second prediction, that the probability of direct synaptic connection, as estimated by the model, is in fact much smaller than the experimentally observed values, we tested the synaptic connectivity in a system lacking gap junctions: the *Cx36*^{-/-} mouse (Kosaka, Deans et al. 2005). By testing $n = 16$ pairs of cells morphologically affiliated to the same glomerulus (Fig. 6B), we found $n = 5$ connections (average amplitude = $0.16 \text{ mV} \pm 0.05$) and a complete lack of gap junctions (Fig. 6C, D) accounting for a probability of synaptic connection $p_s = 0.16$, thus confirming our prediction.

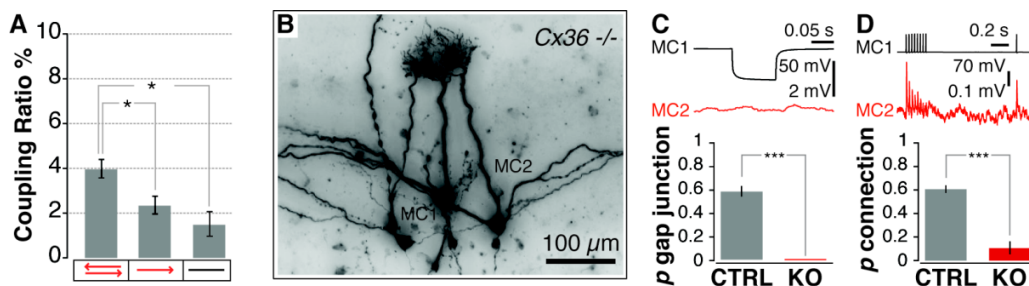


Figure 6 Confirmation of the predictions (A) Coupling Ratio “CR” amplitude plotted as a function of patterns of synaptic connections. CR is higher on reciprocal connections. **(B)** Morphological staining of a pair of *Cx36*^{-/-} MC connected by synaptic excitation. **(C)** Comparison between CTRL and ^{-/-}. None of the

tested pairs displayed gap junctions. **(D)** Comparison between CTRL and $-/-$. The probability of synaptic connection is reduced by 53% but is not annihilated. Error bars represent standard error of the mean.

Experimental verification of the assumptions

We presented four assumptions concerning signal transmission in the olfactory bulb. Here we revisit these assumptions identifying experimental evidence of their validity.

- 1) Action potentials rarely propagate through gap junctions. The low-pass filtering effect prevented spike transmission between MCs but allowed a 0.1 s square pulse to propagate ($n = 29$, action potential CR = 0.0006 ± 0.00007 , square pulse CR = 0.015 ± 0.003 , KS: $P < 0.0001$, Fig. 7A).
- 2) Self-excitation was expressed in Cx36 $-/-$ MC ($n = 5$, average amplitude $1.73 \text{ mV} \pm 0.24$). Furthermore, comparing the average self-excitatory EPSP amplitude with the EPSP amplitude measured on R connection expressing possible direct gap junctions, we estimated a gap junction attenuation at approximately 80% ($A = \text{EPSP}_{\text{reciprocal-gap junction}} / \text{EPSP}^{\text{SE}}$, Fig. 7B).
- 3) Direct synaptic connections were randomly distributed as assumed by our model. The expression of the connectivity patterns measured in the intraglomerular microcircuit of Cx36 $-/-$ mice was matched by a random distribution (Fig. 7C).
- 4) Gap junctions were randomly distributed. Testing the distribution of pairs of consecutive connections revealed a random expression of the three possible patterns: *gap junction* followed by *gap junction*, *gap junction* followed by *no gap junction* and *no gap junction* followed by *no gap junction* Fig 7 D, E, F).

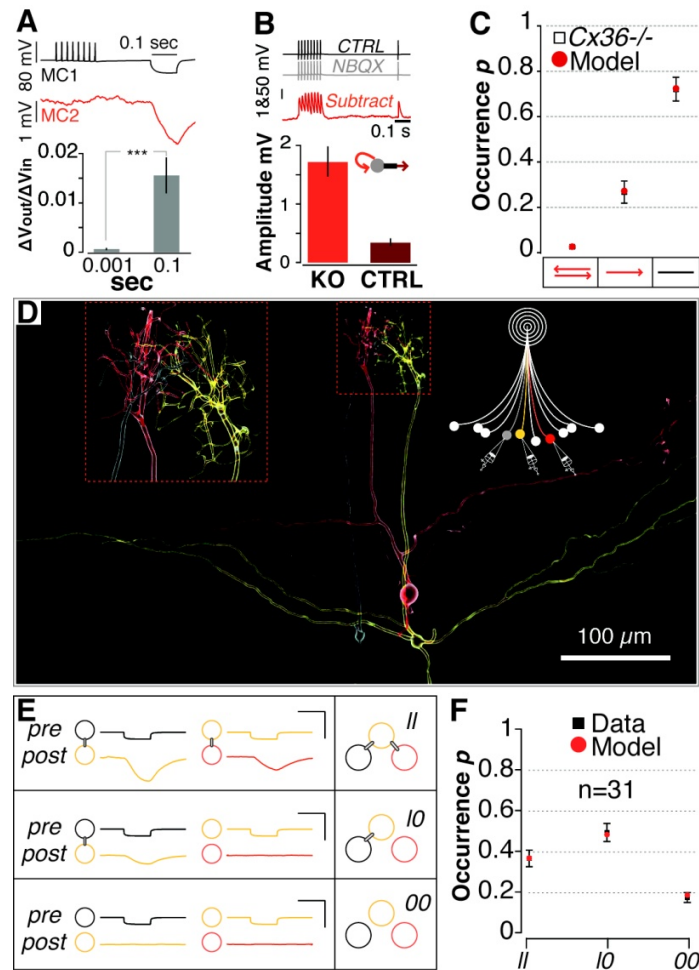


Figure 7 Verification of the assumptions (A) Filtering properties of the gap junctions. Action potentials are completely filtered by gap junctions. **(B)** Relationship between self-excitation amplitude and connection amplitude measured on reciprocally connected cells exhibiting gap junctions. The data provide a substrate to estimate gap junction attenuation ($\approx 80\%$). **(C)** Comparison between observed and expected Cx36^{-/-} synaptic connectivity. Direct synaptic connections are randomly distributed. **(D)** 3D reconstruction of a triplet of MC affiliated to the same glomerulus. **(E)** Pairs of consecutive compartments can interact via gap junctions producing three possible patterns. Scale bars: horizontal 100 ms, vertical presynaptic 100 mV and vertical postsynaptic 0.5 mV. **(F)** Comparison between the distributions of observed and expected patterns in 31 doublets. Gap junctions are randomly distributed. Error bars are computed assuming binomial distribution.

Physiological impact of propagation mediated by gap junctions

The functional interaction between gap junctions and synapses amplifies the global synaptic connectivity of 53%. The distribution of the six possible interaction patterns observed experimentally ($n = 67$ pairs) was significantly (χ^2 -test: $P < 0.05$) different from values obtained

for non-interacting random networks but did not differ significantly from the expected values generated by our model (χ^2 -test: $p = 0.5$, Fig. 8A). Analysis of the distribution of the number of connections established by a single cell revealed an increase in the number of hyperconnected cells when compared to a random network (Figure 8B). The physiological role for such hyperconnectivity might be an increase in network sensitivity and reduction of reaction-time. In fact given the same probability of connection, networks characterized by hyperconnected cells display faster signal propagation (Watts and Strogatz 1998).

Furthermore, a design based on propagation of PSP through gap junctions in a network with a probability of direct synaptic connection $p_s = 0.15$ allows the system to save 77% of the energy required by a network with a probability of direct synaptic connection $P_s = 0.65$ (fraction of energy saved $Es = (P_s - p_s) / P_s$). Therefore, the energy employed by a limited number of release sites is sufficient to produce the functional effect of a hyperconnected network.

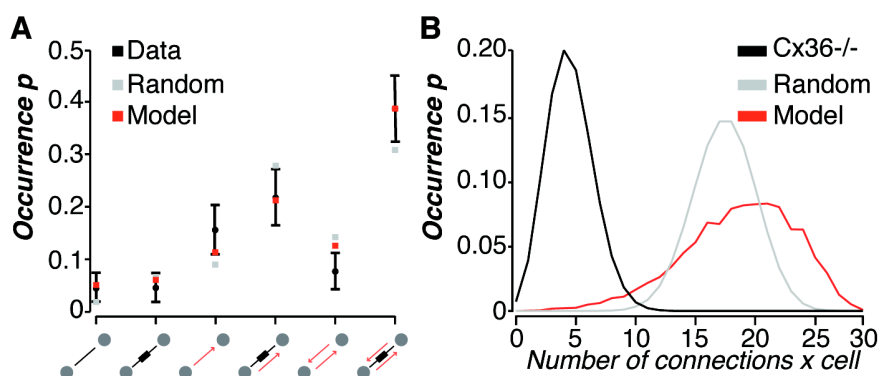


Figure 8 Results of the topologic interaction between gap junctions and synaptic connections (A) Distribution of the possible connectivity patterns. Note the improvement of the fitting achieved by the model when compared to random. **(B)** Distribution of the number of connections established by a single cell for Cx36-/- (black), random (grey) and model (red). Note the increase in the number of hyperconnected cells occurring in case of functional interaction between gap junctions and synaptic connections when compared to a random network. Error bars are computed assuming binomial distribution, $SE = (p(1-p)/n)^{0.5}$, where p is the event probability.

DISCUSSION

We have experimentally quantified the physiological interaction between gap junctions and synaptic connections in the intraglomerular microcircuit of the olfactory bulb. The excitatory cells of the intraglomerular network randomly interact through gap junctions and synaptic connections. Both gap junctions and synaptic connections are located on the tuft of the apical dendrite in the glomerulus. The compact co-localization of these two systems of communication may cause the PSP to propagate to proximal compartments through gap junctions. The result is represented by an expansion and a redistribution of the effect of synaptic connections mediated by gap junctions.

Synaptic transmission between Mitral cells: potential alternatives

Two possible alternative mechanisms described in the literature can be compared to the suggested model in their potential to explain the experimental data on the connectivity in the olfactory bulb: self-excitation propagated by gap junctions and glutamate spillover.

As already revealed by a previous study (Christie, Bark et al. 2005), we confirm the presence of SE in the Cx36^{-/-} suggesting that SE is not generated by gap junctions mediated feedback of a direct synaptic connection. A model where the transmission is mediated exclusively by SE (Schoppa and Westbrook 2002) propagated by gap junctions produces a strong hyperexpression of R connections with the synaptic connectivity strictly dependent on the gap junctions expression. However, the same model cannot justify the expression of the following patterns: gap junctions overlapping NR synaptic connections, gap junctions overlapping N connections and R connection without gap junctions.

Furthermore, by clamping the membrane potential of a postsynaptic MC at +15 mV, we succeeded to reverse the polarity of the EPSP ($n_{\text{reversed}} = 3$ vs $n_{\text{non-reversed}} = 7$) supporting the occurrence of direct synaptic connections. However, the copious non-reversed cases indicate that transmission mediated by gap junctions is also a possibility.

The communication between morphologically disconnected cells can be explained by glutamate spillover as suggested in a recent study (Christie and Westbrook 2006), however, the latency and the rise time (average onset $1.6 \text{ ms} \pm 0.1$, $n = 81$; average rise time $3.5 \text{ ms} \pm 0.7$, $n = 140$) of the connections are close to the monosynaptic transmission described between layer 5 pyramidal cells in the somatosensory cortex (Markram, Lübke et al. 1997), much faster than would be expected in the absence of precisely aligned pre- and postsynaptic terminals. Furthermore, the widespread branching subdivision of the tuft and the range of activity displayed by spillover predict a network characterized by 100% connectivity (*all to all*). One electron-microscopy (EM) study (Pinching and Powell 1971) excluded the presence of synaptic contacts between MCs. Here, we demonstrate a strong morphological clustering of the contact points and a low a probability of direct synaptic connections $p_s = 0.15$ which can explain a potential difficulty in locating these in EM studies. Nonetheless, a more recent EM contribution unequivocally reported clear asymmetric synapses between MCs in the salamander OB (Allen and Hamilton 2000).

Synaptic connections between Mitral cells in the OB of Cx36^{-/-} mice

Our model is supported by the expression of synaptic connections in the OB of Cx36^{-/-} mice. A single study reported the absence of synaptic connections in the *knock out* mice (Christie, Bark et al. 2005). The discrepancy between this finding and our study can be attributed to our larger number of intraglomerular pairs and to the application of a different protocol (train vs single pulse) to screen the synaptic connectivity. Considering that the probability of finding intraglomerularly affiliated pairs is $p_{ko} = 0.05$ and that the probability of finding a synaptic connection is $P_{ko} = 0.15$, the resulting joint probability ($p_{ko} * P_{ko}$) of 0.0075 indicates the probability of connection among neurons in compact clusters of MC in *knock out* mice.

Physiological considerations

Action potentials are strongly filtered by gap junctions. This result differed from a past study focused on the coupling between neocortical interneurons and describing action potentials

spreading through gap junctions (Galarreta and Hestrin 1999). The CR displayed by interneurons in the neocortex is in average more than two-fold greater. Our analysis of the CR revealed a weak coupling, in agreement with past observations (Pimentel and Margrie 2008). Furthermore, hypothetic transmission of action potentials through gap junctions could result in an avalanche affecting all the glomerular compartments electrically coupled. However, as demonstrated in our experiments, the low-pass filtering property of the gap junctions in the olfactory bulb can prevent the spreading of action potentials.

Concerning the spread of PSPs through gap junctions, if we consider a 2 mV PSP generated at the tuft, travelling through a gap junction and suffering an attenuation of 80% followed by a dendritic dissipation of 25% (Djurisić, Antic et al. 2004) we obtain a resulting PSP of 0.3 mV, consistent with our experimental findings. Similarly we can also consider a test signal (0.1 s negative square current injection) of 30 mV, dissipating twice along the pre- and postsynaptic dendrite and attenuated by two consecutive gap junctions, yielding a final value of 0.68 mV and a final CR of 0.02, also consistent with our experimental data.

Despite the degree of non-randomness displayed by the functional relationship between gap junctions and synaptic connections, our study demonstrates that direct synaptic connections and gap junctions are indeed randomly distributed. The non-random character results from the interaction of the two random networks, reflected in the experimentally observed distribution.

Finally, our model shows an expansion and a redistribution of the synaptic connectivity mediated by gap junctions. The connectivity expansion can support a rapid stimulus-induced reaction, whereas the redistribution increases the occurrence of hyperconnected cells enhancing the signal propagation efficiency (Watts and Strogatz 1998). Additionally, the PSP propagation through gap junctions allows the system to save 77% of the energy required by a network with a high probability ($P = 0.65$) of direct synaptic connections. The energy employed on few release sites is enough to produce the functional effect of a hyperconnected network allowing an efficient stimulus reaction at a low metabolic cost.

Future directions

The exact localization of synaptic contacts and gap junctions on the branches of the tuft represent a relevant direction to understanding in full detail the electrotonic propagation of the postsynaptic potential. Gap junctions can be localized on proximal branches, as suggested by our morphological analysis of the potential points of contact distribution. The proximal localization may have a relevant role in promoting the propagation of PSPs.

The dendritic terminals of Mitral cells interact with those of periglomerular cells in the glomerulus, establishing synaptic connections (Pinching and Powell 1971; Kosaka, Deans et al. 2005; Murphy, Darcy et al. 2005). The propagation of the inhibition through gap junctions may support the *center surround inhibition* described in the glomerular layer (Aungst, Heyward et al. 2003).

Finally, our approach is applicable to different cerebral areas like cerebellum, inferior olivary nucleus, trigeminal nucleus, hippocampus, neocortex and striatum. These structures are characterized by co-expression of gap junctions and synaptic connections and may display similar mechanisms for expansion and redistribution of the synaptic connectivity.

METHODS

Dissection. All experiments were performed on P24-P29 C57BL/6J mice (Charles River, France) and on Cx36^{-/-} β -gal reporter mice with a C57BL6/129 background (Deans, Gibson et al. 2001). Animals were anesthetized by isoflurane inhalation before decapitation according to the Swiss Federal Guidelines for animal experimentation. Horizontal slices (300 μ m) were cut with a vibratome (Leica, Germany) in ACSF at 4°C, kept in normal oxygenated ACSF at 34°C for about 30 min, and then stored at 23°C before the experiment. The ACSF contained (in mM): 124 NaCl, 3 KCl, 2 CaCl₂, 1.3 MgSO₄, 25 NaHCO₃, 1.2 NaH₂PO₄, 10 D-glucose with pH = 7.3 and osmolarity of 300 mOsm when bubbled with 95% O₂-5% CO₂. For electrophysiological recordings, individual slices were transferred to a submerged chamber where they were perfused with oxygenated ACSF warmed at 37°C (\pm 0.5°C) at a rate of 2-3 ml/min (Castillo, Carleton et al. 1999).

Electrophysiology. Multiple whole-cell recordings in current clamp mode were performed using an IR-DIC microscope (Olympus BX51) equipped with six motorized manipulators (Luigs & Neumann). Mitral cells (MC) and Tufted cells (TC) were easily identified by their DIC morphology (layer position, large soma and thick apical dendrite) and electrophysiological characteristics (resting membrane potential around -50 mV and input resistance between 50-100 M Ω). Whole cell recordings were established using borosilicate glass pipette with resistances of 6-10 M Ω , filled with the following intracellular solution (mM): 110 K-gluconate, 10 KCl, 10 HEPES, 4 ATP, 0.3 GTP, 10 phosphocreatine and 0.5% biocytin. Access resistance (RA) was monitored throughout the duration of the experiment and data acquisition was suspended whenever the resting membrane voltage was below -45 mV or the RA was beyond 20 M Ω . Recordings were amplified using up to six Axopatch 200B (Axon), filtered at 2 KHz, digitized (5-20 KHz), and acquired using PulseQ electrophysiology package (Funetics) running on Igor Pro (Wavemetrics). Synaptic connections were quantified by stimulation of a single presynaptic MC with a single AP repeated 30 times every 2 s and a train of 8 APs at 10, 20, 30, 50 Hz followed after 500 ms by a recovery AP, repeated 30 times every 5 s. APs were evoked by single 2 ms square pulse. A negative 100 or 300 ms current step of 50 to 100 pA was routinely applied to test for gap junctions. The test was repeated 30 times every 5 s. The presence of synaptic

connections and gap junctions was clearly determined after averaging 30 trials. All the pharmacological compounds were obtained from Sigma. Data are reported in mean \pm sem.

Morphology. Recorded MCs were filled with biocytin for light microscopy identification. After recording, slices were fixed for at least 24 hr in phosphate buffer (pH 7.4) containing 2% paraformaldehyde and 1% glutaraldehyde. Thereafter, slices were rinsed and transferred into phosphate-buffered 3% H₂O₂ to block endogenous peroxidases. After rinsing in phosphate buffer, slices were incubated overnight at 4°C in avidin-biotinylated horseradish peroxidase (ABC-Elite, Vector Labs, 2% A, 2% B, 1% Triton X-100). Sections were then rinsed again in phosphate buffer and developed with diaminobenzidine under bright-field microscope until the cells were visible. The reaction was stopped after transferring the slice in phosphate buffer. Finally, slices were mounted in an aqueous medium. Morphological confirmation of the MCs connection was achieved by light microscopy observation; MCs projecting the apical dendrites to the same glomerulus were considered connected. In some cases, propidium-iodide (5 μ g/ml, 30 min, Molecular Probes) was added as a nuclear stain for glomeruli identification while the MC clusters were revealed using streptavidin-FTIC in order to collect fluorescent images-stacks using a two-photon microscope (Prairie), then assembled in a 3D movie (Image J). Selected clusters of MCs were reconstructed in bright field under a 100X/1.30NA oil immersion objective using Neurolucida system (MicroBrightField). M/T cells can interact by synaptic and electric connections. Therefore, exclusively tight dendrodendritic adjacencies located on the same focal plane were considered as potential points of contact. As confirmed by electron microscopy of points of contact between pairs of electrophysiologically connected pyramidal cells, the accuracy of point of contact detection by light microscopy is 80% (Markram, Lübke et al. 1997). Morphological data analysis was accomplished using Excel (Microsoft Office).

Morphological analysis. Stained cells were reconstructed using Neurolucida (Microbrightfield). Morphological analysis was achieved using Neuroexplorer (Microbrightfield) and Analysis (Olympus). Analysis was restricted to the interaction site: the tuft. Each glomerular tuft was converted into a dendrogram evolving each branching point and characterized by a specific number of branching orders. The length of the segments, the diameter, the number of branches and the number of varicosities were counted on each branching order. To estimate the overlap

between tuft pairs we measure the 3D Convex Hull of each single tuft (C_a and C_b) and 3D Convex Hull for the interacting tufts (C_{ab}). We then defined an overlapping index $O = C_{ab} / (C_a + C_b)$. Having $O > 1$, dendrites are not overlapped, whereas $O < 1$ indicates an overlapping field.

Connectivity. Intraglomerular connectivity was investigated patching a tight cluster of M/T cells having the apical dendrite directed towards the same glomerular region.

The presence of synaptic and electric responses was determined applying the following protocol: 8 depolarizing pulses (50 pA) at 50 Hz, each of 2 ms width, followed after 500 ms by a single recovery pulse, followed again by a 300 or 100 ms hyperpolarizing square pulse (100 pA). Detection was accomplished averaging 30 postsynaptic trials.

The coupling coefficient of gap junctions was estimated with injection of negative square pulse in the cell A which elicits a hyperpolarization V_A in the cell A and a correlated hyperpolarization V_B in the cell B. The coupling coefficient is given by the ratio V_B / V_A .

For synaptic connections the probability of connection P is equal to $P = n_{observed} / n_{tested}$ where $n_{observed}$ represents the number of observed cases and n_{tested} is the number of tested cases. The expected random connectivity was computed assuming binomial distribution of the measured connection probability P . A reciprocal interaction R is expected, in a random network, with a probability P^2 , a non-reciprocal interaction NR, with a probability $2P * (1 - P)$ and a no-connection N, with probability $(1 - P)^2$. The distributions of the observed and expected numbers of cases were then compared by χ^2 test. A Fischer exact test or a χ^2 test, when appropriate, was used for paired comparison of individual motifs; in which case we applied the Bonferroni correction for multiple-hypotheses testing.

Estimation of the network size. Microcircuit size was estimated from the soma diameter (average diameter $15 \mu\text{m} \pm 2.6$, $n = 200$) and from the probability of glomerular affiliation p_m as a function of intersomatic distance. We estimated p_m for intersomatic intervals of $20 \mu\text{m}$ (p_m^{20} , p_m^{40} , p_m^{60} , p_m^{80} , p_m^{100} , p_m^{120}), correcting it from the sampling procedure (Supplementary Fig. 2 A,

B). For each interval we extracted the possible number of cells (surface of the interval divided the soma surface) and therefore the possible number of affiliated cells (fraction of the total cell number in a specific interval). The sum of the all the connected cells was multiplied by two (Mitral cells are mainly distributed in a double layer in the horizontal preparation) resulting in a final number of 32 cells (± 11). The estimation was confirmed comparing the observed and expected probabilities of morphological interaction in a population of cells belonging to different microcircuits, distributed within a radius of 120 μm . A $p_m = 0.07$ observed experimentally ($n = 2599$ pairs) was in line with the calculated $p_m = 0.06$, while for Cx36^{-/-} the connectivity was $p_m = 0.05$ ($n = 709$ pairs).

Modeling the network topology. The method proposed in this study aimed at estimating the network connectivity in case of apposition of synaptic connections and gap junctions.

The reconstruction procedure requires an estimate of the probability of connection for both synaptic connections and gap junctions. Sampling the network connectivity with patch clamp recordings allowed us to extract the probability of synaptic P_s and probability of occurrence of a gap junction P_e , experimentally observed within a microcircuit. In a network of cells interacting exclusively by direct connections, P_s and P_e are independent of the network size. However, considering an interaction between gap junction and synaptic connections, both P_s and P_e will be affected by the network size n (see Equations 1 and 2).

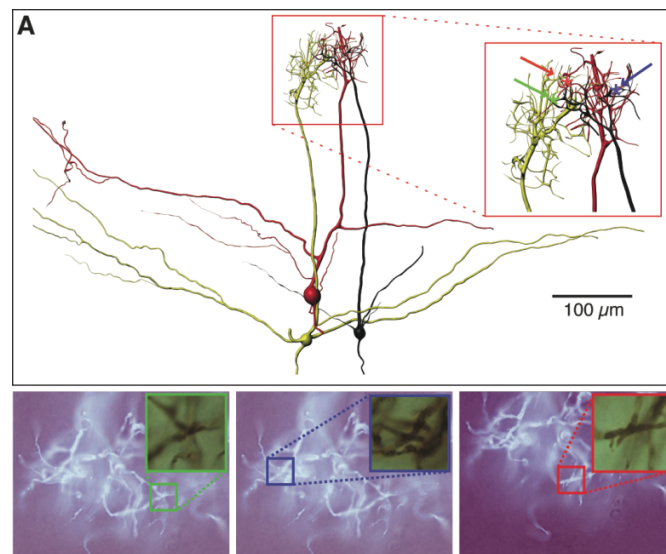
Random networks of $n = 30$ cells were assembled from the calculated values of p_s and p_e . The random distribution of synaptic connections was experimentally confirmed in the Cx36^{-/-} mice ($n = 32$ pairs, $P = 0.15$). The occurrence of reciprocal, non-reciprocal and no connections was in fact predicted by joint probability of p_s .

The random distribution of gap junctions was confirmed by sampling the occurrence of gap junctions in doublets (double pair: A-B-C, where A, B, and C are three cells) of cells belonging to the same glomerulus ($n = 31$).

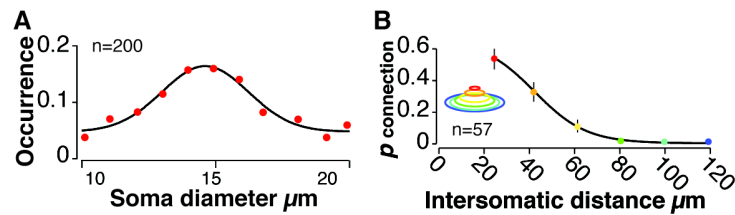
We then generated a connectivity matrix for synaptic connections and another for gap junctions according to p_s and p_e , respectively. The interactions between these two networks yield the functional connectivity matrices for gap junctions and synapses where we capture the expression of the six possible connectivity patterns involving the electrical and chemical synapses.

The multiplication of expected probabilities by the total experimental number of pairs tested for both synaptic connections and gap junctions ($n = 67$) allows generating the expected numbers. The distributions of experimentally observed and expected numbers of the different connectivity patterns were compared by χ^2 test.

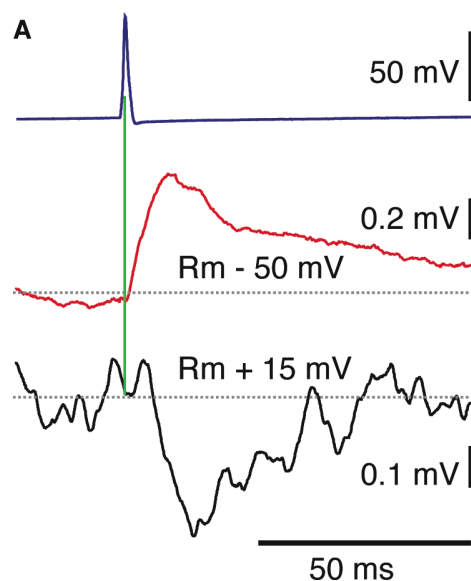
SUPPLEMENTAL FIGURES



Supplementary Figure 1. (A) Morphological identification of contact points between connected Mitral cells. Note the high resolution of three points of contact located on the same focal plane.



Supplementary Figure 2. (A) Occurrence of soma diameters. (B) Probability of synaptic connection plotted as function of the intersomatic distance. The two measurements (in A and B) were employed to estimate the size of microcircuit. $32 (\pm 11)$ Mitral cells constitute the intraglomerular microcircuit. Error bars are computed assuming binomial distribution, $SE = \sqrt{[p(1-p)/n]}$, where p is the event probability.



Supplementary Figure 3. (A) Stimulation of the presynaptic cell elicited an EPSP in the postsynaptic cell characterized by positive polarity at a resting membrane potential -50 mV. The EPSP was reversed at resting membrane of +15 mV.

$$\begin{cases} P_R = p_s^2 \\ P_{NR} = 2p_s(1 - p_s) \end{cases}$$

Supplementary Equation 1. Relationship between the synaptic connection probability (p_s) and reciprocal (P_R) and non-reciprocal (P_{NR}) synaptic connections probabilities in a random network.

Acknowledgements

We especially thank Debasree Banarjee, Alexandra Boussemier and Thibaut Lachaut for the morphological reconstructions and Sebastien Lasserre for the morphological visualization. This work was supported by the Brain Mind Institute, Ecole Polytechnique Fédérale de Lausanne (H.M. and A.C.).

Author Contributions

M.P. performed the electrophysiological experiments and analysis. R.P. performed the microcircuit modeling. A.C., H.M. and M.P. carried out the study conceptualization wrote and edited the manuscript. H.M. supported the project.

REFERENCES

- Allen, D.M., and Hamilton, K.A. (2000). Ultrastructural identification of synapses between mitral/tufted cell dendrites. *Brain Res* 860, 170-173.
- Aungst, J.L., Heyward, P.M., Puche, A.C., Karnup, S.V., Hayar, A., Szabo, G., and Shipley, M.T. (2003). Centre-surround inhibition among olfactory bulb glomeruli. *Nature* 426, 623-629.
- Bacci, A., and Huguenard, J.R. (2006). Enhancement of spike-timing precision by autaptic transmission in neocortical inhibitory interneurons. *Neuron* 49, 119-130.
- Bacci, A., Huguenard, J.R., and Prince, D.A. (2003). Functional autaptic neurotransmission in fast-spiking interneurons: a novel form of feedback inhibition in the neocortex. *J Neurosci* 23, 859-866.
- Belluardo, N., Mudò, G., Trovato-Salinaro, A., Le Gurun, S., Charollais, A., Serre-Beinier, V., Amato, G., Haefliger, J.A., Meda, P., and Condorelli, D.F. (2000). Expression of connexin36 in the adult and developing rat brain. *Brain Res* 865, 121-138.
- Carlson, G.C., Shipley, M.T., and Keller, A. (2000). Long-lasting depolarizations in mitral cells of the rat olfactory bulb. *J Neurosci* 20, 2011-2021.
- Castillo, P.E., Carleton, A., Vincent, J.D., and Lledo, P.M. (1999). Multiple and opposing roles of cholinergic transmission in the main olfactory bulb. *J Neurosci* 19, 9180-9191.
- Christie, J.M., Bark, C., Hormuzdi, S.G., Helbig, I., Monyer, H., and Westbrook, G.L. (2005). Connexin36 mediates spike synchrony in olfactory bulb glomeruli. *Neuron* 46, 761-772.
- Christie, J.M., and Westbrook, G.L. (2006). Lateral excitation within the olfactory bulb. *J Neurosci* 26, 2269-2277.
- Condorelli, D.F., Belluardo, N., Trovato-Salinaro, A., and Mudò, G. (2000). Expression of Cx36 in mammalian neurons. *Brain Res Brain Res Rev* 32, 72-85.
- Deans, M.R., Gibson, J.R., Sellitto, C., Connors, B.W., and Paul, D.L. (2001). Synchronous activity of inhibitory networks in neocortex requires electrical synapses containing connexin36. *Neuron* 31, 477-485.
- Djurisić, M., Antic, S., Chen, W.R., and Zecević, D. (2004). Voltage imaging from dendrites of mitral cells: EPSP attenuation and spike trigger zones. *J Neurosci* 24, 6703-6714.
- Galarreta, M., and Hestrin, S. (1999). A network of fast-spiking cells in the neocortex connected by electrical synapses. *Nature* 402, 72-75.
- Kosaka, T., Deans, M.R., Paul, D.L., and Kosaka, K. (2005). Neuronal gap junctions in the mouse main olfactory bulb: morphological analyses on transgenic mice. *Neuroscience* 134, 757-769.
- Markram, H., Lübke, J., Frotscher, M., Roth, A., and Sakmann, B. (1997a). Physiology and anatomy of synaptic connections between thick tufted pyramidal neurones in the developing rat neocortex. *J Physiol (Lond)* 500 (Pt 2), 409-440.
- Markram, H., Lübke, J., Frotscher, M., and Sakmann, B. (1997b). Regulation of synaptic efficacy by coincidence of postsynaptic APs and EPSPs. *Science* 275, 213-215.
- Murphy, G.J., Darcy, D.P., and Isaacson, J.S. (2005). Intraglomerular inhibition: signaling mechanisms of an olfactory microcircuit. *Nat Neurosci* 8, 354-364.
- Nicoll, R.A., and Jahr, C.E. (1982). Self-excitation of olfactory bulb neurones. *Nature* 296, 441-444.
- Pimentel, D.O., and Margrie, T.W. (2008). Glutamatergic transmission and plasticity between olfactory bulb mitral cells. *J Physiol (Lond)* 586, 2107-2119.
- Pinching, A.J., and Powell, T.P. (1971a). The neuropil of the glomeruli of the olfactory bulb. *J Cell Sci* 9, 347-377.
- Pinching, A.J., and Powell, T.P. (1971b). The neuropil of the glomeruli of the olfactory bulb. In *J Cell Sci*, pp. 347-377.
- Schoppa, N.E., and Urban, N.N. (2003). Dendritic processing within olfactory bulb circuits. *Trends Neurosci* 26, 501-506.
- Schoppa, N.E., and Westbrook, G.L. (2002). AMPA autoreceptors drive correlated spiking in olfactory bulb glomeruli. *Nat Neurosci* 5, 1194-1202.
- Smith, T.C., and Jahr, C.E. (2002). Self-inhibition of olfactory bulb neurons. *Nat Neurosci* 5, 760-766.
- Song, S., Sjöström, P.J., Reigl, M., Nelson, S., and Chklovskii, D.B. (2005). Highly nonrandom features of synaptic connectivity in local cortical circuits. *PLoS Biol* 3, e88.
- Strogatz, S.H. (2001). Exploring complex networks. *Nature* 410, 268-276.
- Tamás, G., Buhl, E.H., and Somogyi, P. (1997). Massive autaptic self-innervation of GABAergic neurons in cat visual cortex. *J Neurosci* 17, 6352-6364.

- Urban, N.N., and Sakmann, B. (2002). Reciprocal intraglomerular excitation and intra- and interglomerular lateral inhibition between mouse olfactory bulb mitral cells. *J Physiol (Lond)* 542, 355-367.
- Watts, D.J., and Strogatz, S.H. (1998). Collective dynamics of 'small-world' networks. *Nature* 393, 440-442.

Chapter 8 Conclusion

Neuronal interactions take place in diverse forms, some apparently inscrutable due to the difficulty to probe the precise compartments where they occur, others due to their minute amplitudes or distributed nature. The relevance of such interactions is not diminished by the challenging nature of the investigation they require. In fact, it becomes clear that many important answers to how perception, memory, and emotions are generated hinge upon a better understanding of how neurons work together. In this chapter the findings reported in this thesis are discussed in wider context in view of the current and future possibilities.

The impact of new technologies on neuroscience

Neuroscience is a scientific field whose progress shows very close relationship with technical and technological advances. Novel discoveries have often been made possible by the development of new a technique. Such was the case with intracellular recordings and the understanding of the chemical synapse, patch-clamp and the recording of single ion-channels, two-photon microscopy and the study of individual spines and in-vivo deep tissue scanning. Novel techniques allow inspection of physiology in greater detail or simply from different angles. A profusion of techniques is available nowadays but their successful application depends substantially on effective integration when it comes to actual experiments. By placing our efforts in careful integration of the components of the patch-clamp technique we have been able to expand its capacity and render possible new kinds of experiments and observations. Also important, we could glimpse the potential of future developments and how to proceed in order to achieve them.

Clustered connectivity in the neocortex

In the complexity of the neocortex lie the keys to neuronal processing responsible for the senses, memory, and higher brain function. The organizing principles of the network of neurons that gives rise to these functions remain elusive. By recording from up to twelve L5 PCs

simultaneously we confirmed the non-randomness of neocortical connectivity (Song, Sjöström et al. 2005) and could extract connectivity principles that could not be inferred until now. We observed distributed clusters, Hebbian assemblies, of neurons with significantly denser connectivity. The connections in these clusters were, in average, also stronger. A very interesting property of the observed connectivity was the proportional influence of the number of common neighbors shared by a given pair of neurons on the connection probability within that pair. We showed that distance-dependent pairwise connectivity profiles together with the common neighbor property can generate networks whose clustering properties resemble experimentally measured ones. Given the constraints imposed to the connection probabilities and strengths in Hebbian assemblies, we hypothesize that such dense clusters of synaptically-coupled neurons constitute elementary blocks of larger-scale ensembles that have more degrees of freedom in which to store information. This hypothesis is consistent with predictions from our model that the strongest connections form clusters with fewer neurons whereas weaker connections are more widely spread.

The influence of local extracellular electrical fields

The long-standing question of how the membrane potential of individual neurons is affected by extracellular fields is a difficult one to address experimentally. Most preparations so far lacked the spatial precision to stimulate and record multiple simultaneous sites (Deans, Powell et al. 2007) which proved to be of extreme importance. We demonstrated that extracellular fields do have significant impact on sub- and suprathreshold activity. More importantly, we showed that such impact can lead to more synchronized spike-timing in different neurons subject to similar fields and that the strength of this effect is greater during slow, high amplitude oscillations.

The ubiquity of FDDI and its recruitment

Interneurons represent roughly one fifth of the neuronal population but play a critical role in shaping the activity of the networks integrate. The large diversity of interneuronal types suggests a number of specific functional niches (Markram, Toledo-Rodriguez et al. 2004). This idea is

further supported by the different innervation patterns and short-term dynamics of interneuronal connectivity. However, the most compelling evidence for the different roles of the varied interneuron may be the different phase preference profiles recorded *in vivo* (Klausberger and Somogyi 2008).

The importance of the role of Martinotti cell mediated FDDI seems to be corroborated by the extent and frequency of its occurrence. The precise nature of this role, on the other hand, is not entirely clear. The facilitating short-term dynamics of the PC-MC synapse leading towards a later onset of their inhibitory action when compared to the inhibition provided by fast-spiking interneurons, provides the cortex with a repertoire of highly sensitive recurrent inhibition with large dynamic range (Kapfer, Glickfeld et al. 2007). The many activity regimes supported by the neocortex are likely to require different mechanisms to balance excitation and inhibition (Wehr and Zador 2003). Our results show that local networks of thick tufted PCs in L5 are surprisingly nearly homogeneously affected by FDDI triggered by brief bursts in few PCs. This illustrates the physiological relevance of FDDI since such bursts have been described *in vivo* (de Kock and Sakmann 2008). Furthermore, FDDI has also been implicated in blocking calcium spikes in the apical dendrites of L5 PCs, enhancing the dynamic range of sensory stimuli (Murayama, Perez-Garci et al. 2009)

Interacting networks

Incompatibilities between our observations and current models explaining electrical and synaptic connectivity in the olfactory bulb (Pinching and Powell 1971; Schoppa and Westbrook 2002) led us to conceive a new mechanism of signal transmission between Mitral cells where PSPs not only influence the direct postsynaptic compartment but can also travel through a gap junction to another compartment. This model required assumptions and generated predictions that were experimentally verified. Importantly, we could confirm the calculated direct synaptic connection probability in *knock out* mice that did not express gap junctions and provide experimental evidence explaining stronger coupling ratios between reciprocally connected MCs. Further

supporting our model, *knock out* mice had synaptic connectivity very close to randomly-distributed and the organization of gap junctions showed no signs of non-random distribution.

We therefore provided compelling evidence for an interaction between electrical and chemical synapses in the olfactory bulb with the possible consequences of enhancing network responsiveness while reducing metabolic cost.

Future directions

Throughout this work the combinatorial character of neuronal interactions is a constant and central element. The explosive nature of combinations, providing myriads of possibilities from much fewer components, should serve as a motivation to consider the possibility that neuronal networks utilize such a resource. In 1972 P. W. Anderson wrote an article entitled *More Is Different* where he states:

“The behavior of large and complex aggregates of elementary particles, it turns out, is not to be understood in terms of a simple extrapolation of the properties of a few particles. Instead, at each level of complexity entirely new properties appear...”

It may well be that in these entirely new properties, emerging from the interaction of the elementary components of the brain, reside key concepts to further explain perception, memory and higher cognitive functions. With this perspective, great potential can be seen in the pursuit of the investigation of interactions in neuronal networks eventually combining multi-electrode whole-cell recordings *in vitro*, and possibly *in vivo*, with other techniques well-adapted to the study of networks such as two-photon microscopy and fluorescent labeling of specific cell populations. A leap in the study of network interactions among neurons could be made possible by the introduction of electrodes based on single carbon nanotubes. Such techniques can significantly assist in explaining the relationship between behavior, neuronal network activity and the properties of individual neurons that collectively give rise to brain function.

Bibliography

- Abbott, L. F. and S. B. Nelson (2000). "Synaptic plasticity: taming the beast." Nat Neurosci **3** **Suppl**: 1178-1183.
- Abbott, L. F., J. A. Varela, et al. (1997). "Synaptic depression and cortical gain control." Science **275**(5297): 220-224.
- Abeles, M., H. Bergman, et al. (1993). "Spatiotemporal firing patterns in the frontal cortex of behaving monkeys." J Neurophysiol **70**(4): 1629-1638.
- Allen, D. M. and K. A. Hamilton (2000). "Ultrastructural identification of synapses between mitral/tufted cell dendrites." Brain Res **860**(1-2): 170-173.
- Amit, D. J., N. Brunel, et al. (1994). "Correlations of cortical Hebbian reverberations: theory versus experiment." J Neurosci **14**(11 Pt 1): 6435-6445.
- Amit, D. J., H. Gutfreund, et al. (1987). "Information storage in neural networks with low levels of activity." Phys Rev A **35**(5): 2293-2303.
- Anastassiou, C. A., S. M. Montgomery, et al. (2010). "The effect of spatially inhomogeneous extracellular electric fields on neurons." J Neurosci **30**(5): 1925-1936.
- Arvanitaki, A. (1942). "Effects evoked in an axon by the activity of a contiguous one." Journal of Neurophysiology **5**(2): 89-108.
- Aungst, J. L., P. M. Heyward, et al. (2003). "Centre-surround inhibition among olfactory bulb glomeruli." Nature **426**(6967): 623-629.
- Bacci, A., J. R. Huguenard, et al. (2004). "Long-lasting self-inhibition of neocortical interneurons mediated by endocannabinoids." Nature **431**(7006): 312-316.
- Barabasi, A. L. and Z. N. Oltvai (2004). "Network biology: understanding the cell's functional organization." Nat Rev Genet **5**(2): 101-113.
- Belluardo, N., G. Mudò, et al. (2000). "Expression of connexin36 in the adult and developing rat brain." Brain Res **865**(1): 121-138.
- Bi, G. Q. and M. M. Poo (1998). "Synaptic modifications in cultured hippocampal neurons: dependence on spike timing, synaptic strength, and postsynaptic cell type." J Neurosci **18**(24): 10464-10472.
- Bikson, M., M. Inoue, et al. (2004). "Effects of uniform extracellular DC electric fields on excitability in rat hippocampal slices in vitro." J Physiol **557**(Pt 1): 175-190.
- Blakemore, C., L. J. Garey, et al. (1978). "The physiological effects of monocular deprivation and their reversal in the monkey's visual cortex." J Physiol **283**: 223-262.
- Bliss, T. V. and T. Lomo (1973). "Long-lasting potentiation of synaptic transmission in the dentate area of the anaesthetized rabbit following stimulation of the perforant path." J Physiol **232**(2): 331-356.
- Bragin, A., G. Jando, et al. (1995). "Gamma (40-100 Hz) oscillation in the hippocampus of the behaving rat." J Neurosci **15**(1 Pt 1): 47-60.
- Brecht, M., M. Schneider, et al. (2004). "Whisker movements evoked by stimulation of single pyramidal cells in rat motor cortex." Nature **427**(6976): 704-710.
- Brock, L. G., J. S. Coombs, et al. (1952). "The recording of potentials from motoneurons with an intracellular electrode." J Physiol **117**(4): 431-460.
- Broser, P., V. Grinevich, et al. (2008). "Critical period plasticity of axonal arbors of layer 2/3 pyramidal neurons in rat somatosensory cortex: layer-specific reduction of projections into deprived cortical columns." Cereb Cortex **18**(7): 1588-1603.

- Brown, S. P. and S. Hestrin (2009). "Intracortical circuits of pyramidal neurons reflect their long-range axonal targets." Nature **457**(7233): 1133-1136.
- Brown, S. P. and S. Hestrin (2009). "Intracortical circuits of pyramidal neurons reflect their long-range axonal targets." Nature.
- Bruno, R. M. and B. Sakmann (2006). "Cortex is driven by weak but synchronously active thalamocortical synapses." Science **312**(5780): 1622-1627.
- Buzsaki, G. (2002). "Theta oscillations in the hippocampus." Neuron **33**(3): 325-340.
- Buzsaki, G. (2004). "Large-scale recording of neuronal ensembles." Nat Neurosci **7**(5): 446-451.
- Buzsaki, G., Z. Horvath, et al. (1992). "High-frequency network oscillation in the hippocampus." Science **256**(5059): 1025-1027.
- Castillo, P. E., A. Carleton, et al. (1999). "Multiple and opposing roles of cholinergic transmission in the main olfactory bulb." J Neurosci **19**(21): 9180-9191.
- Chan, C. Y., J. Hounsgaard, et al. (1988). "Effects of electric fields on transmembrane potential and excitability of turtle cerebellar Purkinje cells in vitro." J Physiol **402**: 751-771.
- Chan, C. Y. and C. Nicholson (1986). "Modulation by applied electric fields of Purkinje and stellate cell activity in the isolated turtle cerebellum." J Physiol **371**: 89-114.
- Chen, C. C., S. Abrams, et al. (2009). "Morphological heterogeneity of layer VI neurons in mouse barrel cortex." J Comp Neurol **512**(6): 726-746.
- Chklovskii, D. B. (2004). "Synaptic connectivity and neuronal morphology: two sides of the same coin." Neuron **43**(5): 609-617.
- Chklovskii, D. B., B. W. Mel, et al. (2004). "Cortical rewiring and information storage." Nature **431**(7010): 782-788.
- Christie, J. M., C. Bark, et al. (2005). "Connexin36 mediates spike synchrony in olfactory bulb glomeruli." Neuron **46**(5): 761-772.
- Christie, J. M. and G. L. Westbrook (2006). "Lateral excitation within the olfactory bulb." J Neurosci **26**(8): 2269-2277.
- Clauset, A., M. E. Newman, et al. (2004). "Finding community structure in very large networks." Phys Rev E Stat Nonlin Soft Matter Phys **70**(6 Pt 2): 066111.
- Compte, A., N. Brunel, et al. (2000). "Synaptic mechanisms and network dynamics underlying spatial working memory in a cortical network model." Cereb Cortex **10**(9): 910-923.
- Condorelli, D. F., N. Belluardo, et al. (2000). "Expression of Cx36 in mammalian neurons." Brain Res Brain Res Rev **32**(1): 72-85.
- de Kock, C. P. and B. Sakmann (2008). "High frequency action potential bursts (≥ 100 Hz) in L2/3 and L5B thick tufted neurons in anaesthetized and awake rat primary somatosensory cortex." J Physiol **586**(14): 3353-3364.
- Deans, J. K., A. D. Powell, et al. (2007). "Sensitivity of coherent oscillations in rat hippocampus to AC electric fields." J Physiol **583**(Pt 2): 555-565.
- Deans, M. R., J. R. Gibson, et al. (2001). "Synchronous activity of inhibitory networks in neocortex requires electrical synapses containing connexin36." Neuron **31**(3): 477-485.
- Djurisić, M., S. Antic, et al. (2004). "Voltage imaging from dendrites of mitral cells: EPSP attenuation and spike trigger zones." J Neurosci **24**(30): 6703-6714.
- Dudai, Y. (2002). Memory from A to Z : keywords, concepts, and beyond. Oxford, UK. ; New York, Oxford University Press.
- Dudai, Y. (2002). "Molecular bases of long-term memories: a question of persistence." Curr Opin Neurobiol **12**(2): 211-216.

- Edward D. de Asis, J., J. Leung, et al. (2009). "High spatial resolution single multiwalled carbon nanotube electrode for stimulation, recording, and whole cell voltage clamping of electrically active cells." Applied Physics Letters **95**(15): 153701.
- Ehrlich, I., M. Klein, et al. (2007). "PSD-95 is required for activity-driven synapse stabilization." Proc Natl Acad Sci U S A **104**(10): 4176-4181.
- Erdos, P. and A. Renyi (1960). "On the Evolution of Random Graphs." Bulletin of the International Statistical Institute **38**(4): 343-347.
- Fagiolini, M. and T. K. Hensch (2000). "Inhibitory threshold for critical-period activation in primary visual cortex." Nature **404**(6774): 183-186.
- Feldmeyer, D., V. Egger, et al. (1999). "Reliable synaptic connections between pairs of excitatory layer 4 neurones within a single 'barrel' of developing rat somatosensory cortex." J Physiol **521 Pt 1**: 169-190.
- Fellous, J. M. and T. J. Sejnowski (2003). "Regulation of persistent activity by background inhibition in an in vitro model of a cortical microcircuit." Cereb Cortex **13**(11): 1232-1241.
- Francis, J. T., B. J. Gluckman, et al. (2003). "Sensitivity of neurons to weak electric fields." J Neurosci **23**(19): 7255-7261.
- Frick, A., D. Feldmeyer, et al. (2007). "Postnatal development of synaptic transmission in local networks of L5A pyramidal neurons in rat somatosensory cortex." J Physiol **585**(Pt 1): 103-116.
- Friedman, R. M., L. M. Chen, et al. (2004). "Modality maps within primate somatosensory cortex." Proc Natl Acad Sci U S A **101**(34): 12724-12729.
- Fries, P., J. H. Reynolds, et al. (2001). "Modulation of oscillatory neuronal synchronization by selective visual attention." Science **291**(5508): 1560-1563.
- Fusi, S. and L. F. Abbott (2007). "Limits on the memory storage capacity of bounded synapses." Nat Neurosci **10**(4): 485-493.
- Fuster, J. M. and G. E. Alexander (1971). "Neuron activity related to short-term memory." Science **173**(997): 652-654.
- Gabernet, L., S. P. Jadhav, et al. (2005). "Somatosensory integration controlled by dynamic thalamocortical feed-forward inhibition." Neuron **48**(2): 315-327.
- Galarreta, M. and S. Hestrin (1999). "A network of fast-spiking cells in the neocortex connected by electrical synapses." Nature **402**(6757): 72-75.
- Ghai, R. S., M. Bikson, et al. (2000). "Effects of applied electric fields on low-calcium epileptiform activity in the CA1 region of rat hippocampal slices." J Neurophysiol **84**(1): 274-280.
- Godde, B., R. Leonhardt, et al. (2002). "Plasticity of orientation preference maps in the visual cortex of adult cats." Proc Natl Acad Sci U S A **99**(9): 6352-6357.
- Gold, C., D. A. Henze, et al. (2006). "On the origin of the extracellular action potential waveform: A modeling study." J Neurophysiol **95**(5): 3113-3128.
- Goldman-Rakic, P. S. (1995). "Cellular basis of working memory." Neuron **14**(3): 477-485.
- Gray, C. M., P. Konig, et al. (1989). "Oscillatory responses in cat visual cortex exhibit inter-columnar synchronization which reflects global stimulus properties." Nature **338**(6213): 334-337.
- Groh, A., C. P. de Kock, et al. (2008). "Driver or coincidence detector: modal switch of a corticothalamic giant synapse controlled by spontaneous activity and short-term depression." J Neurosci **28**(39): 9652-9663.

- Hamill, O. P., A. Marty, et al. (1981). "Improved patch-clamp techniques for high-resolution current recording from cells and cell-free membrane patches." *Pflugers Arch* **391**(2): 85-100.
- Harris, K. D., D. A. Henze, et al. (2002). "Spike train dynamics predicts theta-related phase precession in hippocampal pyramidal cells." *Nature* **417**(6890): 738-741.
- Hebb, D. O. (1949). "The Organization of Behavior - a Neuropsychological Theory." *Wiley, New York*.
- Heidmann, A., T. Heidmann, et al. (1984). "[Selective stabilization of neuronal representations by resonance between spontaneous prerepresentations of the cerebral network and percepts evoked by interaction with the outside world]." *C R Acad Sci III* **299**(20): 839-844.
- Histed, M. H., V. Bonin, et al. (2009). "Direct activation of sparse, distributed populations of cortical neurons by electrical microstimulation." *Neuron* **63**(4): 508-522.
- Hofer, S. B., T. D. Mrsic-Flogel, et al. (2009). "Experience leaves a lasting structural trace in cortical circuits." *Nature* **457**(7227): 313-317.
- Hoffman, D. A., R. Sprengel, et al. (2002). "Molecular dissection of hippocampal theta-burst pairing potentiation." *Proc Natl Acad Sci U S A* **99**(11): 7740-7745.
- Holscher, C., R. Anwyl, et al. (1997). "Stimulation on the positive phase of hippocampal theta rhythm induces long-term potentiation that can be depotentiated by stimulation on the negative phase in area CA1 in vivo." *J Neurosci* **17**(16): 6470-6477.
- Holt, G. R. and C. Koch (1999). "Electrical interactions via the extracellular potential near cell bodies." *J Comput Neurosci* **6**(2): 169-184.
- Holtmaat, A. and K. Svoboda (2009). "Experience-dependent structural synaptic plasticity in the mammalian brain." *Nat Rev Neurosci* **10**(9): 647-658.
- Hopfield, J. J. (1982). "Neural networks and physical systems with emergent collective computational abilities." *Proc Natl Acad Sci U S A* **79**(8): 2554-2558.
- Houweling, A. R. and M. Brecht (2008). "Behavioural report of single neuron stimulation in somatosensory cortex." *Nature* **451**(7174): 65-68.
- Hubel, D. H. and T. N. Wiesel (1970). "The period of susceptibility to the physiological effects of unilateral eye closure in kittens." *J Physiol* **206**(2): 419-436.
- Hull, C., J. S. Isaacson, et al. (2009). "Postsynaptic mechanisms govern the differential excitation of cortical neurons by thalamic inputs." *J Neurosci* **29**(28): 9127-9136.
- Huxter, J., N. Burgess, et al. (2003). "Independent rate and temporal coding in hippocampal pyramidal cells." *Nature* **425**(6960): 828-832.
- Hyman, J. M., B. P. Wyble, et al. (2003). "Stimulation in hippocampal region CA1 in behaving rats yields long-term potentiation when delivered to the peak of theta and long-term depression when delivered to the trough." *J Neurosci* **23**(37): 11725-11731.
- Ikegaya, Y., G. Aaron, et al. (2004). "Synfire chains and cortical songs: temporal modules of cortical activity." *Science* **304**(5670): 559-564.
- Ito, M. (1986). "Long-term depression as a memory process in the cerebellum." *Neurosci Res* **3**(6): 531-539.
- Jefferys, J. G. (1995). "Nonsynaptic modulation of neuronal activity in the brain: electric currents and extracellular ions." *Physiol Rev* **75**(4): 689-723.
- Jefferys, J. G. and H. L. Haas (1982). "Synchronized bursting of CA1 hippocampal pyramidal cells in the absence of synaptic transmission." *Nature* **300**(5891): 448-450.

- Ji, D. and M. A. Wilson (2007). "Coordinated memory replay in the visual cortex and hippocampus during sleep." *Nat Neurosci* **10**(1): 100-107.
- Kali, S. and P. Dayan (2004). "Off-line replay maintains declarative memories in a model of hippocampal-neocortical interactions." *Nat Neurosci* **7**(3): 286-294.
- Kalisman, N., G. Silberberg, et al. (2003). "Deriving physical connectivity from neuronal morphology." *Biol Cybern* **88**(3): 210-218.
- Kalisman, N., G. Silberberg, et al. (2005). "The neocortical microcircuit as a tabula rasa." *Proc Natl Acad Sci U S A* **102**(3): 880-885.
- Kamondi, A., L. Acsady, et al. (1998). "Theta oscillations in somata and dendrites of hippocampal pyramidal cells in vivo: activity-dependent phase-precession of action potentials." *Hippocampus* **8**(3): 244-261.
- Kampa, B. M., J. J. Letzkus, et al. (2006). "Cortical feed-forward networks for binding different streams of sensory information." *Nat Neurosci* **9**(12): 1472-1473.
- Kandel, E. R. (2001). "The molecular biology of memory storage: a dialogue between genes and synapses." *Science* **294**(5544): 1030-1038.
- Kandel, E. R. (2006). "In Search of Memory: The Emergence of a New Science of Mind."
- Kant, I. and J. M. D. Meiklejohn (1872). *Critique of pure reason*. London., Bell & Daldy.
- Kapfer, C., L. L. Glickfeld, et al. (2007). "Supralinear increase of recurrent inhibition during sparse activity in the somatosensory cortex." *Nat Neurosci* **10**(6): 743-753.
- Katzner, S., I. Nauhaus, et al. (2009). "Local origin of field potentials in visual cortex." *Neuron* **61**(1): 35-41.
- Kilgard, M. P. and M. M. Merzenich (1998). "Cortical map reorganization enabled by nucleus basalis activity." *Science* **279**(5357): 1714-1718.
- Kirkwood, A. and M. F. Bear (1994). "Homosynaptic long-term depression in the visual cortex." *J Neurosci* **14**(5 Pt 2): 3404-3412.
- Kirkwood, A., S. M. Dudek, et al. (1993). "Common forms of synaptic plasticity in the hippocampus and neocortex in vitro." *Science* **260**(5113): 1518-1521.
- Klausberger, T. and P. Somogyi (2008). "Neuronal diversity and temporal dynamics: the unity of hippocampal circuit operations." *Science* **321**(5885): 53-57.
- Knight, B. W. (1972). "The relationship between the firing rate of a single neuron and the level of activity in a population of neurons. Experimental evidence for resonant enhancement in the population response." *J Gen Physiol* **59**(6): 767-778.
- Koch, C. (1998). *Biophysics of Computation: Information Processing in Single Neurons (Computational Neuroscience)*, Oxford University Press, USA.
- Kosaka, T., M. R. Deans, et al. (2005). "Neuronal gap junctions in the mouse main olfactory bulb: morphological analyses on transgenic mice." *Neuroscience* **134**(3): 757-769.
- Kreiman, G., C. P. Hung, et al. (2006). "Object selectivity of local field potentials and spikes in the macaque inferior temporal cortex." *Neuron* **49**(3): 433-445.
- Krieger, P., T. Kuner, et al. (2007). "Synaptic connections between layer 5B pyramidal neurons in mouse somatosensory cortex are independent of apical dendrite bundling." *J Neurosci* **27**(43): 11473-11482.
- Kubota, K. and H. Niki (1971). "Prefrontal cortical unit activity and delayed alternation performance in monkeys." *J Neurophysiol* **34**(3): 337-347.
- Kurotani, T., K. Yamada, et al. (2008). "State-dependent bidirectional modification of somatic inhibition in neocortical pyramidal cells." *Neuron* **57**(6): 905-916.

- Land, P. W. and K. Kandler (2002). "Somatotopic organization of rat thalamocortical slices." J Neurosci Methods **119**(1): 15-21.
- Landisman, C. E. and B. W. Connors (2007). "VPM and PoM nuclei of the rat somatosensory thalamus: intrinsic neuronal properties and corticothalamic feedback." Cereb Cortex **17**(12): 2853-2865.
- Le Be, J. V. and H. Markram (2006). "Spontaneous and evoked synaptic rewiring in the neonatal neocortex." Proc Natl Acad Sci U S A **103**(35): 13214-13219.
- Le Be, J. V., G. Silberberg, et al. (2007). "Morphological, electrophysiological, and synaptic properties of corticocallosal pyramidal cells in the neonatal rat neocortex." Cereb Cortex **17**(9): 2204-2213.
- Lefort, S., C. Tómm, et al. (2009). "The excitatory neuronal network of the C2 barrel column in mouse primary somatosensory cortex." Neuron **61**(2): 301-316.
- Lehmann, K. and S. Lowel (2008). "Age-dependent ocular dominance plasticity in adult mice." PLoS ONE **3**(9): e3120.
- Letzkus, J. J., B. M. Kampa, et al. (2006). "Learning rules for spike timing-dependent plasticity depend on dendritic synapse location." J Neurosci **26**(41): 10420-10429.
- Li, C. Y., J. T. Lu, et al. (2004). "Bidirectional modification of presynaptic neuronal excitability accompanying spike timing-dependent synaptic plasticity." Neuron **41**(2): 257-268.
- Li, C. Y., M. M. Poo, et al. (2009). "Burst spiking of a single cortical neuron modifies global brain state." Science **324**(5927): 643-646.
- Lisman, J. (2003). "Long-term potentiation: outstanding questions and attempted synthesis." Philos Trans R Soc Lond B Biol Sci **358**(1432): 829-842.
- Logothetis, N. K., C. Kayser, et al. (2007). "In vivo measurement of cortical impedance spectrum in monkeys: implications for signal propagation." Neuron **55**(5): 809-823.
- Logothetis, N. K., J. Pauls, et al. (2001). "Neurophysiological investigation of the basis of the fMRI signal." Nature **412**(6843): 150-157.
- Lu, J., Y. Cui, et al. (2008). "Early auditory deprivation alters expression of NMDA receptor subunit NR1 mRNA in the rat auditory cortex." J Neurosci Res **86**(6): 1290-1296.
- Lu, X., S. Miyachi, et al. (2007). "Topographic distribution of output neurons in cerebellar nuclei and cortex to somatotopic map of primary motor cortex." Eur J Neurosci **25**(8): 2374-2382.
- Lubenov, E. V. and A. G. Siapas (2009). "Hippocampal theta oscillations are travelling waves." Nature **459**(7246): 534-539.
- Lubke, J. and D. Feldmeyer (2007). "Excitatory signal flow and connectivity in a cortical column: focus on barrel cortex." Brain Struct Funct **212**(1): 3-17.
- MacLean, J. N., B. O. Watson, et al. (2005). "Internal dynamics determine the cortical response to thalamic stimulation." Neuron **48**(5): 811-823.
- Malenka, R. C. and R. A. Nicoll (1999). "Long-term potentiation--a decade of progress?" Science **285**(5435): 1870-1874.
- Markram, H. (1997). "A network of tufted layer 5 pyramidal neurons." Cereb Cortex **7**(6): 523-533.
- Markram, H., J. Lubke, et al. (1997). "Physiology and anatomy of synaptic connections between thick tufted pyramidal neurones in the developing rat neocortex." J Physiol **500** (Pt 2): 409-440.

- Markram, H., J. Lübke, et al. (1997). "Physiology and anatomy of synaptic connections between thick tufted pyramidal neurones in the developing rat neocortex." *J Physiol (Lond)* **500** (Pt 2): 409-440.
- Markram, H., J. Lubke, et al. (1997). "Regulation of synaptic efficacy by coincidence of postsynaptic APs and EPSPs." *Science* **275**(5297): 213-215.
- Markram, H., M. Toledo-Rodriguez, et al. (2004). "Interneurons of the neocortical inhibitory system." *Nat Rev Neurosci* **5**(10): 793-807.
- Markram, H. and M. Tsodyks (1996). "Redistribution of synaptic efficacy between neocortical pyramidal neurons." *Nature* **382**(6594): 807-810.
- Marshall, L., H. Helgadottir, et al. (2006). "Boosting slow oscillations during sleep potentiates memory." *Nature* **444**(7119): 610-613.
- Martin, S. J., P. D. Grimwood, et al. (2000). "Synaptic plasticity and memory: an evaluation of the hypothesis." *Annu Rev Neurosci* **23**: 649-711.
- Martin, S. J. and R. G. Morris (2002). "New life in an old idea: the synaptic plasticity and memory hypothesis revisited." *Hippocampus* **12**(5): 609-636.
- Maskery, S. and T. Shinbrot (2005). "Deterministic and stochastic elements of axonal guidance." *Annu Rev Biomed Eng* **7**: 187-221.
- Maurer, A. P., S. L. Cowen, et al. (2006). "Organization of hippocampal cell assemblies based on theta phase precession." *Hippocampus* **16**(9): 785-794.
- McNaughton, B. L. (2003). "Long-term potentiation, cooperativity and Hebb's cell assemblies: a personal history." *Philosophical Transactions of the Royal Society of London Series B-Biological Sciences* **358**(1432): 629-634.
- Moore, T. and M. Fallah (2004). "Microstimulation of the frontal eye field and its effects on covert spatial attention." *J Neurophysiol* **91**(1): 152-162.
- Moussiades, L. and A. Vakali (2010). "Clustering dense graphs: A web site graph paradigm." *Information Processing & Management In Press, Corrected Proof*.
- Mumm, J. S., P. R. Williams, et al. (2006). "In vivo imaging reveals dendritic targeting of laminated afferents by zebrafish retinal ganglion cells." *Neuron* **52**(4): 609-621.
- Murayama, M., E. Perez-Garci, et al. (2009). "Dendritic encoding of sensory stimuli controlled by deep cortical interneurons." *Nature*.
- Murphy, G. J., D. P. Darcy, et al. (2005). "Intrglomerular inhibition: signaling mechanisms of an olfactory microcircuit." *Nat Neurosci* **8**(3): 354-364.
- Newman, M. E. and M. Girvan (2004). "Finding and evaluating community structure in networks." *Phys Rev E Stat Nonlin Soft Matter Phys* **69**(2 Pt 2): 026113.
- Nicolelis, M. A., L. A. Baccala, et al. (1995). "Sensorimotor encoding by synchronous neural ensemble activity at multiple levels of the somatosensory system." *Science* **268**(5215): 1353-1358.
- O'Keefe, J. and M. Recce (1993). "Phase relationship between hippocampal place units and the EEG theta rhythm." *Hippocampus* **3**(3): 317-330.
- Ohki, K., S. Chung, et al. (2005). "Functional imaging with cellular resolution reveals precise micro-architecture in visual cortex." *Nature* **433**(7026): 597-603.
- Parisi, G. (1986). "A Memory Which Forgets." *Journal of Physics a-Mathematical and General* **19**(10): L617-L620.
- Pastalkova, E., V. Itskov, et al. (2008). "Internally generated cell assembly sequences in the rat hippocampus." *Science* **321**(5894): 1322-1327.

- Perez-Garci, E., M. Gassmann, et al. (2006). "The GABAB1b isoform mediates long-lasting inhibition of dendritic Ca²⁺ spikes in layer 5 somatosensory pyramidal neurons." Neuron **50**(4): 603-616.
- Petreaunu, L., T. Mao, et al. (2009). "The subcellular organization of neocortical excitatory connections." Nature.
- Pimentel, D. O. and T. W. Margrie (2008). "Glutamatergic transmission and plasticity between olfactory bulb mitral cells." J Physiol (Lond) **586**(8): 2107-2119.
- Pinching, A. J. and T. P. Powell (1971). "The neuropil of the glomeruli of the olfactory bulb." J Cell Sci **9**(2): 347-377.
- Poirazi, P., T. Brannon, et al. (2003). "Arithmetic of subthreshold synaptic summation in a model CA1 pyramidal cell." Neuron **37**(6): 977-987.
- Polsky, A., B. W. Mel, et al. (2004). "Computational subunits in thin dendrites of pyramidal cells." Nat Neurosci **7**(6): 621-627.
- Poulet, J. F. and C. C. Petersen (2008). "Internal brain state regulates membrane potential synchrony in barrel cortex of behaving mice." Nature **454**(7206): 881-885.
- Radman, T., Y. Su, et al. (2007). "Spike timing amplifies the effect of electric fields on neurons: implications for endogenous field effects." J Neurosci **27**(11): 3030-3036.
- Rieck, R. W. and R. G. Carey (1985). "Organization of the rostral thalamus in the rat: evidence for connections to layer I of visual cortex." J Comp Neurol **234**(2): 137-154.
- Rothman, J. S., L. Cathala, et al. (2009). "Synaptic depression enables neuronal gain control." Nature **457**(7232): 1015-1018.
- Rubin, D. D. and S. Fusi (2007). "Long memory lifetimes require complex synapses and limited sparseness." Front Comput Neurosci **1**: 7.
- Sabatini, B. L., T. G. Oertner, et al. (2002). "The life cycle of Ca²⁺ ions in dendritic spines." Neuron **33**(3): 439-452.
- Schoppa, N. E. and G. L. Westbrook (2002). "AMPA autoreceptors drive correlated spiking in olfactory bulb glomeruli." Nat Neurosci **5**(11): 1194-1202.
- Schrlau, M. G., N. J. Dun, et al. (2009). "Cell electrophysiology with carbon nanopipettes." ACS Nano **3**(3): 563-568.
- Sebeo, J., K. Hsiao, et al. (2009). "Requirement for protein synthesis at developing synapses." J Neurosci **29**(31): 9778-9793.
- Sejnowski, T. J. and A. Destexhe (2000). "Why do we sleep?" Brain Res **886**(1-2): 208-223.
- Silberberg, G. and H. Markram (2007). "Disynaptic inhibition between neocortical pyramidal cells mediated by Martinotti cells." Neuron **53**(5): 735-746.
- Singer, W. (1995). "Development and plasticity of cortical processing architectures." Science **270**(5237): 758-764.
- Singer, W. and C. M. Gray (1995). "Visual feature integration and the temporal correlation hypothesis." Annu Rev Neurosci **18**: 555-586.
- Sjostrom, P. J. and M. Hausser (2006). "A cooperative switch determines the sign of synaptic plasticity in distal dendrites of neocortical pyramidal neurons." Neuron **51**(2): 227-238.
- Sjostrom, P. J., G. G. Turrigiano, et al. (2001). "Rate, timing, and cooperativity jointly determine cortical synaptic plasticity." Neuron **32**(6): 1149-1164.
- Skaggs, W. E., B. L. McNaughton, et al. (1996). "Theta phase precession in hippocampal neuronal populations and the compression of temporal sequences." Hippocampus **6**(2): 149-172.

- Song, S., P. J. Sjöström, et al. (2005). "Highly nonrandom features of synaptic connectivity in local cortical circuits." *PLoS Biol* **3**(3): e68.
- Stent, G. S. (1973). "A physiological mechanism for Hebb's postulate of learning." *Proc Natl Acad Sci U S A* **70**(4): 997-1001.
- Stepanyants, A., J. A. Hirsch, et al. (2008). "Local potential connectivity in cat primary visual cortex." *Cereb Cortex* **18**(1): 13-28.
- Steriade, M., A. Nunez, et al. (1993). "Intracellular analysis of relations between the slow (< 1 Hz) neocortical oscillation and other sleep rhythms of the electroencephalogram." *J Neurosci* **13**(8): 3266-3283.
- Steriade, M., A. Nunez, et al. (1993). "A novel slow (< 1 Hz) oscillation of neocortical neurons in vivo: depolarizing and hyperpolarizing components." *J Neurosci* **13**(8): 3252-3265.
- Stoney, S. D., Jr., W. D. Thompson, et al. (1968). "Excitation of pyramidal tract cells by intracortical microstimulation: effective extent of stimulating current." *J Neurophysiol* **31**(5): 659-669.
- Stopfer, M., S. Bhagavan, et al. (1997). "Impaired odour discrimination on desynchronization of odour-encoding neural assemblies." *Nature* **390**(6655): 70-74.
- Stuart, G., N. Spruston, et al. (2007). *Dendrites*. Oxford ; New York, Oxford University Press.
- Stuart, G. J. and B. Sakmann (1994). "Active propagation of somatic action potentials into neocortical pyramidal cell dendrites." *Nature* **367**(6458): 69-72.
- Taylor, C. P. and F. E. Dudek (1982). "Synchronous neural afterdischarges in rat hippocampal slices without active chemical synapses." *Science* **218**(4574): 810-812.
- Tehovnik, E. J., A. S. Tolias, et al. (2006). "Direct and indirect activation of cortical neurons by electrical microstimulation." *J Neurophysiol* **96**(2): 512-521.
- Thomson, A. M., A. P. Bannister, et al. (2002). "Target and temporal pattern selection at neocortical synapses." *Philos Trans R Soc Lond B Biol Sci* **357**(1428): 1781-1791.
- Thomson, A. M., J. Deuchars, et al. (1993). "Large, deep layer pyramid-pyramid single axon EPSPs in slices of rat motor cortex display paired pulse and frequency-dependent depression, mediated presynaptically and self-facilitation, mediated postsynaptically." *J Neurophysiol* **70**(6): 2354-2369.
- Thomson, A. M. and O. T. Morris (2002). "Selectivity in the inter-laminar connections made by neocortical neurones." *J Neurocytol* **31**(3-5): 239-246.
- Thomson, A. M., D. C. West, et al. (2002). "Synaptic connections and small circuits involving excitatory and inhibitory neurons in layers 2-5 of adult rat and cat neocortex: triple intracellular recordings and biocytin labelling in vitro." *Cereb Cortex* **12**(9): 936-953.
- Trachtenberg, J. T., B. E. Chen, et al. (2002). "Long-term in vivo imaging of experience-dependent synaptic plasticity in adult cortex." *Nature* **420**(6917): 788-794.
- Traub, R. D., F. E. Dudek, et al. (1985). "Simulation of hippocampal afterdischarges synchronized by electrical interactions." *Neuroscience* **14**(4): 1033-1038.
- Tsodyks, M., A. Uziel, et al. (2000). "Synchrony generation in recurrent networks with frequency-dependent synapses." *J Neurosci* **20**(1): RC50.
- Tsodyks, M. V. and H. Markram (1997). "The neural code between neocortical pyramidal neurons depends on neurotransmitter release probability." *Proc Natl Acad Sci U S A* **94**(2): 719-723.
- Vallbo, A. B., K. A. Olsson, et al. (1984). "Microstimulation of single tactile afferents from the human hand. Sensory attributes related to unit type and properties of receptive fields." *Brain* **107** (Pt 3): 727-749.

- van Rossum, M. C., G. Q. Bi, et al. (2000). "Stable Hebbian learning from spike timing-dependent plasticity." *J Neurosci* **20**(23): 8812-8821.
- Vanderwolf, C. H. (1969). "Hippocampal electrical activity and voluntary movement in the rat." *Electroencephalogr Clin Neurophysiol* **26**(4): 407-418.
- von Melchner, L., S. L. Pallas, et al. (2000). "Visual behaviour mediated by retinal projections directed to the auditory pathway." *Nature* **404**(6780): 871-876.
- Watts, D. J. and S. H. Strogatz (1998). "Collective dynamics of 'small-world' networks." *Nature* **393**(6684): 440-442.
- Watts, J. and A. M. Thomson (2005). "Excitatory and inhibitory connections show selectivity in the neocortex." *J Physiol* **562**(Pt 1): 89-97.
- Wehr, M. and A. M. Zador (2003). "Balanced inhibition underlies tuning and sharpens spike timing in auditory cortex." *Nature* **426**(6965): 442-446.
- West, D. C., A. Mercer, et al. (2006). "Layer 6 cortico-thalamic pyramidal cells preferentially innervate interneurons and generate facilitating EPSPs." *Cereb Cortex* **16**(2): 200-211.
- Wiesel, T. N. (1971). "Effects of monocular deprivation on the cat's visual cortex." *Trans Am Acad Ophthalmol Otolaryngol* **75**(6): 1186-1198.
- Wiesel, T. N. and D. H. Hubel (1965). "Comparison of the effects of unilateral and bilateral eye closure on cortical unit responses in kittens." *J Neurophysiol* **28**(6): 1029-1040.
- Womelsdorf, T., J. M. Schoffelen, et al. (2007). "Modulation of neuronal interactions through neuronal synchronization." *Science* **316**(5831): 1609-1612.
- Woolsey, T. A. and H. Van der Loos (1970). "The structural organization of layer IV in the somatosensory region (SI) of mouse cerebral cortex. The description of a cortical field composed of discrete cytoarchitectonic units." *Brain Res* **17**(2): 205-242.
- Wright, J. W., E. A. Kramer, et al. (2002). "Extracellular matrix molecules, long-term potentiation, memory consolidation and the brain angiotensin system." *Peptides* **23**(1): 221-246.
- Ylinen, A., A. Bragin, et al. (1995). "Sharp wave-associated high-frequency oscillation (200 Hz) in the intact hippocampus: network and intracellular mechanisms." *J Neurosci* **15**(1 Pt 1): 30-46.
- Yoshimura, Y., J. L. Dantzker, et al. (2005). "Excitatory cortical neurons form fine-scale functional networks." *Nature* **433**(7028): 868-873.
- Young, J. Z. (1979). "Learning as a process of selection and amplification." *J R Soc Med* **72**(11): 801-814.
- Yu, C., D. Derdikman, et al. (2006). "Parallel thalamic pathways for whisking and touch signals in the rat." *PLoS Biol* **4**(5): e124.
- Yu, Y. C., R. S. Bultje, et al. (2009). "Specific synapses develop preferentially among sister excitatory neurons in the neocortex." *Nature*.
- Zito, K., V. Scheuss, et al. (2009). "Rapid functional maturation of nascent dendritic spines." *Neuron* **61**(2): 247-258.

Appendix A Abbreviations

<i>Ase</i>	absolute synaptic efficacy
ACSF	artificial cerebrospinal fluid
AHP	after hyperpolarization
AMPA	α -amino-5-hydroxy-3-methyl-4-isoxazole propionic acid
AMPA R	AMPA receptor
AP	action potential
APV	R-2-amino-5-phosphonopentanoate (NMDAR antagonist)
BBB	blood brain barrier
CNQX	6-cyano-7-nitroquinoxaline-2,3-dione (AMPA R and kainite receptor antagonist)
CNS	central nervous system
CNT	carbon nanotube
<i>D</i>	time constant for depression
DA	dopamine
EPSC	excitatory postsynaptic current
EPSP	excitatory postsynaptic potential
<i>F</i>	facilitation time constant
FS	fast spiking interneuron
fMRI	functional magnetic resonance imaging
GABA	gamma-aminobutyric acid
GABA _A R	GABA receptor of type A
GABA _B R	GABA receptor of type B
GluR	glutamate receptor
GluR2	glutamate receptor subunit type 2
IPSC	inhibitory postsynaptic current
IPSP	inhibitory postsynaptic potential
IQ	intellectual quotient
ISI	interspike interval
KO	knock-out
L5	Layer V
LTD	long-term depression
LFP	local field potential
LTP	long-term potentiation
mPFC	medial prefrontal cortex
NBQX	3-dihydroxy-6-nitro-7-sulfamoyl-beno(f)quinoxaline (AMPA R antagonist)
NE	norepinephrine
NL	neuroligin
NMDA	<i>N</i> -methyl-D-aspartic acid
NMDAR	NMDA receptor
OB	olfactory bulb
PB	phosphate buffer
PC	pyramidal cell
PET	positron emission tomography
PN	postnatal day

<i>Pr</i>	probability of release
PV	parvalbumin
QX-314	sodium channel blocker
SD	standard deviation
S.E.M.	standard error mean
SFC	spike field coherence
SOM	somatostatin
SPW	sharp-wave
STA	spike-triggered average
S1	primary somatosensory cortex
<i>U</i>	utilization
VIP	vasoactive intestinal protein
5-HT	serotonin

Appendix B Software

The entire code for the computer-assisted patch-clamp interface is under version control (SVN) in the following repository: <https://bbpteam.epfl.ch/svn/PatchAssistant/trunk>. This repository is managed by the Blue Brain Project team.

Documentation is available with the code under the folder *doc*.

Additional installation and utilization instructions and hardware drivers can be found at: <http://wiki.epfl.ch/Inmc/patchassistantsetup> and <http://wiki.epfl.ch/Inmc/patchpatchassistant>.

Full featured PatchAssistant requires previous installation of the following software (available in the repository under the folder `..\PatchAssistant\Utils`):

- [Microsoft .NET Framework Version 1.1 Redistributable Package](#)
- [DirectX End-User Runtimes](#)
- [OpenCV 1.0](#)

The acquisition package PulseQ is also under version control in a repository administered by the BBP team: <https://bbpteam.epfl.ch/svn/PulseQ/trunk>.

Documentation is available with the code under the folder *doc*.

Additional installation instructions and hardware drivers can be found at: <http://wiki.epfl.ch/Inmc/pulseq>.

Table 1 Input device commands

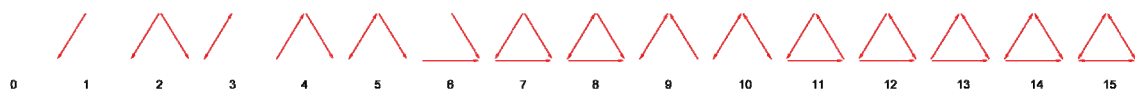
Control	A+	B+	C+	X+	Y+	Z+
POV	-	Arrow Keys	-	Y: Adjust Pipette Offset	X: Bridge Balance Y: Holding Current	-
Left XY	-	Mouse Cursor	-	Y: Adjust Pipette Offset	X: Bridge Balance Y: Pipette Capacitance	-
	-	Enter Key	Lock Manipulator	-	-	Control Positive Pressure
Z	-	-	Update Pipette Relative Position	-	-	-
Y	-	-	-	-	-	Apply Negative Pressure
X	-	-	-	-	-	Release Pressure
B	-	-	Locate Pipette Tip on Screen	-	-	-
	Microscope to Search Position	Left Mouse-click	Microscope to Assigned Cell	Zap	Send Data	-
R6	Recede Microscope	Right mouse-click	Microscope to Pipette	Automatic Pipette Offset	Automatic Pipette Offset	-
	Pipette to Search Position	Scroll Down	Approach Cell with Pipette and Microscope	Toggle Holding Potential	Toggle Holding Current	-
L5	Recede Pipette	Scroll Up	Pipette To Center of Screen	Toggle Seal Test	Toggle Tuning	-

Appendix C Clustered Connectivity Analysis

Table 2 Exhaustive listing of three neuron pattern codes

Simplified code	Pattern Code	(C1-C2) x1	(C1-C3) x2	(C2-C1) x4	(C2-C3) x8	(C3-C1) x16	(C3-C2) x32
0	0	0	0	0	0	0	0
1	1	1	0	0	0	0	0
1	2	0	1	0	0	0	0
2	3	1	1	0	0	0	0
1	4	0	0	1	0	0	0
3	5	1	0	1	0	0	0
4	6	0	1	1	0	0	0
5	7	1	1	1	0	0	0
1	8	0	0	0	1	0	0
4	9	1	0	0	1	0	0
6	10	0	1	0	1	0	0
7	11	1	1	0	1	0	0
2	12	0	0	1	1	0	0
5	13	1	0	1	1	0	0
7	14	0	1	1	1	0	0
8	15	1	1	1	1	0	0
1	16	0	0	0	0	1	0
4	17	1	0	0	0	1	0
3	18	0	1	0	0	1	0
5	19	1	1	0	0	1	0
6	20	0	0	1	0	1	0
9	21	1	0	1	0	1	0
9	22	0	1	1	0	1	0
10	23	1	1	1	0	1	0
4	24	0	0	0	1	1	0
11	25	1	0	0	1	1	0
9	26	0	1	0	1	1	0
12	27	1	1	0	1	1	0
7	28	0	0	1	1	1	0
12	29	1	0	1	1	1	0
13	30	0	1	1	1	1	0
14	31	1	1	1	1	1	0
1	32	0	0	0	0	0	1
6	33	1	0	0	0	0	1
4	34	0	1	0	0	0	1
7	35	1	1	0	0	0	1
4	36	0	0	1	0	0	1

9	37	1	0	1	0	0	1
11	38	0	1	1	0	0	1
12	39	1	1	1	0	0	1
3	40	0	0	0	1	0	1
9	41	1	0	0	1	0	1
9	42	0	1	0	1	0	1
13	43	1	1	0	1	0	1
5	44	0	0	1	1	0	1
10	45	1	0	1	1	0	1
12	46	0	1	1	1	0	1
14	47	1	1	1	1	0	1
2	48	0	0	0	0	1	1
7	49	1	0	0	0	1	1
5	50	0	1	0	0	1	1
8	51	1	1	0	0	1	1
7	52	0	0	1	0	1	1
13	53	1	0	1	0	1	1
12	54	0	1	1	0	1	1
14	55	1	1	1	0	1	1
5	56	0	0	0	1	1	1
12	57	1	0	0	1	1	1
10	58	0	1	0	1	1	1
14	59	1	1	0	1	1	1
8	60	0	0	1	1	1	1
14	61	1	0	1	1	1	1
14	62	0	1	1	1	1	1
15	63	1	1	1	1	1	1



Supplementary Figure C1 All simplified three-neuron connectivity patterns

Appendix D Analysis of interactions between synapses and gap junctions in the olfactory bulb

Matlab code used to solve Equation 1

```
function rg=gapjunction(pg,n,nnot)

pgd=sym('pgd');           %create symbolic variable

%define polynom
pol=sym2poly((1-pgd)*(1-pgd^2)^(n-2-nnot)-1+pg);%
r=roots(pol);             %find roots

%select applicable roots
ind1=find(imag(r)==0);
rg=r(ind1);
ind1=find((rg)<=1);
rg=rg(ind1);
ind1=find((rg)>=0);
rg=rg(ind1);
```

Matlab code used to solve Equation 2

```
function rc=synapc(pgd,pc,n,nnot)

pcd=sym('pgd');           %create symbolic variable

%define polynom
pol=sym2poly((1-pgd)*(1-pcd)*(1-pcd*pgd)^(n-2-nnot)-1+pc);
r=roots(pol);             %find roots

%select applicable roots
ind1=find(imag(r)==0);
rc=r(ind1);
ind1=find((rc)<=1);
rc=rc(ind1);
ind1=find((rc)>=0);
rc=rc(ind1);
```

Network simulation function to extract model predictions for experimental values of synaptic connection and gap junction probabilities

```

function [c,g,equivo]=MP_equivNet(pg,pc,n,tol)
%generate a random synaptic connectivity network whose
%connection probability is between pc-tol and pc+tol
c=0;g=0;
while( tol < abs(pc-1/n/(n-1)*(sum(sum(c)))) )
    c=(rand(n,n)<pc).*(1-eye(n));
end
%generate a simmetric random gap-junction network whose
%gap-junction probability is between pg-tol and pg+tol
while( tol < abs(pg-1/n/(n-1)*(sum(sum(g)))) )
    g=(rand(n,n)<pg).*(tril(ones(n,n),-1));
    g=g+g';
end
ge=g; %initial equivalent gap-junction network
ce=c; %initial equivalent synaptic network
for(i=1:n)
    for(j=i+1:n) %for all pairs
        if(g(i,j)) %if a direct gap-junction exists
            ce(i,j)=1; %a reciprocal synaptic connection
            ce(j,i)=1; %is assigned to the equivalent network
        end
        for(k=1:n) %for every other cell
            if(k==i || k==j) %not in the pair
                continue
            end
            if(c(i,k) && g(k,j))%identify indirect synaptic connections
                ce(i,j)=1; %assign equivalent network
            end
            if(c(j,k) && g(k,i))%identify indirect synaptic connections
                ce(j,i)=1; %assign equivalent network
            end
            if(g(i,k) && g(k,j))%identify indirect gap-junctions
                ge(j,i)=1; %assign equivalent network
                ge(i,j)=1;
            end
        end
    end
end
equiv=zeros(8,1); %calculate distribution of equivalent patterns
equivo=zeros(6,1);
for(i=1:n)
    for(j=i+1:n)
        val=ge(i,j)+ce(i,j)*2+ce(j,i)*4+1;
        equiv(val)=equiv(val)+1;
    end
end
equivo(1)=equiv(1); %simplify patterns
equivo(2)=equiv(2);
equivo(3)=equiv(3)+equiv(5);
equivo(4)=equiv(4)+equiv(6);
equivo(5)=equiv(7);
equivo(6)=equiv(8);
equivo=2*equivo/n/(n-1); %normalize by the number of pairs

```

Acknowledgements

This PhD work, realized between the years 2004 and 2010 in the Laboratory of Neuronal Microcircuitry (LNMC) at the Ecole Polytechnique Fédérale de Lausanne, has been a particularly enriching experience both on a professional as well as on a private perspective. The results presented in this manuscript would not have been obtained would I not have benefited from the help and support of several people to whom I would like to express my sincere gratitude.

I thank Prof. Henry Markram, my thesis supervisor, for having accepted me as a PhD student in his team and for the confidence he put in me by giving me the opportunity to work in his lab on such an interesting subject.

I thank Prof. Ralf Schneggenburger (Laboratory of Synaptic Mechanisms, EPFL, Lausanne) for accepting to be the president of the jury of the PhD oral defense. I also thank Prof. Matthew Larkum (Department of Physiology, University of Bern, Bern), Prof. Magnus Richardson (Warwick Systems Biology Centre, University of Warwick, UK) and Prof. Carl Petersen (Laboratory of Sensory Processing, EPFL, Lausanne), for having accepted to serve on my jury and for all of their time and effort.

I specially thank Sonia Garcia, my future wife, for all the support and encouragement which meant very much to me during all the years of my PhD.

I would also like to thank my parents who always had kind words and wise advice to help me through the most difficult moments.

Finally I'd like to thank my fellow lab members and the BBP team. Special thanks to Michele Pignatelli, Rajnish Ranjan, Shruti Muralidhar, Luca Gambazzi, Thomas Berger and Gilad Silberberg who were always cheerful and glad to lend a helping hand.

Curriculum Vitae

Rodrigo de Campos Perin

Av. Victor-Ruffy, 16b

1012 Lausanne

Switzerland

Phone: 078-6392514

rodrigo.perin@epfl.ch

Nationalities: USA and Brazilian

Birth: 25/01/1980 Ann Arbor, MI, USA

Work Experience

2004 – 2010 PhD Thesis

“Emergent Dynamics in Cortical Microcircuits“

Supervisor: Henry Markram, PhD

Laboratory of Neural Microcircuitry, Brain and Mind Institute, Sciences de la Vie

Ecole Polytechnique Fédérale de Lausanne, Lausanne, Switzerland

Recording electrical activity from single neurons is a very delicate operation. The complexity of the task limits the number of neurons that can actually be studied simultaneously. By developing an interface to control all of the necessary equipment I rendered possible the study of up to twelve cells at the same time. This led to a ten-fold increase in the neural connections that can be observed, opening way to new kinds of experiments on how neurons organize and communicate.

2003 – 2003 Field Project Assistant

Vector Engineering and Automation Systems, Americana, SP, Brazil

Main Projects:

- “Automation of the Water Treatment and Elevation Stations”

DESO, State of Sergipe, Brazil

- “Automation of the Water Treatment and Elevation Stations”

Water and Wastewater Department - DAE, Bauru, SP, Brazil

- Supervisory Control and Data Acquisition Software (Eclipse E3 SCADA)

The state of Sergipe is a small and poor region in Brazil where many people still do not have treated water supply. In this project I assisted in the documentation of existing equipment and participated in providing solutions to achieve better water distribution for thousands of people.

1998 – 2000 Volunteer Work,
Public Access Community Cable Television, NET Campinas, SP, Brazil
Collaborator, Equipment Operator and Event Organization Assistant

During this period the community channel transmissions were unreliable due to power oscillations and shortage. Among other attributions, I participated in technical improvements aimed at increasing the reliability of transmissions.

Education

1998 - 2003 Control and Automation Engineering Undergraduate Program
Mechanical Engineering Department
State University of Campinas (UNICAMP) Campinas, SP, Brazil

2000 - 2001 “Sandwich” Undergraduate Program
Texas A&M University, College Station, Texas, USA
Brazilian Federal Sponsor – CAPES, Brasilia, DF

Academic Experience

- 2003 – 2004 Internship
- Research Project: *“Automatic Positioning of 12 Pipettes in patch-clamping assembly with Vision System”*
- Advisor: Henry Markram, PhD
- Sponsor – Brain and Mind Institute, Ecole Polytechnique Fédérale de Lausanne
- Brain and Mind Institute, Sciences de la Vie
- Ecole Polytechnique Fédérale de Lausanne, Lausanne, Switzerland
-
- 2002 – 2003 Diploma Project
- Research Project: *“Environment Recognition based on Neural Networks for Robotic Machine Vision”*
- Advisor: Eurípedes G. O. Nóbrega, PhD
- Computational Mechanics, Mechanical Engineering Department, UNICAMP, Campinas
-
- 2001 Undergraduate Summer Research Program
- Research Project: *“Two Robots Carrying a Tray in a Perfectly Known Environment”*
- Advisor: Nancy Amato, PhD
- Sponsor – Texas A&M Undergraduate Summer Research Grants Program
- Parasol Lab, Department of Computer Science
- Texas A&M University, College Station, Texas, USA
-
- 1999-2000 Undergraduate Research Program
- Research Project: *“Finite Element Method Applied to Heat Conduction”*
- Advisor: Prof. Dr. Renato Pavanello
- Brazilian State Sponsor – FAPESP São Paulo, SP
- Computational Mechanics, Mechanical Engineering Department, UNICAMP, Campinas

Workshops and Seminars

- 1999,2000,2002 I,II, and IV Mechatronics Engineering Week
UNICAMP, Campinas, SP, Brazil
- 2001 I ENECA - National Control and Automation Engineering Students Meeting
Federal University of Santa Catarina - UFSC, Florianópolis, SC, Brazil
- 2003 Linguistics and Cognition Conference Language Studies Institute - IEL, UNICAMP,
Campinas, SP, Brazil
- 2005 Society for Neuroscience Annual Meeting – Presentation of Automated Patch-clamp Setup
Washington, USA
- 2006 FENS Annual Meeting, Viena, Austria - Poster presentation: “Properties of synaptic convergence
revealed by 12-patch clamping recordings in neocortical slices”
- 2007 Society for Neuroscience Annual Meeting – Poster presentation: “Motifs of Neocortical
Microcircuit Connectivity”
- 2008 FENS Annual Meeting, Geneva, Switzerland - Poster presentation: “Motifs of Neocortical
Connectivity”
- 2009 Society for Neuroscience Annual Meeting, Chicago, USA - Poster presentation: “Local anatomical
and functional clustering of neocortical neurons”

Languages

Portuguese , English and French: fluent

Computing Skills

Programming Languages:

Experienced with:

- C/C++, C#, Visual Basic , MATLAB, IGOR, Pascal, Java

Good skills in micropositioning, image processing, data acquisition (National Instruments, Instrutech and Data Translation) and programming for hardware control and simulation and modeling of neural networks.

Interests

Tennis, snowboarding, diving, traveling and reading.

Publications

Frequency-dependent disynaptic inhibition in the pyramidal network - a ubiquitous pathway in the developing rat neocortex. Berger TK, Perin R, Silberberg G, Markram H. *J Physiol*. 2009 Sep 21.